^{57}Fe MÖSSBAUER STUDIES OF PHOSPHATE - BASED GLASS SYSTEMS

GAVIN LEWIS WILLIAMS B.Sc.

A thesis submitted in partial fulfilment of the requirements
of the Council for National Academic Awards
for the degree of Doctor of Philosophy.

September 1990

Sponsoring Establishment: Sheffield City Polytechnic

Collaborating Establishment: Pilkington C.R.S.
Bishops Stortford, Hertfordshire

^{57}Fe Mössbauer Studies of Phosphate - Based Glass Systems

by

Gavin Lewis Williams B.Sc.

The structure-property relationships for a range of alkali and alkaline-earth phosphate glasses containing iron have been investigated. All the glasses were found to dissolve congruently in water, their durability showing a marked dependence on chemical composition and yielding dissolution rates ranging from 10^{-2}mg/mm^{2}hour down to 10^{-6}mg/mm^2 hour. S.I.M.S. and C.E.M.S. studies of the degraded glasses indicated a depletion of iron and sodium from the near surface regions.

All the glasses yielded spectra typical of octahedrally coordinated Fe^{3+} and Fe^{2+} with no evidence of tetrahedral sites or magnetic ordering. No compositional dependence of the Mössbauer parameters could be determined for two series of $Na_2O\_(K_2O)\_P_2O_5\_Fe_2O_3$ glasses. However, in the $xNa_2O\_20CaO\_(78\text{-}x)P_2O_5\_2Fe_2O_3$ glass system, the Fe^{2+} sites became more ordered as x increased. This was accompanied by a sixty fold decrease in durability over the same interval.

Use of a quadrupole doublet distribution fitting program indicated that in most of the glasses the Fe^{2+} and Fe^{3+} ions each occupy a single type of site within the glass. However, if all the iron is forced into either the ferric or ferrous state (by control of glass composition, furnace atmosphere and melt time) then it may occupy two types of site within the glass.

Spectra recorded from 12K upto 600K enabled effective Debye temperatures to be calculated. Absorption area data gave $\theta_D \sim 300$K, whilst second order Doppler shift (S.O.D.S.) calculations yielded higher values. The average Fe^{3+}/Fe^{2+} recoil-free fraction was 1.2 indicating the stronger bonding of the ferric iron. All Fe^{2+} S.O.D.S. data showed unexpected discontinuities at ~ 290K. A crystal field model led to a distortion parameter $\Delta_1 \sim 350$ cm^{-1} for the Fe^{2+} ions and also suggested that the ferrous iron sites are more distorted than those of the ferric iron.

CONTENTS

CHAPTER ONE - GLASS

1.1 Controlled Release Glass - An Introduction

The modern farmer employs a wide range of chemical and biochemical agents to modify natural processes. For instance, insecticides, herbicides and fungicides are used to protect crops and fertilisers are applied to stimulate their growth. Dietary supplements and drugs are administered to livestock in order to maintain and enhance their development. Ideally these agents should be supplied at the minimum effective rate, since any overdose is economically wasteful and may be harmful to the biosystem. In many areas other than agriculture there are similar requirements to supply active agents to aqueous systems at predetermined rates.

A number of methods for controlled agent delivery have been developed [1] which aim to maximise delivery efficiency. Most of the methods involve the incorporation of the active agent into an elastomeric matrix. The active agent is then released into the biosystem via one of a number of diffusion/dissolution mechanisms. With these elastomers it proves difficult to achieve a constant release rate. The elastomer is usually insoluble and will remain in the biosystem long after the active agent has been released.

As possible alternatives to the elastomeric delivery system a wide range of materials based on soluble glass are under development. The active agent(s) can be incorporated into the glass and by careful control of the chemical composition and preparation conditions a glass can be formed with virtually any desired dissolution rate. When placed in an aqueous environment the glass dissolves at a predetermined rate, releasing the active agents. Unlike elastomers there is no insoluble residue because the glass dissolves completely,

adding only harmless base glass compounds to the environment. Also, since the material is homogeneous, the active agents are released at a steady rate.

It is possible to fabricate glass in a wide range of physical forms to suit the application (Table 1.1). Solid blocks (boluses) of controlled release glass (CRG) have proved effective in supplying the vital trace elements cobalt, selenium and copper to lambs and steers [2,3,4]. The bolus is force fed to the animal and lies in the rumen. It dissolves at a constant rate and has been shown to supply a beneficial dose for as long as six months.

Powdered CRGs containing copper have proved to be an effective moluscide [5]. In particular they may be useful in preventing bilharziasis (schistosomiasis), a chronic disease endemic in certain parts of Africa, which is carried by parasites of certain watersnails. The powdered glass is spread over the waterways and settles on the bottom. The dissolution of the glass over a period of months results in a steady sub parts per million concentration of Cu^{2+} ions in the water. This dosage is lethal to the watersnails, yet is not toxic to higher organisms (including man). The CRG offers a large improvement over the conventional control method. This involves adding powdered copper sulphate which quickly dissolves, producing a giant peak in the Cu^{2+} concentration, and then falls rapidly as the ions are dispersed.

Refined glass processing techniques have created potential applications for CRG in medicine and industry. The glass can be drawn into fibres and then woven into a cloth for incorporation into complex structures. Interest has been shown in using soluble glass as a biomaterial for bone repair. In vivo trials have shown that CRG implanted into bone cause little or no cytoxic

effects and slowly dissolve allowing normal bone recovery [6,7]. CRG has also been used to monitor the wearing of dental braces [8].

The high processing temperatures necessary for glass formation make it impossible to incorporate drugs directly into the glassy matrix. However, by sintering a powdered CRG a porous material can be produced. This can then be loaded with a drug which will be released as the glass dissolves. One could imagine, for instance, a sintered glass implant loaded with insulin which would remove the dependence of many diabetics on daily injections. By using CRG as a soluble plug it is possible to devise pulse release systems, for example, the periodic addition of a corrosion inhibiter to a radiator system.

The first application of CRG technology was patented in 1974 by C.F. Drake [9] following development work at Standard Telephones and Cables Limited. The patent described a series of vitreous controlled release fertilisers. The fertiliser comprised a glassy matrix with phosphorus pentoxide as the main constituent, together with a number of other inorganic oxides and calcium cyanamide. The dissolution of the glass released phosphates and nitrogen compounds into the soil. Many further patents have since been filed, covering an ever wider range of compositions and applications [10,11,12]. Unlike the more familiar glasses based on amorphous silica most CRG are based around another glass forming oxide, phosphorus pentoxide P_2O_5. Other CRG may be based on boric oxide or even on chalcogenides.

The dissolution rate of a phosphate glass in an aqueous environment is a function of its exact chemical composition and specifically the amount and identity of other oxides incorporated into the glass. The work presented in

this thesis concerns phosphate glass containing varying amounts of iron oxide as a possible dissolution rate controller. ^{57}Fe Mössbauer spectroscopy has been used to investigate the iron sites within the glass and combined with other analytical techniques has enabled the rôle of the iron in the dissolution process to be established.

Table 1.1 The potential scope of applications of C.R.G.

Physical form	Potential Applications
Solid Block	Trace element delivery Biomaterial (bone repair) Corrosion prevention
Powdered Glass	Algicide, fungicide, bactericide, herbicide, insecticide, fertiliser
Sintered Glass	Drug delivery
Foam Glass	Moluscide, algicide
Glass fibre matting Surface coating	Marine fouling control

1.2 Structural Chemistry of Glass

1.2.1 General Aspects

Glass is popularly defined as an inorganic product of fusion which has cooled to a rigid condition without crystallisation. This definition is usually made with reference to the familiar silicate window glass, yet there are many glasses which do not fit this narrow definition, such as organic glasses and those prepared by low pressure vapour deposition. By considering the physical properties which unite all glasses an improved definition may be derived which is based on phenomenological rather than generic criteria.

X-ray diffraction studies show that the radial distribution function of a glass is unlike a crystalline solid and instead resembles that of a liquid (Fig. 1.1). As in a liquid the constituent atoms of a glass lack any long range topological order. The physical relationship between the glass, crystalline solid and liquid phases of a material can be explained by reference to the variation of volume with temperature (Fig. 1.2). As the material in its liquid phase is cooled its volume will decrease linearly until its freezing point T_f is reached. If the cooling rate is slow and nucleation sites are present within the melt than crystallisation will occur. If the liquid is cooled rapidly then crystallisation may not occur at T_f and instead a super- cooled liquid is produced which continues to contract at the same rate as the liquid.

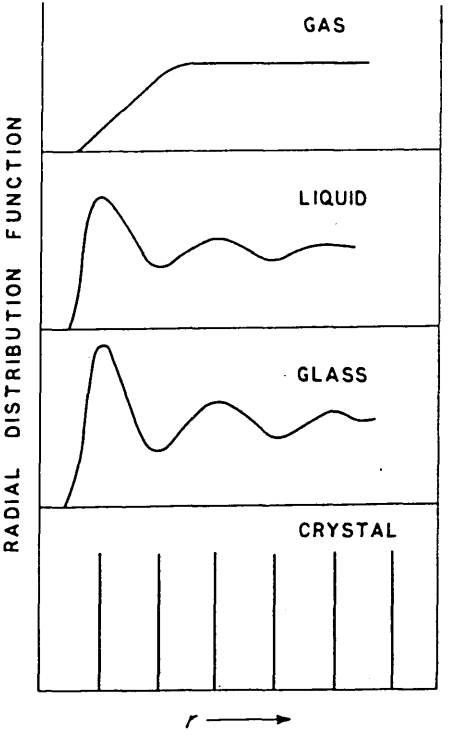

Figure 1.1 (after Paul [13]) Representative radial distribution functions for different physical states of a material.

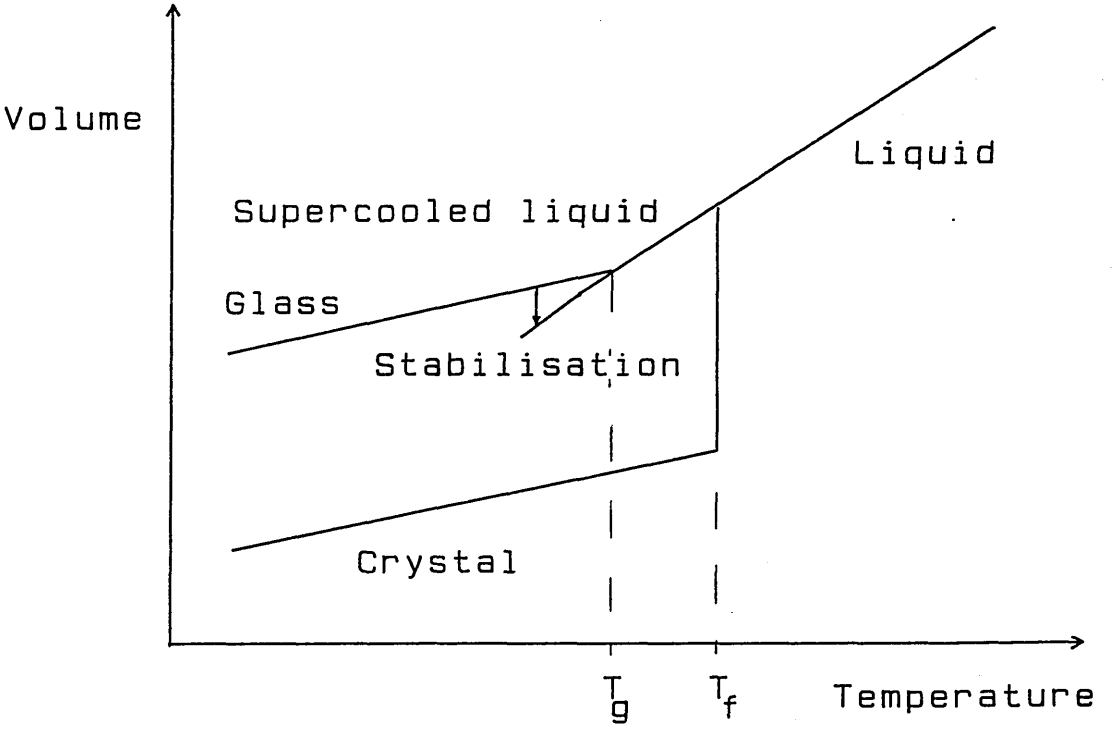

Figure 1.2 (after Jones [14]) The relationship between the different physical states.

The supercooled liquid has a higher free energy than the solid phase at the same temperature, hence there is a tendency towards crystallisation. However, associated with the formation of a supercooled liquid is a large increase in viscosity from ~10^2 poise to ~10^6 (1 poise = 0.1 $kgms^{-1}$) which inhibits this trend. Only in a narrow temperature range below T_f is crystallisation likely. At a temperature below T_f there is a significant change in the rate of contraction. This temperature is knows as the glass transition temperature T_g and occurs once the viscosity of the supercooled liquid had reached ~10^{13} poise. Below T_g the material contracts at a similar rate to the crystal. A material held at a temperature just below T_g will gradually contract until it meets the extrapolation of the liquid cooling curve, a process known as stabilisation. However, the viscosity below T_g increases to ~10^{20} poise and in practice the material follows the upper cooling curve if taken appreciably below T_g. It is this physical state below T_g which can be defined as constituting a glass. It has the internal energy and atomic arrangement of a liquid, whilst having an extremely high viscosity and thus the appearance of a solid.

1.2.2 Glass Forming Materials

In principle any material can be made into a glass if it is cooled sufficiently quickly through the region of T_f. However, in the majority of instances crystallisation intervenes. By far the most important glasses are based on inorganic oxides but there are many other chemical systems which will enter the vitreous state. Phosphorus, sulphur and selenium are the only individual elements which will form a glass. Added to these are many glasses based on the chalcogenides (S, Se, Te) with additions of Group IVB, VB, VIB elements [15]. Organic compounds, such as glycerol, will form a glass as

well as aqueous solutions of glucose. Water will form an amorphous phase if small droplets are cooled sufficiently rapidly [16]. Much interest is being exhibited in amorphous metals [17] because of their novel electronic and magnetic properties. Glasses have also been prepared from inorganic fluorides and chlorides.

Of the glass forming inorganic oxides silica (SiO_2) is the most widely used, although there are five other oxides including P_2O_5 which will form a glass (Table 1.2). In addition to the six glass forming oxides there are a number of 'conditional' glass forming oxides from which glasses can be made if mixed with a second oxide. Metal oxides will not form a glass alone but can be incorporated by suitable combination with a glass former. The metal oxides tend to disrupt the structure of the glass and are known as glass modifiers.

Table 1.2 (after Rawson [18]) Elements with glass forming oxides and conditional glass forming oxides ( ).

III B	IV A	IV B	V A	V B	VI A	VI B
B	(Ti)	(C)	(V)	(N)	(Mo)	(S)
(Al)		Si		P	(W)	(Se)
(Ga)		Ge		Sb		(Te)

Our present ideas concerning oxide glass structure are based on the theory developed by Zachariasen [19]. He argued that since the mechanical properties of glasses are similar to those of associated crystals, the forces linking the atoms in a glass must be essentially the same as those existing in the crystal. This implies that the structural units of the two phases are the

same, namely that each cation is surrounded by an oxygen polyhedron. In a crystalline solid, these structural units form a periodic lattice, but X-ray diffraction studies reveal no such periodicity for a glass. Instead the oxygen polyhedra form a disordered random network. A comparison between crystalline and glassy phases is shown in Figure 1.3.

Energy considerations concerning the alignment of the oxygen polyhedra led Zachariasen to formulate a number of criteria concerning oxide glass formation:

i) the oxygen atoms should be linked to not more than two glass forming cations.

ii) the coordination number of the cation should be small.

iii) the oxygen polyhedra should share corners with each other, not edges or faces

iv) at least three corners of each oxygen polyhedron should be shared.

These criteria are fulfilled for the oxides B_2O_3, As_2O_3 and Sb_2O_3 which form glasses based on oxygen triangles whilst SiO_2, GeO_2, P_2O_5 and Sb_2O_5 form glasses based on oxygen tetrahedra. There is some evidence that TeO_2 forms glasses based on oxygen octahedra. Smekal [20] has commented that the chemical bonds in a vitreous network can be neither fully covalent nor fully ionic. Purely covalent bonds imply fixed bond lengths and bond angles which are incompatible with the stable random arrangement of a glass. Purely ionic bonds are non-directional and hence there would be no opposition to crystallisation.

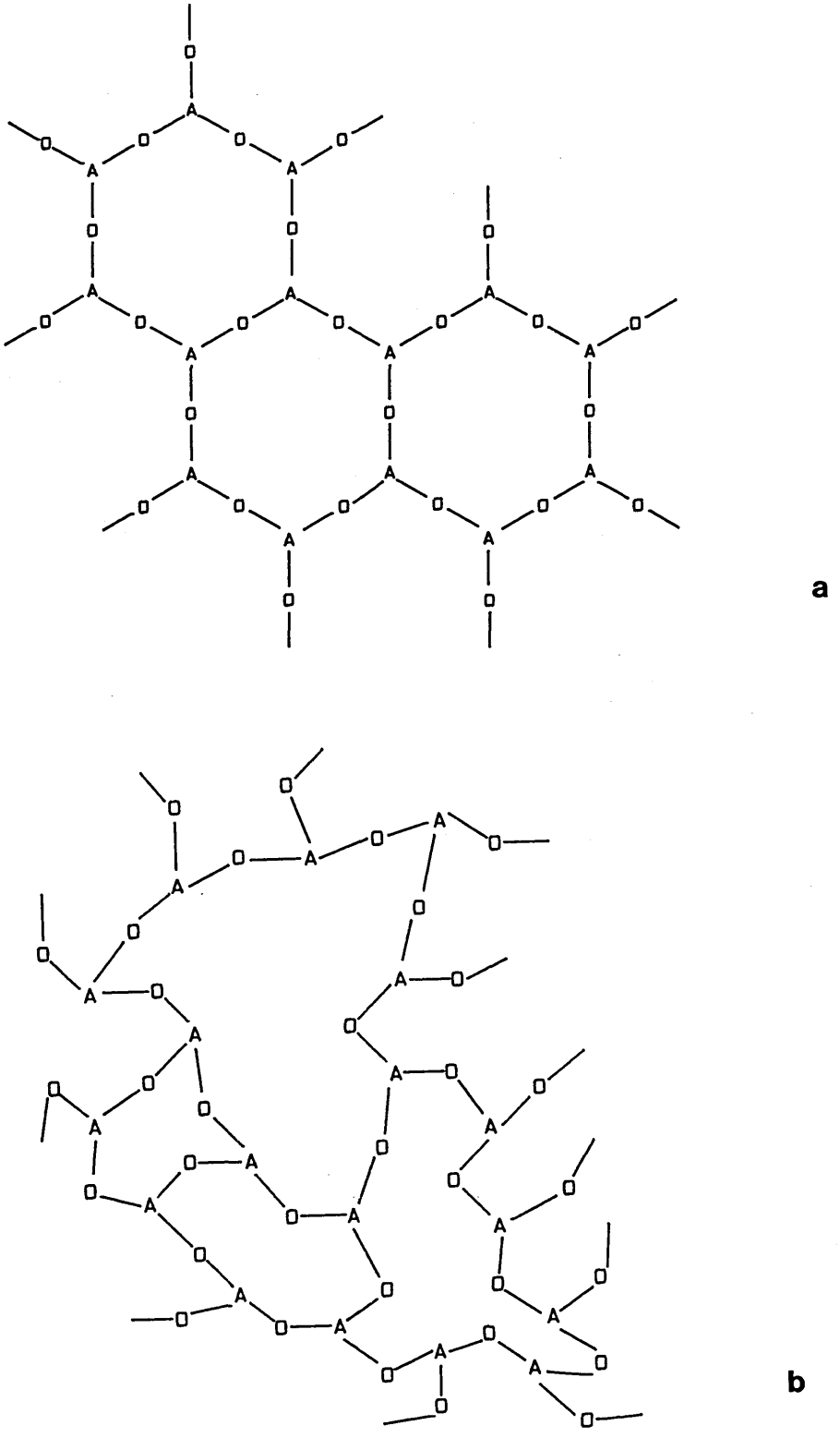

Figure 1.3 (after Zachariasen [19]) Two dimensional representation of the crystalline (a) and glassy (b) phases of a hypothetical oxide 'A_2O_3'.

Modifying oxides may be added to any of the above glass formers. The cations occupy the large voids in the network. They should have a low charge/radius ratio so that they do not greatly increase the potential energy of the glass by interaction with the glass forming cations. Hence typical modifying cations are Na^+, K^+, Ca^{2+}, Ba^{2+}, Pb^{2+}. According to the Zachariasen model these cations occupy a 'statistical distribution' of holes within the network, but recent work using the extended X-ray absorption fine structure technique (E.X.A.F.S) has suggested that they can posses a well defined short range order [21]. The extra oxygen introduced as part of the modifying oxide will alter the random network. Some of the oxygens involved in bridging between adjacent structural units will be converted into non-bridging oxygens (NBO's). For example $Si\text{-}O\text{-}Si + O^{2-} \rightarrow Si{=}O + Si{=}O$. The addition of a modifying oxide thus reduces the continuity of the network and introduces bonding of a more ionic nature between the modifying cations and their surrounding oxygens (Fig. 1.4). A third group of oxides, including Al_2O_3 and Fe_2O_3, is able to act as either a modifier or a former (Fig. 1.4).

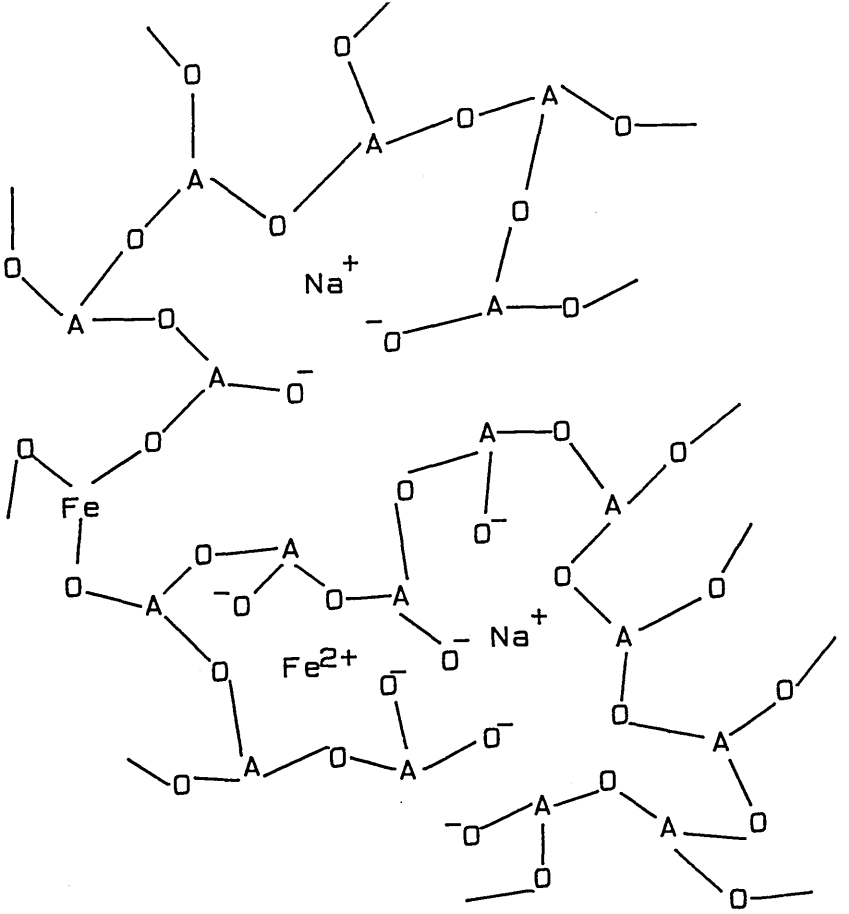

Figure 1.4 The effect of modifying oxides (e.g. Na_2O) and amphoteric oxides (e.g. Fe_2O_3) on the structure of 'A_2O_3'.

1.3 Phosphate Glass

1.3.1 Phosphate Glass Structure

Phosphorus pentoxide P_2O_5 is the only oxide of phosphorus known to form a glass. X-ray diffraction studies show that, as for silica SiO_2, the structural unit in P_2O_5 is an oxygen tetrahedron. In silica all four of the oxygen atoms are involved in linking to adjacent tetrahedra resulting in a regular three dimensional structure. This is not the case for the two crystalline allotropes of P_2O_5. The orthorhombic form is composed of two dimensional sheets of PO_4 tetrahedra each joined at three corners to surrounding tetrahedra, whilst the hexagonal form consists of isolated P_4O_{10} molecules which are comprised of four tetrahedra in a three dimensional pyramidal arrangement [22]. A continuous three dimensional crystalline arrangement of PO_4 tetrahedra is not possible because one of the oxygen atoms must be double bonded to the pentavalent phosphorus is order to maintain charge neutrality. The PO_4 tetrahedra is thus distorted as the P=O double bond (a non bridging oxygen) is shorter than the P-O single bond (a bridging oxygen) (Fig. 1.5).

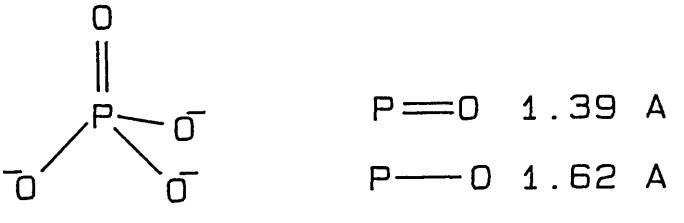

Figure 1.5 The PO_4 structural unit in crystalline P_2O_5. [22]

The P-O bond is neither fully covalent nor fully ionic hence variation in the bond length and P-O-P bond angle are possible in vitreous P_2O_5. The

glassy form of P_2O_5 consists of a three dimensional network of PO_4 tetrahedra, each linked at three corners to adjacent tetrahedra.

The addition of modifying oxides to vitreous P_2O_5 serves to disrupt the network. Van Wazer [23] has argued that phosphates where three oxygen atoms are shared per phosphorus atom are unstable with respect to those with two shared oxygen atoms. Thus the addition of a modifying oxide reduces the cross-linkage of the network of PO_4 tetrahedra. This is substantiated by X-ray and neutron diffraction studies of crystalline and glassy forms of sodium metaphosphate $(NaPO_3)_x$. The crystalline phase consists of helical chains of PO_4 tetrahedra linked at two corners [24]. The mean bond length for the bridging oxygen atoms is 1.61 Å and 1.48 Å for non-bridging oxygens (N.B.O.) [25] indicating some degree of distortion compared to pure P_2O_5 (Fig. 1.5). The sodium ions are five coordinate to the non-bridging oxygens (N.B.O.) (Na-O=2.42 Å) with a sixth oxygen a further 0.4 Å distant. The glassy phase [26,27] consists of long chains of PO_4 tetrahedra with cross-linking between chains occurring through N.B.O.-Na-N.B.O. bonds. The mean P=O bond length is 1.50 Å whilst the bridging oxygen bonds (P-O) have a mean value of 1.64 Å. The P=O bond is substantially longer than in the crystalline form. The neutron diffraction studies also suggest that the coordination number of N.B.O. around Na(~2) is much lower than for the crystalline phase (~5).

Van Wazer [28] has divided sodium phosphate glasses into two distinct categories dependent upon the Na_2O/P_2O_5 ratio. For Na/P<1 the glass consists of a branched network of PO_4 tetrahedra in accordance with the Zachariasen model. The fraction of PO_4 units involved in branching is given by (P-Na)/P.

For Na/P≥1 there can be no branching points, hence the tetrahedra adopt a polymer type structure consisting of rings and linear chains.

Extensive use has been made of paper chromatography to examine glasses with an Na/P ratio greater than unity [28,29,30]. The technique is based on the assumption that there is no rearrangement of the structural units of the glass on dissolution and thus the dissolution results solely from the hydrolysis of the ionic cross-linkages between the chains. The results confirm that high alkali glasses consist of variable length linear and cyclic chains of PO_4 tetrahedra, with the average chain length increasing towards infinity as the Na/P ratio decreased towards Na/P=1. This shows the complexity of even a simple binary phosphate glass and indicates the considerable structural reorganisation required in order for crystallisation to occur.

Paper chromatography has been applied to phosphate glass containing other alkali oxides K_2O, Li_2O, Rb_2O [31,32,33,34,35]. The results show quantitative differences suggesting that while the stoichiometry of the glass determines its general structure the species of cation does cause some variation in the chain length distributions.

Alkaline earth cations also occupy modifying sites within phosphate glass. X-ray diffraction studies of a simple $CaO-P_2O_5$ glass have shown that the calcium ions have about seven nearest neighbours [35]. Phosphate glass with high calcium and zinc contents have been analysed using paper chromatography [31] yielding results similar to those for alkali oxide-phosphate glass. One interesting difference was that instead of using distilled water a complex aqueous solution was required to dissolve the CaO and ZnO phosphate glass (§1.3.2).

Phosphate glasses have been prepared with many other metal oxides [37]. The cations occupy glass modifying sites, although there is some indication from electron paramagnetic resonance (E.P.R.) studies that ferric iron Fe^{3+} may occupy tetrahedrally coordinated network forming sites [38]. There is also the suggestion of tetrahedral Al^{3+} and B^{3+} in a limited composition range of phosphate glass [39].

In addition to the metal oxides the incorporation of water into the phosphate glass network must be considered. Even when precautions are taken to minimise the water content as much as 7 mol% H_2O (0.4 wt.%) may be present within the glass [40]. The hydronium ion H_3O^+ may substitute for modifying cations or effect the cross link density by cleaving P-O-P bonds resulting in the formation of hydroxyl groups [41].

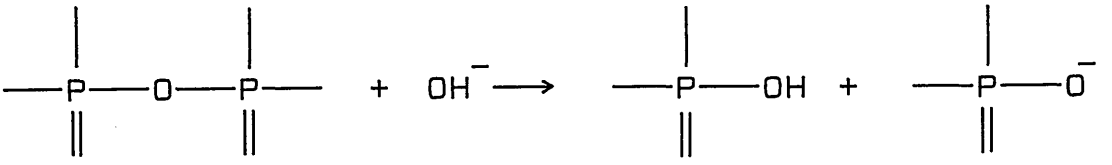

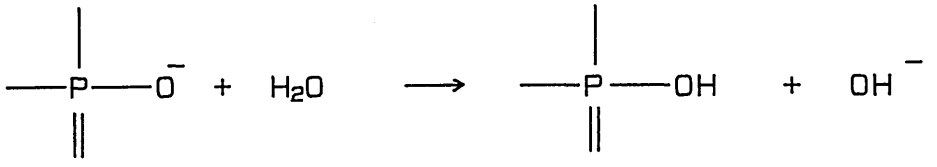

The water content may be sufficient to alter the physical properties of phosphate glass [42] and should be accounted for in order to accurately predict the glass structure.

1.3.2 Phosphate Glass Durability

The chemical durability of a glass is a measure of its resistance to attack by chemical agents. The physical forms which the glass may take and the nature and conditions of the chemical attack are many and various. This means that there is no one standard measure of durability and glasses are instead classified relative to one another after subjection to the same experimental conditions. Various methods are used to assess the results of durability experiments. Weight loss measurement will give a value for the bulk dissolution rate of the glass. Constituents of the glass passing into solution may be analysed using chromatographic titration and conductivity methods whilst a full compositional analysis can be made using inductively coupled plasma (I.C.P.) spectroscopy. The eroded surface of the glass may be analysed using a wide range of techniques including Auger electron spectroscopy (A.E.S.), secondary ion mass spectrometry (S.I.M.S.) and energy dispersive X-ray analysis (E.D.A.X.). The surface studies will usually require bulk glass, whereas solubility studies and solute analysis can be performed on both bulk and powdered glass.

The corrosion mechanism of a glass in contact with an aqueous solution consists of two complementary processes. The diffusion of water into the surface layers and the dissolution of the glass as a whole. The dissolution can be modelled to an equation of the form [43]:

$$M = at^{1/2} + bt \qquad 1.1$$

M = mass of dissolved glass

t = time

a,b = constants (determined empirically)

For a simple silicate glass the diffusion of water into the glass is accompanied by the leaching of sodium ions out of the glass resulting in a alkali depleted surface layer. The dissolution of $(50\text{-}x)M_2O\text{-}xCaO\text{-}5OP_2O_5$ glass can also be modelled by Eq. 1.1 [44]. However, inductively coupled plasma (I.C.P.) analysis reveals that, unlike silicate glass, there is no selective leaching of cations from the glass and instead the glass dissolves uniformly.

Equations of the form of Eqn. 1.1 are able to model the dissolution of most oxide glasses although there have inevitably been more rigorous and comprehensive treatments [45]. These models all assume that there is no build up of glass dissolution products in the aqueous solution. The potential use of inorganic glasses in the vitrification of nuclear wastes has focused attention on corrosion mechanisms in a limited volume of water [46]. The models developed account for changes in pH of the solution and possible back reactions with the glass [47].

The durability of a glass can be assessed by the time taken before it exhibits a linear dissolution rate. This is most easily determined by a logarithmic plot of weight loss versus time. A slope of 0.5 implies $t^{\frac{1}{2}}$ dependency (diffusion controlled) whilst a slope of 1.0 implies linear dissolution. For a low durability glass linear dissolution is reached within a few minutes, whilst a high durability glass will still exhibit $t^{\frac{1}{2}}$ behaviour after many days of leaching.

There are two possible mechanisms by which water can react with phosphate glass. It may directly hydrolyse the covalent, network forming P-O-P bonds or it may attack the ionic cross links of the network. Phosphate tetrahedra which are bonded to three neighbouring PO_4 groups (i.e. cross linking tetrahedra) are highly unstable with respect to those bonded to two PO_4 groups [48]. Hence, any cross links will be quickly hydrolysed in aqueous solutions (Fig. 1.6). This hydrolysis results in linear phosphate chains.

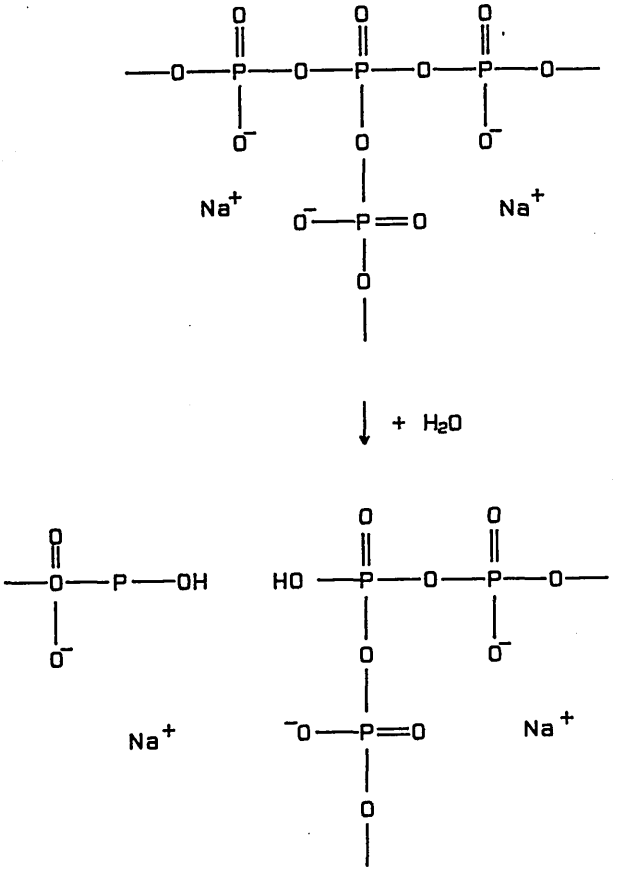

Figure 1.6 The hydrolysis of cross linked phosphate tetrahedra.

High modifier content phosphate glass also consists of linear chains cross linked by modifier cations. The linear P-O-P bond is resistant to hydrolysis [49] and any dissolution is a result of hydration of the modifier cations. Once a phosphate chain is fully surrounded by water it is free to pass into solution intact. The durability of a phosphate glass will increase as the chain

length increases, hence maximum durability will occur near the metaphosphate composition (50 mol% P_2O_5) [50]. For this composition the theoretical chain length is infinite but in practice, due to structural water, the maximum chain length is approximately forty PO_4 units.

There are a number of types of cross linking between linear phosphate chains. Hydroxyl groups may be linked by hydrogen bonding resulting in an increase in the effective length of the phosphate chains. Monovalent cations will form weak ionic cross links between the non-bridging oxygens of the PO_4 tetrahedra. Divalent cations such as Ca^{2+} and Mg^{2+} dramatically increase phosphate glass durability [44]. A metal chelate structure [51] has been proposed for these cross links (Fig. 1.7). Amphoteric oxides, such as Al_2O_3, will increase the durability of phosphate glass [52] by creating network forming tetrahedra which can cross link the phosphate chains (Fig. 1.8). As well as these predominantly ionic cross links it is possible to create covalent bonds between the chains by the incorporation of nitrogen into the glassy matrix [53]. The addition of 5 mol.% N to $Na_2O\_P_2O_5$ glass results in a ten fold increase in durability [54].

Phosphate glass durability shows a marked pH dependence. It has a maximum durability at pH~7 but shows pronounced increases in solubility in both acid and alkali solutions. Acid solutions will lead to the protonation of the phosphate chains and subsequent cleavage of the ionic cross linkages. Hence the phosphate chains will become hydrated more rapidly leading to a larger dissolution rate. In alkali solutions the dissolution rate may be enhanced because the terminal groups of the phosphate chains are not interconnected by hydrogen bonding [44].

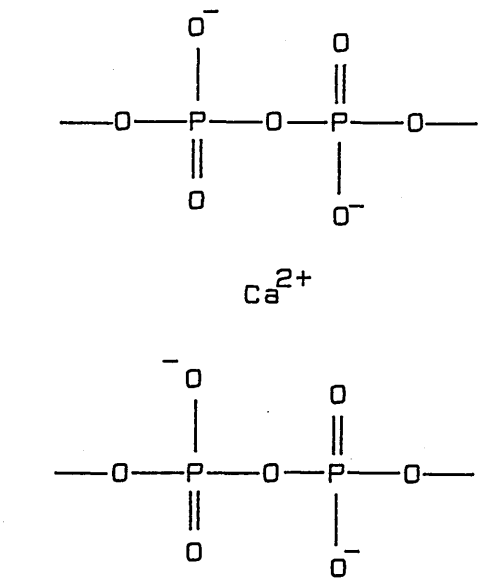

Figure 1.7 The metal chelate structure of a Ca^{2+} cross link.

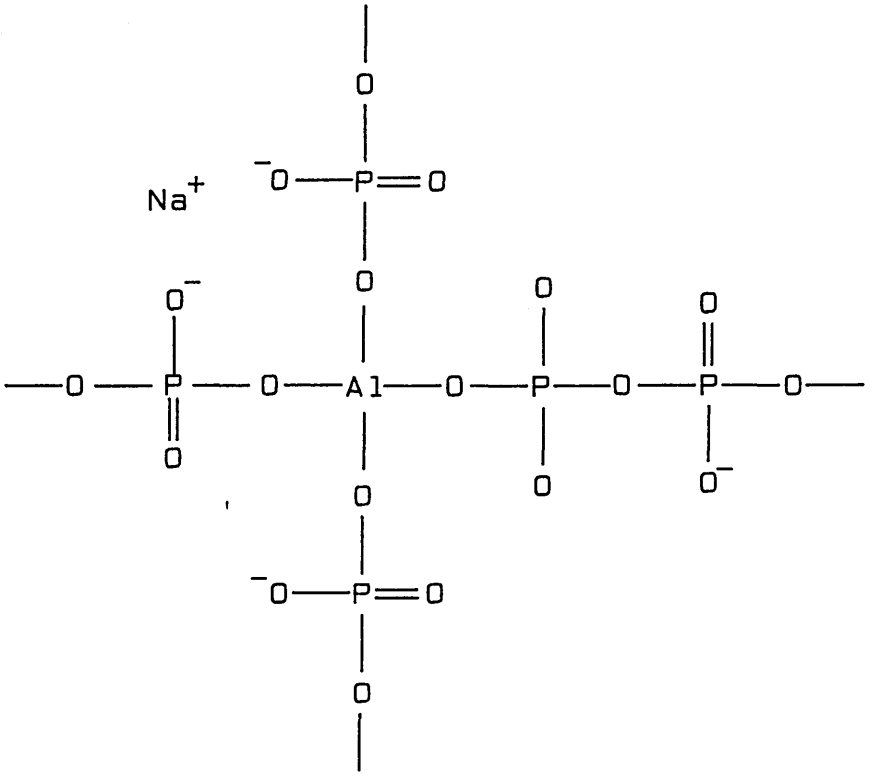

Figure 1.8 Cross linking of linear phosphate chains via the formation of $AlPO_4$.

1.4 Glass Production

1.4.1 Preparative Methods

Oxide glasses have been known to man for many centuries and have been used to produce decorative articles and household items. Their early development was on a purely empirical basis and not until the early nineteenth century was any serious attempt made to explain the nature of glassy materials. This interest was prompted by the desire to improve the quality of glass used in telescopes and other optical instruments. Oxide glasses are now used in a vast range of technical applications, each with its own set of chemical and physical requirements. For CRG this necessitates careful control of the chemical composition and the forming conditions in order to create a glass with the desired durability.

Reagent grade chemicals were used as the starting materials for the phosphate glasses examined in this study. The proportion of phosphorus pentoxide P_2O_5 used was kept to a minimum because of its hydroscopic nature. Instead, metal-hydrogen-phosphates were used to provide as much as possible of the desired amount of both P_2O_5 and alkali/alkaline earth oxides. Depending on the desired cation/phosphorus ratio the mono-, di- or tri- metal hydrogen phosphate could be used. Extra metal oxide was provided in the form of the carbonate, whilst extra P_2O_5 could be added as the ammonium salt. All of the necessary iron was added in the form of the ferric oxide Fe_2O_3.

To produce a desired glass composition weighed proportions of the appropriate chemicals were mixed together using a pestle and mortar. The

batch weight for each glass was approximately 20g. This mixture was then placed in a small ceramic crucible. Platinum crucibles were available, but they are not suitable for melting glass containing iron because of the possibility of alloying with the crucible walls. The crucible was placed in an electrically heated muffle furnace held at between 600°C and 700°C for twenty minutes. This preheating was sufficient to drive off the gaseous components CO_2, H_2O and NH_3 from the frit. The crucibles were reweighed to confirm the expected weight loss and then transferred to a second muffle furnace at 1100°C to complete the melting. After a further twenty minutes the molten glass was removed from the furnace and immediately cooled.

One of three cooling methods were used, depending on the required form of the glass and its tendency towards devitrification. The principle method involved splat cooling the glass directly onto a steel plate. For thinner samples, a second steel sheet could be pressed onto the top surface of the glass. The second method involved casting the molten glass into 4mm diameter moulds. It was found necessary to preheat the moulds to ~320°C in order to prevent shattering of the glass. The glass rods were removed from the moulds as quickly as possible (~30 seconds) and transferred to an oven held at 325°C. After annealing for a few hours they were slowly cooled to room temperature at a rate of 25°C/hour. This slow cooling, from a temperature in the region of T_g (the glass transition temperature), is essential if tensile stresses are to be avoided as these would rapidly shatter the rods. Both the steel plates and the moulds had a light coating of a carbon preparation 'Aquadag' to prevent their adhesion to the glass. For glass samples at the extremes of the glass forming region an even faster cooling method was used. This involved pouring the molten glass directly into a bath

of cold water. A somewhat steamy procedure! The resulting sinuous glass threads were quickly removed from the water and dried.

The majority of the glass were melted in an ambient atmosphere, although a few were melted under a flow of argon gas to assess the effect of oxygen fugacity on glass properties.

1.4.2 Compositional Analysis

The amorphous nature of the glass produced was checked by X-ray diffraction analysis using a Philips generator and goniometer with a graphite monochromater. The spectra did not display any sharp lines which would have been indicative of crystalline phases.

Checking of the glass compositions was performed using a Jarell Ash ICAP 900 inductively coupled plasma spectrometer [55]. 0.1g of the finely ground glass was dissolved in 8ml of concentrated nitric acid. Once fully dissolved the solution was made up to a volume of 100ml with distilled water. This led to a concentration in the order of one hundred ions per million water molecules (100 p.p.m). Known concentration solutions of the various elements were used to calibrate the instrument, along with a blank standard of distilled water. With the exception of phosphorus all the relevant elements had a permanent photomultiplier channel assigned to them. The phosphorus was monitored using a tuneable photomultiplier which was set at 253.50nm. This corresponds to one of the secondary transitions in phosphorus. The principle line could not be used because of interference from an iron emission line.

The results obtained are in the form of elemental concentrations in p.p.m. These can easily be manipulated to give a mol.% oxide compositional analysis. In general the P_2O_5 content always tended to be lower than expected, due to volatilisation of P_2O_5 during the melting phase. Compensation was made for this trend by adding a slight excess of P_2O_5 during the preparation of later glass samples.

1.5 References

1. Cardarelli N.
'Controlled Release Pesticide Formulations',
CRC Press. 1976

2. Allen W.M.; Sansom B.F.; Gleed P.T.; Mallinson C.B.; Drake C.F.
The Vetinary Record 115, 55, 1984

3. Allen W.M.; Sansom B.F.; Mallinson C.B.; Stebbings R.J.; Drake C.F.
The Vetinary Record 116, 175, 1985

4. Care A.D.; Anderson P.J.B.; Illingworth D.V.; Zervas G.; Telfer S.B.
in 'Trace Elements in Man and Animals', Proceedings from the 5th International Symposium on Trace Elements in Man and Animals. Editors: Mills, Bremner and Chesters, Commonwealth Agriculture Bureau, TEMA 5, 717

5. Jeswbury J.M.; Tripp M.; Drake C.F.
Transactions of the Royal Society of Tropical Medicine and Hygiene 73, (3), 323, 1979

6. Burnie J.; Gilchrist T.; Duff S.R.I.; Drake C.F.; Harding N.G.L.; Malcolm A.J.
Biomaterials 2, 244, 1981

7. Burnie J.; Gilchrist T.
in 'Ceramics in Surgery' Editor: Vincenzini P., Elsevier. p.169, 1983

8. Savage M.

British Journal of Orthodontics 9, 190, 1982.

9. Drake C.F.

Vitreous Controlled Release Fertiliser Composition. British Patent 1 512 637, 1974.

10 Drake C.F.

Improvements in Biocidal Compositions. British Patent 1 542 064, 1976

11. Drake C.F.; Layton D.E.

Arrangements for the controlled release of biologically active material British Patent 1 542 414, 1977

12. Drake C.F.; Tripp M.

Glass composition: $CuO-P_2O_5-M_2O+Al_2O_3$ and subcutaneous implant thereof. British Patent 2 037 735, 1978.

13. Paul A.

'Chemistry of Glass', Chapman and Hall, p.2, 1982

14. Jones G.O.

'Glass', Chapman and Hall, p.2, 1971

15. Rawson H.

'Inorganic glass forming systems', Academic Press, p.249, 1967

16. ibid. p.225

17. Elliot S.R.

'Physics of Amorphous Materials', Longman, p.311, 1983

18. Rawson H.

'Inorganic glass forming systems', Academic Press, p.9, 1967

19. Zachariasen W.H.

Journal of the American Chemical Society, 54, 3841, 1932

20. Smekal A.

Journal of the Society of Glass Technology, 35, 411, 1951

21. Greaves G.N.; Fontaine A.; Longarde P. Raoux D.; Gurman S.J.

Nature. 293, 611, 1981

22. Van Wazer J.R.

'Phosphorus and its compounds. Volume 1: Chemistry', Interscience p.270, 1958

23. Van Wazer J.R.; Holst K.A.

Journal of the American Chemical Society, 72(2), 639, 1950

24. Jost K.H.

Acta Crystallographica 14, 844, 1961

25. McAdam A.; Jost K.H.; Beagley B.

Acta Crystallographica B24, 1621, 1968

26. Brady G.W.

Journal of Chemical Physics 28(1), 48, 1958

27. Suzuki, K.; Heno M.

Journal de Physique 46, C8-261, 1985

28. Van Wazer J.R.

Journal of the American Chemical Society 72, 644, 1950

29. Van Wazer J.R.

Journal of the American Chemical Society 72, 647, 1950

30. Westman A.E.R.; Crowther J.

Journal of the American Ceramic Society 37(a), 420, 1954

31. Meadowcroft T.R.; Richardson F.D.

Transacations of the Faraday Society 61, 54, 1965

32. Westman A.E.R.; Gartaganis P.A.

Journal of the American Ceramic Society 40(9), 293, 1957

33. Murthy M.K.; Smith M.J.; Westman A.E.R.

Journal of the American Ceramic Society 44(3), 97, 1961

34. Murthy M.K.; Westman A.E.R.

Journal of the American Ceramic Society 44(10), 475, 1961

35. Murthy M.K.; Westman A.E.R.

Journal of the American Ceramic Society 45(9), 401, 1962

36. Biscoe J.; Pincus A.G.; Smith C.S.; Warren B.E.

Journal of the American Ceramic Society 24(4), 116, 1941

37. Nelson, B.N.; Exarhos G.J.

Journal of the Chemical Physics 71(7), 2739, 1979

38. Nishida T.; Shiotsuki T.; Takashima Y.

Journal of Non-Crystalline Solids 43, 115, 1981

39. Kreidl N.J.; Weyl W.A.

Journal of the American Ceramic Society 24, 372, 1941

40. Gray P.E.; Klein L.C.

Glass Technology 23(4), 177, 1982

41. Ray N.H.; Lewis C.J.

Journal of Materials Science 7, 47, 1972

42. Arriagada J.C.; Burckharott W.; Feltz A.

Journal of Non-Crystalline Solids 91, 375, 1987

43. Paul A.

'Chemistry of Glass' Chapman and Hall, p.111, 1982

44. Bunker, B.C.; Arnold G.W.; Wilder J.A.

Journal of Non-Crystalline Solids 64, 291, 1984

45. Isard J.O.; Allnatt A.R.; Melling P.J.

Physics and Chemistry of Glass 23(6), 185, 198

47. Van Iseghem P.; Timmermans W.; De Batist R.

Materials Research Society Symposium Proceedings 26, 527, 1984

48. Van Wazer J.R.

'Phosphorus and its compounds. Volume 1: Chemistry', Interscience p.437, 1964

49. Crowther J.; Westman A.E.R.

Canadian Journal of Chemistry 34, 969, 1956

50. Ray N.H.; Laycock J.N.C.; Robinson W.D.

Glass Technology 14(2), 55, 1973

51. Van Wazer J.R.; Campanella D.A.

Journal of the American Chemical Society 72, 655, 1950

52. Takashima K.

Technical Papers, Sixth International Congress on Glass, Washington

p.366, 1962

53. Peng Y.B.; Day D.E.

Journal of the American Ceramic Society 70(4), 232, 1987

54. Bunker B.C.; Arnold G.W.; Rajaram M.; Day D.E.

Journal of the American Ceramic Society 70(6), 425, 1987

55. Ebdon L.

'An Introduction to Atomic Absorption Spectroscopy', Heyden Press, 1982

CHAPTER TWO - MÖSSBAUER SPECTROSCOPY

2.1 Mössbauer Spectroscopy - Theory

2.1.1 Introduction

The emission and resonance absorption of optical quanta is a well known and widely utilised phenomenon. It results from the transition of electrons between atomic, or molecular, energy levels and gives rise to important analytical techniques such as atomic absorption spectroscopy (A.A.S.) and infra-red spectroscopy (I.R.S.). The nuclear analogue involves transitions between nuclear energy levels and the resulting emission and absorption of γ-rays. Special experimental procedures are required in order to observe these transitions since motion of the nuclei will normally Doppler shift the γ-ray energies sufficiently to destroy any resonance between an emitter and an absorber. The motion of the nuclei has two components; firstly the thermal motion of each nucleus on its lattice site and secondly the recoil of the nucleus on emission or absorption of a γ-ray.

In 1951 P.B. Moon [1] first achieved nuclear resonance by mounting a radioactive source on an ultracentrifuge. The Doppler energy supplied to the source was sufficient to compensate for the recoil of the nuclei and the resultant γ-ray could be resonantly absorbed by a stationary ground state absorber of the same material.

In 1958 Rudolf Mössbauer discovered the phenomenon which now bears his name - that of recoil-free nuclear resonance fluorescence [2]. He observed an unusual temperature dependence for the absorption cross-section of the 129 KeV γ-ray produced by the decay of ^{191}Ir. At low temperatures the cross-section showed a substantial increase. This was contrary to expectations

- lower temperatures should lead to a narrowing of the thermal absorption and emission profiles, hence a decrease in their degree of overlap and hence a slight decrease in cross-section.

The phenomenon can be explained by postulating that, as the temperature falls, there is an increase in the number of nuclei which become 'frozen' within the lattice. These 'frozen' nuclei have no thermal motion and are unable to recoil, hence they will emit/absorb γ-rays with an energy exactly equivalent to the nuclear transition energy. Hence the cross-section increases as the temperature of either the source, absorber or both is decreased.

About forty isotopes are known to exhibit this phenomenon of recoil-less γ-ray transitions [3]. Of these, ^{57}Fe and ^{119}Sn are the most commonly used for chemical applications.

The γ-rays produced by these isotopes have an exceptionally narrow line width ($\sim 10^{-8}$eV) which may be used to probe the hyperfine structure of nuclear energy levels. The spectral energy resolution is of the order of $1:10^{12}$ - a sensitivity unrivalled by any other spectroscopic technique.

2.1.2 Free Atom Energetics

On a superficial basis the emission and absorption profiles for a given transition of energy E_o will not coincide at E_o because of energy shifts due to recoil of the nucleus. There will, however, be some overlap as a result of thermal broadening of the lines. (Fig. 2.1)

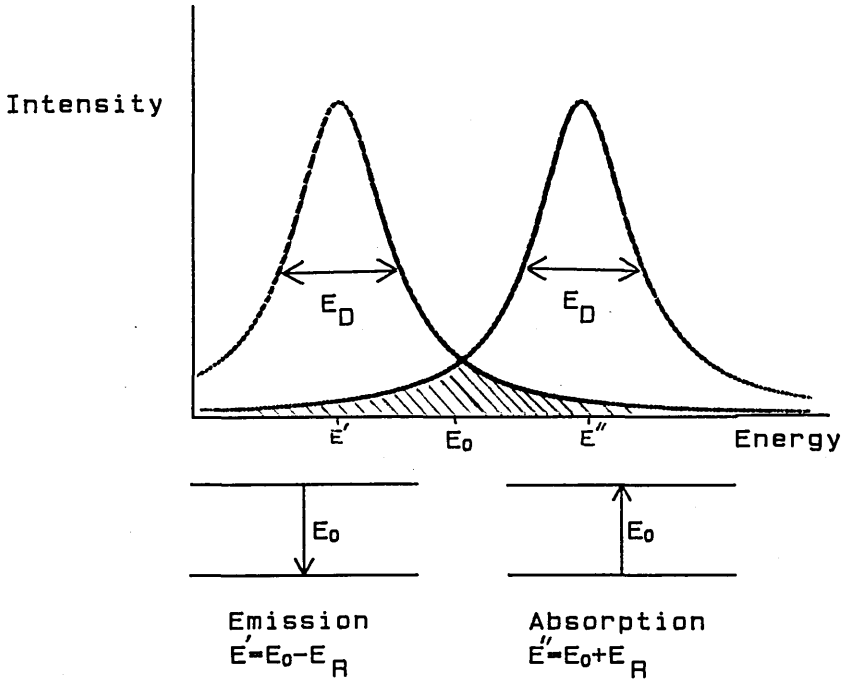

Figure 2.1 Absorption and emission profiles for a free atom transition.

For the emission and absorption of a quanta resulting from a transition energy E_o:

$$E^I = E_o - E_R \qquad 2.1$$

$$E^{II} = E_o + E_R \qquad 2.2$$

These profiles have a width E_D which may be defined in terms of the root mean square thermal velocity of the assembly of atoms $\bar{v}$, which will itself be temperature dependent:

$$E_D = \frac{\overline{v}}{c} E_o \qquad 2.3$$

Non relativistic mechanics lead to a simple equation for the recoil energy E_R.

$$E_R = \frac{p_n^2}{2m} \qquad 2.4$$

Where p_n is the momentum of the nucleus after emission or absorption of a quanta and m is the mass of the nucleus. By conservation of momentum p_n is equal to the momentum of the quanta p_γ:

$$p_n = p_\gamma = \frac{E_\gamma}{c} \qquad 2.5$$

hence, substituting into Eqn. 2.4:

$$E_R = \frac{E_\gamma^2}{2mc^2} \qquad 2.6$$

but $E_\gamma = E_o \pm E_R$ and since $E_R << E_o$; $E_\gamma \simeq E_o$ therefore:

$$E_R = \frac{E_o^2}{2mc^2} \qquad 2.7$$

Note that the recoil energy E_R is proportional to the square of the transition energy E_o (Eqn. 2.7) whilst the Doppler width E_D is directly proportional to E_o (Eqn. 2.3). It is instructive to derive values for E_R and E_D from typical values of E_o for electronic and nuclear transitions (Table 2.1). For an electronic transition the recoil energy E_R is insignificant compared to the Doppler width E_D, hence there is total overlap between the absorption and emission profiles. Clearly recoil may be disregarded for atomic resonance experiments. However, for the higher energy nuclear transitions E_R becomes comparable to E_D hence there is only a small degree of overlap in the wings of the absorption and emission profiles. The recoil energy becomes a very real obstacle to the observation of nuclear resonance.

Table 2.1 Typical parameter values for electronic and nuclear transitions within a free atom of mass 100 a.m.u.

Parameter	Electronic Transition	Nuclear Transition
E_o Transition Energy (eV)	10	10^5
E_R Recoil Energy (eV)	5×10^{-10}	0.1
E_D Doppler Width (eV)	10^{-5}	0.1
Overlap of profiles (%)	~100	~0

2.1.3 Recoilless Emission

The previous section dealt with the energetics of free atoms and indeed in the gaseous phase it is not possible to detect nuclear resonance fluorescence. However, in the solid, and exceptionally the liquid, phase the chemical bonding of the atoms may inhibit their ability to recoil on emission or absorption of a γ-ray, thus permitting some resonance.

The solid lattice may be considered as a single, quantum mechanical system and as such its vibrational energy levels are quantised. The form of this phonon quantisation will be extremely complex, yet it is instructive to examine two approximations. The first is the Einstein model of solids [4] which assumes a single lattice vibration frequency ω_E, with allowed energy levels given by:

$$E_n = (n+\tfrac{1}{2})\hbar\omega_E \qquad 2.8$$

Where n is any positive integer - a quantum number (Fig. 2.2).

The minimum quantum of energy which the lattice will accept is thus:

$$E_E = \hbar \omega_E \qquad 2.9$$

Where E_E is defined as the Einstein energy.

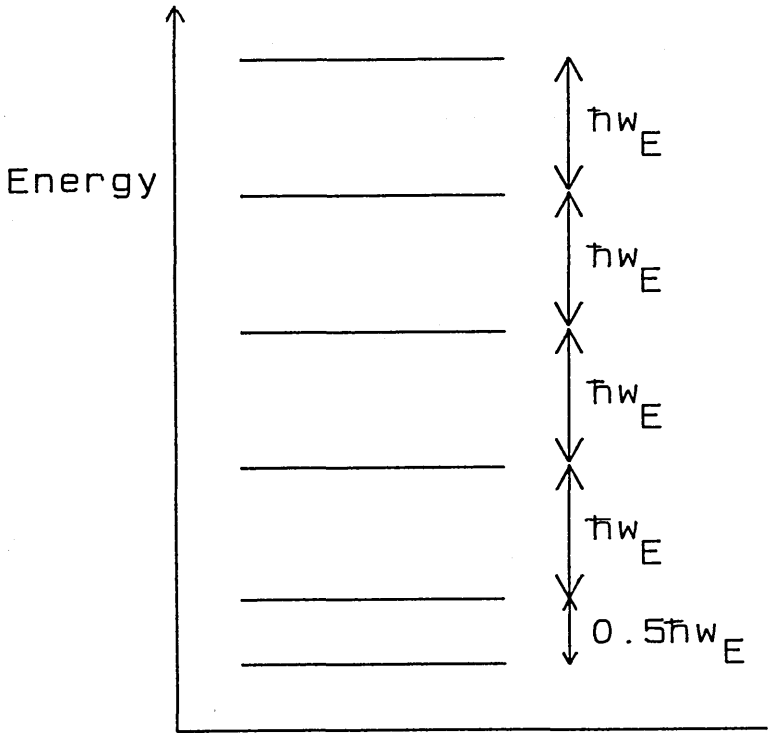

Figure 2.2 The allowed energy levels of an Einstein solid.

The outcome of a nuclear transition in such a material will depend on the transition energy. With the emission of high energy γ-rays in excess of a few MeV, the associated nuclear recoil energy is comparable to typical atomic binding energies (~10eV). Hence it may be possible to eject the atom from its lattice site. γ-rays with energies between 0.1-1 MeV are unlikely to cause lattice defects, but they will create a large number of phonons due to the displacement of the nucleus from its mean position. The important γ-ray energy range as regards to Mössbauer effect is 10-100 KeV. The associated recoil-energy may now be less than the Einstein energy of the solid (E_E). Hence the recoil energy cannot be absorbed into the phonon spectrum. The

energy from this zero phonon transition is instead taken up by the recoil of the solid as a whole. The recoiling mass in Eqn. 2.7 becomes the total mass of the lattice and leads to typical values of $E_R \sim 10^{-20}$ eV.

This value is insignificant compared to the natural linewidth of the γ-ray ($\Gamma \sim 10^{-8}$eV) (§2.1.4) and thus the emitted γ-ray does not suffer a Doppler shift, but carries the full transition energy E_o.

A better approximation to the vibrational quantisation is given by the Debye model [5]. This assumes a range of allowed frequencies from zero up to a maximum ω_D, the Debye frequency. The frequency distribution for these modes is of the form:

$$g(\omega) = \frac{9N}{\omega_D^3}\ \omega^2 \qquad \omega \leq \omega_D \qquad 2.10$$

$$g(\omega) = 0 \qquad \omega > \omega_D$$

N = number of atoms in sample

Note that unlike the Einstein model there is a quasi-continuous distribution of energy levels (Fig. 2.3). However, there can still be a finite probability of recoilless emission f. Consider the probability P of a phonon transition between initial (L_i) and final (L_f) vibrational states.

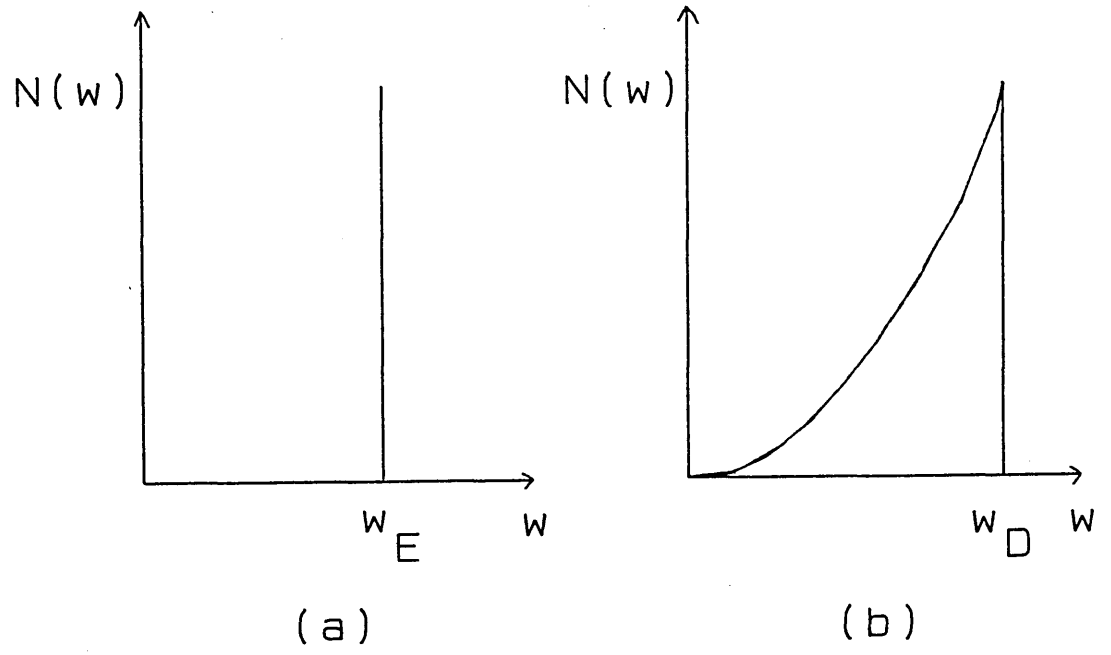

Figure 2.3 Distribution of allowed phonon frequencies in (a) Einstein solid and (b) Debye solid.

It will be of the form of Eqn. 2.11 [6].

$$P = C \left| \langle L_f \rangle e^{ikx} \langle L_i \rangle \right|^2 \qquad 2.11$$

Where C is a constant; k is the wave vector of the γ-ray and x is the displacement of the nucleus from its mean position. For a recoilless transition we require the vibrational state of the nucleus to be unaltered, i.e. $L_i = L_f$. Hence the recoil-free transition probability f is given by Eqn. 2.12.

$$f = C \left| \langle L_i \rangle e^{ikx} \langle L_i \rangle \right|^2 \qquad 2.12$$

Since L is normalised this can be simplified:

$$f = \left| e^{ikx} \right|^2$$

$$\therefore \quad f = \exp \left[- k^2 \langle x^2 \rangle \right] \qquad 2.13$$

f is known as the recoil-free fraction. It is not necessary for the nucleus to be in the vibrational ground state L_o in order to have a zero phonon transition, although the probability will decrease for higher states because of the increase in $\langle x^2 \rangle$. Boyle and Hall [7] have shown that if the lattice vibrational frequencies are short compared to the mean life time of the excited state then the time dependence of x can be neglected. I.e., the γ-ray energy is not subject to any Doppler broadening due to thermal motion of the atom.

The Debye model can be used to generate a quantitative expression for f in terms of the recoil energy E_R, the absolute temperature T and the Debye temperature of the material θ_D (§3.2). θ_D is defined thus:

$$\theta_D = \frac{\hbar \omega_D}{k_B} \qquad 2.14$$

Where $k_B = 1.381 \times 10^{-23}$ JK^{-1}, Boltzmans constant

Applications of the Debye model to Mössbauer studies will be examined further in §3.2.

2.1.4 Natural line shape

The γ-ray produced as a result of a recoil free transition carries the full transition energy. However, the lifetime of the excited state nucleus is small, hence the Heisenburg uncertainty principle must be invoked. The uncertainty in the energy of the γ-ray, ΔE, is related to the mean lifetime of the excited state Δt:

$$\Delta E . \Delta t \geq \hbar \qquad 2.15$$

where $\hbar$ = 1.055×10^{-34} Js, Planck's constant

ΔE is the natural line width of the source, normally denoted by capital gamma Γ. The mean life Δt is related to the half life $t_{1/2}$ of the excited state:

$$\Delta t = \frac{t_{1/2}}{\ln 2} \qquad 2.16$$

Hence

$$\Gamma = \frac{\hbar \ln 2}{t_{1/2}} \qquad 2.17$$

The 14.4KeV excited state level of the ^{57}Fe nucleus has a half life of 98μs [7] which equates to a natural line width of 4.6×10^{-9} eV. Thus the theoretical resolution of this γ-ray is given by:

$$\text{resolution} = \frac{\Gamma}{E_0} = \frac{4.6 \times 10^{-9}}{14.4 \times 10^{3}} \approx \frac{1}{10^{13}} \qquad 2.18$$

Note that only the relative energy between different nuclei of the same isotope can be measured to this accuracy.

The energy distribution N(E) of a recoil-free γ-ray will have a Lorentzian line shape defined by the Breit-Wigner formula [8].

$$N(E)\,dE = \frac{f_s \Gamma}{2\pi} \cdot \frac{1}{(E - E_0^2) + \left[\frac{\Gamma}{2}\right]^2} \cdot dE \qquad 2.19$$

Where f_s = recoil free fraction of source.

2.1.5 Hyperfine Interactions

2.1.5.1 Introduction

The extremely high resolution (Eqn. 2.18) which can be achieved with recoil-free γ-rays allows the hyperfine structure of the nuclear energy levels of Mössbauer nuclei to be examined. This structure is the sum of three interactions between the nucleus and its environment. The first is the electrostatic interaction between the nucleus and its surrounding electrons. This serves to produce a slight shift in the transition energy. Magnetic dipole and electric quadrupole interactions involve coupling of the nuclear spin with electric and magnetic fields and result in multiple transitions. The three interactions offer a great possibility for extracting information concerning the physical and chemical properties of materials containing a Mössbauer isotope.

2.1.5.2 Chemical Isomer Shift δ

The chemical isomer shift δ results from the change in the electrostatic interaction between the nucleus and its orbital electrons during a γ-ray transition. The transition will cause a slight change δR in the nuclear volume R. The wavefunctions of orbital s-electrons imply a non-zero charge density within the nuclear volume, hence the transition will be accompanied by a slight change in the electrostatic interaction energy between the penetrating s-electrons and the nucleus. The energy change causes perturbations to the nuclear energy levels and hence a small shift in the nuclear transition energy (Fig. 2.4). This shift cannot be measured directly but it is possible to compare the relative shift between different materials.

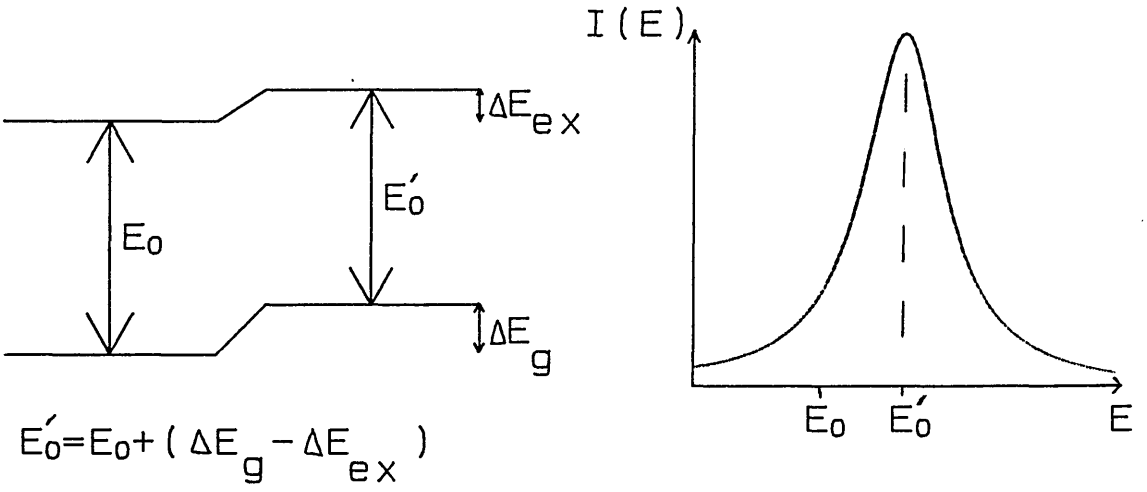

Figure 2.4 The chemical isomer shift

By assuming a uniform charge density within a spherical nucleus of radius R an equation may be derived for the difference in electrostatic interaction between two materials A and B [9]:

$$\delta = \frac{4}{5}\pi\ Ze^2\left[\left|\Psi_A(0)\right|^2 - \left|\Psi_B(0)\right|^2\right]\left[R^2\frac{\partial R}{R}\right] \qquad 2.20$$

Where Z = atomic number of nucleus

ψ_A = non relativistic Schrodinger wavefunction for material A,

hence $|\psi_A(0)|^2$ = total electronic charge density at the nucleus.

Equation 2.20 has two components. Firstly a nuclear term, $\frac{4}{5}\pi\ Ze^2\left[R^2\frac{\partial R}{R}\right]$ which is constant for a given transition. Secondly a chemical term, $(|\psi_A(0)|^2 - |\psi_B(0)|^2)$ which equates to the difference in electronic charge density at the nucleus for materials A and B. Only s-shell electrons have wavefunctions which are non-zero within the nuclear volume,

hence these are the only orbitals to affect δ. However, the s-orbitals will be perturbed by p, d and f orbitals and by the chemical bonding of the atom, hence δ will indicate differences in the outer electronic structure between two materials A and B. The classic use of isomer shift measurements is the characterisation of valence state for a material. The variation of isomer shift with temperature may also be used to estimate the Debye temperature of a material (§3.2.3).

For the 14.4 KeV transition in ^{57}Fe, $\frac{\partial R}{R}$ is negative, i.e. the nucleus contracts when it is raised into the excited state. Hence an increase in isomer shift implies a decrease is s-electron density at the nucleus. Fe^{2+} compounds exhibit larger isomer shifts than Fe^{3+} compounds when measured against a calibration standard. This is because the extra 3d electron in Fe^{2+} further shields the $3s^2$ electrons from the nucleus.

2.1.5.3 The Electric Quadrupole Interaction ΔE_Q

The above explanation of the chemical isomer shift assumed a spherical nuclear charge distribution. However, this holds true only for nuclei with a total spin angular momentum I = 0,1/2. For I>1/2 the nucleus has an ellipsoidal charge distribution, resulting in a nuclear quadrupole moment eQ [10].

$$e\,Q = \int_v \rho_v\, r^2\,(3\cos^2\theta - 1)\, dv \qquad 2.21$$

Where e = electronic charge

ρ_v = charge density in volume element dv

r = distance of volume element dv from the centre of the nucleus

θ = angle of volume element dv with respect to the nuclear spin quantisation axis.

The sign of Q will depend on whether the nucleus is oblate (Q<0) or prolate (Q>0) with respect to the nuclear spin quantisation axis.

In general, the charge distribution about a nucleus will not be symmetric, hence the nucleus will be subjected to an electric field gradient (E.F.G.). The axis system for the electric field is taken such that the second derivative of the electrostatic potential with respect to the z-axis gives the maximum value of the E.F.G., defined as eq:

$$\frac{\partial^2 V}{\partial Z^2} \equiv V_{zz} \equiv eq \qquad 2.22$$

For each possible orientation of the nuclear spin with respect to the z-axis there will be an interaction energy between the nuclear quadrupole moment Q and the E.F.G. In addition to Eqn. 2.22, the Laplace equation (Eqn. 2.23) enables us to define the E.F.G. completely with two parameters, V_{zz} and an asymmetry parameter η.

$$V_{xx} + V_{yy} + V_{zz} = 0 \qquad 2.23$$

$$\eta = \frac{V_{xx} - V_{yy}}{V_{zz}} \qquad 2.24$$

By convention $V_{xx} > V_{yy}$, hence $0 \leq \eta \leq 1$.

The interacation Hamiltonian may be solved exactly for nuclei with a total spin angular momentum $I \leq 3/2$. It leads to an expression for the energy shift E_Q in terms of I and its z-component m_I [11].

$$E_Q = \frac{e^2 q\, Q}{4I(2I-1)} \left[3m_I^2 - I(I+1)\right]\left[1+\frac{\eta^2}{3}\right]^{\frac{1}{2}} \qquad 2.25$$

As with the expression for the chemical isomer shift (Eqn. 2.20) there is a nuclear term in Eqn. 2.25, which remains constant for a given transition, and a chemical term, dependent on the environment of the probe nucleus. For I = 3/2 there are two possible values of E_Q corresponding to $m_I = \pm 3/2$, $m_I = \pm 1/2$, whilst for I = 1/2. $E_Q = 0$. Thus the quadrupole interaction in an I = 3/2 → 1/2 transition will result in <u>two</u> possible transition energies. The difference between these two energy levels can be derived from Eqn.2.25 and is known as the quadrupole splitting ΔE_Q:

$$\Delta E_Q = E_Q(m_I = \pm 3/2) - E_Q(m_I = \pm 1/2)$$

$$\Delta E_Q = \frac{e^2 q Q}{2}\left[1+\frac{\eta^2}{3}\right]^{\frac{1}{2}} \qquad 2.26$$

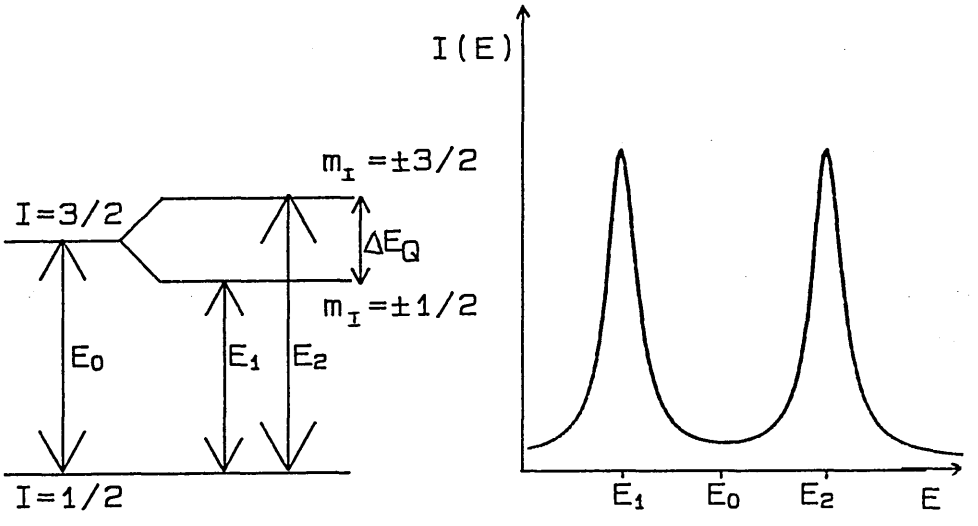

Figure 2.5 Quadrupole Splitting in an I = 3/2 → 1/2 transition.

The E.F.G. is the result of all the surrounding charges, thus it includes contributions from incomplete electron shells of the atom and from charges on surrounding ligands. For instance, high spin trivalent iron has a spherically symmetric $3d^5$ outer shell ($^6S_{5/2}$) which will not produce an E.F.G., hence any observed quadrupole splitting is solely the result of an asymmetric charge distribution created by the surrounding ligands. In contrast, high spin divalent iron has an outer $3d^6$ shell which is not symmetric ($^5D_4$). This leads to an E.F.G. at the nucleus and hence a quadrupole interaction. Any distortion from a symmetrical ligand environment will also affect ΔE_Q of these Fe^{2+} sites. It is generally found that Fe^{2+} states exhibit larger quadrupole splittings than Fe^{3+} states.

The total E.F.G. can be written as the sum of valence and lattice contributions.

$$V_{zz} = eq_{lattice} + eq_{valence} \qquad 2.27$$

$eq_{lattice}$ can be calculated by summing the electric fields generated by the surrounding ligands, however, this crystal field will also polarise the core electrons of the atom which will further enhance the E.F.G. $eq_{valence}$ is due to asymmetric valence shells which will also polarise the core electrons and alter the E.F.G. The core electron polarisation is accounted for by means of Sternheimer shielding R and antishielding γ_∞ factors [12] hence Eqn.2.27 becomes:

$$V_{zz} = e\ (1 - \gamma_\infty)\ q_{lattice} + e\ (1 - R)\ q_{valence} \qquad 2.28$$

For iron compounds $\gamma_\infty \cong -10$, $R \cong 0.2$ hence any $eq_{lattice}$ contribution due to departures from cubic symmetry will cause a large change in V_{zz} and hence ΔE_Q.

The quadrupole splitting of a Mössbauer transition line enables the coordination sphere of the probe nucleus to be investigated. For instance, it is possible to differentiate between octahedrally and tetrahedrally coordinated Fe^{2+}.

It is possible to calculate the relative probabilities for transitions between the various allowed values of m_I [13] and hence the relative area of the two lines of a quadrupole doublet. The area ratio will depend on the orientation of the source-absorber-detector geometry with respect to the principal axis of the E.F.G. For polycrystalline samples the ratio is 1:1, hence only the magnitude of ΔE_Q can be measured.

2.1.5.4 Magnetic Hyperfine Interaction

The third hyperfine interaction results from the coupling of the nuclear magnetic dipole moment μ which the Mössbauer nucleus may possess with any magnetic field H at the nucleus. The magnetic moment can be expressed in terms of the total spin angular momentum I:

$$\mu = \mu_N g I \qquad 2.29$$

where g = Landé splitting factor

$\mu_N = \frac{e\hbar}{2mc}$ the nuclear Bohr magneton

m = mass of nucleus

The shifts to the energy levels are given by:

$$E_m = -\mu H \frac{m_I}{I} = -\mu_N g H m_I \qquad 2.30$$

Thus any magnetic field will split a nuclear energy level into (2I+1) sub-levels with an equal spacing of $\mu_N gH$. Conservation of angular momentum and parity considerations lead to a selection rule for m_I in any dipole transition:

$$\Delta m_I = 0,\pm 1 \qquad 2.31$$

The 14.4 KeV excited state of ^{57}Fe has I = 3/2 and hence four sub-levels corresponding to m_I = +3/2, +1/2, -1/2, -3/2. The ground state has I = 1/2, hence m_I = +1/2, -1/2. Applying the selection rule (Eqn. 2.31) this results in the familiar six line spectrum (Fig. 2.6).

The magnetic field H may originate within the material itself or be due to an external source.

$$H = H_{internal} + H_{external} \qquad 2.32$$

$H_{internal}$ originates from a number of factors arising from the motion of electrons within the material [14]. These factors can produce field strengths at the nucleus of $H_{internal}$ = 10-100KG. In many materials the electronic spins which produce $H_{internal}$ are relaxing at a rate comparable to or faster than the Mössbauer event time. Hence the time averaged field is zero and no magnetic splitting is detected. The magnetic splitting of the nuclear transition energy may enable the unique identification of a material by its characteristic $H_{internal}$ value. Variation of $H_{internal}$ with temperature may reveal spin relaxation phenomena and be used to identify magnetic phase changes.

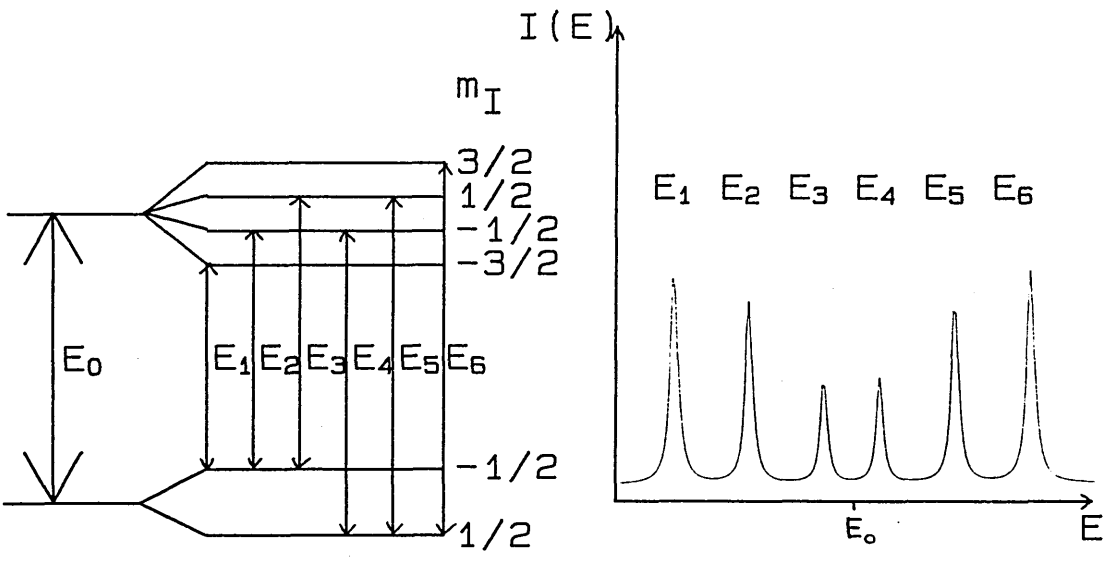

Figure 2.6 Magnetic splitting of an I = $^3/_2 \rightarrow \frac{1}{2}$ transition

2.2 Mössbauer Spectroscopy - Experimental

2.2.1 Introduction

As has been demonstrated in the previous sections the Mössbauer effect produces γ-rays with an energy resolution sufficient to resolve hyperfine interactions within the nucleus. There are no available γ-ray detectors which can directly resolve these changes in energy, hence a more subtle experimental technique must be employed.

It is possible to alter the energy of a γ-ray by applying a velocity to the γ-ray source. Provided the velocity is small compared to the speed of light c, non-relativistic Doppler effect equations may be used to derive an equation for the energy shift ΔE of a γ-ray of energy E_o by a Doppler velocity v:

$$\Delta E = \frac{v}{c} E_o \qquad 2.33$$

For Mössbauer spectroscopy applications it is normal to use a γ-ray source which contains the excited state Mössbauer isotope in a highly symmetric environment which precludes any splitting of the resonance line. By systematic application of different velocities to the source it is possible to scan the single emission line through an energy spectrum. The normal experimental arrangement (Fig. 2.7) has three main components.

(i) A radioactive source containing the Mössbauer isotope in its excited state. The source is mounted on carriage which moves to provide the Doppler velocity.

(ii) An absorber containing the Mössbauer isotope in the ground state. The chemical and physical environment of the absorber is generally different to that of the source.

(iii) A γ-ray detector and counter.

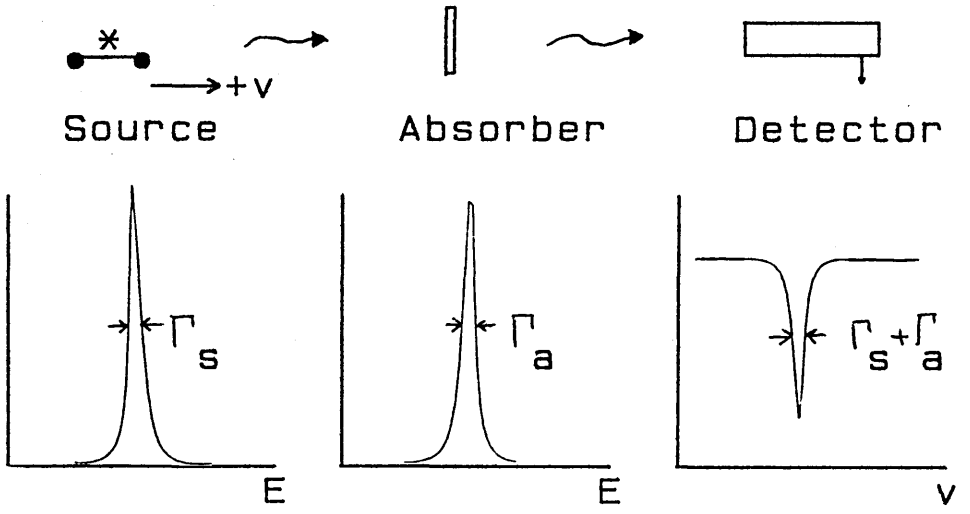

Figure 2.7 Schematic representation of the standard Mössbauer spectroscopy experimental arrangement. The energy and velocity spectra refer to the simplest case with identical source and absorber environments.

By recording the γ-ray count rate as a function of Doppler velocity the energy spectrum of the absorber is obtained. For identical source and absorber in cubic, non-magnetic environments the count rate will show a single minimum at zero Doppler velocity (Fig. 2.7). The width of the resonance line will be equal to the sum of the line widths of the source Γ_s and the absorber Γ_a, which in the ideal case will be twice the width derived from the Heisenburg uncertainty relation (Eqn. 2.17). In general the source and absorber will not be in an identical environment, hence the recorded line may be shifted from zero velocity by an isomer shift and split due to quadrupole and

magnetic interactions. By convention, absorption line energies are quoted in terms of the required Doppler velocity of the source. A positive velocity corresponds to motion of the source towards the absorber.

The line width derived from the Heisenburg uncertainty relation for the 14.4 KeV transition in ^{57}Fe:

$\Gamma = 4.6 \times 10^{-8}$ eV

hence, by Eqn. 2.33

$$v = \frac{\Gamma}{E_o} c = \frac{4.6\times10^{-9}}{14.4\times10^{3}} \times 3\times10^{11}$$

$= 0.096$ mm/s

If $\Gamma_s = \Gamma_a = \Gamma$ (i.e. no line broadening), then the width of the resonance line will equal 2v.

$\therefore$ Minimum line width of ^{57}Fe resonance = 0.192 mm/s.

2.2.2 The Mössbauer γ-ray source

The chief requirement of a Mössbauer γ-ray source is the production of large numbers of recoil-free γ-rays. For this reason the source isotope is usually embedded in a metal or metal oxide host matrix which will have a high Debye temperature and hence a high recoil free fraction. The matrix, in the form of a thin foil, will usually contain the source isotope in a single, cubic, non-magnetic environment in order to prevent quadrupole and magnetic interactions which would cause splitting of the resonance line. The single environment ensures that all the source nuclei are subject to the same isomer shift. Self absorption by ground state nuclei of the source isotope causes the

width of resonance lines to exceed the value defined by the Heisenburg uncertainty relation (Eqn. 2.17), thus the source matrix should not contain the stable, ground state nucleus is appreciable amounts. Non-resonant scattering of the γ-rays by other nuclei in the host matrix is reduced by minimising the thickness of the matrix foil.

There are a number of ways to produce the Mössbauer isotope in its excited state. A radioactive precursor may exist which decays via mechanisms such as α, β^- decay or electron capture enabling the excited level to be populated. Alternatively a nuclear reaction may be necessary to create the excited state nucleus. For example, the sources used for ^{119}Sn studies are created by neutron irradiation of ^{118}Sn to produce metastable 89.54 KeV exited state ^{119}Sn ($t_{1/2}$ = 250 day).

The 14.4 KeV level of ^{57}Fe can be populated by an electron capture mechanism in ^{57}Co (Fig. 2.8). The decay has a half life of 270 days which makes it practicable to produce Mössbauer sources which are usable for a number of years. A ^{57}Co source dispersed in a rhodium (Rh) metal matrix has been used for these studies. Its initial activity (May 1987) was 25 mCi. It is in the form of a 6μm foil sealed in a perspex holder and produces a single line with width Γ_s = 0.098mm/s and recoil-free fraction at a room temperature f = 0.77 [15]. The line has an isomer shift of $\delta = +0.106$ mm/s with respect to the centre of the α-iron sextet. All isomer shifts in this thesis are quoted relative to α-iron unless otherwise stated, however, zero velocity of the displayed Mössbauer spectra remains corresponding to the stationary ^{57}Co(Rh) source.

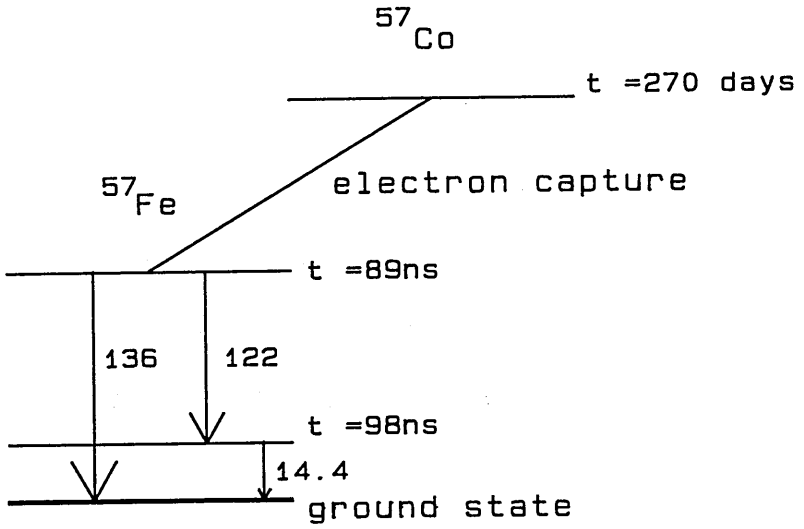

Figure 2.8 The radioactive decay scheme for ^{57}Co

2.2.3 Absorber Preparation

The preparation of a sample of material for Mössbauer spectroscopic analysis must take into account a number of factors concerning its physical size and composition. The resulting absorber disc should contain enough of the resonant isotope to enable a spectrum to be collected within a reasonable time period, but there exists an upper limit to the isotope concentration above which the resonance lines will become appreciably broadened due to self absorption. Other elements within the absorber may also have high (non-resonant) cross-sections for the γ-ray. If the material contains too much of the resonant isotope then it may prove necessary to dilute the absorber with graphite or another inert dilutant. Too little resonant isotope may necessitate artificial enrichment, but this is a costly process and should be regarded as a last resort.

The effective thickness of an absorber t_A can be defined thus:

$$t_A = \beta n f_A \sigma_O \qquad 2.34$$

Where β = multiplicity of the absorber spectrum, i.e. $\beta = 1$ for a singlet;

$\beta = 0.5$ for a doublet; etc.

n = number of resonant nuclei per unit cross sectional area (cm^{-2})

f_A = recoil-free fraction of absorber

σ_o = maximum absorption cross-section (cm^2)

For $t_A >> 1$ saturation effects will distort the absorption line shapes, whilst for $t_A << 1$ the line intensities are small. Optimum conditions are obtained when $t_A \simeq 0.1$. For ^{57}Fe this implies an isotopic concentration given by:

$$n = \frac{0.1}{\beta f_A \sigma_o} \qquad 2.35$$

Consider the case where $\beta = 0.5$, $f_A = 0.77$, $\sigma_o = 256 \times 10^{-20}$ cm^2

$$\therefore \quad n \simeq 1.0 \times 10^{17} \ cm^{-2}$$

The natural abundance of ^{57}Fe, a = 2.19%.

hence, the concentration of natural iron n(Fe) = n/a

$$= 4.6 \times 10^{18} \ cm^{-2}$$

$$= 0.44 \ mg \ cm^{-2}$$

Hence it is desirable to produce absorbers containing of the order of one mg cm^{-2} of natural iron. For materials containing a few mole percent natural iron this leads to the preparation of absorbers of 0.5-2.00mm thickness.

It is standard procedure to grind absorber materials prior to analysis in order to prevent distortion of the spectra by the possible orientation of the crystallites with respect to the γ-ray beam. The ground absorbers are housed within hollow perspex or iron-free graphite discs with diameters ranging from 15-25mm depending on the required experimental geometry.

2.2.4 γ-ray detectors

There are three main types of detector which can be used to identify and record Mössbauer γ-rays. Lithium drifted Ge/Si detectors; scintillation counters and gas-filled proportional counters. For the detection of low energy γ-rays ($E_\gamma \leq$ 40 KeV) a proportional counter offers the best choice so long as high energy resolution is not required. For these studies a detector built at A.E.R.E. Harwell containing a mixture of 95% argon, 5% methane quench gas has been used. The detector is used in an end-on cylindrical geometry to maximise the detection efficiency of the 14.4 KeV γ-ray. The detector window is made from a thin sheet of aluminised plastic ('Mylar'). The single wire anode is held at -2.6 kV with respect to ground by an Ortec Model 459 H.T. supply. Pulses from the detector are amplified by a Ortec Model 451 amplifier. This assembly is sufficient to resolve the 14.4 KeV γ-ray from other γ-ray transitions, the 7.3 KeV conversion X-ray peak and low energy amplifier noise. A multichannel analyser (Canberra M.C.A. Series 30) operating in pulse height analysis mode can be used to record the pulse height spectrum (Fig. 2.9). High and low pass filters of a single channel analyser (S.C.A.) within the M.C.A. unit are used to discriminate against unwanted portions of the spectrum. The resolution of the detector leads to an energy window of approximately 11 - 18 KeV.

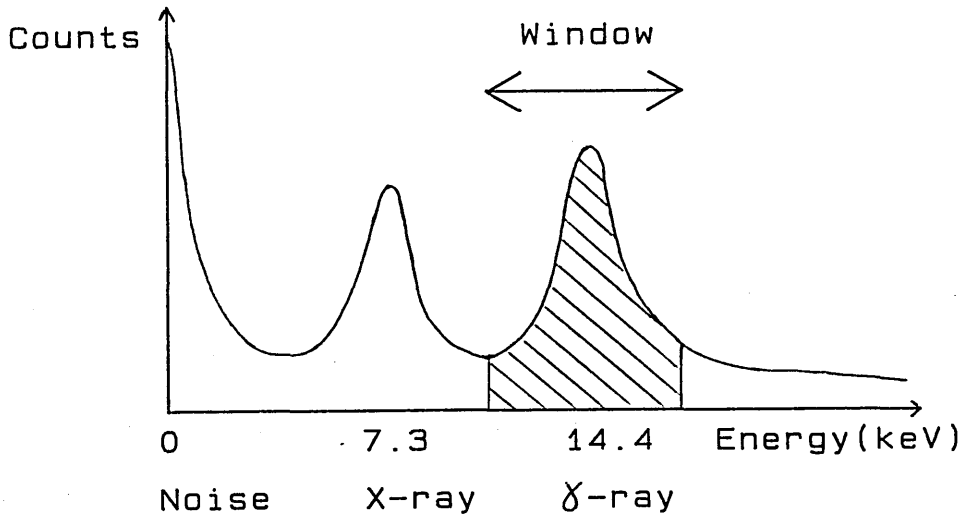

Figure 2.9 The pulse height spectrum of a ^{57}Co source obtained using a gas-filled proportional counter.

2.2.5 The Mössbauer Spectrometer

A schematic representation of the whole spectrometer assembly is shown in Fig. 2.10. When collecting a Mössbauer spectrum the multi-channel analyser (M.C.A.) is operated in multi-channel scan repeat mode. An external master function generator (M.F.G.) (Elscint MFG-N-5) supplies channel advance and reset pulses to the M.C.A. which causes it to step through its memory locations ('channels') at a constant rate, then fly back to the start and repeat the cycle. The M.F.G. operates at 5.5 Hz which corresponds to a dwell time of ~320μs per channel when the M.C.A. is divided into 512 channels. The M.F.G. also produces a triangular waveform which is fed to a servo amplifier (Elscint MDF-N-5). The servo amplifier drives an electro-mechanical transducer (Elscint MVT4) which carries the radioactive source. The triangle wave causes the velocity of the source to increase and then decrease at a

steady rate, i.e. a constant acceleration (Fig. 2.11). A pick-up coil on the transducer monitors the actual motion of the source and is used in a negative feedback loop to stabilise the velocity waveform. The amplitude of the triangle wave defines the velocity range through which the source is cycled and can take values between ± 1mm/s and ± 600 mm/s. The normal ranges for ^{57}Fe Mössbauer studies are from ± 4mm/s upto ± 12 mm/s.

The synchronisation between the channel advance of the M.C.A. and the motion of the source means that each channel corresponds to a distinct velocity increment. Thus the M.C.A. records the transmitted counts as a function of Doppler velocity, resulting in the absorption energy profile of the absorber - a Mössbauer spectrum. Because the source moves through each velocity increment twice in any one cycle a mirror image spectrum will be recorded. Superimposed on the spectrum will be a cosine term due to the changing source-absorber separation. The cosine term is substantially reduced during the first stage of data processing in which one half of the spectrum is folded onto its mirror image ($3.1.2).

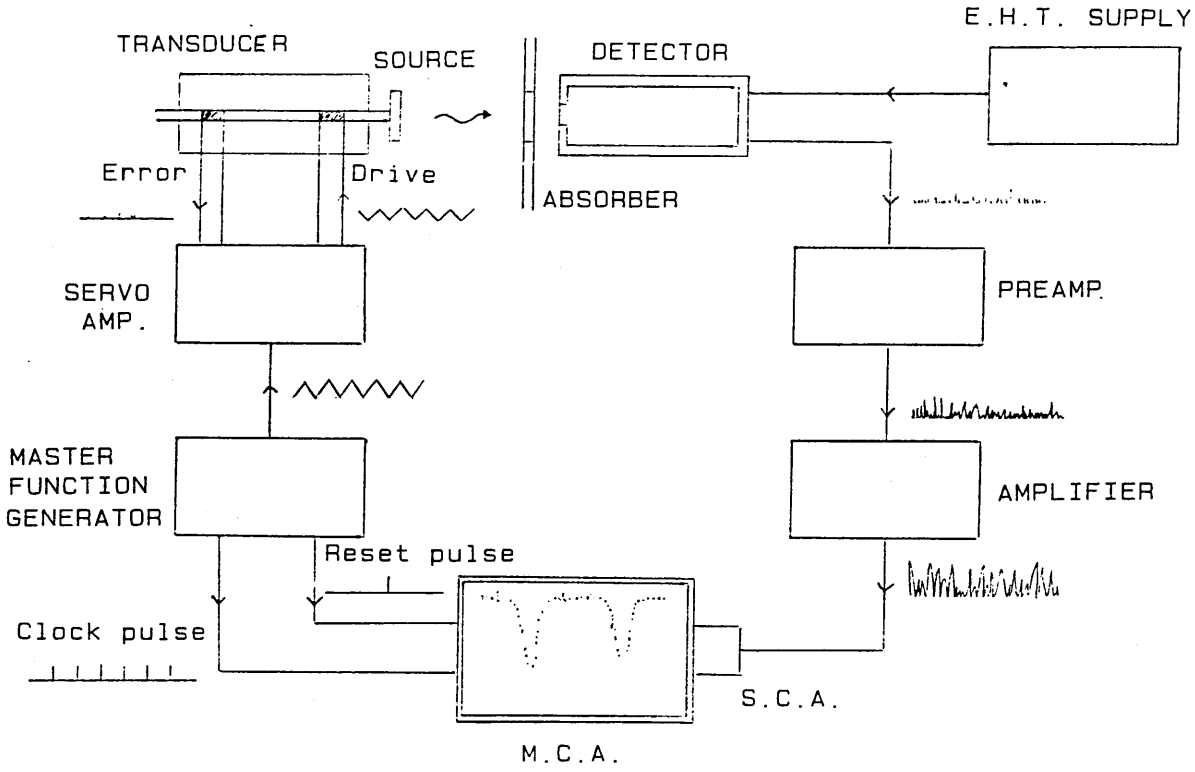

Figure 2.10 Schematic representation of a constant acceleration mode Mössbauer spectrometer.

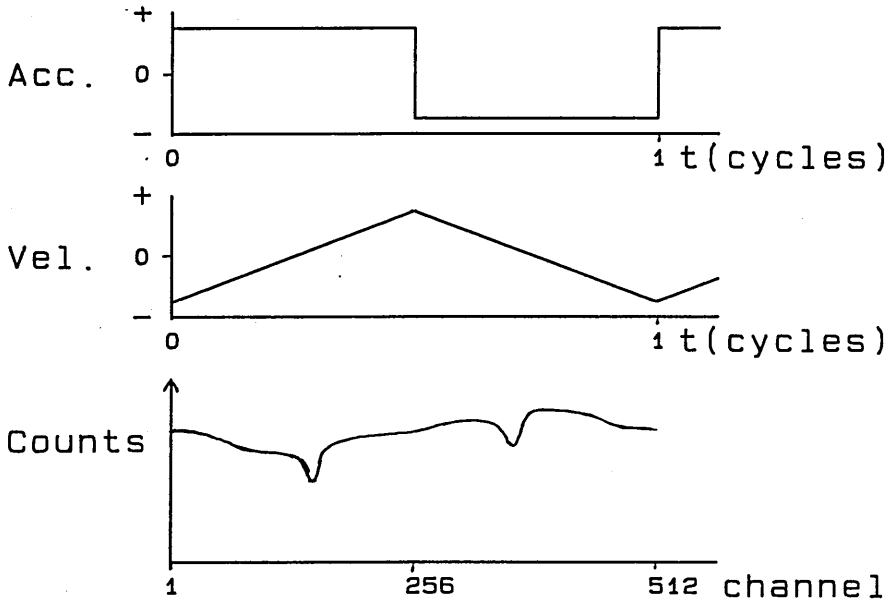

Figure 2.11 Acceleration and velocity waveforms and the simulated spectrum for a singlet.

2.2.6 Velocity Calibration

It is important to calibrate the drive unit of the spectrometer prior to any sample analysis. The absolute velocity limits of the transducer must be determined, since the values set using the potentiometer of the Master Function Generator can only be regarded as nominal. Also it is desirable to assess the linearity of the velocity scale. The standard method of calibration is to record the spectrum of a material with known Mössbauer parameters. For ^{57}Fe Mössbauer studies the usual standard is a α-iron metal, although sodium nitro-prusside (S.N.P.) may be used for small velocity ranges. The absolute line positions for these materials have been determined by recourse to high precision optical techniques [16,17].

The α-iron absorber, in the form of a 2.5 μm foil, has been enriched to ~90% abundance of ^{57}Fe. This enables a well resolved spectrum to be recorded quickly (~½ hour). The resulting six line magnetic hyperfine spectrum (Fig. 2.12a) allows for both velocity calibration and assessment of drive linearity. The splittings of the three pairs of lines (L_1 - L_6; L_2 - L_5; L_3 - L_4) are known from data tables [18] and can be used to calculate a calibration constant for the spectrometer. The distances between successive lines (L_1 - L_2; L_2 - L_3; L_4 - L_5; L_5 - L_6) should be equal and thus give an indication of the linearity of the drive unit. Broadening of the absorption lines may also indicate the departure from a constant drive signal.

For velocity ranges less than ±4 mm/s the outer lines of the α-Fe sextet are lost. Calibration may still be performed using the inner four lines or alternatively an SNP absorber can be used. This produces a single quadrupole doublet [18] (fig. 2.12b), hence no linearity check is possible.

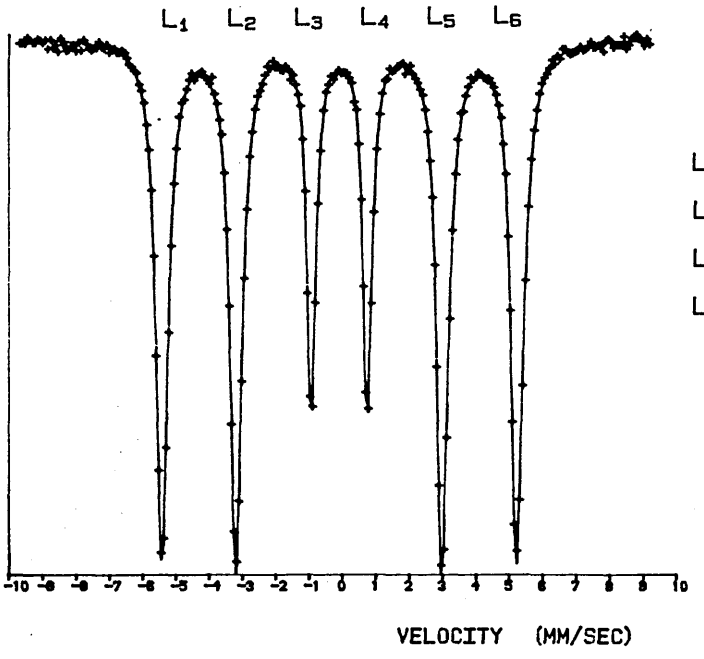

L_1-L_6 = 10.6246 mm/s

L_2-L_5 = 6.1520 mm/s

L_3-L_4 = 1.6794 mm/s

L_1-L_2=L_2-L_3=L_4-L_5=L_5-L_6 = 2.2363 mm/s

(a) Alpha Iron (α-Fe)

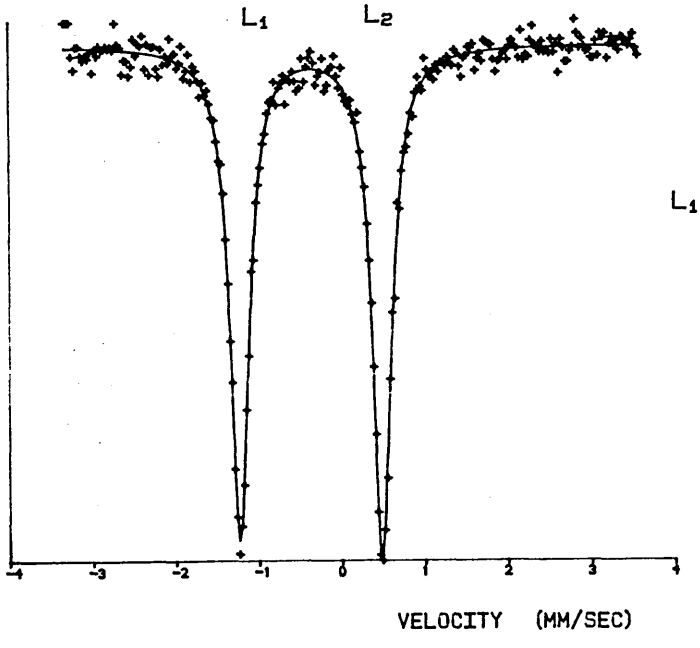

L_1-L_2 = 1.7040 mm/s

(b) Sodium Nitroprusside (SNP)

$Na_2Fe(CN)_5NO.2H_2O$

Figure 2.12 Room temperature spectra of ^{57}Fe Mössbauer reference compounds.

2.2.7 Cryostats and Furnaces

2.2.7.1 Introduction

It is often desirable to record Mössbauer spectra above or below room temperature. Lower temperatures will be necessary for materials with a low Debye temperature. Variable temperature studies allow the change in hyperfine parameters to be investigated. The ^{57}Co(Rh) source has a high recoil-free fraction at room temperature, hence it is only ever necessary to heat or cool the absorber. This greatly simplifies the experimental apparatus design.

In order to be suitable for Mössbauer spectroscopy, furnaces and cryostats must satisfy two criteria. The absorber must not be subject to extraneous vibrations, as these would destroy any resonance conditions. The geometry of the sample cell must allow for the unimpeded passage of γ-rays. For these studies a helium gas cryostat has been used to achieve absorber temperatures between ambient and a minimum of 12K. Temperatures upto 600K have been achieved using a home-built electric furnace.

2.2.7.2 The 'Displex' Cryostat

The cryostat is based on the 'Displex' system supplied by Air Products and Chemicals Inc. It comprises a compressor (AP1RO2W); expansion module (AP DE202); mechanical interface (AP DMX20); temperature controller (AP DE3700) and a vacuum system (Fig. 2.13). Cooling of the absorber is achieved by the expansion of helium gas within a cold finger assembly. The cold finger is mechanically isolated from the absorber to preclude any vibration.

High pressure helium gas (275 Torr) from the water cooled compressor unit enters the cryostat through a rotating valve. It flows into the heat exchangers and through the passages of the slack cap. The heat exchangers, cooled during the previous cycle, cool the incoming gas. The helium flowing through the slack cap forces the slack cap up, engaging and thus raising the displacer unit. This upward movement increases the available expansion volumes at the two heat stations. Gas above the slack cap is also forced through a narrow passage into the surge volume. The rotating valve closes and the subsequent compression of gas above the slack cap prevents the displacer from colliding with the inlet duct.

The rotating valve soon opens the exhaust port and high pressure helium within the heat exchangers is free to expand. This exhaust gas returns to the compressor unit. It is the expansion of the helium which cools the two heat stations. The first has a base temperature of 80K, whilst the second will reach 10K after approximately one hour of operation. The drop in pressure causes gas to bleed out of the surge volume, forcing the slack cap and displacer unit down. Residual gas within the displacer dampens this downwards motion and prevents the heat stations from colliding with the surrounding jacket. The rotating valve closes once more with the displacer unit positioned for the start of the next cycle.

For most applications of this system it is sufficient to mount the sample at the base of the second heat station. However, for Mössbauer studies vibration of the absorber due to motion of the displacer and valve motor are enough to destroy any resonance [19]. Vibration isolation has been achieved by mounting the whole of the above assembly on a rigid platform, specifically

by bolting it to one of the concrete pillars which constitute the framework of the building. The absorber and its associated heat exchanger is attached to a separate platform bolted to the floor of the laboratory. The only couplings between the two components are via a flexible rubber bellows and through the floor of the laboratory. The graphite absorber disc is positioned within an indium sealed sleave at the base of a heat exchange unit. This unit has protruding fins which interleave with fins on the cold finger of the second heat station. Helium at an excess pressure of 25mm Hg is used as an exchange gas between these fins. An electric heater within the absorber heat exchanger allows the absorber to be maintained at any temperature between 12K and room temperature, although there is a marked decrease in temperature stability at temperatures in excess of 200K. The heater, which has a maximum power output of 25W is stabilised by an electronic temperature controller which responds to a thermocouple embedded in the absorber heat exchanger.

A final vacuum jacket encloses the whole arrangement, with the residual pressure being maintained at 10^{-6} Torr by a diffusion/rotary pump combination. Thin beryllium windows in this jacket enable the normal transmission geometry to be maintained.

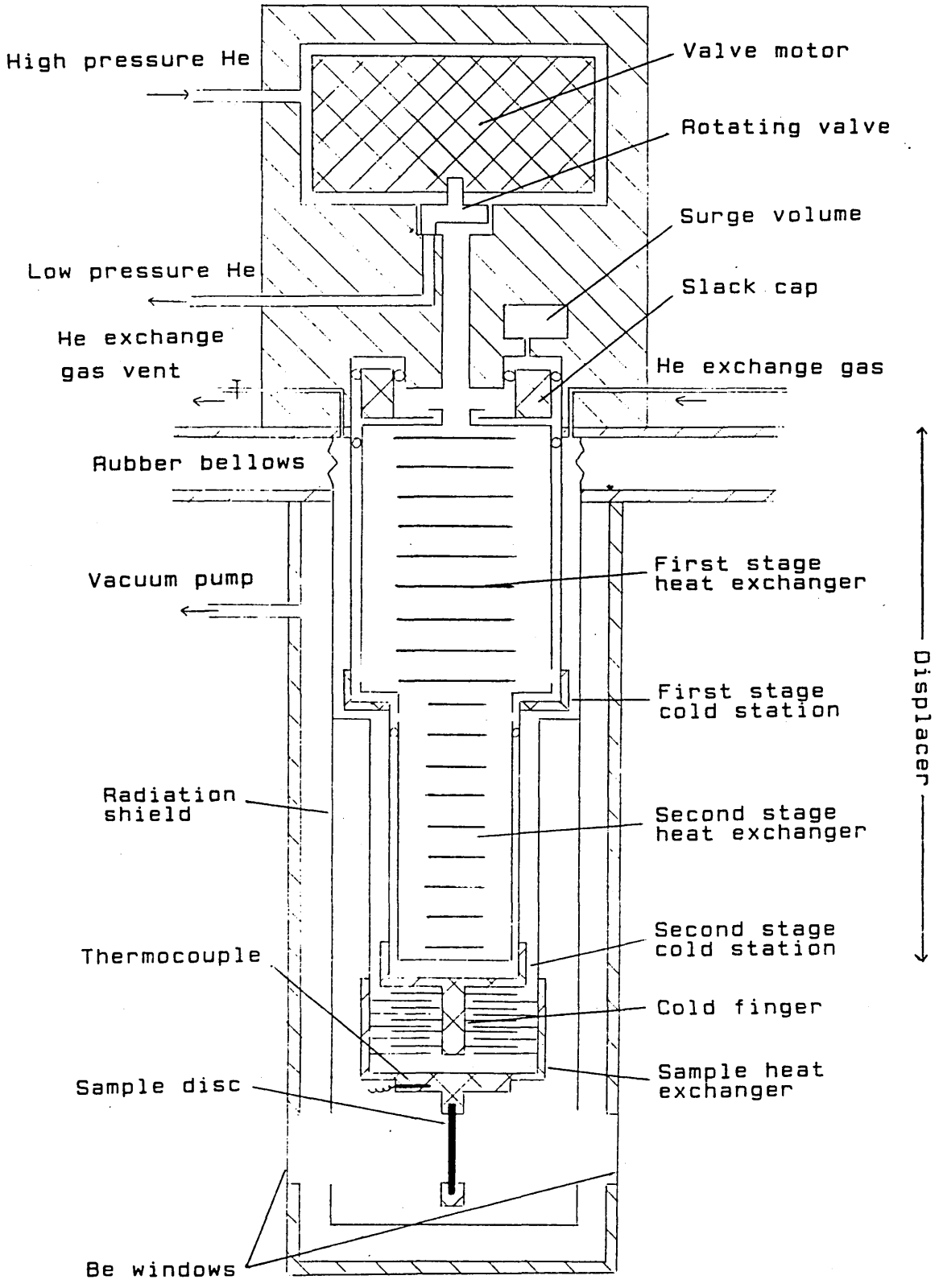

Figure 2.13 The Displex Cryostat (not to scale)

2.2.7.3 The Electric Furnace

Absorber temperatures above ambient have been achieved using an in-house built electric furnace (Fig. 2.15). The powdered sample, dispersed in graphite to ensure isothermal conditions, is held in a 15mm diameter by 1mm thickness graphite disc. The disc is clamped to a copper support within a cylindrical brass chamber. The support is thermally isolated from the chamber by an insulating spacer. Power is supplied by a temperature controller (EMECG.61) to a heating coil wrapped around the copper support. Two constantan-copper thermocouples are sited within the support. The first provides a feedback signal for the controller in order to stabilise the furnace temperature. The second is connected to a cold junction held in an ice-water mixture and used to determine the absolute temperature. In order to further isolate the copper support and heater coils the chamber is evacuated to a residual pressure of ~0.05 Torr using a rotary pump. Thin aluminised 'Mylar' windows at either end of the chamber allow the passage of γ-rays. The physical size of the chamber puts a lower limit on the source - detector separation and hence an upper constraint on the achievable count rate from a given source.

The maximum temperature obtainable with the above system is ~340°C (613K). This limit is not due to the temperature controller or sample properties, but to the rapid failure of the Mylar windows at higher temperatures.

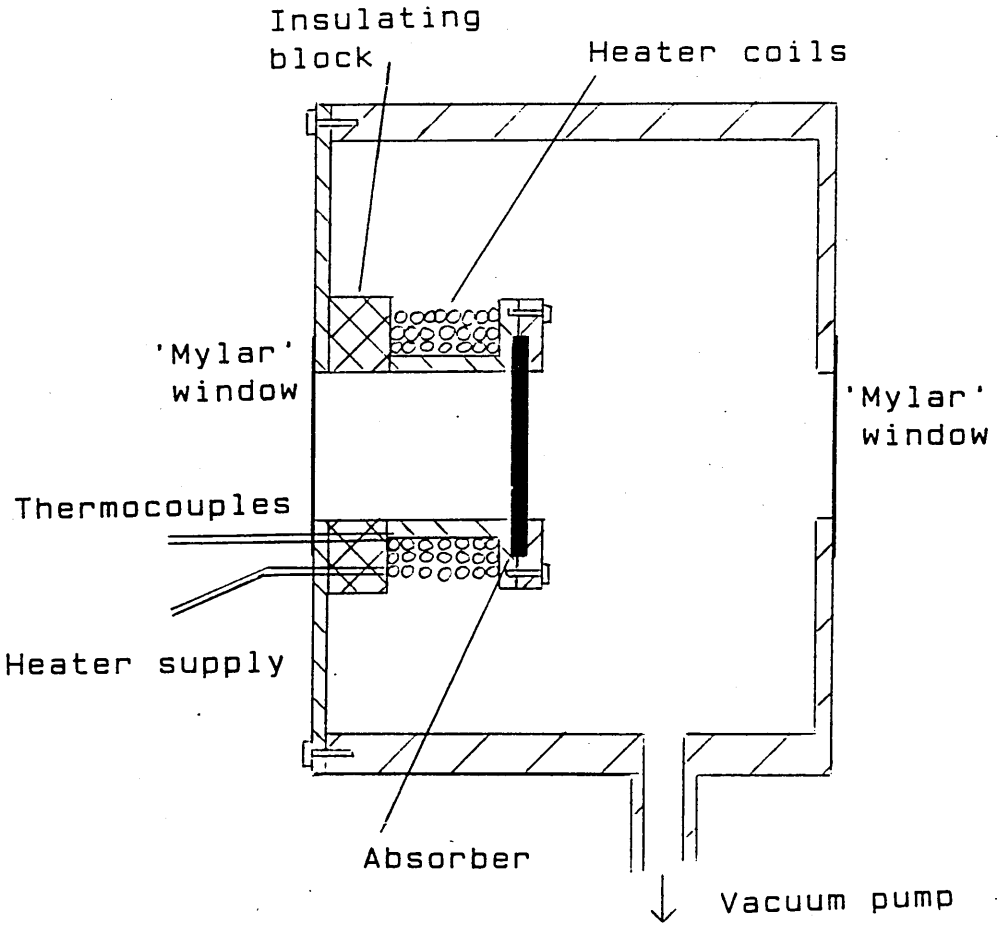

Figure 2.14 Electric furnace for high temperature Mössbauer studies.

2.3 Review of Mössbauer Studies of Oxide Glass Systems

2.3.1 Introduction

Work carried out by Pollack [20] first demonstrated that amorphous solids are sufficiently rigid materials to allow the resonant absorption of γ-rays. Early research concentrated on the more common borate and borosilicate glasses, but the technique is now applied to the full range of amorphous materials including metallic glasses [21,22]; chalcogenides [23] as well as more complex oxide glasses, and, exceptionally, liquids [24].

Common to all these materials is the absence of a periodic lattice, instead each atom occupies a unique environment and is subject to its own set of hyperfine interactions. This distribution in sites may manifest itself as a broadening of the Mössbauer absorption lines and a departure from Lorentzian line shapes even for 'thin' absorbers. Standard computer fitting algorithms may allow the average Mössbauer parameters which describe the spectrum to be obtained, but it is necessary to invoke more complex algorithms in order to investigate the distribution of sites which have led to the spectrum (§3.1.4).

There is only one Mössbauer isotope ^{73}Ge which has a glass forming oxide. A number of other elements with Mössbauer isotopes (Sb, Te, W) have conditional glass forming oxides, however, for most studies of oxide glass the probe atom is present in the form of a modifying oxide. ^{57}Fe Mössbauer studies enable the rôle of iron within the glassy matrix to be established, as well as allowing some inference as to the likely siting of similar ions. These may include many of the first row transition metals as well as Ca^{2+}, Mg^{2+}, Al^{3+} and Ga^{3+}.

The usual room temperature spectrum of an oxide glass containing iron consists of two broadened doublets corresponding to ferric (Fe^{3+}) and ferrous (Fe^{2+}) iron (Fig. 2.15). The ferrous/ferric ratio may be dependent upon the initial oxidation state of the iron added to the glass frit as well as preparation conditions such as the furnace temperature, oxygen fugacity and quench rate [25]. The lower velocity peak of the ferrous doublet is usually superimposed on the ferric lines, further complicating the fitting procedure (§3.1.3).

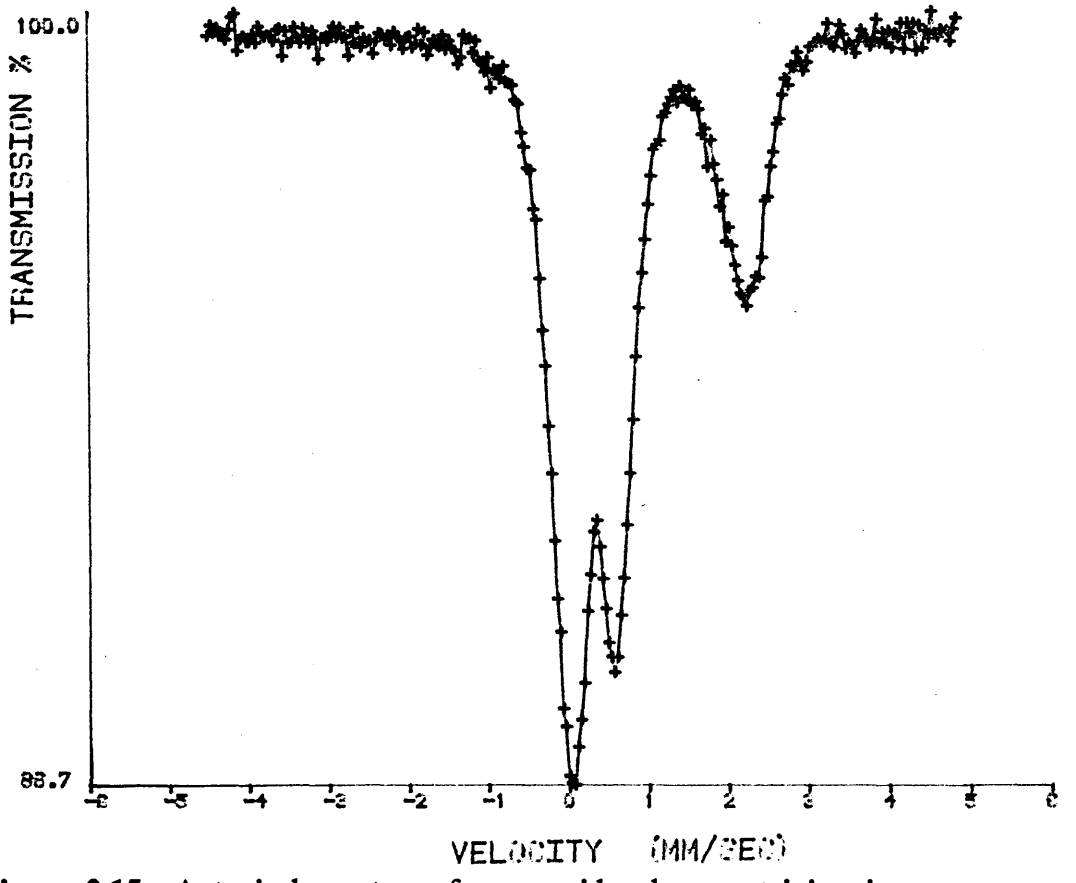

Figure 2.15 A typical spectrum for an oxide glass containing iron.

Interpretation of spectra is facilitated by reference to published Mössbauer parameter ranges [26,27,28]. In oxide glasses we are concerned with high spin Fe^{2+} and Fe^{3+} and the other electron configurations and charge states can generally be ignored. The valency of an iron site can normally be identified unambiguously from its isomer shift value. Ferric sites having a much lower isomer shift value than ferrous sites due to the additional shielding of the

s-electrons from the nucleus by the extra 3d electron ($2.1.5.2). Within this categorisation a higher coordination number produces a higher isomer shift due to the increased ionicity of the site. Quadruple splittings show a broad range of values, reflecting the varying degrees of distortion to which the iron sites may be subject. Fe^{2+} exhibits larger ΔE_Q values than Fe^{3+} due to its asymmetrical $3d^6$ outer shell ($2.1.5.3).

Coey [27] and Dyer [28] have complied graphs showing δ versus ΔE_Q for a range of iron-glasses (Fig. 2.16).

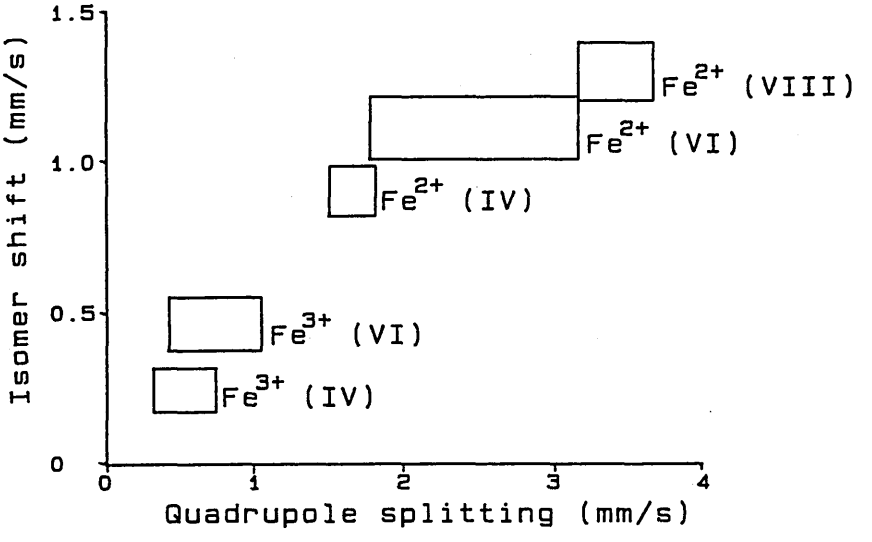

Figure 2.16 (after Dyer [28]) δ versus ΔE_Q for various oxide glasses containing iron.

Extensive studies of borate and silicate glasses [29,30] have revealed that the standard sites for iron atoms are as follows: Fe^{2+} invariably occupies octahedral, network modifying, sites whilst Fe^{3+} may occupy both octahedral and network forming tetrahedral sites. In contrast to this there is no conclusive evidence of tetrahedral Fe^{3+} in phosphate glass.

Under certain conditions iron-glass may exhibit a magnetic hyperfine interaction. Iron oxide has a low solubility in borate glass and precipitates of Fe_2O_3 have been identified [31]. Fe_2O_3 crystallites have also been observed in the sodium-iron-silicate glass system [32]. For widely separated ions the electron spin relaxation time may be large compared to the nuclear Larmor precision time so that the nucleus is subject to a static magnetic hyperfine interaction which manifests itself in the splitting of the absorption lines. This phenomenon of superparamagnetism has been observed for Fe^{3+} in a low iron content sodium trisilicate glass [33].

2.3.2 Mössbauer Studies of Phosphate Glasses

The first phosphate glasses to be studied by Mössbauer spectroscopy were inevitably vitreous forms of the crystalline iron phosphates. Kurkjian [33] compared crystalline and glassy forms of iron metaphosphate $Fe(PO_3)_3$) i.e. Fe_2O_3-$3P_2O_5$). At room temperature the crystal showed a single doublet due to octahedral Fe^{3+} whilst the glass exhibited two doublets, one due to octahedral Fe^{3+} and the other octahedral Fe^{2+} (Table 2.2). Spectra recorded at 4K showed the well resolved anti-ferromagnetic state of the crystal (H=533 KG) whilst the glass gave a very broad magnetic sextet (H ~ 437 KG) superimposed over the remnants of ferric and ferrous iron doublets. Owing to the high iron concentration it is unlikely that the magnetic splitting is due to superparamagnetism but instead may be caused by some short range magnetic ordering of the iron sites. The extensive broadening of the lines is due to the variation in Néel temperature throughout the material. The broadened line widths of the glass were attributed to the local distortion of the iron sites.

Table 2.2 Room temperature Mössbauer parameters for a selection of iron-phosphate glasses.

Composition *	δmm/s	ΔE_Q mm/s	Γmm/s	Comments		Reference
$Fe(PO_3)_3$	0.51	0.37	0.53	Crystalline	Fe^{3+}	33
$Fe(PO_3)_3 \equiv 25Fe_2O_3\ 75P_2O_5$	0.50 1.15	0.88 2.16	0.64 0.64		Fe^{3+} Fe^{2+}	33
$4Fe_2O_3\ 48Na_2O\ 48P_2O_5$	0.31	0.36	-		Fe^{3+}	35
$Fe_3O_4\ 30NaPO_3$	0.26 1.31	0.00 2.98	-		Fe^{3+} Fe^{2+}	35
$70Fe_2O_3\ 30P_2O_5$	0.43 1.06	1.18 2.45	0.72 0.72		Fe^{3+} Fe^{2+}	36
$42Fe_2O_3\ 58P_2O_5$	0.38 0.42 1.14	1.24 0.70 2.47	0.39 0.44 -	'oct' 'tet'	Fe^{3+} Fe^{3+} Fe^{2+}	37
$6Fe_2O_3\ 94P_2O_5$	0.42 1.04	0.80 2.43	0.51 0.44		Fe^{3+} Fe^{2+}	38
$6Fe_2O_3\ 28K_2O\ 66P_2O_5$	0.43 1.18	0.44 2.15	0.48 0.53		Fe^{3+} Fe^{2+}	38
$6Fe_2O_3\ 47K_2O\ 47P_2O_5$	0.42 1.09	0.49 2.25	0.46 0.53		Fe^{3+} Fe^{2+}	38
$6Fe_2O_3\ 67K_2O\ 27P_2O_5$	0.45 0.24	0.53 0.63	0.30 0.39	tetrahedral	Fe^{3+} Fe^{3+}	38
$Fe_2\ Na_{98}\ P_{81}\ O_{210}\ F_{89}$	0.45 1.22 1.24	0.36 2.25 1.50	0.46 0.44 0.55		Fe^{3+} Fe^{2+} Fe^{2+}	41
$Fe_{39}\ Na_{61}\ P_{36}\ O_{122}\ F_{92}$	0.42 1.23 1.28	0.53 2.52 1.86	0.38 0.38 0.63		Fe^{3+} Fe^{2+} Fe^{2+}	41
$0.01Fe_2O_3\ 33MgO\ 67P_2O_5$	1.21	2.24	-0.8	Reducing atmosphere	Fe^{2+}	44
$0.01Fe_2O_3\ 33CaO\ 67P_2O_5$	1.05	2.36	-0.8		Fe^{2+}	44
$4Fe_2O_3\ 32MgO\ 64P_2O_5$	0.38 1.10	0.85 2.30	-0.8 -0.8		Fe^{3+} Fe^{2+}	44
$4Fe_2O_3\ 32MgO\ 64P_2O_5$	0.40 1.07	0.80 2.15	-0.8 -0.8		Fe^{3+} Fe^{2+}	44
$12Fe_2O_3\ 44PbO\ 44P_2O_5$	0.39 0.42	0.96 0.40	0.50 0.50		Fe^{3+} Fe^{3+}	51

* Where possible compositions are expressed to the nearest mole percent of the appropriate oxide.

Various vitreous compositions of Grahams salts, Fe_2O_3 x($NaPO_3$) and Fe_3O_4 x($NaPO_3$) were examined by Takashima [34] and Kamo [35] along with a range of crystalline ferric iron salts. The Mössbauer parameters were different to those of the pure oxide, confirming that the iron had entered into some bonding with the other constituents of the glass. Glasses made with Fe_2O_3 yielded a single ferric doublet. The magnitude of the quadrupole splitting increased as the Fe_2O_3 content decreased. It was suggested that an increase in the average phosphate chain length, associated with a decrease in Fe_2O_3 content, might lead to a more distorted environment for the iron atoms. The glasses made with Fe_3O_4 as a starting material showed absorption lines which were tentatively resolved into two Fe^{2+} doublets and a Fe^{3+} singlet. Glass samples containing dissolved iron hydroxide produced spectra comprising a single, unresolved ferric doublet. The width and intensity of the line could be correlated with the average phosphate chain length, suggesting that an increase in chain length leads to more distorted, less strongly bound iron sites.

More recently Tanaka [36] has followed the devitrification of a simple iron phosphate glass on annealing at a range of temperatures. Three techniques were used to follow the crystallisation process: Mössbauer spectroscopy; electron spin resonance (E.S.R.) and X-ray diffraction. The results illustrate the comparative advantages and limitations of the analysis methods. Firstly, a range of glasses were prepared from the xFe_2O_3 (100-x) P_2O_5 system. X-ray analysis showed evidence of crystallisation for $x \geq 0.77$, whilst the E.S.R. and Mössbauer techniques could detect microcrystals for $x \geq 0.75$. For this reason a glass with composition $70Fe_2O_3$ $30P_2O_5$ was used for the annealing studies. It yielded a Mössbauer spectrum characteristic of

octahedral Fe^{3+} and Fe^{2+} (Table 2.2). After annealing at 420°C for 5 hours small Fe_2O_3 crystallites could be observed by X-ray analysis and above 500°C these were supplemented by various iron phosphate crystals. Both Mössbauer and E.S.R. were able to detect changes in the sample with annealing temperatures starting at 300°C. The linewidths of both the E.S.R. and Mössbauer resonance lines decreased whilst the isomer shifts of the ferric and ferrous doublets showed monotonous changes and the quadrupole splittings also showed significant variation. Only for annealing temperatures in excess of 500°C could Mössbauer spectroscopy detect any magnetic phase (Fe_2O_3) in the glass. Below this limit the crystalites are undergoing superparamagnetic relaxation and thus the time averaged magnetic field is zero, hence only paramagnetic doublets are observed.

Courant [37] has studied the effect of the intercalation of lithium and sodium ions into $40Fe_2O_3$ - $60P_2O_5$ glass. The alkali ions were added to the glass by reaction of the halide, dissolved in an organic solvent, and the base glass under an inert atmosphere. Intercalation ratios of upto 0.6 Li ions per Fe ion were achieved, yet the percentage volume growth did not exceed 5%. The reaction was carried out at 20°C, thus precluding any structural rearrangement of the ion sites (for instance changes from octahedral symmetry).

The Mössbauer spectra were fitted to two ferric doublets plus three separate lines to account for the ferrous component. The area of the low velocity ferrous line was found experimentally to be approximately equal to the sum of the areas of the two other ferrous lines, thus supporting the adopted fitting hypothesis. As expected the Fe^{2+}/Fe^{3+} ratio increased on intercalation since the addition of the monovalent alkali cations serves to reduce some of

the ferric iron to ferrous iron. The parameters for the first ferric doublet are typical of octahedral coordination, whilst those for the second suggest a tetrahedral environment, an unusual occurrence in phosphate glasses. Energy considerations dictate that the alkali ions will reside preferentially at octahedral sites, hence the Fe^{3+}('oct')/Fe^{3+}('tet') ratio should decrease as the Fe^{3+}('oct') ions are reduced to Fe^{2+}('oct'). This is found to be false. The Fe^{3+}('oct')/Fe^{3+}('tet') remains constant, hence both must be octahedral sites. The Fe^{2+} parameters show little change hence the 'new' Fe^{2+} sites produced by the reduction of Fe^{3+} must be the same as existing Fe^{2+} sites. In conclusion the authors propose a single iron site within the glass with distorted octahedral symmetry and suggest that the best method of fitting the spectrum would be with a distribution of hyperfine parameters. The work illustrates the care which must be taken in fitting the spectra of amorphous materials. The simple fitting procedure produces parameters suggestive of tetrahedral Fe^{3+} and it is only by a sophisticated argument that these are discounted.

Nishida and co-workers have examined the xK_2O $(100-x)P_2O_5$ $7Fe_2O_3$ glass system for x = 0-70 [38,39]. With x <50 the spectra comprised ferric and ferrous doublets with isomer shifts typical of octahedral oxygen coordination. As the K_2O content was increased upto x = 30 the quadrupole splitting of both doublets decreased, which they interpreted as suggesting an increase in symmetry around the iron sites. This is in agreement with the Zachariasen model (§1.2.2) which predicts an increase in the number of non-bridging oxygens (N.B.O.'s) as the modifying oxide content is increased. These N.B.O.'s are able to coordinate with the iron, thus increasing the symmetry of the sites and hence lowering ΔE_Q. In the same composition

region the area of the Fe^{2+} doublet increased at the expense of the Fe^{3+} doublet. This trend can also be attributed to the creation of more N.B.O.'s which will be available to reduce the Fe^{3+} to Fe^{2+}.

E.S.R. studies were made on iron free glass from the same system. The glass were first irradiated with a high flux of ^{60}Co γ-rays to produce positive holes at oxygen sites [40]. The intensity of the PO_4^{2-} E.S.R. line was seen to increase monotonously with x and this was interpreted as implying a continuous increase in the N.B.O. fraction. In contrast the Fe^{2+} percentage area starts to fall above x = 30, i.e. less reduction of Fe^{3+}. These two apparently contradictory results can be explained by postulating a change in symmetry for the iron sites. This is supported by the increase in ΔE_Q above x = 30. For x = 60, 70 the ferrous iron doublet is absent and the spectrum instead is fitted to two ferric iron doublets, one due to octahedral sites and the other tetrahedral. It appears that for these high alkali content glasses Fe^{3+} substitutes for P^{5+} in network forming 'FeO_4' tetrahedra.

Menil et al [41] have made a fundamentally different interpretation of the compositional variation of Fe^{2+} quadrupole splitting in iron-sodium-flurophosphate glass. According to Bancroft [42] and Ingalls [43] the quadrupole splitting of high spin Fe^{2+} decreases from a maximum value of ~3.7 mm/s as site distortion increases. This is because the $q_{lattice}$ component of Eqn. 2.28 is of the opposite sign to $q_{valence}$ and thus reduces the quadrupole splitting from the 'free ion' value. Their results show that the quadrupole splittings of both Fe^{2+} and Fe^{3+} sites increase with iron content and they deduce that the ions must be on distinctly different sites. For small iron loadings the Fe^{3+} ions preferentially occupy fully fluorinated $Fe^{3+}F_6$ octahedral

sites, but as the iron concentration is increased they also take up partially oxygenated $Fe^{3+}(O,F)_6$ sites with a subsequent increase in quadrupole splitting. The ferrous envelope is fitted to two doublets, although a continuous distribution of quadrupole splittings is felt to be more realistic. An almost fully oxygenated $Fe^{2+}O_6$ coordination is proposed for the ferrous ions. The ferrous sites will become more symmetric as the ion loading is increased, hence there is an increase in quadrupole splitting. This interpretation must be treated with some caution as it has only been verified experimentally for crystalline materials and opposes the structural interpretations made by Nishida [38,39] and other workers.

Simple alkaline earth phosphate glasses containing iron have been examined by Hirayama [44] and Frischat [45]. Both groups reported super-paramagnetic Fe^{3+} behaviour in glasses with less than 1 mole percent Fe_2O_3. Frischat observed a factor of two increase in line width as the iron concentration fell from 8 mol.% to 0.6 mol.%. The paramagnetic doublets were superimposed on a broad background signal due to incipient magnetic splitting. Hirayama prepared identical composition glasses under both oxidising and reducing atmospheres. Whilst the low iron content oxidised glasses showed superparamagnetism, the reduced glasses showed a single doublet due to octahedral Fe^{2+}. At a higher iron loading (11 mol.% Fe_2O_3) even the reduced glasses showed both ferrous and ferric doublets. No spectra could be recorded for glasses containing barium oxide due to bariums high γ-ray absorption cross-section. Complementary E.S.R. measurements suggested that a small fraction (5-15%) of the Fe^{3+} ions occupy tetrahedral sites although the Mössbauer spectra were of insufficient quality to support this result.

The x Fe_2O_3 (50-x)CaO $50P_2O_5$ system has been investigated by Sanad [46]. The ferrous/ferric ratio was seen to increase with increasing calcium content (50-x). This is due to the ability of the CaO to create N.B.O. which could then reduce ferric iron to the ferrous state.

^{119}Sn Mössbauer studies of alkaline earth phosphate glasses have been made by Eissa [47]. All the spectra consisted of a single broadened quadrupole doublet with parameters typical of octahedral Sn^{4+}. The isomer shift of the doublet decreased as the size of the alkaline earth cation increased in the order $Mg^{2+} \rightarrow Ca^{2+} \rightarrow Sr^{2+} \rightarrow Ba^{2+}$. The larger cations have smaller charge/ionic radius ratios and hence will polarise the surrounding oxygen ions to a lesser extent. This in turn leads to a higher electron density at the tin nucleus and thus a higher isomer shift. The quadrupole splitting values, all in the range 0.1-0.5 mm/s, are all less than the theoretical minimum line width (0.63 mm/s) and hence the doublets are unresolved. The authors suggest that the asymmetry of the doublet is a result of the Goldanskii-Karyagin effect although it is well knows that broad, assymmetric lines reflect the non-stoichiometry of glassy materials.

A large volume of work has been undertaken to assess the suitability of various oxide glasses for use in the vitrification of nuclear waste materials. Of major importance are the redox conditions under which the glass is produced. Too oxidising an atmosphere will cause the molten glass to foam, interfering with the furnace operation, whilst too low an oxygen content will induce the formation of precipitates within the melt [48]. Assessment of the Fe^{2+}/Fe^{3+} ratio by Mössbauer spectroscopy has been suggested as a method for measuring the redox potential [49]. Lead-iron phosphate glasses have distinct

advantages over borosilicate waste glasses including lower preparation temperatures and much lower aqueous corrosion rates [50]. Fundamental Mössbauer spectroscopy studies have been undertaken by Sales [51] on the base glass xFe_2O_3 (100-x) ($Pb0.P_2O_5$) with x = 22. The spectra consist of a broadened Fe^{3+} doublet superimposed on a weak unresolved absorption between ±3 mm/s. The ferric envelope was fitted to two quadrupole doublets, each with parameters consistent with octahedral coordination. This assignation was supported by complementary Raman spectroscopy studies. No attempt was made to account for the incipient magnetic hyperfine absorption which is the presumable source of the broad background. The x = 22 glass proved to be 700 times more resistant to corrosion than the iron free glass.

Gzowski [52] has investigated a series of phosphate glasses containing two transition metals, vanadium and iron. The Mössbauer parameters for glasses from the $(50-x)Fe_2O_3$ xV_2O_5 $50P_2O_50$ system suggest octahedral coordination for both Fe^{2+} and Fe^{3+}. This is in contrast to alkali vanadate glasses in which the iron occupies tetrahedral sites [53,54]. The Fe^{2+}/Fe^{3+} ratio was seen to increase monotonously with increasing Fe_2O_3 content.

2.4 References

1. Moon P.B.

   Proceedings of the Physical Society 64, 76, 1951

2. Mössbauer R.L.

   Zeitschrift für Physik 151, 124, 1958

3. Gonser U.

   'Mössbauer Spectroscopy', Springer-Verlag 1975, p.7

4. ibid. p.12

5. Rosenberg H.M.

   'The Solid State' Clarendon Press, 1978, p.87

6. Visscher W.M.

   Annals of Physics 9, 194, 1960

7. Boyle A.J.F.; Hall H.E.

   Reports on Progress in Physics 25, 441, 1962

7. Stevens J.G.; Stevens V.E.

   'Mössbauer Effect Data Index', IFI/Plenum 1975, p.54

8. Goldanskii V.I.; Herber R.H.

   'Chemical Applications of Mössbauer Spectroscopy', Academic Press 1968, p.4

9. Greenwood N.N.; Gibb T.C.

   'Mössbauer Spectroscopy', Chapman and Hall 1971, p.49

10. ibid. p.54

11. ibid. p.56

12. Sternheimer R.M.

Physical Review 80, 102, 1950

13. Gonser U.

'Mössbauer Spectroscopy', Springer-Verlag 1975, p.102

14. Greenwood N.N.; Gibb T.C.

'Mössbauer Spectroscopy', Chapman and Hall 1971, p.60

15. Edwards R.A.

Delivery notes for ^{57}Fe source, Ammersham International plc.

16. DeWaard H.

Review of Scientific Instruments 36, 1728, 1965

17. Spijkerman J.J.; Ruegg F.C.; De Voe J.R.

IAEA Technical Report Series No. 50, Vienna, p.53, 1966

18. Stevens J.G.; Stevens V.E.; Gettys W.L.

Mössbauer Effect Reference and Data Journal, 3(4), 99, 1980

19. Thorpe S.C.

'Surface Corrosion Studies by Mössbauer Spectrosopy', Ph.D Thesis, S.C.P., 1987, p.114.

20. Pollack H.; de Coster M.; Amerlinckx. S.

Proceedings of the 2nd International Conference on the Mössbauer Effect, Saclay 1961, p.298 Editors: Compton D.M.J. & Schoen A.H. Publishers: John Wiley, New York

21. Gupta A.; Verma R.P.; Kane S.N.; Lal S.

Hyperfine Interactions, 35, 659, 1987

22. Cusido A.J.; Tejada J.

Journal of Materials Science Letters, 5, 75, 1986

23. Boolchand P.

Materials Research Society Symposium Proceedings, 61, 57, 1986

24. Vértes A.; Burger K.; Takacs L.; Horvath I.

Journal of Radioanalytical and Nuclear Chemistry, 86, 195, 1984

25. Dyar M.D.; Birnie III D.P.

Journal of Non Crystalline Solids, 67, 397, 1984

26. Greenwood N.N.; Gibb T.C.

Mössbauer Spectroscopy, Chapman and Hall 1971, p.91

27. Coey J.M.D.

Journal de Physique, 35, C6-89, 1974

28. Dyar M.D.

Journal of the American Ceramic Society, 69,(7), C-160, 1986

29. Sekhon S.S.; Kamal R.

Physics and Chemistry of Glasses, 29(4), 157, 1988

30. Kurkjian C.R.

Journal of Non-Crystalline Solds, 3, 157, 1970

31. Sekhon S.S.; Kamal R.

Journal of Applied Physics, 49,(6), 3444, 1978

32. Belyustin A.A.; Ostanevich Yu.M.; Pisarevskii A.M.; Tomilov S.B.; Bai-shi U.; Cher L.

Soviet Physics - Solid State, 7(5), 1163, 1965

33. Kurkjian C.R.; Buchanan D.N.E.

Physics and Chemistry of Glasses, 5(3), 63, 1964

34. Takashima Y.; Ohashi S.

Bulletin of the Chemical Society of Japan, 38(10), 1684, 1965

35. Kamo H.; Takashima Y.; Ohashi S.

Bulletin of the Chemical Society of Japan, 40, 2812, 1967

36. Tanaka K.; Soga N.; Ota R.' Hirao K.

Bulletin of the Chemical Society of Japan, 59, 1079, 1986

37. Courant S.; Duclot M.; Pagnier T.; Ribes M.

Solid State Ionics, 15, 147, 1985

38. Nishida T.; Shiotsuki T.; Takashima Y.

Journal of Non-Crystalline Solids, 43, 115, 1981

39. Nishida T.; Shiotsuki T.; Takashima Y.

Journal of Non-Crystalline Solids, 43, 123, 19881

40. Kobayashi Y.; Matsuura N.

Bulletin of the Chemical Society of Japan, 46, 1346, 1973

41. Menil F.; Fournes L.; Dance J.M.; Videau J.J.

Journal of Non-Crystalline Solids, 34, 209, 1979

42. Bancroft G.M.

'Mössbauer Spectroscopy' McGraw-Hill, 1973 p.190

43. Ingalls R.

Physical Review, 133 (3A), 787, 1964

44. Hirayama C.; Castle Jnr J.E.; Kuriyama M.

Physics and Chemistry of Glass, 9 (4), 109, 1968

45. Frischat G.H.; Tomandl G.

Glastechnische Berichte, 44(5), 173, 1971

46. Sanad A.M.; Kashif I.; Khaled M.A.; Aly S.A.; Farouk H.

Physics and Chemistry of Glass, 30(1), 27, 1989

47. Eissa N.A.; Shaisha E.E.; Bahgat A.A.

Acta Physica Hungarica, 56, 21, 1984

48. Fanning J.C.; Hunter R.T.

Journal of Chemical Education, 65 (10), 889, 1988

49. Karraker D.G.

Advanced Ceramic Materials, 3 (4), 337, 1988

50. Sales B.C.; Boatner L.A.

Journal of Non-Crystalline Solids, 79, 83, 1986

51. Sales B.C.; Abraham M.M.; Bates J.B.; Boatner L.A.

Journal of Non-Crystalline Solids, 71, 103, 1985

52. Gzowski O.; Murawski L.; Lizak W.; Binczycka H.; Sawicki J.

Journal of Physics D : Applied Physics, 14, L77, 1981

53. Nishida T.; Takashima Y.

Bulletin of the Chemical Society of Japan, 60, 941, 1987

54. Nishida T.; Ogata M.; Takashima Y.

Bulletin of the Chemical Society of Japan, 60, 2887, 1987

CHAPTER THREE - COMPUTER INTERPRETATION OF MÖSSBAUER DATA

3.1 Computer Fitting of Mössbauer Spectra

3.1.1 Data Handling of Mössbauer Spectra

For each Mössbauer spectrum it is necessary to perform some degree of data handling in order to accurately determine the Mössbauer parameters which describe the data. This data handling consists of data transfer from the M.C.A. to a mainframe computer; determination of a calibration constant and subsequent computer fitting of theoretical line shapes to the data.

The data collected on the M.C.A. is downloaded onto an H.P.86 microcomputer, situated in the laboratory, via a standard R.S.232 serial link. (Fig. 3.1) A BASIC routine (MOSSPLOT9K) reads the data and stores it on a floppy disc. The program also has the facility to create a 'join the dots' plot of the raw data on a HP7475A plotter. Computer fitting of the data takes place on an IBM4341 mainframe computer. Transfer of the data from the HP86 to the IBM4341 is achieved using a KERMIT interface program which allows the HP86 to emulate a mainframe terminal. A successful transfer results in the creation of a file on the mainframe containing the raw data. Subsequent data processing can either be undertaken from the HP86 (acting as a line mode terminal) or by using a Tektronix 4010 graphics work station. The IBM4341 also gives access to a Calcomp plotter and a line printer for hard copies of graphics and output data. This system has recently been updated with the installation of an Apollo 570 minicomputer and IBM-AT microcomputers with E.G.&.G., M.C.A. and M.C.S. dedicated software.

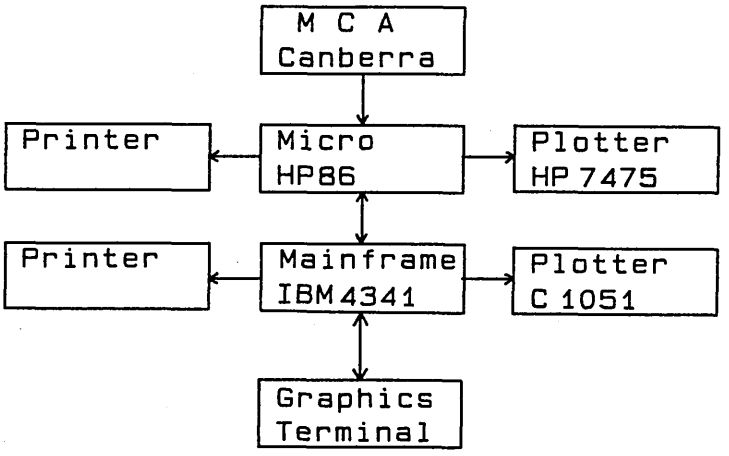

Figure 3.1 The computer architecture of the Mössbauer system.

3.1.2 The 'Folding' of Raw Data. MOSFOLD

Once the raw data has been transferred to the mainframe the first step in the data processing procedure is to reduce the mirror image spectrum produced by the M.C.A. ($2.2.5) to a single data set. This is accomplished using the FORTRAN F.77 program MOSFOLD. For any given number of data points NCHAN (the default is 512) a series of twenty one folding positions are taken between ±5 channels of the central channel. The folding positions are at regular half channel intervals. For each folding position a chi-squared test is applied to the result of reflecting one half of the data onto its mirror image. The final folding position is taken at the point corresponding to the lowest chi-squared value. The resulting folded data file has (NCHAN/2)-7 data points. Five folded data points are lost because of the possible shift of the folding position by upto 5 channels from the central channel. Two further folded data points are lost because the first and last channel of the raw data do not contain count information.

This folding procedure allows for any d.c. drift in the synchronisation of the source velocity with the sweep of the M.C.A. and also dramatically reduces the cosinusoidal background count rate (§2.2.5).

3.1.3 The Fitting Program, MOSFIT

The general fitting program MOSFIT is based on work by Longworth at U.K.A.E.A., Harwell [1]. It takes as input a set of folded data and a file containing the initial guess to the parameters which describe the spectrum. The fitting parameters are adjusted until the best fit to the data is achieved. Output from the program consists of the generated fit to the data and the associated final parameter values. MOSFIT can be used to fit both experimental data and calibration spectra.

Calibration spectra are fitted to independent Lorentzian line shapes with no constraints placed on their relative position, width or depth. No scaling of the velocity range is undertaken, instead the fit is generated in terms of channels. This enables a calibration constant CAL (channels/mms^{-1}) to be determined and allows for an assessment of transducer drive linearity (§2.2.6).

The calibration constant enables the velocity scale for successive spectra of 'unknown' materials to be defined. The fit to these 'unknown' materials can then be generated in terms of Doppler velocity (mms^{-1}) rather than channels. The initial guess for the Mössbauer parameters which describe the fit are made in terms of logical Mössbauer 'phases'. A phase is either a singlet, doublet or sextet. This system leads to the imposition of certain logical constraints on the relative position, width and depth of the lines of each phase.

The program operates so as to minimise the sum of the squares of the residuals R(i).

$$R(i) = \frac{FIT(i) - DATA(i)}{(DATA(i))^{\frac{1}{2}}} \qquad 3.1$$

$$\text{hence, } \chi^2 = \frac{1}{NCHAN - N} \sum (R(i))^2 \qquad 3.2$$

NCHAN = number of (folded) data points

N = number of independent fitting parameters

FIT(i) = calculated value of the spectrum in channel i

DATA(i) = experimental value of the spectrum in channel i

For this data capture process the errors in DATA(i) will be due to counting statistics and will have a standard deviation of $(DATA(i))^{1/2}$. Hence the denominator in Eqn. 3.1 is the statistical weighting factor.

The values of FIT(i) are composed of a single background count value BGND and the sum of contributions from each phase present in the spectrum:

$$FIT(i) = BGND + \sum_{j=1}^{NP} B(j)COUNT(i,j) \qquad 3.3$$

NP = number of phases

B(j) = depth of phase j

COUNT(i,j) = calculated value of phase j at channel i

The program proceeds as follows:

i) Read the initial guesses to the Mössbauer parameters PRMTR(k) which describe the spectrum DATA(i).

ii) Derive values for COUNT (i,j) using the parameters PRMTR(k).

iii) Calculate the 'best' values for BGND and B(j) using a linear least squares regression algorithm (LISFT)

iv) Calculate FIT(i) using Eqn. 3.3

v) Calculate chi-squared using Eqn. 3.2

vi) Adjust the parameters PRMTR(k) using the routine VA05A.

vii) Repeat steps ii), iii), iv), v), vi) until a minimum chi-squared value is reached.

viii) Write FIT(i) and COUNT(i,j) to an output file and the final values of the parameters PRMTR(k) to a listing file.

The routine VA05A contains a non-linear least squares regression algorithm which uses aspects from Newton-Raphson, steepest descent and Levenberg-Marquardt methods [2]. For a simple spectrum, for instance two quadrupole doublets, the minimum chi-squared value is found within approximately twenty calls to VA05A. This assumes that reasonable guesses are made for the initial parameter values PRMTR(k).

Each phase will be described by a number of fitting parameters.

For each singlet there are two parameters:

PRMTR(1) = δ (Chemical isomer shift)

PRMTR(2) = $\Gamma/2$ (half width at half height)

hence the contributions to the COUNT array will describe a Lorentzian line (Eqn. 2.19) with a half width $\Gamma/2$ centred at δ :

$$\text{COUNT(i,singlet)} = \frac{1}{\pi \frac{\Gamma}{2} (1+P^2)} \qquad 3.4$$

$$P = (i - \delta)/\Gamma_{/2}$$

For each doublet there are four parameters :

PRMTR(3) = δ (chemical isomer shift)

PRMTR(4) = Q (half quadrupole splitting)

PRMTR(5) = $\frac{\Gamma_L}{2}$ (half width of lower velocity line)

PRMTR(6) = $\frac{\Gamma_R}{2}$ (half width of higher velocity line)

hence contributions to the COUNT array is the sum of two Lorentzian lines :

$$\text{COUNT(i,doublet)} = \frac{1}{2(\pi\frac{\Gamma_L}{2}(1+P_L^2) + \pi\frac{\Gamma_R}{2}(1+P_R^2))} \qquad 3.5$$

$$P_L = \frac{i - \delta + Q}{\frac{\Gamma_L}{2}} \quad ; \quad P_R = \frac{i - \delta - Q}{\frac{\Gamma_R}{2}}$$

The situation for a sextet is even more complex with seven independent fitting parameters.

PRMTR(7) = δ (chemical isomer shift)

PRMTR(8) = H (magnetic field strength

PRMTR(9) = ε (quadrupole perturbation)

PRMTR(10) = Γ (half width of lines)

PRMTR(11) = $\partial\Gamma$ (incremental half width)

PRMTR(12) = I_{25} (relative intensity of lines 2 and 5)

PRMTR(13) = I_{16} (relative intensity of lines 1 and 6)

The magnetic field strength H is expressed as the half splitting (in mm/s) of lines 1 and 6 of the sextet. The incremental width $\partial\Gamma$ is designed to cope with slight distributions in field strength which will result in the 3 pairs of lines having different widths. The half widths of the lines are given by:

$$W_k = \Gamma + (\delta\Gamma \times H_k) \qquad 3.6$$

H_k = half splitting of each pair of lines

The relative intensity parameters I_{25} and I_{16} allow for any orientation and magnetisation effects in the absorber which may alter the transition probabilities. For a polycrystalline absorber I_{25} = 0.67 and I_{16} = 1.0. The contribution to the COUNT array from a sextet is given by :

$$\text{COUNT(i,sextet)} = \sum_{k=1}^{6} \frac{RI(k)}{\pi W_k (1+P_k^2)} \qquad 3.7$$

RI(k) is the relative intensity of each pair of lines :

$RI(1) = RI(6) = I_{16} / (I_{16} + I_{25} + 0.33)$

$RI(2) = RI(5) = I_{25} / (I_{16} + I_{25} + 0.33)$

$RI(3) = RI(4) = 0.33 / (I_{16} + I_{25} + 0.33)$

Starting from the most negative velocity line :

$P_1 = (i - \delta - \varepsilon + H) / (\Gamma + \partial\Gamma)$

$P_2 = (i - \delta + \varepsilon + ZH) / (\Gamma + Z\partial\Gamma)$

$P_3 = (i - \delta + \varepsilon - 2ZH) / (\Gamma + 2Z\partial\Gamma)$

$P_4 = (i - \delta + \varepsilon + 2ZH) / (\Gamma + 2Z\partial\Gamma)$

$P_5 = (i - \delta + \varepsilon - ZH) / (\Gamma + Z\partial\Gamma)$

$P_6 = (i - \delta - \varepsilon - H) / (\Gamma + \partial\Gamma)$

Where $Z = \frac{\text{separation of lines 5 and 6}}{H}$

$= \frac{\text{separation of lines 4 and 5}}{H}$

Various constraints may be placed on the otherwise independent variation of the fitting parameters PRMTR(k) by the routine VA05A. The parameters may be fixed at their starting values, for instance it may be desirable to force the incremental line width $\partial\Gamma$ to remain at 0.0mm/s. It is also possible to link parameters so that they vary, yet maintain the same starting ratio. This is often of use for forcing the line widths of a quadrupole doublet to be equal. The facility exists for forcing different phases of a fit to account for a set percentage of the total absorption area. This constraint could conceivably be employed if the ratio of two (or more) chemical sites had been determined by an independent analytical method. It must be assumed that the chemical sites yield the same recoil-free fraction in order to apply this constraint.

The regression routine VA05A operates so as to minimise the chi-squared value of the fit. A final chi-squared value close to or below unity can be regarded as satisfactory. However, it is difficult to use the chi-squared test to compare the adequacy of fits of different spectra unless they have been recorded under identical conditions. Better chi-squared values automatically follow from poorer quality data. For this reason a second goodness-of-fit parameter is also calculated which is independent of the quality of the data. This parameter is known as MISFIT [3]:

3.8

$$\text{MISFIT} = \frac{\text{Discrepancy}}{\text{Signal}} = \frac{D}{S}$$

The discrepancy D is defined in a similar manner to chi-squared :

$$D = \sum_{i=1}^{NCHAN} \left[\left[\frac{FIT(i)-DATA(i)}{(DATA(i))^{1/2}} \right]^2 - 1 \right] = NCHAN\,(\chi^2 - 1) \qquad 3.9$$

The signal S is a measure of the difference between the data DATA(i) and the background count BGND. Its value is dependent upon the count rate and duration of the experiment, hence a higher signal S implies higher quality data:

$$S = \sum_{i=1}^{NCHAN} \left[\left[\frac{BGND-DATA(i)}{(DATA(i)^{1/2}} \right]^2 - 1 \right] \qquad 3.10$$

If the fit is a close match to the data then the discrepancy D will be small, hence MISFIT will approach zero. For a poor fit the values of FIT(i) will be similar to the background BGND, hence the discrepancy D will compare with the signal S, hence MISFIT will tend towards unity. MISFIT is not applicable to fits with a chi-squared less than unity because this equates to a negative D and hence a negative MISFIT. The parameter is only valid when comparing fits with chi-squared greater than unity.

3.1.4 Enhanced Computer Fitting Techniques For Amorphous Materials

3.1.4.1 Summary of Parameter Distribution Fitting Algorithms

The general fitting program MOSFIT is designed to fit the spectra of crystalline material where there is a small number of chemical sites and hence a finite number of absorption lines. If MOSFIT is used to fit the spectra of amorphous materials it can only yield average parameter values since the

variation in the chemical sites means that each Mössbauer nucleus will have its own unique environment (§2.3.1). In order to determine the nature of the parameter distribution it is necessary to use enhanced fitting algorithms.

The simplest techniques consists of replacing the Lorentzian line shape by a Gaussian function or a more complex Pearson VII function which can vary between a Lorentzian and a Gaussian [4]. Whilst giving better fits (lower chi-squared) this approach still only yields average Mössbauer parameter values.

The deconvolution of experimental spectra in terms of standard spectra has been used to examine iron-silicate glass [5]. The spectra of glass samples prepared under extreme reducing and extreme oxidising conditions were used as standards and all other spectra were fitted as a function of these two spectra. The Fe^{2+}/Fe^{3+} ratios derived by this method were in agreement with wet chemical analysis. This method involves five fitting parameters, whilst a simpler method has been used to fit magnetic spectra as a linear combination of standard spectra with just two fitting parameters [6].

Spectra can be fitted to a large set of sub spectra which have some pre-defined distribution in their Mössbauer parameters. The assumed shapes include Gaussian and binominal distributions [7]. The broadened ferric doublet of an iron-borate glass has been fitted using a Gaussian distribution of isomer shifts [8]. Each doublet was given an identical quadrupole splitting. The fit results in a reduction in chi-squared when compared to a fit made in terms of two doublets corresponding to tetrahedral and octahedral Fe^{3+}. Their analysis calls into question the existence of two distinct types of iron site within borate

glass. Gaussian distributions of quadrupole doublets have been used to fit spectra of iron-silicate glass [9]. No indication is made of any correlation between the isomer shift and quadrupole splitting of the component doublets. The success of assumed parameter distribution functions for fitting spectra relies critically on the choice of the function. There should be some independent justification for the use of a particular function and hence the method cannot be regarded as generally applicable.

More general methods have been developed which make no initial assumptions as to the shape of the parameter distribution function. Window [10] has developed an algorithm for which the distribution is represented as a Fourier series. This method can be applied to the deconvolution of magnetic spectra although it has been shown that care must be taken when assigning values for the isomer shift, quadrupole splitting, line width and intensity ratio, none of which are varied in the iteration procedure [11]. The truncation of the Fourier series also causes spurious oscillations in the distribution function [12].

A distribution comprising a discrete set of equally spaced parameter values has been described by Varret [13] and extended by Hesse and Rübartsch [11]. The equations to be solved are the form:

$$\mathrm{DATA}(i) + \mathrm{ERROR}(i) = \mathrm{DIST}(y)\ A(i,y) \qquad 3.11$$

DATA(i) = experimental data point i

ERROR(i) = error at point i

DIST(y) = distribution function of parameter y

A(i,y) = expression defining the elementary spectra at point i

These equations can be solved numerically following the method developed by Phillips [14] and Twomey [15]. The algorithm has subsequently been refined to force all the parameter values to be positive [16] and constraints have been added which control the values of the end points of the distribution function [17].

The distribution fitting methods assume a correlation between some of the Mössbauer parameters whilst giving the other Mössbauer parameters constant fixed values. The linewidth of each component sub-spectrum of a distribution is usually set at a constant value. For magnetic spectra it is usual to fix the intensity ratio and to assume a constant value for δ and ΔE_Q or a linear correlation between δ and H and between ΔE_Q and H. Fitting algorithms for paramagnetic spectra generally assume a linear correlation between δ and ΔE_Q, although matrix methods have been used which assume no correlation [18].

3.1.4.2 The Distribution Fitting Program. PQH

The distribution fitting routine PQH is based on a program written by E. Vandenberge using the procedure developed by Wivel and Morup [17]. It proceeds in a grossly similar manner to MOSFIT (§3.1.3): a data set DATA(i) and initial guesses to the parameters which describe the spectrum are provided and an iteration algorithm seeks to adjust the parameters so as to minimise chi-squared (Eqn. 3.2). The added complexity in PQH is the presence of extra parameters which describe the distribution of the Mössbauer parameter values.

The generated fit FIT(i) can be described as the convolution of an expression describing the elementary Mössbauer spectrum A(i,y) with a weighting factor DIST(y) which describes the distribution function. For instance, A(i,y) might describe a pair of quadrupole doublets whilst DIST(y) would describe the allowed ranges of quadrupole splittings and isomer shifts and their relative intensities:

$$FIT(i) = \int_{y_1}^{y_2} DIST(y)A(i,y)dy \qquad 3.12$$

The limits of the integral y_1, y_2 imply that the distribution function DIST(y) is only non-zero over a limited range.

Due to statistical fluctuations in the counting there will always be an error ERROR(i) between each data point DATA(i) and a theoretical fit FIT(i):

$$FIT(i) = DATA(i) + ERROR(i) \qquad 3.13$$

$$DATA(i) + ERROR(i) = \int_{y_1}^{y_2} DIST(y)A(i,y)dy \qquad 3.14$$

The integral in Eqn. 3.14 can be approximated to a summation over N points and the equation can be expressed in matrix form:

$$DATA + ERROR = DIST\ A \qquad 3.15$$

Morup [17] has extended the method developed by Phillips [14] and Twomey [15] for determining DIST from Eqn. 3.15 for a given set of elementary spectra described by A. The method involves placing a number of constraints on the solution.

i) the sum of the squares of the errors (U_1) is minimised

$$U_1 = \sum_i \text{ERROR}(i)^2 \qquad 3.16$$

ii) the distribution function DIST(y) is smoothed. Specifically the sum of squares of the second differences in DIST(y) is minimised (U_2):

$$U_2 = \sum_j ((\text{DIST}_{j+1} - \text{DIST}_j) - (\text{DIST}_j - \text{DIST}_{j-1}))^2 \qquad 3.17$$

iii) the distribution function DIST(y) is subject to a specified behaviour.

Normally that each value of DIST_j tends towards a defined value K_j with a certain strength given by a set of Lagrangian multipliers β_j. Only the end points of the distribution function used need be constrained to be close to zero, hence all $\beta = 0$ except β_1 and β_N and K is a null vector.

$$U_3 = \sum_j \beta_j (\text{DIST}_j - K_j)^2 \qquad 3.18$$

These three conditions must be satisfied simultaneously and are linked via a second Lagrangian multiplier γ:

$$U = U_1 + \gamma (U_2 + U_3) \qquad 3.19$$

We wish to minimise Eqn. 3.19 with respect to DIST_j:

$$\therefore \frac{\partial U}{\partial \text{DIST}_j} = 0$$

$$\therefore 2\gamma (\text{DIST}_{j-2} - 4\text{DIST}_{j-1} + (6 + \beta_j)\,\text{DIST}_j - 4\text{DIST}_{j+1} + \text{DIST}_{j+2}) +$$

$$2 \sum_i \text{ERROR}_i A_{i,j} - 2\gamma \beta_j K_j = 0 \qquad 3.20$$

Simplification of Eqn. 3.20 and substitution into Eqn. 3.15 leads to the following result, in matrix notation:

$$(A^+ A + \gamma R)\ DIST = A^+\ DATA \qquad 3.21$$

A^+ is the transpose of A and R is an i×j matrix whose elements constitute the terms of Eqn. 3.20 plus β_1 and β_N as appropriate.

Eqn. 3.21 enables DIST to be calculated for a given set of data DATA elementary spectra A and Lagrangian multipliers β_1, β_N, γ contained in R. The calculation is part of an iterative procedure in which the elementary spectra A are varied until a minimum chi-squared is obtained. The iteration procedure makes use of the IMSL Inc. non-linear least squares regression algorithm ZXSSQ [19]. The full program PQH proceeds as follows:

i) Read data DATA(i); initial guess to the parameters which describe the elementary spectra A and the parameters which describe the distribution function DIST.

ii) Calculate DIST using Eqn. 3.21.

iii) Calculate FIT(i) using Eqn. 3.12.

iv) Calculate chi-squared using Eqn. 3.2.

v) Adjust elementary spectra parameters using ZXSSQ.

vi) Repeat ii), iii), iv), v) until a minimum chi-squared is reached.

vii) Write FIT to an output file and the final parameter values to a listing file.

The lines of a quadrupole doublet due to ferrous of ferric iron in glass are usually unequally broadened. The peaks have the same absorption area, but the higher velocity line is broader and less intense than the lower velocity line. This suggests that there is some average correlation between the isomer shift δ and the quadrupole splitting ΔE_Q of the individual iron sites. To a first approximation a linear correlation may be assumed:

$$\delta = \overline{\delta} + \eta(\Delta E_Q - \overline{\Delta E_Q}) \equiv \xi + \eta \Delta E_Q \qquad 3.22$$

ξ and η are the two parameters which describe an elementary spectrum A for a quadrupole doublet. It is these which are varied by ZXSSQ. Similar linear correlations exist between the Mössbauer parameters describing the elementary spectrum of a magnetic material.

If the variation in quadrupole splitting is symmetric then it has been shown that it is possible to construct two different distributions which fit the data equally well. The two distributions correspond to different values for ξ and η [17], however, it is usually possible to discount one of the distributions because it gives physically unrealistic values for isomer shifts and quadrupole splittings. The Lagrangian multipliers γ and β should both be set as large as possible. γ is set at the highest value which does not produce a significant increase in chi-squared. Typically $\gamma \simeq 1$. Any feature lost from the distribution function by having this maximum value for γ must be regarded as insignificant. β is set just large enough ($\beta \simeq 10$) to ensure the desired end point behaviour of the distribution function.

3.2 Applications of the Debye Theory of Solids

3.2.1 Introduction

Most Mössbauer experiments are concerned with the identification of the hyperfine interactions which a sample may exhibit. In addition it is possible to examine the vibrational properties of the Mössbauer atom by the recording of a series of variable temperature spectra. From these spectra there are two independent methods for determining the Debye temperature θ_D and hence the recoil-free fraction f_A of the absorber. The first method involves the accurate measurement of the change in absorption line area with temperature (\$3.2.2) whilst the second makes use of the second order Doppler shift of the resonance line, which produces a small, but measurable temperature dependent component to the chemical isomer shift (\$3.2.3). Both methods assume that the vibrational properties of the sample can be represented by the Debye model of solids (\$2.1.3). This is not strictly true for a metal, and certainly not for a phosphate glass, which means that the results can only be treated qualitatively or on a comparative basis.

3.2.2 The Temperature Dependence of the Absorption Line Area

3.2.2.1 The Physical Basis of Absorption Line Area Calculations

The probability f of recoilless emission of a γ-ray has been derived in \$2.1.3:

$$f = \exp [-k^2 \langle x^2 \rangle] = \exp [-2W] \qquad 3.23$$

The exponential factor is often referred to as the Debye-Waller factor 2W since it was derived prior to the discovery of the Mössbauer effect as a part of X-ray scattering theory. For a monatomic cubic lattice the Debye-Waller factor is given by [20]:

$$2W = \frac{E_0^2}{2Mc^2\hbar} \int_0^\infty \frac{N(\omega)}{\omega} \coth\left[\frac{\hbar\omega}{2k_B T}\right] d\omega \qquad 3.24$$

where E_o = γ-ray energy

M = mass of nucleus

$N(\omega)$ = normalised density of states with angular frequency ω

Assuming that $N(\omega)$ can be represented by the Debye model function $g(\omega)$ (Eqn. 2.10), Eqn. 3.24 can be simplified:

$$2W = \frac{3E_0^2}{Mc^2 k_B \theta_D}\left[\frac{1}{4} + \left[\frac{T}{\theta_D}\right]^2 \int_0^{\theta_{D/T}} \frac{x}{e^x - 1}\, dx\right] \qquad 3.25$$

Eqn. 3.25 describes the temperature dependence of the recoil-free fraction f for given values of E_o, M and θ_D. There are high and low temperature approximations to Eqn. 3.25:

$$2W = \frac{3E_0^2}{4Mc^2 k_B \theta_D} \qquad T = 0 \qquad 3.26$$

$$2W = \frac{3E_0^2 T}{Mc^2 k_B \theta_D^2} \qquad T \geq \frac{\theta_D}{2} \qquad 3.27$$

At high temperatures it is often found that 2W is non-linear with respect to the temperature T [21]. This indicates a departure from the Debye model, which assumes a harmonic potential for the vibrational modes [22]. High temperature data of amorphous polymers has been successfully fitted to an anhormonic potential [23].

The absorption line area A(t) can be expressed as a function of the Mössbauer absorber thickness t (\$2.2.3) [24].

$$A(t) = f_s \Gamma_A \pi \frac{t}{2} \exp\left[-\frac{t}{2}\right] \left[I_0\left(\frac{t}{2}\right) + I_1\left(\frac{t}{2}\right)\right] \qquad 3.28$$

I_o, I_1 = zero and first order Bessel functions

f_s = recoil-free fraction of source

Γ_A = line width of absorber

For small values of t ($t \leq 1$) Eqn. 3.28 can be simplified by a series expansion of t [25]:

$$A(t) = K f_s t \left(1 - \frac{t}{4} + \left[\frac{t}{4}\right]^2 + \ldots\ldots\right) \qquad 3.29$$

Where K = constant

The Mössbauer absorber thickness t is proportional to the recoil free fraction of the absorber f_A (Eqn. 2.34), hence for small t:

$$A \propto f_A \qquad 3.30$$

$$\therefore \quad A \propto \exp\,[\,-2W\,] \qquad 3.31$$

Using Eqn. 3.31 it is possible to determine the Debye temperature θ_D and recoil-free fraction f_A of a sample. Mössbauer spectra of a 'thin' absorber ($t \leq 1$) are recorded over a range of temperatures under identical experimental conditions. A plot of the normalised area versus temperature will be of the form of Eqn. 3.32:

$$A(T) = K \exp[-2W] = K \exp\left[\frac{-3E_0^2}{Mc^2 k_B \theta_D^2}\right]\left[\frac{1}{4}+\left[\frac{T}{\theta_D}\right]^2 D_1\left[\frac{\theta_D}{T}\right]\right] \qquad 3.32$$

Where D_1 represents the Debye integral:

$$D_1 = \int_0^Z \frac{x}{e^x - 1}\,dx \qquad 3.33$$

Where $Z = \frac{\theta_D}{T}$

It may be appropriate to use the high temperature approximation (Eqn. 3.27) to obtain θ_D. A more general solution involves the evaluation of the Debye integral D_1. It cannot be solved analytically but a number of numerical methods have been devised. The value of the integral has been tabulated for Z=0.1 to Z=20 using a Simpson's rule integration [26]. An approximation of the integral has been derived by fitting an arbitrary function to the tabulated data and employing a least squares minimisation routine to determine the best values for the constants [27]. The resulting approximation to D_1 is given by:

$$D_1 = 1.6449\ (\ 1 - \exp\ [\ -0.64486Z\ ]) \qquad 3.34$$

Eqn. 3.34 gives a maximum 6% error in D_1, which can be reduced to 2% by the addition of a second arbitrary error function.

A second numerical method has been described by Heberle [28] which evaluates the Debye integral in terms of infinite series. Two formulae are derived which give less than 0.1% error within the specified ranges of Z:

High temperature formula:

$$D_1(Z) = Z\left[1 - \frac{Z}{4} + \frac{Z^2}{36} - \frac{Z^4}{3600}\right] \qquad 0 \leq Z \leq 2.2 \qquad 3.35$$

Low temperature formula:

$$D_1(Z) = \frac{\pi^2}{6} + Z\log(1-y) - y - \frac{y^2}{4} \qquad 1.7 \leq Z \leq \infty \qquad 3.36$$

Where $y = \exp(-Z)$

3.2.2.2 The Area Versus Temperature Fitting Program. LNAT

Both of the Mössbauer spectra fitting programs MOSFIT and PQH calculate absorption line areas. For MOSFIT the area of each phase is calculated, as well as the area of the total absorption profile, whilst for PQH the area of each parameter distribution set is derived. The absorption areas will be critically dependent upon the experimental conditions (source-absorber geometry, activity of source, Mössbauer absorber thickness) under which the spectra are recorded. It is thus important to record variable temperature spectra under identical conditions so that all the factors which effect the absorption area A(T), except the temperature dependence of the recoil-free fraction f_A, are constant.

The areas are computed as the difference between the profile of either the total envelope or an individual phase/distribution envelope and the average background count rate BGND.

$$\text{Area} = \sum_{i=1}^{NCHAN} \text{PROFILE}(i) - \text{BGND} \qquad 3.37$$

For absorption spectra these areas will be negative. In order to compare spectra the areas must be normalised to account for differences in count rate and experiment duration, both of which lead to differing values for BGND. Normalisation is achieved by dividing the area by BGND:

$$\text{Normalised Area} = \frac{\text{Area}}{\text{BGND}} \qquad 3.38$$

The variable temperature absorption area fitting programme LNAT uses a non-linear least squares routine LMDIF1 based on a modified version of the Levenburg-Marquardt algorithm [29]. LMDIF1 has two variables, a premultiplying factor K and the Debye temperature θ_D. It aims to minimise the sum of squares of the residuals by varying K and θ_D:

$$\chi^2 \sum_{i-1}^{N} (Kf(i) - DATA(i))^2 \qquad 3.39$$

where f(i) is the recoil-free fraction at data point i as described in Eqn.3.32.

The data DATA(i) consists of the normalised absorption area of a particular profile as a function of absorber temperature. A routine FFACT utilises the low and high temperature formulae for D_1 derived in §3.2.2.1 (Eqns. 3.35, 3.36). An additional parameter M_{eff} allows the effective recoiling mass to be defined. Its default value is that of an ^{57}Fe nucleus, but it may be desirable to increase M_{eff} when dealing with certain polymeric materials [23]. An inbuilt graphics routine enables LNAT to produce a plot of the data with the generated fit to the Debye model.

3.2.3 Second Order Doppler Shift

3.2.3.1 The Physical Basis of Second Order Doppler Shift Calculations

In the discussion of recoilless γ-ray emission (§2.1.3) it was stated that the average displacement of the nucleus during a Mössbauer transition is zero and hence the γ-ray linewidth is not thermally broadened. There is, however, a term in the relativistic Doppler equation (Eqn. 3.40) which is dependent on v^2, the square of the thermal velocity of the nucleus:

$$\nu^1 = \nu\left[1 - \frac{v}{c}\right]\left[1 - \frac{v^2}{c^2}\right]^{-\frac{1}{2}} \qquad 3.40$$

where ν^1 = observed frequency of γ-ray for nucleus moving with thermal velocity v.

ν = γ-ray frequency for a stationary nucleus.

Using series of expansion for $\frac{v^2}{c^2} << 1$:

$$\nu^1 = \nu\left[1 - \frac{v}{c}\right]\left[1 + \frac{v^2}{2c^2} + \ldots\right]$$

But $\langle v \rangle = 0$

$$\nu^1 = \nu\left[1 + \frac{\langle v^2 \rangle}{2c^2}\right] \qquad 3.41$$

The mean value $\langle v^2 \rangle$ is non zero hence there is a frequency shift in the emitted γ-ray.

The change in energy dE due to the thermal motion of the nucleus is given by:

$$dE = h\nu - h\nu' = h\nu - h\nu \left[1 + \frac{\langle v^2 \rangle}{2c^2}\right]$$

$$\therefore \quad dE = -E \frac{\langle v^2 \rangle}{2c^2}$$

Hence the fractional energy change is given by:

$$\frac{dE}{E} = -\frac{\langle v^2 \rangle}{2c^2} \qquad 3.42$$

This is also the definition of the second order Doppler shift:

$$\frac{dE}{E} = \frac{\delta_{SODS}}{c} \qquad 3.43$$

Hence

$$\delta_{SODS} = \frac{-\langle v^2 \rangle}{2c} \qquad 3.44$$

This small shift in the γ-ray line position is dependent upon the mean thermal energy of the nucleus $\frac{1}{2}m\langle v^2 \rangle$ and thus produces a small temperature component to the chemical isomer shift δ [30].

If the atoms of a solid are assumed to experience a harmonic potential then the mean kinetic energy will be half the mean lattice energy per unit mass U [31]:

$$\frac{1}{2} mU = \frac{1}{2} m \langle v^2 \rangle$$

$$\therefore \quad U = \langle v^2 \rangle \qquad 3.45$$

Substituting into Eqn. 3.44:

$$\delta_{SODS} = - \frac{U}{2c} \qquad 3.46$$

Assuming that the density of vibrational states can be described by the Debye model an expression may be derived for U [32]. The expression (Eqn. 3.47) has a temperature dependent component as well as a zero point energy term:

$$U = \frac{9}{8} \frac{k_B \theta_D}{M} + \frac{9 k_B T}{M} \left[\frac{T}{\theta_D}\right]^3 \int_0^{\theta_{D/T}} \frac{x^3}{e^x - 1} \, dx \qquad 3.47$$

Where M = mass of nucleus

$$\therefore \quad \delta = \frac{-9}{16} \frac{k_B \theta_D}{Mc} - \frac{9}{2} \frac{k_B T}{Mc} \left[\frac{T}{\theta_D}\right]^3 D_3 \left[\frac{\theta_D}{T}\right] \qquad 3.48$$

Where

$$D_3(Z) = \int_0^Z \frac{x^3}{e^x - 1} \, dx \qquad 3.49$$

D_3 is another Debye integral and like D_1 (Eqn. 3.33) it has no analytical solution. There are, however, high and low temperature approximations [28] which give a less than 0.1% error within the specified ranges of Z:

High temperature:

$$D_3(Z) = \frac{Z^3}{3}\left[1 - \frac{3Z}{8} + \frac{Z^2}{20} - \frac{Z^4}{1680} + \frac{Z^6}{90720}\right] \quad 0 \le Z \le 2.5 \qquad 3.50$$

Low temperature:

$$D_3(Z) = \frac{\pi^4}{15} + Z^3 \log(1-y) - 3\sum_{n=1}^{2}\frac{y^n}{n^4} - (n^2Z^2 + 2nZ + 2) \quad 2.5 \le Z < \infty \qquad 3.51$$

Where $y = \exp[-Z]$

3.2.3.2 The Second Order Doppler Shift Fitting Program ISODS

The chemical isomer shift δ of a Mössbauer absorption line can be considered as the sum of two components: the second order Doppler shift δ_{SODS}, which is temperature dependent, and the intrinsic isomer shift, which is a constant for all temperatures:

$$\delta = \delta_{SODS} + \delta_{int} \qquad 3.52$$

Hence from Eqn. 3.48 : [33,34]

$$\delta = \delta_{int} - \frac{9\ k_B\theta_D}{16\ Mc} - \frac{9\ k_BT}{2\ Mc}\left(\frac{T}{\theta_D}\right)^3 D_3\left(\frac{\theta_D}{T}\right) \qquad 3.53$$

The ISODS program seeks to fit a set of isomer shift data $\delta_{exp}(i)$ recorded at different temperatures T(i) to an equation of the form of Eqn. 3.53.

There is a single fitting parameter θ_D which is varied by a simplex optimisation routine SIMIT [35] until a minimum chi-squared is obtained.

$$\chi^2 = \sum_{i=1}^{N} \left(\delta_{theory}(i) - \delta_{exp}(i) \right)^2 \qquad 3.54$$

Where

$\delta_{theory}(i) = \overline{\delta}_{int} + \delta_{SODS}(i)$ = theoretical value of isomer shift at point i

and

$\overline{\delta}_{int} = \frac{1}{N} \sum_{i=1}^{N} \delta_{exp}(i) - \delta_{SODS}(i)$ = average intrinsic isomer shift

The second order Doppler shifts $\delta_{SODS}(i)$ are calculated for a given θ_D in a routine SODS which employs the approximation to the Debye integral D_3 stated in §3.2.3.1 (Eqns. 3.50, 3.51). The recoil-free fractions at each temperature $f_A(i)$ are calculated in a routine DWFAC using the same method as LNAT (§3.2.2.2). A plot routine allows a graphical representation of the theoretical fit to the data to be obtained.

3.3 The Mössbauer Program Suite MOSBAR

To facilitate swift data processing the various Mössbauer associated programs are contained in a single menu driven package MOSBAR [36]. It allows for the maximum use of default file names and options. An experienced user can proceed from a raw set of experimental data to a plot of the fitted data in a very short time period. This speed makes it possible to examine different spectra fitting schemes with little time penalty, an important factor if attempting to describe a complex spectrum.

In addition to the data processing routines described in §3.1 and §3.2 the MOSBAR suite contains a number of graphics routines. The routines utilise the GINO-F Mark 2.6 graphics libraries and allow for both hard copy plots and V.D.U. presentation. The simplest routine MOSPLOT is designed to display a folded data set with or without its accompanying fit. The second routine PHASPLOT displays a folded data set and fit plus the constituent 'phases' from which the fit is comprised. Two routines allow data sets to be stacked in order to show spectra variation. MULTPLOT and SCALPLOT plot the spectra vertically above one another, taking into account any differences in calibration constant. MULTPLOT depicts each component spectrum with the same intensity, whereas SCALPLOT scales each spectrum so that any variation in the percentage effect will become evident. The final graphics program DISPLOT displays the quadrupole and/or hyperfine field distributions derived from PQH.

3.4 References

1. Longworth G.

'Spectral data reduction and refinement' in Mössbauer Spectroscopy Applied to Inorganic Chemistry Volume 1' editor Long G.J.; Plenum Press Chapter 4, p.43, 1984

2. Belward J.A.

in 'Numerical Algorithms'. Ed. Mohamed J.L.; Walsh J. Oxford Science Publications, 1986, p.275

3. Ruby S.L.

Mössbauer Effect Methodology, 8, 263, 1973

4. Vandenberghe R.E.; Gryffroy D.; DeGrave E.

Nuclear Instruments and Methods in Physics Research, B26, 603, 1987

5. Massiot D.

Journal of Non-Crystalline Solids, 69, 371, 1985

6. Varret F.

Hyperfine Interactions, 30, 135, 1986

7. Vincze. I.

Solid State Communications, 25, 689, 1978

8. Saini M.S.; Kamal R.

Journal of Non-Crystalline Solids, 87, 103, 1986

9. Yuanfu H.; Rongchuan L.; Jing J.F.; Gonser U.; Engelmann H.

Hyperfine Interactions, 27, 409, 1986

10. Window B.

Journal of Physics E: Scientific Instruments, 4, 401, 1971

11. Hesse J.; Rübartsch A.

Journal of Physics E: Scientific Instruments, 7, 526, 1974

12. Keller H.

Journal of Applies Physics, 52(8), 5268, 1981

13. Varret F.; Gerard A.; Imbert P.

Physics Status Solid; B43, 723, 1971

14. Phillips D.L.

Journal of the Association of Computing Machinery, 9, 84, 1962

15. Twomey S.

Journal of the Association of Computing Machinery, 10, 97, 1963

16. LeCaer G.; Dubois J.M.

Journal of Physics E: Scientific Instruments, 12, 1083, 1979

17. Wivel C.; MØrup S.

Journal of Physics E: Scientific Instruments, 14, 605, 1981

18. Levitz P.; Bounin D.; Calas G.; Legrand A.P.

Journal of Physics E; Scientific Instruments, 13, 427, 1980

19. Belward J.A.

in 'Numerical Algorithms' Ed. Mohamed J.L.; Walsh J., Clarendon Press 1986, p.275

20. Boyle A.J.F.; Hall H.E.

Reports on Progress in Physics, 25, 441, 1962

21. Bharati S.; Parthasorathy R.; Rao K.J.; Rao C.N.R.

Solid State Communications, 46(6), 457, 1983

22. Boyle A.J.F.; Burbury D.St.P.; Edwards C.; Hall H.E.

Proceedings of the Physical Society, 77, 129, 1960

23. Brooks J.S.; Care C.M.; Plimley S.; Corfield G.C.

Hyperfine Interactions, 20, 151, 1984

24. Goldanskii V.I.; Herber R.H.

'Chemical Applications of Mössbauer Spectroscopy', Academic Press 1968, p.27

25. Williams J.M.; Brooks J.S.

Nuclear Instruments and Methods, 128, 363, 1975

26. Muir A.H.

'Tables and graphs for computing Debye-Waller factors in Mössbauer effect studies' Atomics International, 1962

27. Hardy K.A.; Parker F.T.; Walker J.C.

Nuclear Instruments and Methods, 86, 171, 1970

28. Heberle J.

Mössbauer Effect Methodology, 7, 299, 1971

29. Moré J.J.

Lecture Notes in Mathematics, 630, 105, 1978

30. Pound R.V.; Rebka G.A.

Physical Review Letters, 4(6), 274, 1960

31. Josephson B.D.

Physical Review Letters, 4(7), 341, 1960

32. Decker A.J.

'Solid State Physics', Macmillan and Co., 1958, p.42 and p.130

33. Schiffer J.P.; Parks P.N.; Heberle J.

Physical Review, 133, (6A), 1553, 1964

34. Lafleur L.D.; Goodman C.

Physical Review, B4(9), 2915, 1971

35. Cave M.

'Fundamental Studies of the analytical applications of an inductively coupled plasma source', Ph.D. Thesis, S.C.P., 1980, p.53

36. Williams G.L.

'Using MOSBAR under VM/CMS', Sheffield City Polytechnic Computer Services V6/3.56, 1988

CHAPTER FOUR - PRELIMINARY MÖSSBAUER STUDIES

4.1 Room Temperature Spectra of Preliminary Iron-Phosphate Glasses

Initial ^{57}Fe Mössbauer studies were carried out on five sodium-potassium-iron-phosphate glasses (Table 4.1). The glass samples were in the form of opaque 5mm thick sheets. The Mössbauer thickness (§3.2.2.1) of these sheets was far in excess of unity, therefore it was necessary to make absorbers from powdered samples of the glass dispersed in graphite. A collection time of the order of 18 hours was sufficient to produce satisfactorily resolved spectra with approximately 500,000 counts per channel.

Table 4.1 Composition of preliminary iron-phosphate glasses

Sample Code	Fe_2O_3	Na_2O	K_2O	P_2O_5 (MOL/%)
J 1	16	41	0	43
J 2	17	34	6	43
J 3	19	25	13	43
J 4	22	15	22	41
J 5	26	0	35	39

Spectra recorded over a velocity range of ±12 mm/s did not reveal any magnetic hyperfine phases within the glass. This implies that the Fe_2O_3 is not present as microcrystalline impurities but has instead been fully dissolved into the glass. X-ray diffraction studies support this view. The majority of the subsequent spectra were recorded over a velocity range of ±4 mm/s which is sufficient to cover absorption lines due to paramagnetic species.

The spectra were initially fitted to two quadrupole doublets using MOSFITN (§3.1.3). These two doublets, by comparison with accepted parameter ranges (§2.3.1) can be assigned to octahedral ferric and ferrous iron sites (Table 4.2). The substantial broadening of the absorption lines and the

departure from Lorentzian shapes are immediately apparent from the fits (Fig. 4.1). This is indicative of the considerable distortion of the lattice sites within the glass. As a starting point for MOSFITN all four lines were given an equal width, however it was usual for these to be substantially modified by the fitting algorithm. MOSFITN allows the component lines of each doublet to adopt different widths, with the constraint that the line areas remain equal. This amounts to a simple attempt to allow for distributions of site parameters. The program will not allow equal linewidths with unequal line areas, a fitting scheme which would be indicative of texture effects [1] or the Goldanskii-Karyagin effect [2].

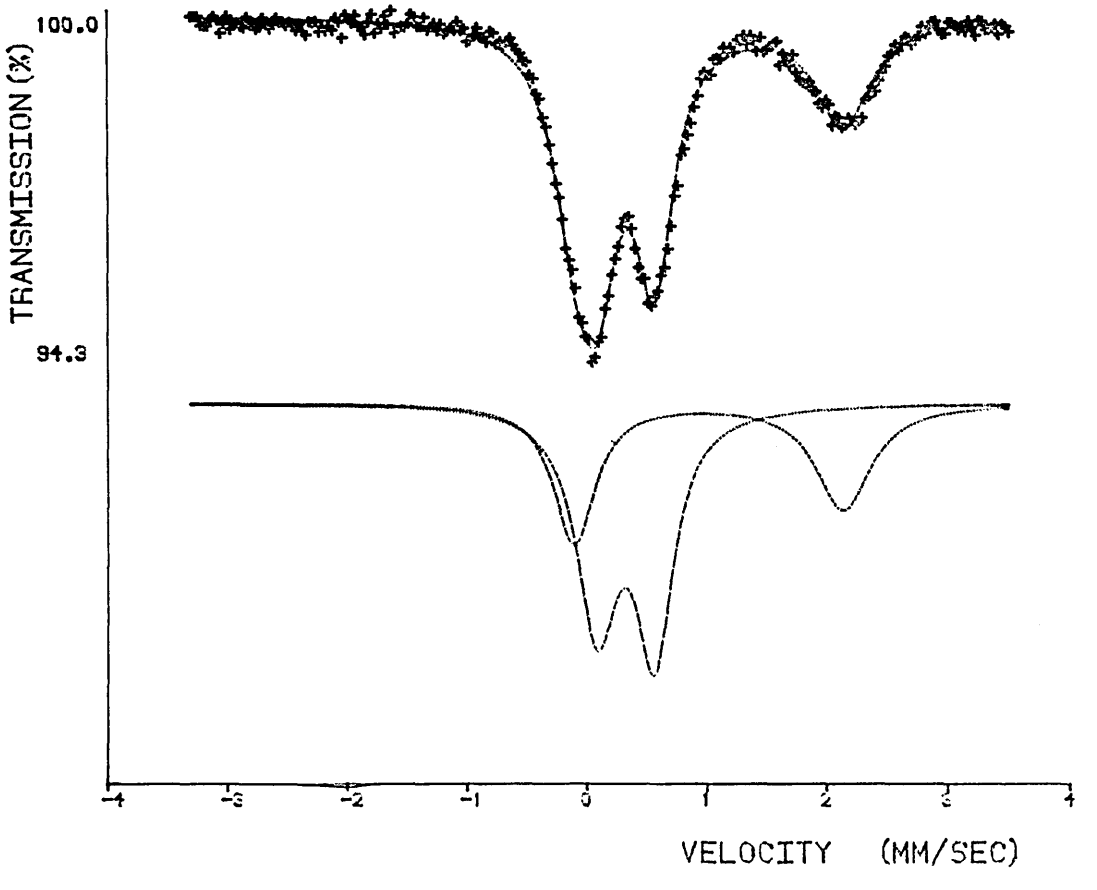

Figure 4.1 Room temperature spectrum of J3 fitted using MOSFITN

Table 4.2 Room temperature Mössbauer parameters of preliminary glasses. (MOSFITN)

Sample Code	Fe^{3+}					Fe^{2+}					χ^2
	δ	ΔE_Q	Γ_L	Γ_R	A%	δ	ΔE_Q	Γ_L	Γ_R	A%	
J 1	0.46	0.50	0.52	0.42	58	1.18	2.27	0.48	0.57	42	0.98
J 2	0.42	0.56	0.57	0.42	51	1.23	2.18	0.58	0.65	49	1.54
J 3	0.44	0.48	0.42	0.38	60	1.13	2.24	0.42	0.56	40	0.94
J 4	0.46	0.52	0.52	0.44	56	1.14	2.30	0.50	0.60	44	1.03
J 5	0.45	0.58	0.54	0.46	63	1.11	2.32	0.46	0.57	37	1.05

The widths of the absorption lines give some information concerning the distributions of iron sites within the glass. The lines are up to three times as broad as the Heisenburg width (0.192 mm/s) (§2.2.1) indicating the wide range of quadrupole interactions to which the iron ions are subject. For the ferric iron the lower velocity line is generally broader than the high velocity line, whilst the converse is true for the ferrous sites. These observations indicate that there is also some variation in the isomer shifts of the individual iron sites which causes the asymmetry of the doublets.

An added complication to the fitting of these spectra is the considerable overlap between the two doublets. The position and width of the lower velocity ferrous iron peak cannot be identified uniquely because of its coincidence with the ferric iron peaks, which usually have a much greater intensity. The Mössbauer parameters derived for the ferrous iron doublet are thus open to a degree of variation with little effect on the quality of the fit.

From assessments of drive linearity it is usual to quote errors of ±0.01 mm/s for the isomer shift and linewidth and 0.02 mm/s for the quadrupole splitting of 'thin' crystalline materials recorded over a range of ±4 mm/s. However, owing to the departure of the absorption lines from a Lorentzian shape and the uncertainty in assigning values to the ferrous iron parameters, larger error values have been specified for these studies. In theory the errors should be calculated independently for each spectrum, since they will depend on the quality of the data and the fit, the velocity range and the number of data points. In practice, error values of ±0.02 mm/s for the isomer shift and linewidth and ±0.04 mm/s for the quadrupole splitting have been adopted for all the spectra [3]. The error on absorption area is taken as ±5%.

In order to learn more about the distribution of iron sites within the glass the spectra have also been fitted using a quadrupole splitting distribution program PQH (§3.1.4.2). Two distributions, each of forty one constituent doublets, have been used to fit the spectra. The allowed quadrupole splittings for each distribution range from 0 mm/s to 4 mm/s in steps of 0.1 mm/s. The distribution fits (Figs. 4.2, 4.3) give a factor of two decrease in the chi-squared when compared to the two doublet fits (Table 4.3).

Table 4.3 Room temperature Mössbauer parameters of preliminary glasses (PQH)

Sample code	Fe^{3+}							Fe^{2+}							χ^2
	ξ	η	$\overline{\Delta}$	$\overline{\delta}$	Δ_m	δ_m	A%	ξ	η	$\overline{\Delta}$	$\overline{\delta}$	Δ_m	δ_m	A%	
J 1	0.43	0.00	0.62	0.43	0.5	0.43	59	1.35	-0.07	2.11	1.21	2.2	1.21	41	0.39
J 2	0.45	-0.05	0.63	0.42	0.5	0.43	53	1.28	-0.20	2.10	1.24	2.2	1.24	47	0.47
J 3	0.43	-0.01	0.42	0.42	0.5	0.42	59	1.12	-0.01	2.08	1.11	2.3	1.11	41	0.56
J 4	0.46	-0.05	0.66	0.42	0.6	0.42	56	1.29	-0.04	2.09	1.19	2.2	1.19	44	0.49
J 5	0.43	0.02	0.52	0.44	0.6	0.44	54	0.95	0.04	2.07	1.03	2.4	1.06	46	0.48

Note: $\overline{\Delta}$ is the average quadrupole splitting and $\overline{\delta}$ is the corresponding isomer shift, Δ_m is the quadrupole splitting corresponding to the maximum area and δ_m is the corresponding isomer shift.

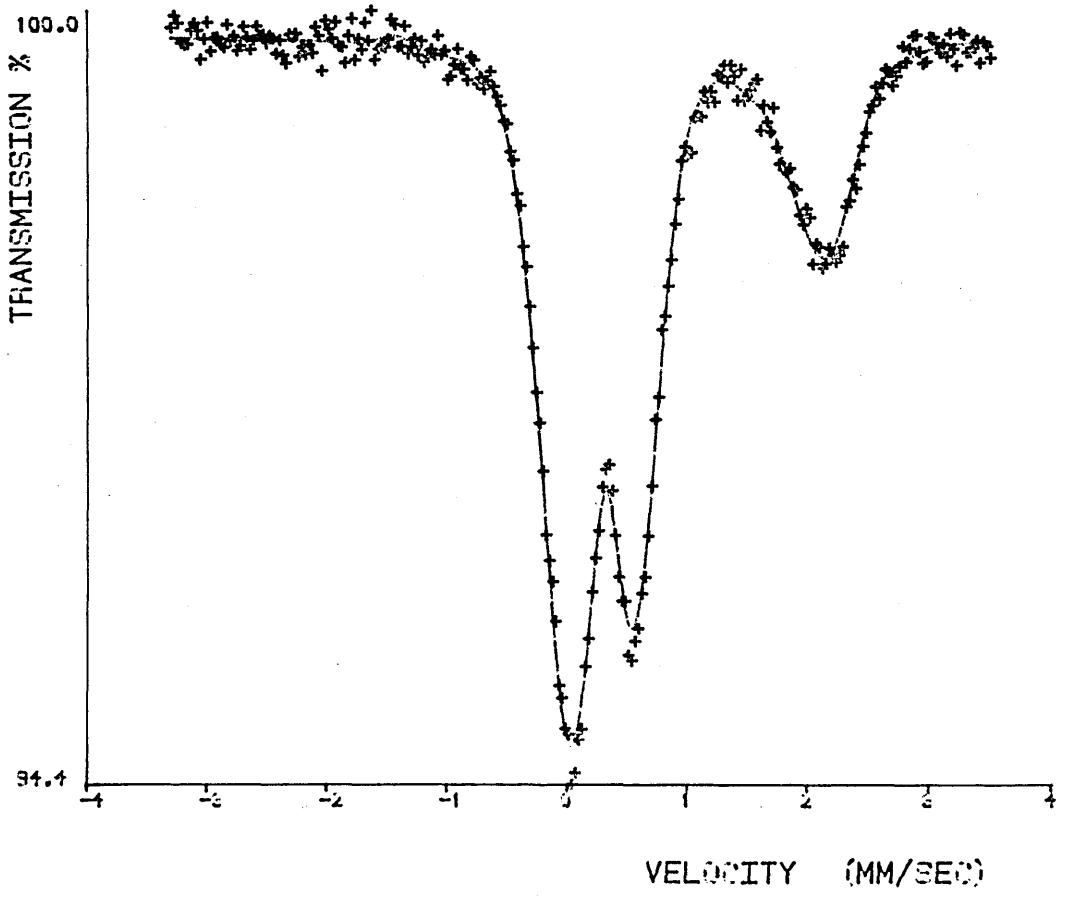

Figure 4.2 Room temperature spectrum of J3 fitted using PQH. $\beta = 1, \gamma = 0.1$.

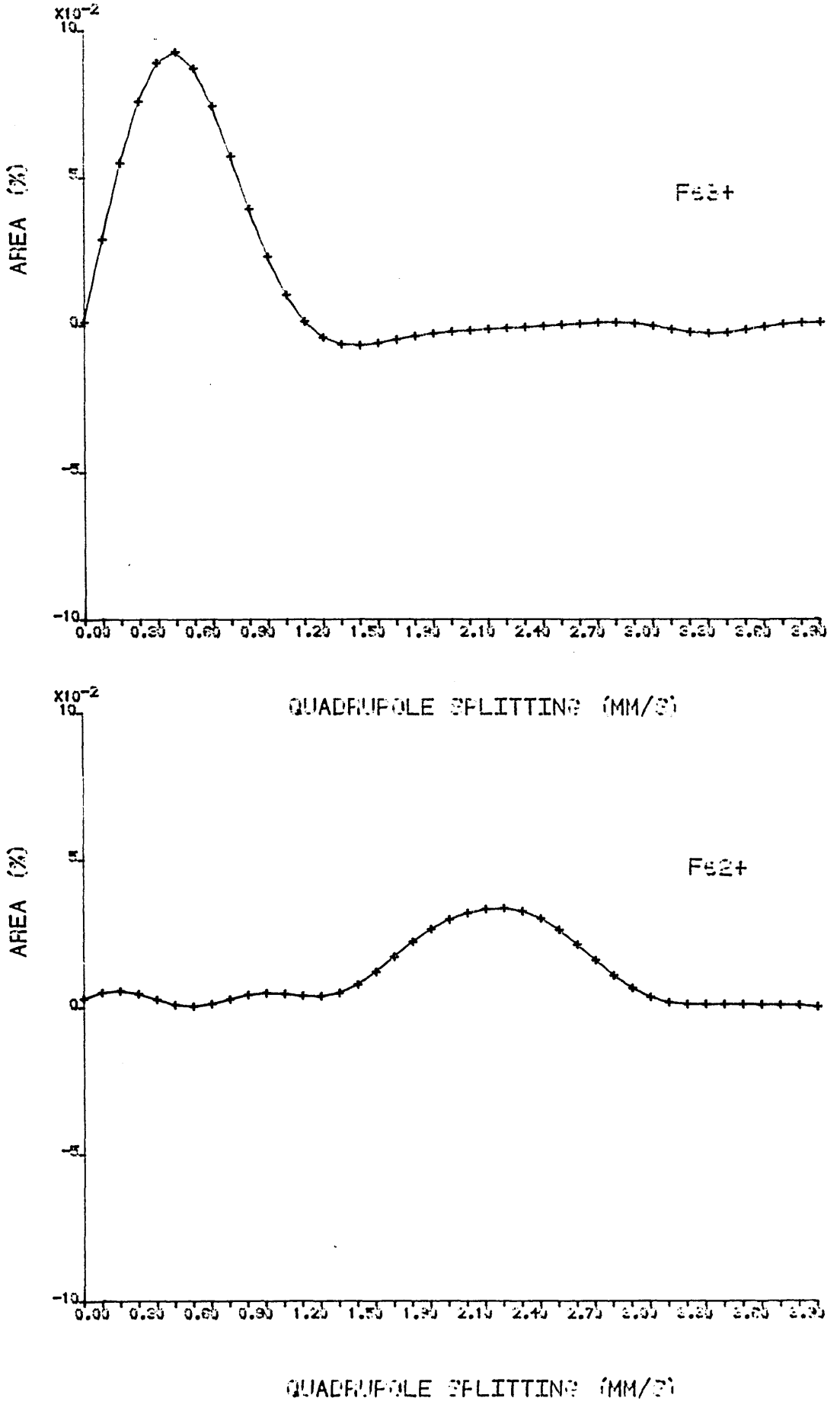

Figure 4.3 Quadrupole splitting distributions for J3. $\beta = 1, \gamma = 0.1$

The values for the two distribution fitting parameters β and γ (\$3.1.4.2) were chosen after extensive trials to examine their effect on the quality of the fit to J3. β governs the end point behaviour of the distributions. With the limits to the allowed quadrupole splitting values set at 0.0 and 4.0 mm/s, well outside expected values, it was found that the quality of the fit was fairly insensitive to changes in β (Fig. 4.4). The value of β has been set at unity for the remainder of these fits. Lower values for β allow physically meaningless quadrupole doublets at the limits of the distributions.

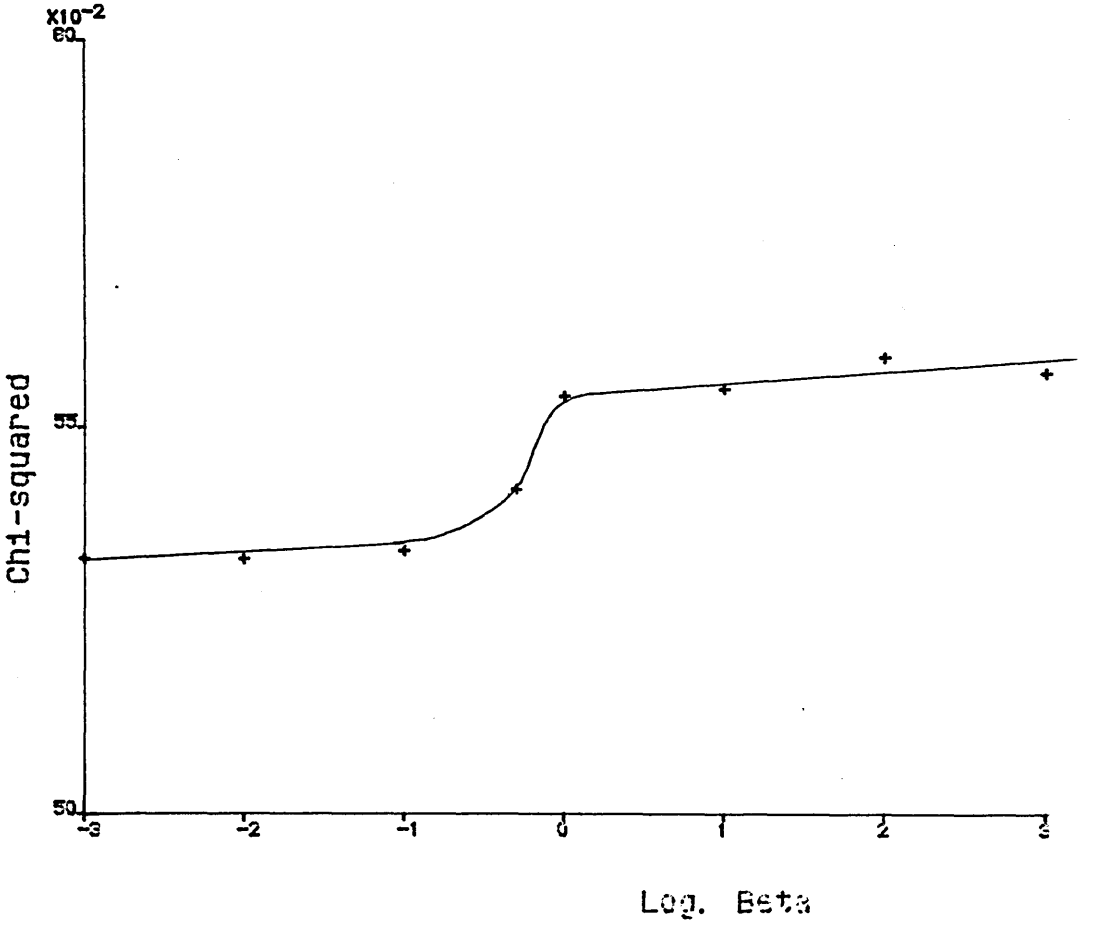

Figure 4.4 Effect of the distribution fitting parameter β on the quality of the fit to J3.

The Lagrangian multiplier γ governs the smoothing of the quadrupole splitting distributions. A value of zero for γ gives a very good fit (Fig. 4.5) (χ^2 = 0.30) but the distributions show totally unrealistic oscillations, (Fig. 4.6). A large value for γ (10000) gives over smoothed distributions (Fig. 4.8) and a poor fit (χ^2 = 47.9) (Fig. 4.7).

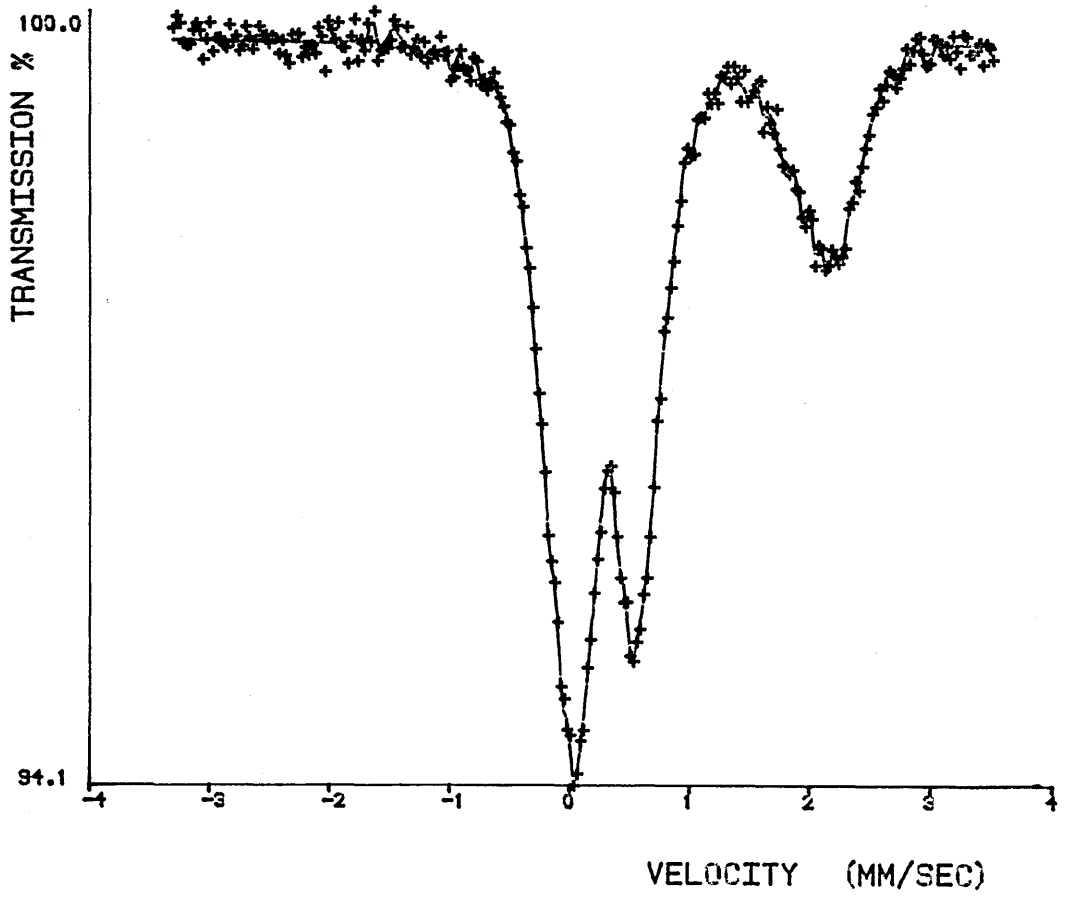

Figure 4.5 PQH fit to J3 with $\beta = 1, \gamma = 0$

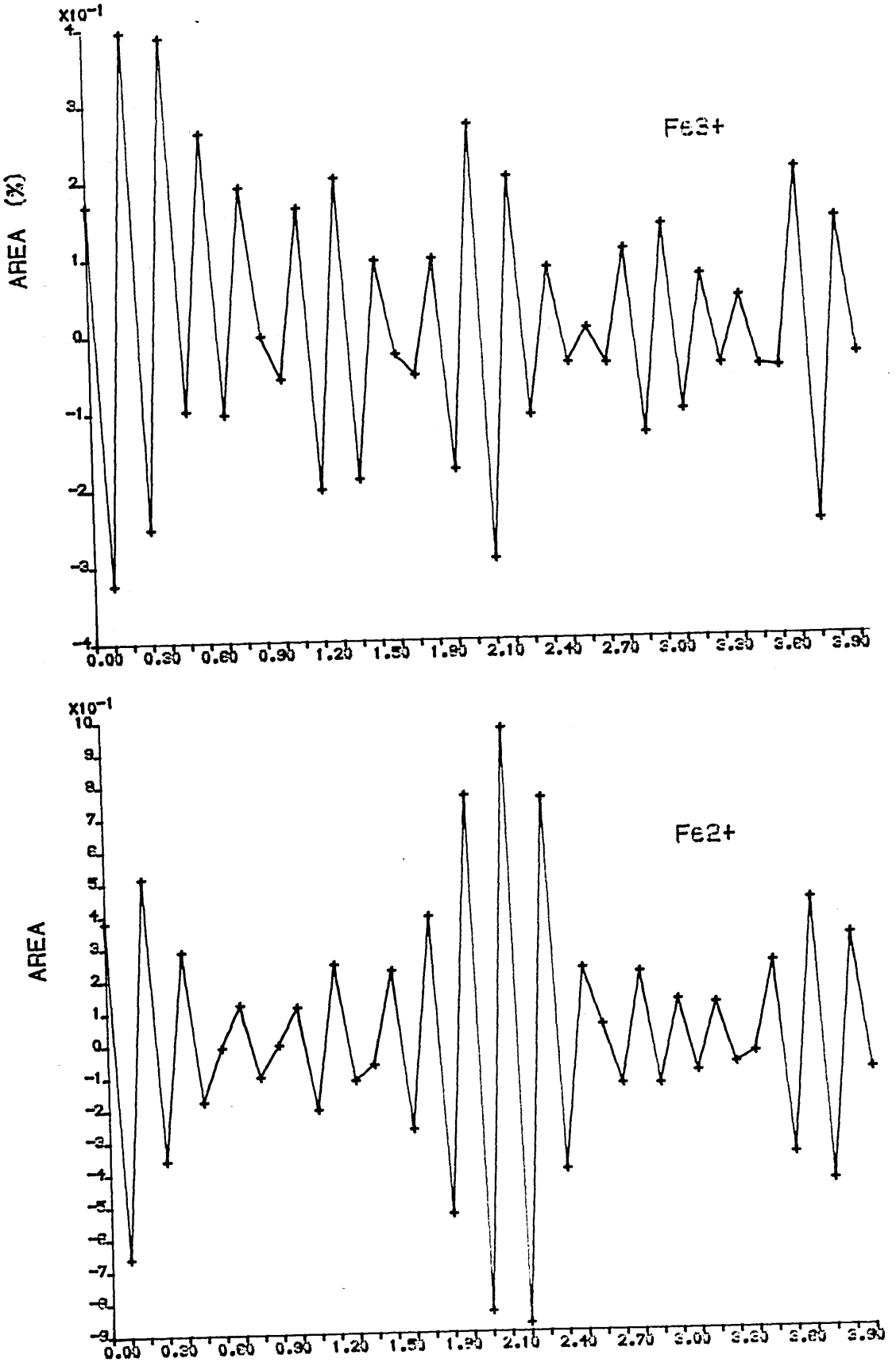

Figure 4.6 Quadrupole splitting distributions for J3. $\beta = 1, \gamma = 0$

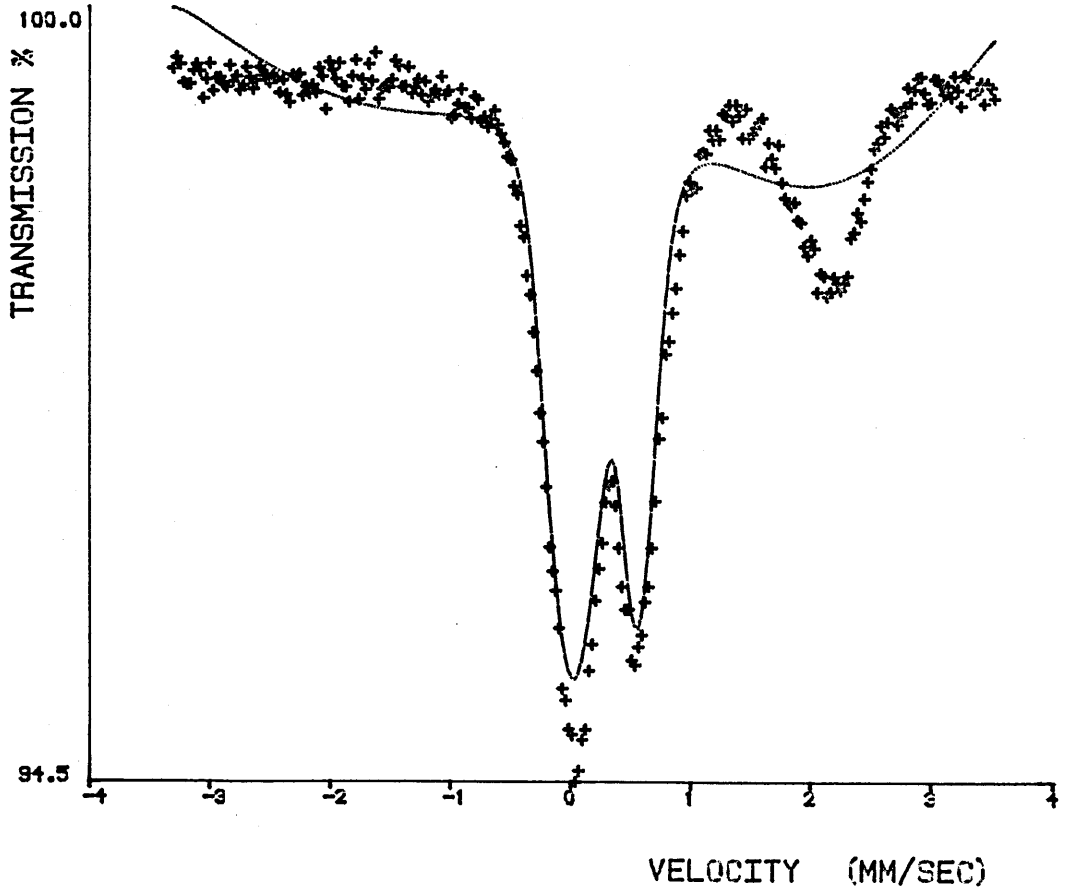

Figure 4.7 PQH fit to J3 with $\beta = 1, \gamma = 10000$

The quality of the fit to J3 is insensitive to γ for $\gamma < 1$ but rapidly deteriorates with higher values of γ (Fig. 4.9). This is in qualitative agreement with Wivel and MØrup [4] who chose a value of $\gamma = 1$ for their fits. For these studies a lower value of $\gamma = 0.1$ is thought appropriate.

The optimum fit (Fig. 4.2) is able to accurately describe the spectrum, including the peak shoulders which MOSFITN was unable to duplicate. The lines of each of the eighty two elementary doublets have been assigned a full width of 0.23 mm/s. This is equal to the width of the inner lines of an unenriched iron metal sextet recorded under the same experimental conditions and may be regarded as the minimum achievable linewidth with this system.

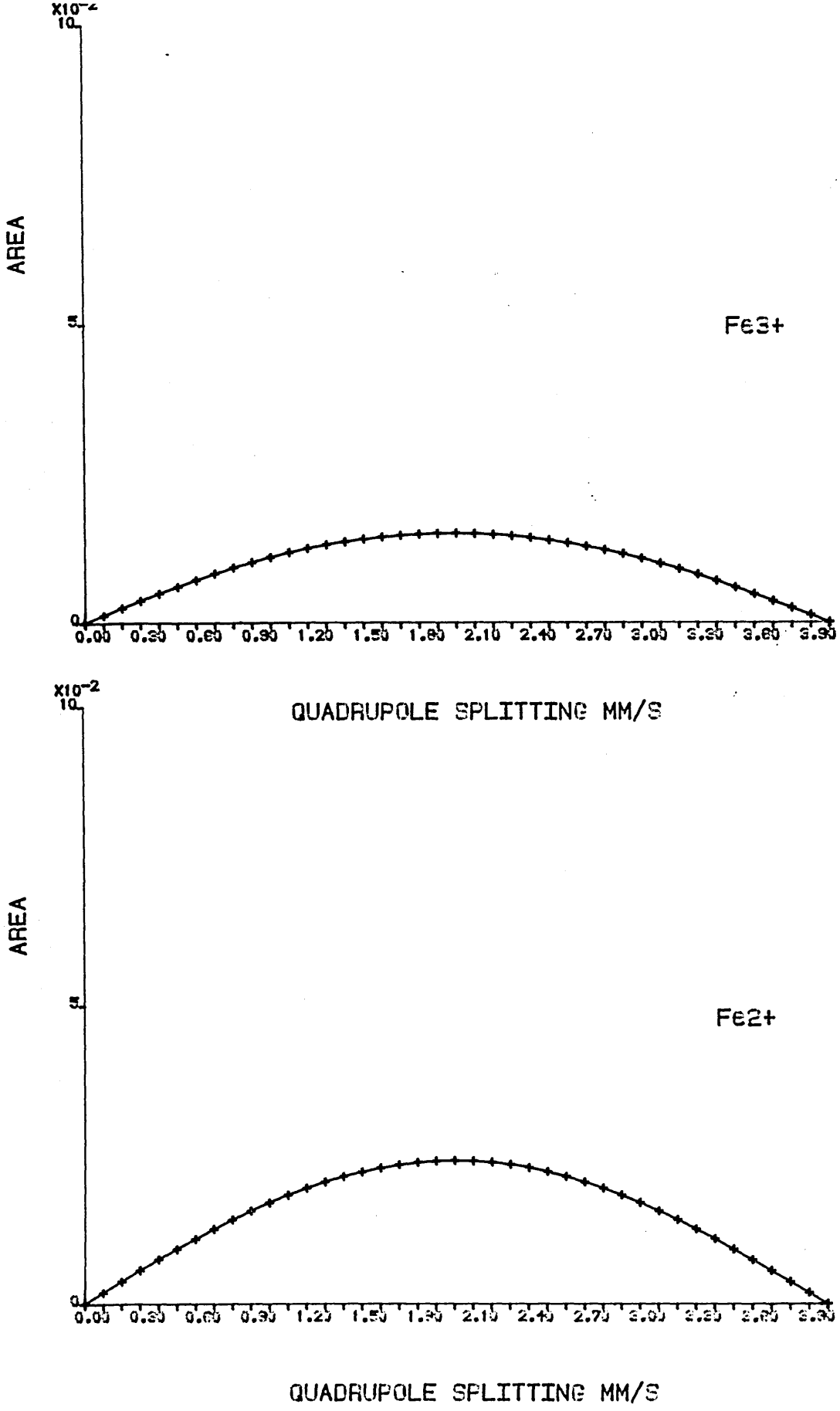

Figure 4.8 Quadrupole splitting distributions for J3 $\beta = 1, \gamma = 10000$

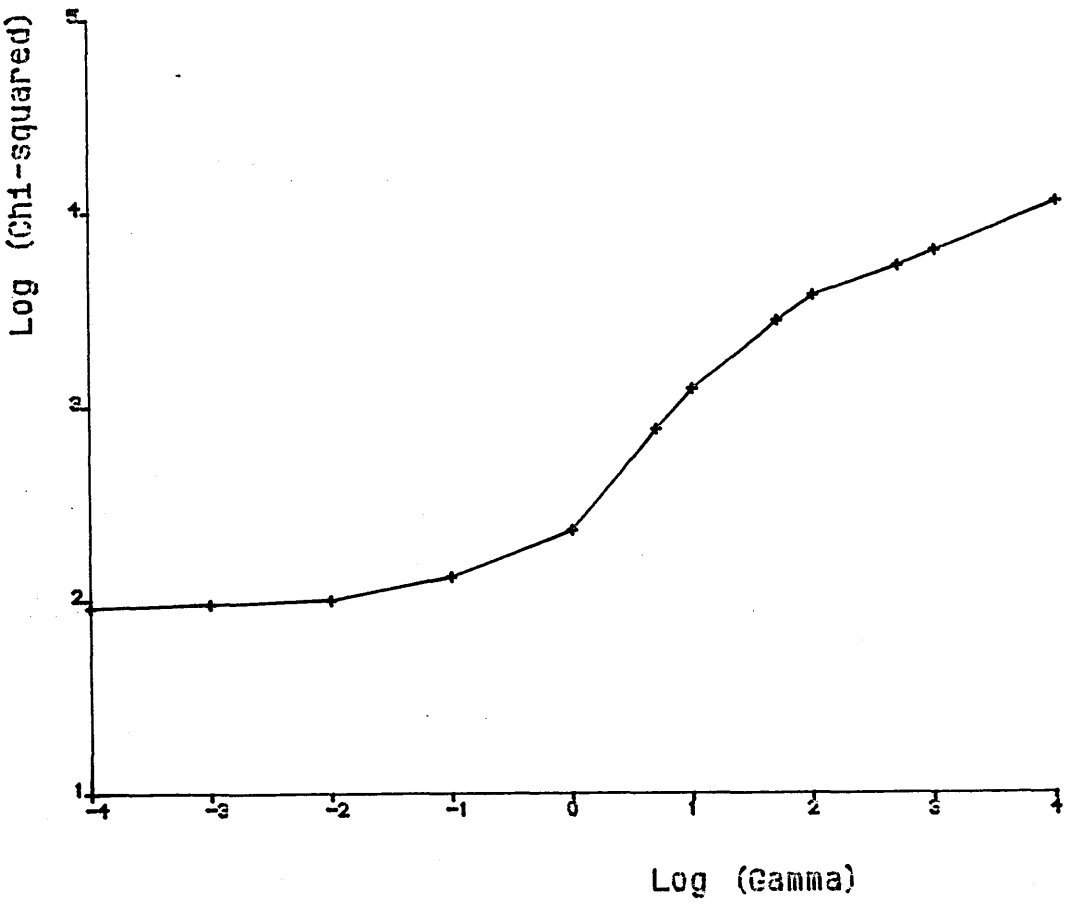

Figure 4.9 Effect of the distribution fitting parameter γ on the quality of the PQH fit to J3.

Both the ferric and ferrous iron components of J3 show predominantly a single peak in the quadrupole splitting distribution profiles (Fig. 4.3). This suggests that the two oxidation states each occupy just one type of site within the glass. The values for the mean and maximum quadrupole splittings and isomer shifts remain consistant with octahedral iron. A model has been proposed which fits these distributions to Gaussian line shapes [5], but in the absence of complex distribution profiles this has not been thought necessary. The width of the Fe^{2+} quadrupole doublet distribution (full width at half height $\simeq$0.8mm/s) is greater than that of the Fe^{3+} distribution (f.w.h.h. $\simeq$0.6mm/s) in agreement with the trend observed for the MOSFITN linewidths.

PQH requires initial guesses to be made for the two spectra fitting parameters ξ and η. A method has been devised which uses the Mössbauer parameters generated by a simple two doublet fit (MOSFITN). MOSFITN can be regarded to generate average values for the isomer shift δ_{AV} and quadrupole splitting Δ_{AV} of the ferric iron sites. These can be related by a linear equation. ($3.1.4.2):

$$\delta_{AV} = \xi + \eta\Delta_{AV} \qquad 4.1$$

If the linewidths are equal $\Gamma_L = \Gamma_R$ then this implies no average correlation between the isomer shift δ_i and quadrupole splitting Δ_i of each elementary doublet, hence $\eta = 0$ and $\xi = \delta_{AV}$. If $\Gamma_L > \Gamma_R$ this implies a negative value for η, whilst $\Gamma_L < \Gamma_R$ implies a positive value for η. For $\eta = \pm 0.5$ either the high or low velocity lines of each elementary doublet with have an identical position, hence the line width should be 0.23mm/s. This has not been observed, indicating that η lies between 0 and ± 0.5. By examining the Γ_L / Γ_R ratio an empirical value for η is obtained. Once the guesses have been made for η guesses for ξ can be calculated from Eqn.4.1. Despite this approach there seems to be little correlation between the final values for η and the linewidth ratios derived from MOSFITN. PQH often produces values of η of the opposite sign to those expected from the MOSFITN analyses.

4.2 Variable Temperature Study of $25Na_2O$-$13K_2O$-$43P_2O_5$-$19Fe_2O_3$

4.2.1 Introduction

A full variable temperature study of $25Na_2O$-$13K_2O$-$43P_2O_5$-$19Fe_2O_3$ (J3) was performed. Due to operating requirements some of the low temperature spectra were recorded using a Oxford Scientific Instruments liquid nitrogen cryostat to cool the absorber, whilst the remainder were recorded using the Displex system (§2.2.7.2) or the electric furnace (§2.2.7.3). The absorber for all the spectra consisted of 0.03g of powdered glass dispersed in graphite and held in a 15mm diameter graphite disc. This had a Mössbauer thickness t = 0.5 (§2.2.3). A total of twenty six spectra were collected between a base temperature of 12K and an upper limit of 506K. The recorded spectra were all of the same form, namely two broadened quadrupole doublets. They were fitted using both MOSFITN and PQH to the same basic fitting scheme as described for the room temperature spectrum (§4.1). The temperature dependence of the Mössbauer parameters describing the spectra have been evaluated and will be discussed in turn.

4.2.2 Temperature dependence of absorption area

There is an immediate problem in fitting a Debye function (§3.2.2.1) to the full set of absorption area data because of the three different experimental arrangements under which the data was obtained. Each cryostat/furnace demanded a different source-absorber geometry and separation which led to a different mean count rate and hence a different normalised absorption area. The individual data subsets can be treated separately (Fig. 4.10) and, as will be seen, yield consistent results.

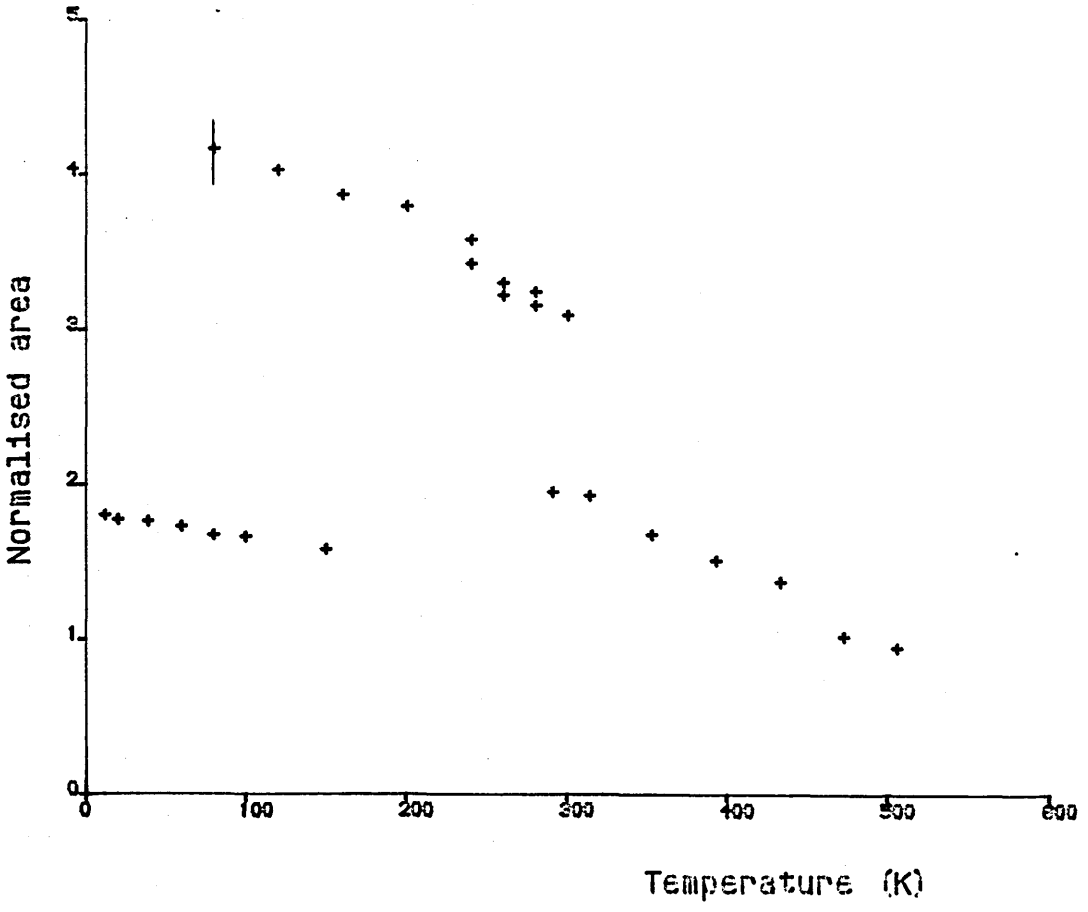

Figure 4.10 Normalised total absorption area data for J3.

A means of merging these three data subsets has been devised. It consists of a simple program (ADDON) which can add or subtract variable amounts to each data subset. The merged data set is then fitted to the Debye function using LNAT (\$3.2.2.2) and the χ^2 for the fit is recorded. By varying the ADDON constants a minimum χ^2 can be obtained. The overlap regions of each subset can be used to derive good initial guesses to the ADDON constants. This 'best fit' method, whilst not being mathematically rigorous does allow full use to be made of the variable temperature data (Table 4.4).

Table 4.4 Debye temperatures and room temperature recoil-free fractions of J3 derived from absorption area data.

Temperature	Fitting	Total			Fe^{3+}			Fe^{2+}		
Range (K)	Method	θ_D(K)	f(291)	χ^2	θ_D(K)	f(291)	χ^2	θ_D(K)	f(291)	χ^2
12 - 150	MOSFITN	308	0.65	0.001	378	0.75	0.001	250	0.52	0.001
	PQH	306	0.65	0.002	376	0.75	0.028	280	0.60	0.040
80 - 300	MOSFITN	301	0.63	0.078	344	0.70	0.021	257	0.53	0.022
	PQH	302	0.63	0.073	340	0.70	0.074	263	0.55	0.096
291 - 506	MOSFITN	260	0.54	0.025	304	0.63	0.015	210	0.40	0.004
	PQH	251	0.53	0.030	289	0.61	0.041	210	0.40	0.009
12 - 506	MOSFITN	296	0.63	0.866	328	0.68	0.785	251	0.53	1.413
	PQH	283	0.6	0.904	327	0.68	0.976	281	0.60	1.700
12 - 433	MOSFITN	302	0.63	0.516	337	0.69	0.458	256	0.54	0.853
	PQH	290	0.62	0.553	335	0.69	0.923	293	0.62	0.350

If the total absorption area data for all twenty six spectra is fitted using LNAT the two doublet fits (Fig. 4.11) yield a Debye temperature θ_D = 296K, whilst the distribution fits yield θ_D = 283K. The top two data points (T = 473K and T = 506K) depart from the expected behaviour, possibly because of anharmonicity in the lattice vibrations [6], the onset of softening of the glass [7], or an accidental change in the source-absorber geometry. Their

omission causes a 30% improvement in the quality of the fit and leads to final values for the Debye temperature of θ_D = 302K (using MOSFITN) or θ_D = 290K (using PQH). These values are within ±15K of the 12-150K and 80-300K range results suggesting that the data subset merging procedure is valid. The departure of the 291-506K range results from the final values is presumably due to the influence of the top two data points on the fit.

An identical procedure has been adopted for the Fe^{3+} and the Fe^{2+} data. This yields Debye temperatures of θ_D = 337K (MOSFITN) and θ_D = 335K (PQH) for the ferric iron, whilst for the ferrous iron θ_D = 256K (MOSFITN) and θ_D = 293K (PQH) (Fig. 4.12). This corresponds to a room temperature recoil-free fraction of 0.69 for ferric iron and for ferrous iron 0.54 (MOSFITN) or 0.62 (PQH). There is a maximum 30K discrepancy between the Debye temperatures computed from the two sets of data. This suggests that the simple two doublet fix, despite being a crude approximation to the spectrum, is able to generate reasonable absorption areas.

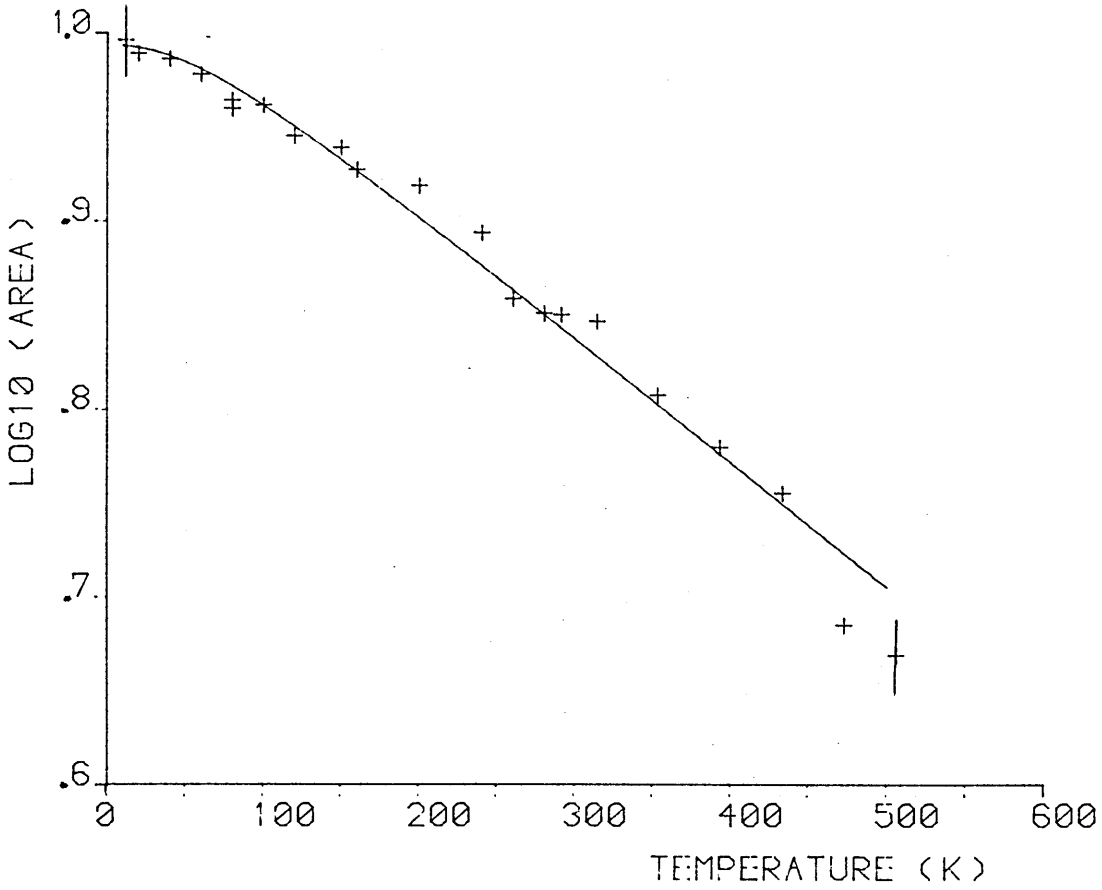

Figure 4.11 Merged normalised total absorption area data for J3 (MOSFITN data)

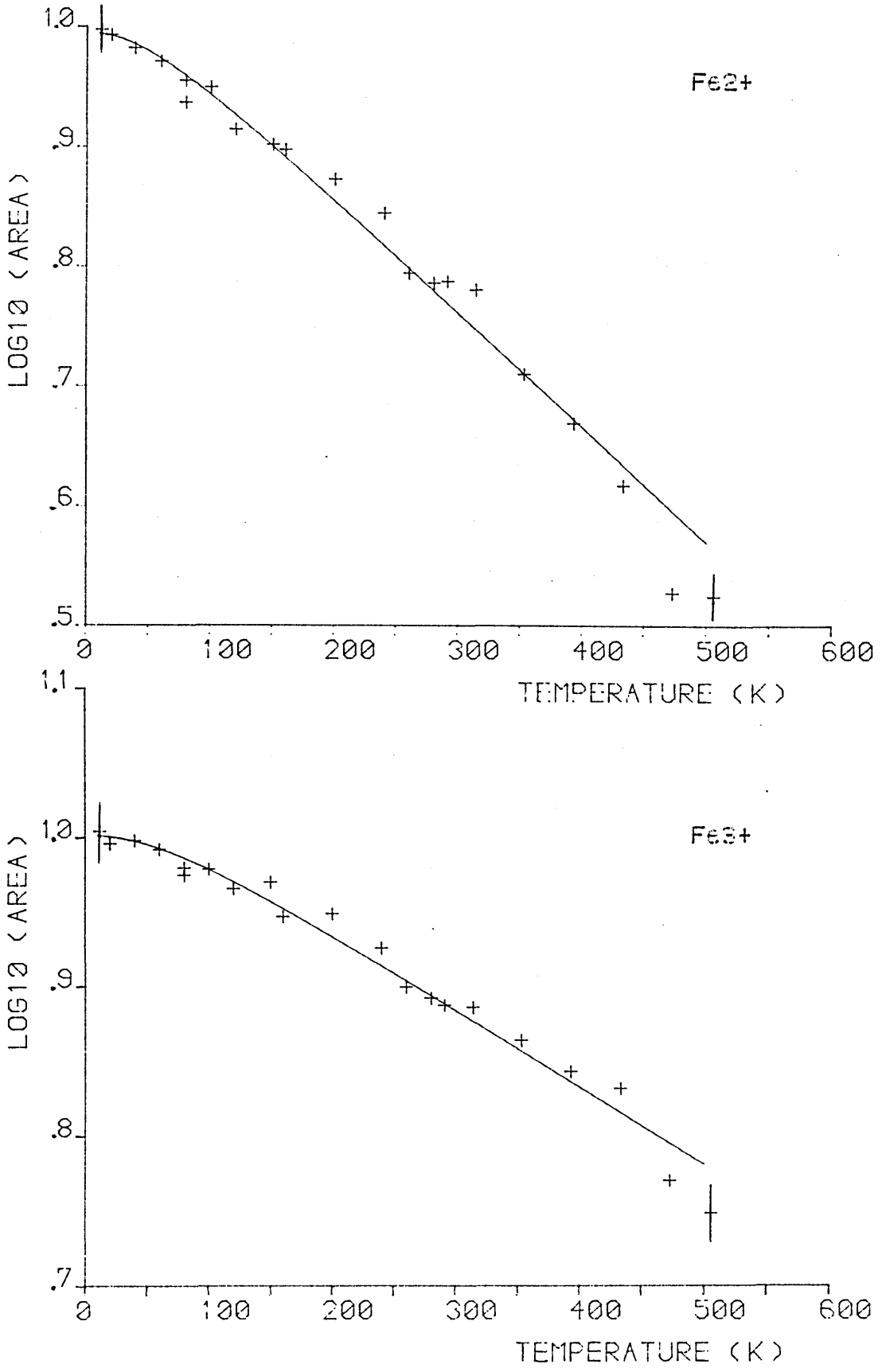

Figure 4.12 Merged normalised absorption area data for the Fe^{2+} and Fe^{3+} sites in J3 (MOSFITN data)

4.2.3 Temperature dependence of the isomer shift

Unlike the absorption area data no manipulation is required of the isomer shift data derived from the three experimental arrangements. The isomer shift data has been fitted to a Debye function (Eqn. 3.48) using ISODS (\$3.2.3.2). As with LNAT the effective recoiling mass M_{eff} has been taken as one ^{57}Fe atom. Increasing M_{eff} to the mass of ^{57}Fe plus its six oxygen ligands leads to much lower Debye temperatures, but much poorer quality fits.

The isomer shift of the ferric iron doublet can be fitted to the Debye model with a corresponding Debye temperature of θ_D = 550K (Fig. 4.13). This corresponds to a room temperature recoil-free fraction of $f(Fe^{3+})$ = 0.87. However, ISODS cannot cope with the ferrous iron isomer shift data, giving an unsatisfactorily high χ^2 (Fig. 4.13). This poor fit may be due to the large errors involved in estimation of the Mössbauer parameters of the ferrous site, as discussed previously (\$4.1).

The distribution fits have also been used to generate values for θ_D. The isomer shifts of the component doublet with the maximum absorption area from the ferric and ferrous iron distributions (δ_m) were fitted using ISODS (Fig. 4.14). The Fe^{3+} distributions yield θ_D = 400K whilst for Fe^{2+} a Debye temperature of θ_D = 270K is obtained.

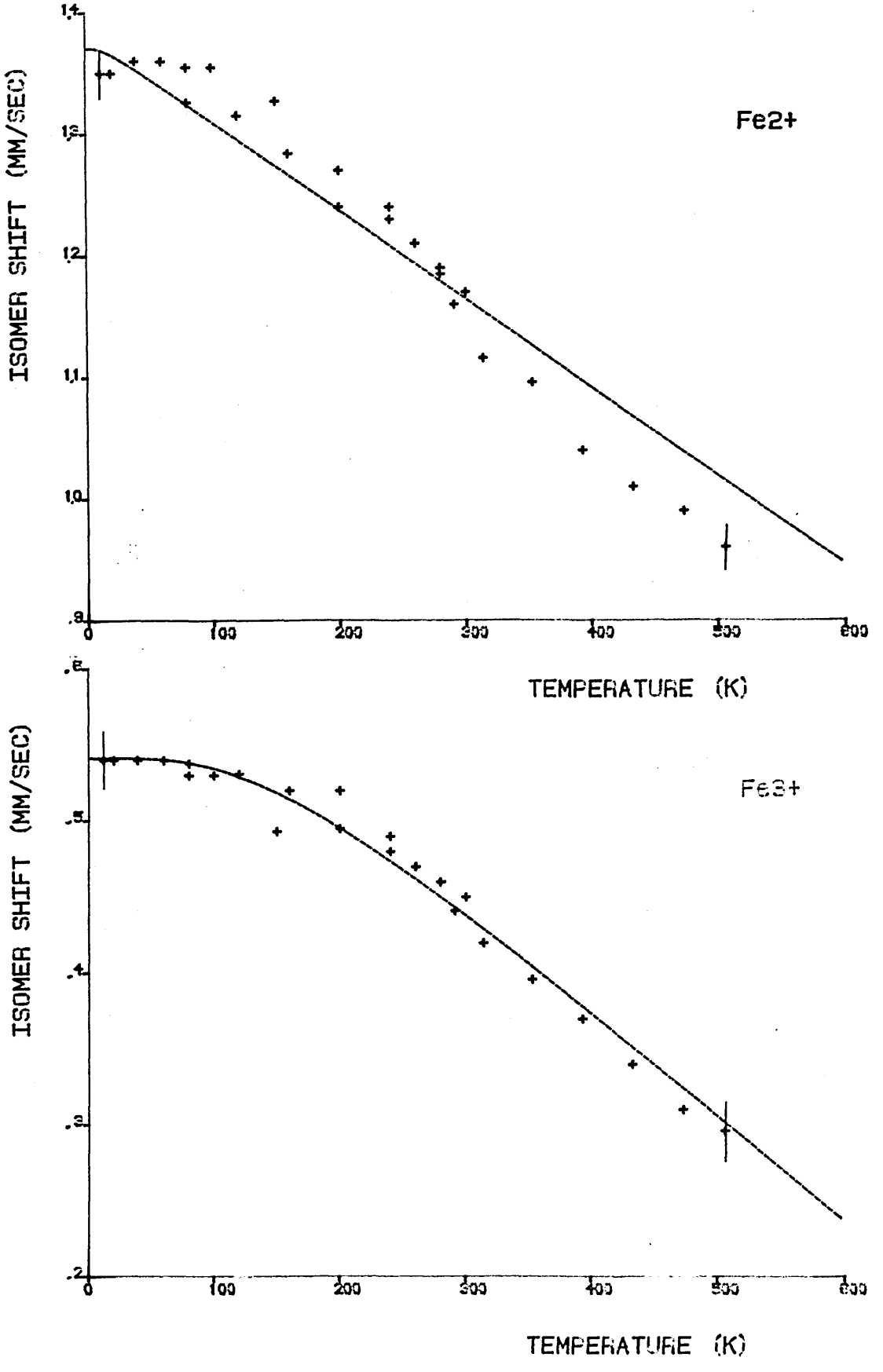

Figure 4.13 MOSFITN isomer shift data for J3

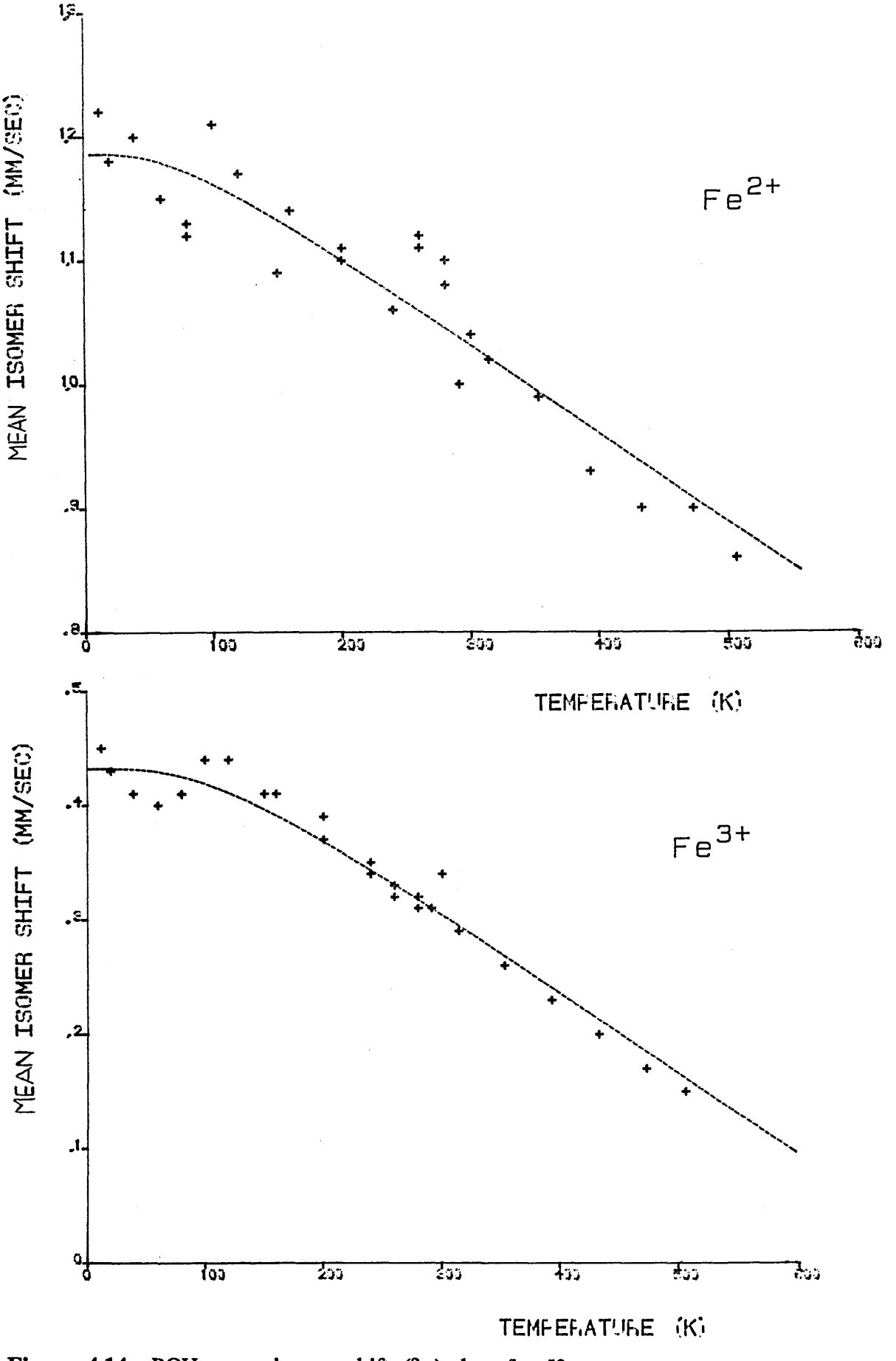

Figure 4.14 PQH mean isomer shift (δ_m) data for J3.

For all the ISODS fits (Figs. 4.13, 4.14) the high temperature isomer shifts are consistently below the calculated values. This suggests a high temperature departure from the Debye model. As with the absorption area data this may be caused by anharmonicity of the iron lattice sites. Using solely the temperature region below 300K ISODS yields Debye temperatures of θ_D (Fe^{3+}) = 650K and θ_D (Fe^{2+}) = 150K from the MOSFITN data and θ_D (Fe^{3+}) 480K and θ_D (Fe^{2+}) = 450K from the PQH data. Fitting the 291-506K region alone gave very low values for the Debye temperature ($\theta_D \simeq 20K$).

4.2.4 Temperature dependence of the quadrupole splitting

The quadrupole splitting ΔE_Q of high spin ferrous iron is in the main part due to its non-spherical $3d^6$ ($^5D_4$) electron shell (§2.1.5.3). The temperature dependence of the valence component of the quadrupole splitting ΔE_Q (val) can be derived using crystal field theory [8] and expressed in terms of a reduction factor F(T):

$$\Delta E_Q(T) = \Delta E_Q(val)(0)F(T) + \Delta E_Q(lat) \qquad 4.2$$

Where ΔE_Q (val)(0) - the valence component of the quadrupole splitting at 0 Kelvin.

ΔE_Q(lat) - the lattice component of the quadrupole splitting.

The lattice contribution ΔE_Q (lat) always acts in the opposite sense to ΔE_Q (val) [9] and this reduces ΔE_Q from its maximum value.

The analysis assumes that there is a zero probability of thermal occupancy of the d_γ levels (Fig. 4.15) because of the large energy difference. For instance, the $[Fe\ (H_2O)_6]^{2+}$ species gives $E(d_\gamma) - E(d_\varepsilon) = 10{,}400\ cm^{-1}$ [10]. Axial and rhombic distortions of the crystal field remove the degeneracy of the d_ε levels resulting in two excited states separated by energies Δ_1 and Δ_2 from the ground state (Fig. 4.15). At all temperatures above absolute zero these excited states will be thermally occupied. If spin-orbit coupling is neglected then F(T) can be expressed as a series of Boltzman functions :

$$F(T) = \frac{\left[1 + e^{\frac{-2\Delta_1}{kT}} + e^{\frac{-2\Delta_2}{kT}} - e^{\frac{\Delta_1}{kT}} - e^{\frac{\Delta_2}{kT}} - e^{\frac{-(\Delta_1+\Delta_2)}{kT}} \right]^{1/2}}{1 + e^{\frac{-\Delta_1}{kT}} + e^{\frac{-\Delta_2}{kT}}} \qquad 4.3$$

Where k = Boltzmans constant

Using the approximation employed by Gosselin et al [11]

$$\Delta_1 = \frac{\Delta_2}{2} \qquad 4.4$$

Eqn. 4.3 reduces to:

$$F(T) = \frac{\{ 1 - B - B^3 + B^4 \}^{\frac{1}{2}}}{1 + B + B^2} \qquad 4.5$$

where $B = e^{\frac{-\Delta_1}{KT}}$

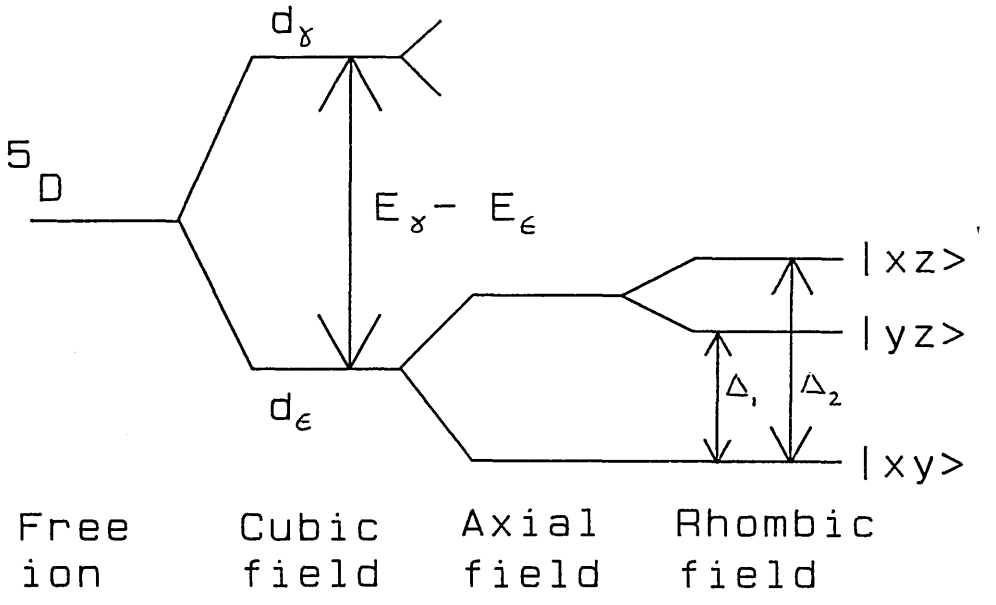

Figure 4.15 Crystal field splitting of the high spin Fe^{2+} ion.

In contrast to Fe^{2+}, high spin ferric iron has a spherical $3d^5$ ($^6S_{5/2}$) valence shell, hence any quadrupole splitting is due solely to the lattice contribution $\Delta E_Q(lat)$ (§2.1.5.3). In the absence of any theoretical expression the temperature dependence of the Fe^{3+} quadrupole splitting can be adequately fitted to a linear function:

$$\Delta E_Q(T) = \Delta E_Q(lat)(T) = mT + \Delta E_Q(lat)\ (0) \qquad 4.6$$

Where m - gradient (mm/sK)

$\Delta E_Q(lat)(0)$ - quadrupole splitting at 0K.

The temperature dependence of the Fe^{3+} quadrupole splitting is typically an order of magnitude less than for Fe^{2+} [12] indicating the large effect of $\Delta E_Q(val)$ on ΔE_Q. For J3 a least squares fit to the Fe^{3+} data gave m = -1.9 $\times$ 10^{-4} mm/sK and $\Delta E_Q(lat)(0)$ = 0.55 mm/s (Fig. 4.16)

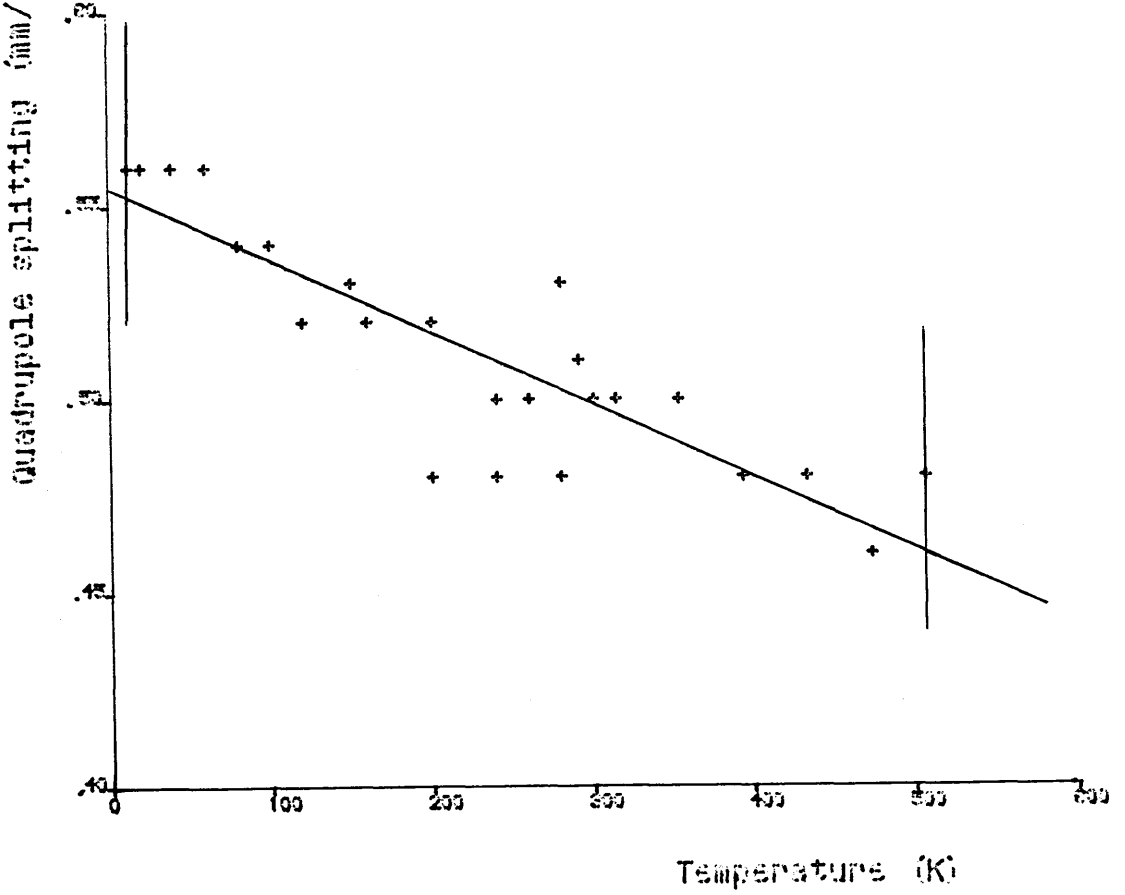

Figure 4.16 Temperature dependence of ferric iron quadrupole splitting (J3)

The ferrous iron data for J3 has been fitted to the theoretical function (Eqn. 4.2) and yields Δ_1 = 355 cm^{-1}, Δ_2 = 710 cm^{-1} (since $\Delta_2 = 2\Delta_1$) and $\Delta E_Q(0)$ = 2.67 mm/s (Fig. 4.17). These crystal field splitting values are smaller than those found for an iron-silicate glass (Δ_1 = 660 cm^{-1}, Δ_2 = 1300 cm^{-1}) [13]. The lattice component of the quadrupole splitting $\Delta E_Q(lat)$ = 1.04 mm/s is considerably larger than for the ferric iron site ($\Delta E_Q(lat)(0)$ = 0.55 mm/s). This implies that the ferrous iron lattice sites are more distorted than those of ferric iron. To examine the reliability of this assessment the Fe^{2+} data has been refitted to a modified version of Eqn. 4.2 in which $\Delta E_Q(lat)$ is no longer a fitting variable but is instead defined by the expression derived for the temperature dependence of the ferric iron quadrupole splitting (Eqn. 4.6). This scheme inevitably leads to a higher χ^2 for the fit and yields Δ_1 = 470 cm^{-1} and Δ_2 = 940 cm^{-1} (Fig. 4.18). The poor quality of the experimental

data and the approximations used in the fitting function cast doubt upon the very large ΔE_Q(lat) component for the Fe^{2+} generated by the free fit (Fig. 4.17). The constrained fit (Fig. 4.18) may instead be closer to the true situation. Taragin et al [14] have performed a similar study on an alumino-phosphate glass. They fitted the Fe^{2+} quadrupole splitting data to Eqn. 4.2, but assumed that ΔE_Q(lat) = 0. Using this approximation on the J3 data produced a yet higher χ^2 value for the fit with Δ_1 = 510 cm^{-1}, Δ_2 = 1020 cm^{-1}.

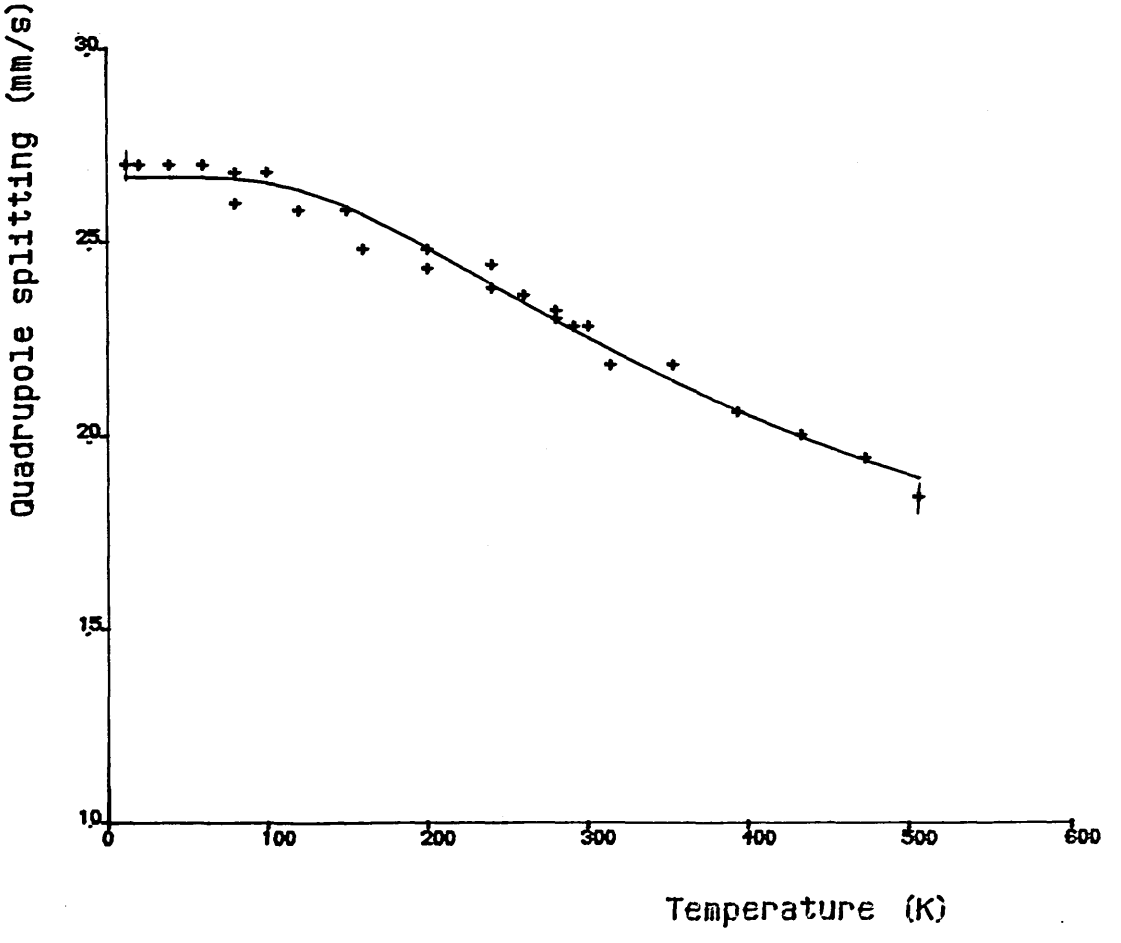

Figure 4.17 Temperature dependence of ferrous iron quadrupole splitting (J3) Free Fit.

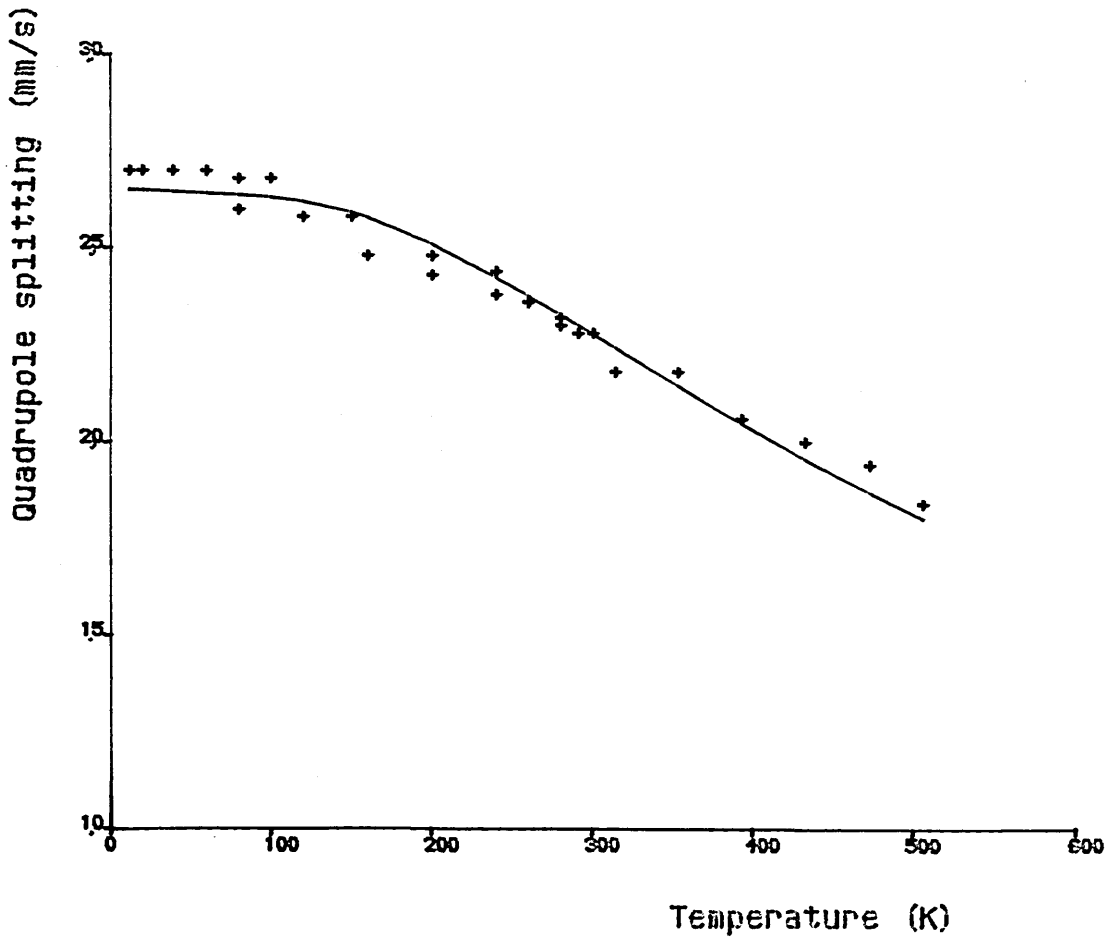

Figure 4.18 Temperature dependence of ferrous iron quadrupole splitting (J3) Constrained fit.

4.3 Fe^{2+} glasses prepared under an argon atmosphere

Under the glass forming conditions employed for these phosphate glasses the majority of the iron remains in the Fe^{3+} oxidation state. Typical Fe^{2+}/Fe^{3+} ratios are anywhere between 1/2 and 1/9. This ratio is a complex function of the furnace temperature and atmosphere, melting time, glass composition [15] and cooling rate [16]. For a sodium-iron-silicate glass it has been shown that the oxidation-reduction reaction of the iron can be described by a simple redox equation [17]:

$$4\,Fe^{3+} + 2O^{2-} \overset{K}{\rightleftharpoons} 4\,Fe^{2+} + O_2 \qquad 4.7$$

The equilibrium is found to move to the right as the furnace temperature is increased. A considerable melt time (~24 hours) may be necessary to reach the equilibrium because the reaction is governed by the slow diffusion of the iron ions through the melt. Faster ~~equilibrium~~ equilibration is promoted by stirring the melt [18] and using small batch weights.

The rate constant K for the reaction is given [17] by:

$$K = \left(\frac{[Fe^{2+}]}{[Fe^{3+}]}\right)^4 pO_2 \qquad 4.8$$

Where $[Fe^{2+}], [Fe^{3+}]$ - concentration of Fe^{2+}, Fe^{3+}

pO_2 - oxygen partial pressure

The equation assume a fixed O^{2-} concentration within the melt. This is not an unreasonable supposition as a typical oxide glass contains at least 50 mol.% oxygen. It has been verified experimentally for a number of silicate glasses [17,18] by plotting the logarithm of the final Fe^{2+}/Fe^{3+} ratio versus $\log(1/pO_2)$. This yielded a gradient of 4 in line with Eqn. 4.8.

Provided the equilibrium ratio has been achieved the final Fe^{2+}/Fe^{3+} ratio should be independent of the initial oxidation state of the iron in the glass frit. This is the justification for using Fe_2O_3 as the sole source of iron for the phosphate glasses.

According to Eqn. 4.8 the Fe^{2+}/Fe^{3+} ratio is inversely proportional to the oxygen partial pressure of the melt. Hence decreasing the oxygen content of the furnace from the ambient value of 0.21 atmospheres will increase the Fe^{2+}/Fe^{3+} ratio. Using this phenomenon a series of phosphate glass frits were melted under an argon atmosphere ($pO_2 \sim 10^{-7}$ atmospheres). The Mössbauer spectra revealed a total absence of Fe^{3+} from the glass (Fig. 4.19); instead a single non-Lorentzian doublet was recorded. This is in agreement with spectra of complex iron-silicate glasses prepared in oxygen deficient atmospheres [19,20]. The spectrum can be crudely fitted to two quadrupole doublets with similar isomer shifts characteristic of octahedral Fe^{2+}, but with very different quadrupole splittings (Table 4.5). The smaller splitting (1.66 mm/s) is at the lower limit of the Fe^{2+} range (Fig. 2.16).

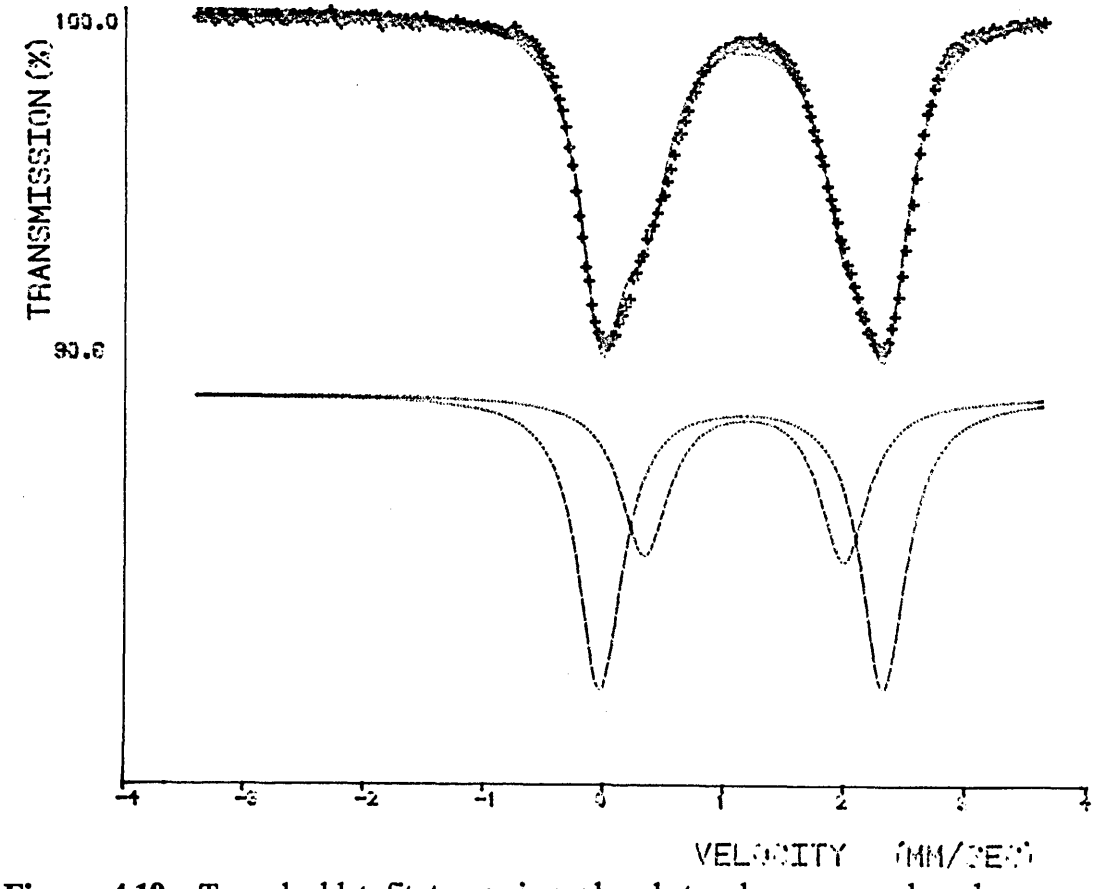

Figure 4.19 Two doublet fit to an iron-phosphate glass prepared under argon (AR1)

Table 4.5 Mössbauer parameters for $9Fe_2O_3$-11NaO-$80P_2O_5$ (AR1) prepared under argon. (MOSFITN)

Doublet	δ	ΔE_Q	Γ_L	Γ_R	A%	χ^2
Fe^{2+}(1)	1.27	2.35	0.45	0.45	63	6.214
Fe^{2+}(11)	1.28	1.66	0.49	0.47	37	

The quadrupole splitting distribution fit to AR1 supports the MOSFITN interpretation of two iron sites. Fitting the spectrum to a single distribution of doublets (Table 4.6) yields a non-symmetric distribution (Fig. 4.20). This appears to consist of the supposition of two Gaussian lines with maxima at ~2.1 mm/s and ~1.4 mm/s, in qualitative agreement with the MOSFITN data. It has proved impossible to separate the two Gaussian lines by fitting the spectrum to two distributions. The result is always two profiles of the same shape with similar values for η and ξ. This suggests that all the iron sites can be related by a single isomer shift - quadrupole splitting correlation equation (Eqn. 3.22).

Table 4.6 Mössbauer parameters for AR1 (PQH)

ξ	η	ΔE_Q	δ	ΔE_{Qm}	δ_m	χ^2
1.19	-0.02	2.07	1.16	2.3	1.15	1.06

The first doublet Fe^{2+}(1) has Mössbauer parameters typical of Fe^{2+} sites in glasses prepared under normal conditions (Table 4.2) and may therefore be assumed to represent the same type of sites within the glass. The second doublet Fe^{2+}(11), with its much lower quadrupole splitting represents a distinctly different ferrous iron site within the glass.

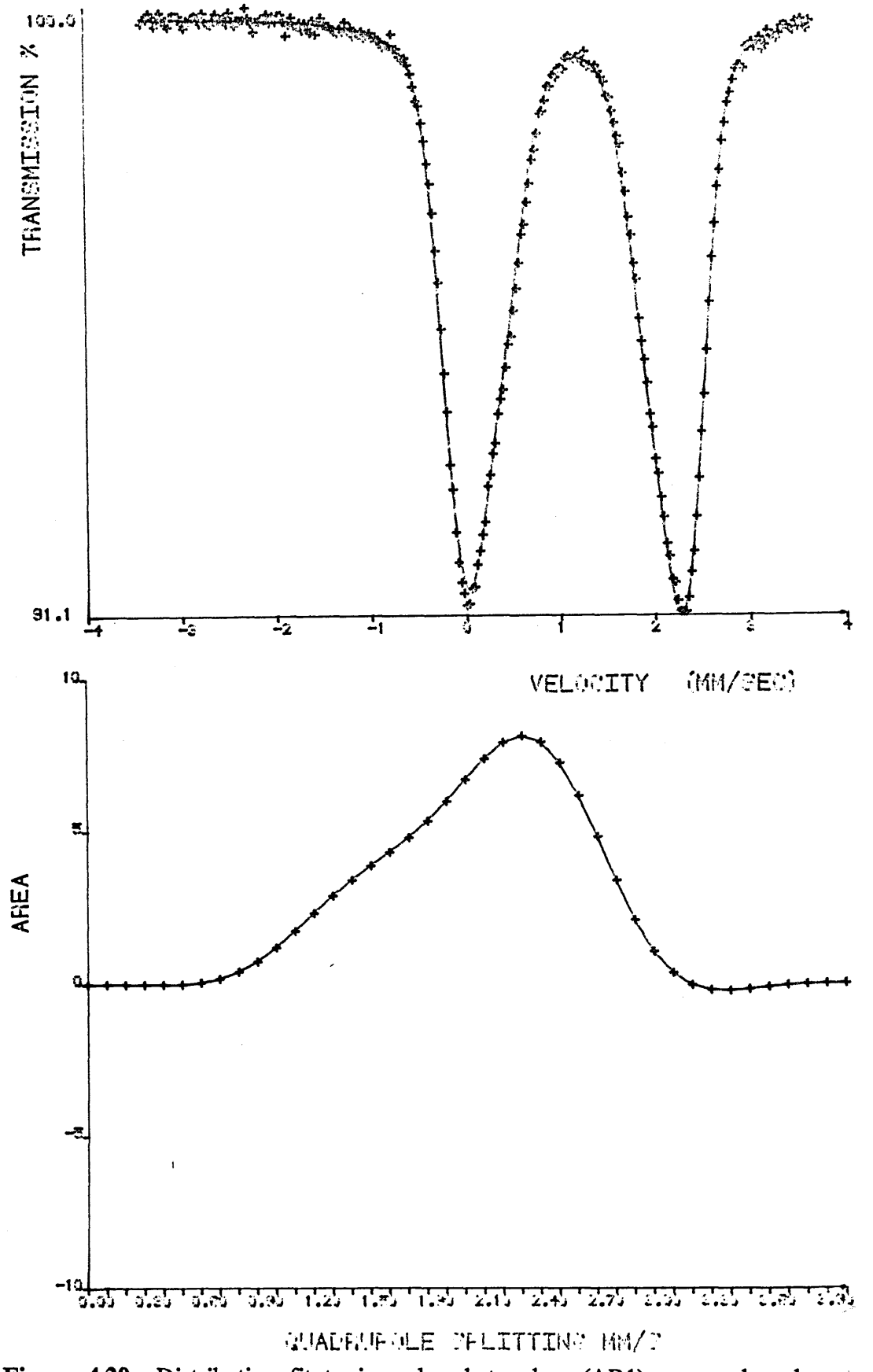

Figure 4.20 Distribution fit to iron-phosphate glass (AR1) prepared under argon.

4.4 Discussion

These preliminary studies have confirmed the rôle of iron in the phosphate glass network. Both Fe^{2+} and Fe^{3+} are present in distorted octahedral environments. These equate to glass modifying sites within the framework of the glass. Neither the two doublet fits nor the quadrupole doublet distribution fits show any evidence for tetrahedrally coordinated iron. The two doublet approximations show no significant misfitting at the expected line positions for tetrahedral iron whilst the quadrupole distributions consist of a single Gaussian line shape with fitting parameters inconsistent with tetrahedral iron.

A variable temperature study has led to a Debye temperature of θ_D = 300K for a sodium-potassium-iron-phosphate glass. This high value, similar to those for Fe_3O_4 ($\theta_D \simeq$ 325K) [21], implies that the iron is tightly bound within its oxygen cage. The data for the two oxidation states reveal marked differences in θ_D and hence in the recoil free fraction. The absorption area data gives a room temperature ratio $f(Fe^{3+})/f(Fe^{2+})$ = 1.28, whilst the second order Doppler shift (SODS) data leads to a ratio of 1.36. These compare to $f(Fe^{3+})/f(Fe^{2+})$ = 1.87 obtained for an alumino-phosphate glass [14]. The errors on these ratios are large but it is still apparent that the Fe^{3+} ions have a considerably higher recoil-free fraction. This is due to the higher charge on the ferric iron which is thus more strongly bound to the glass network than ferrous iron [22]. The difference in recoil free fractions makes it impossible to derive actual Fe^{3+}/Fe^{2+} ratios within a glass unless a variable temperature study has been performed. It accounts for the discrepancies between chemical and Mössbauer analyses of iron redox ratios in glasses [23].

The Debye temperatures derived from the absorption area data are consistently lower than those from corresponding SODS data. For ferric iron θ_D(Area) = 335K and θ_D(SODS) = 405K, whilst for ferrous iron θ_D(Area) = 255K and θ_D(SODS) = 270K. This is a direct consequence of the methods by which the Debye temperatures are calculated. In the general case, for harmonic interatomic forces, the mean square vibrational amplitude $\langle x^2 \rangle$ of a nucleus is given by [24]:

$$\langle x^2 \rangle = \frac{\hbar}{m} \sum_{i=1}^{3N} \left[\frac{1}{2} + \frac{1}{\exp\left[\frac{\hbar\omega_i}{kT}\right] - 1} \right] \frac{b_{xi}^2}{\omega_i} \qquad 4.9$$

Where m - mass of nucleus

N - number of atoms in solid

b_{xi} - coordinate transformation coefficient

ω_i - frequency of i^{th} vibrational mode

The model leads to a similar equation for the mean square velocity $\langle v^2 \rangle$:

$$\langle v^2 \rangle = \frac{\hbar}{m} \sum_{i=1}^{3N} \left[\frac{1}{2} + \frac{1}{\exp\left[\frac{\hbar\omega_i}{kT}\right] - 1} \right] \left[b_{xi}^2 + b_{yi}^2 + b_{zi}^2 \right] \omega_i \qquad 4.10$$

The absorption area and SODS data have been fitted using the Debye model to describe the density of vibrational states in the summations of Eqn. 4.9 and Eqn. 4.10. For the absorption area (Eqn. 3.30:

$$\ln(\text{Area}) \propto \langle x^2 \rangle$$

Whilst for the second order Doppler shift (Eqn. 3.44):

$\delta \propto \langle v^2 \rangle$

Using series expansions of θ_D/T to evaluate the Debye integrals (Eqns. 3.35, 3.36, 3.50, 3.51) leads to the following relationships:

$$\ln(\text{Area}) = K_1/\theta_D + K_2 + K_3\,\theta_D + K_4\,\theta_D^2 + .. \qquad 4.11$$

$$\delta = K_5 + K_6\,\theta_D + K_7\,\theta_D^2 + ... \qquad 4.12$$

Where all K_N are constants

The Debye temperature θ_D is defined by:

$$\theta_D = \frac{\hbar}{k}\,\omega_D \qquad 4.13$$

Where k - Boltzmans constant

ω_D - Debye frequency.

It can be seen from both the general harmonic model (Eqn. 4.9) and the Debye approximation (Eqn. 4.11) that the mean square vibrational amplitude $\langle x^2 \rangle$ is weighted towards lower frequencies because the $1/\omega$ term, whilst the mean square thermal velocity $\langle v^2 \rangle$ is weighted towards higher frequencies. Hence a higher characteristic temperature is derived from the SODS data.

Analysis of the quadrupole splitting data indicates that ferrous iron possesses a larger $\Delta E_Q(\text{lat})$ component than ferric iron. This suggests that Fe^{2+} sites are more disordered than Fe^{2+} sites. The linewidths of the two doublet fits support this conclusion with the Fe^{3+} lines consistently narrower than Fe^{2+} lines ($\Gamma(Fe^{3+}) / \Gamma(Fe^{2+}) = 0.87$). The distribution fits further reinforce this,

with the Fe^{2+} distribution having a width of ~0.8 mm/s whilst the Fe^{3+} has a width of ~0.6 mm/s.

The glasses prepared under argon reveal two octahedral Fe^{2+} sites. The first $Fe^{2+}(1)$ is due to the normal Fe^{2+} component, whilst the second $Fe^{2+}(11)$ may correspond to Fe^{2+} occupying Fe^{3+} type sites. This is in agreement with Menil (§2.3.2) who interpreted a decrease in quadrupole splitting as indicating an increase in site symmetry. A variable temperature study would allow this hypothesis to be tested by measuring the Debye temperatures and crystal field splittings of the two sites. If the $Fe^{2+}(11)$ site corresponded to an Fe^{3+} type location then it might be expected to have a higher Debye temperature and a lower $\Delta E_Q(lat)$ component than $Fe^{2+}(1)$.

The ferric and ferrous iron sites in the glass, whilst both being octahedral, exhibit markedly different degrees of distortion from the symmetric arrangement of six oxygen ligands. The Debye temperatures and crystal field splittings must be regarded as crude estimates because of the number of approximations made during the analysis. Nevertheless they do yield realistic values and enable qualitative comparisons to be made between different glass compositions.

4.5 References

1. Gibb T.C.; Greatrex R.; Greenwood N.N.
   Journal of the Chemical Society (A), 1968, 890

2. Greenwood N.N.; Gibb T.C.
   'Mössbauer Spectroscopy', Chapman and Hall, 1971 p.74

3. Taragin M.F.; Eisenstein J.C.
   Journal of Non-Crystalline Solids, 3, 311, 1970

4. Wivel C.; MØrup S.
   Journal of Physics, E13, 427, 1980

5. DeGrave E.; Vochten R.
   Solid State Communications, 65(5), 315, 1988

6. Brooks J.S.; Care C.M.; Plimley S.; Cornfield G.C.
   Hyperfine Interactions, 20, 151, 1984

7. Mostafa A.G.; Awadallah R.M.; Sanad A.M.; Salah S.H.
   Journal of Materials Science, 21, 965, 1986

8. Ingalls R.
   Physical Review, 133A (3), 787, 1964

9. Bancroft G.M.
   'Mössbauer Spectroscopy' McGraw-Hill 1973, p.23

10. Cotton F.A.; Wilkinson G.
    'Advanced Inorganic Chemistry', 4th Edition, Wiley 1980, p.646

11. Gosselin J.P.; Shimony U.; Grodzins L.; Cooper A.R.

Physics and Chemistry of Glass, 8(2), 56, 1967

12. DeGrave E.; Vanleerberghe R.; Verdonck L.; DeGeyter G.

Physics and Chemistry of Minerals, 11, 85, 1984

13. Mattern P.L.

Ph.D. Thesis, Cornell University, USA, 1966

14. Taragin M.F.; Eisenstein J.C.; Haller W.

Physics and Chemistry of Glass, 13(5), 149, 1972

15. Paul A.

'Chemistry of Glasses', Chapman and Hall, 1982, p.148

16. Dyer M.D.; Birnie III D.P.

Journal of Non-Crystalline Solids, 67, 397, 1984

17. Johnston W.D.

Journal of the American Ceramic Society, 47(4), 198, 1964

18. Johnston W.D.

ibid. 48(4), 185, 1965

19. DeGrave E.; Van Iseghem P.

'Applications of ^{57}Fe Mössbauer spectroscopy to the characterisation of silicate glasses' in 'Industrial Applications of Mössbauer Spectroscopy', Plenum Press, 1988

20. Virgo D.; Mysen B.O.

Physics and Chemistry of Minerals 12, 65, 1985.

21. Greenwood N.N.; Gibb T.C.

'Mössbauer Spectroscopy' Chapman and Hall, 1971, p.253

22. Dyer M.D.

Journal of the American Ceramic Society, 69(7), C160, 1986

23. Karraker D.G.

Advanced Ceramic Materials, 3(4), 337, 1988

24. Lafleur L.D.; Goodman C.

Physical Review, 4B(9), 2915, 1971

CHAPTER FIVE - FURTHER MÖSSBAUER STUDIES

5.1 The xNa_2O-$(36-x)K_2O$-$56P_2O_5$-$8Fe_2O_3$ glass system

A series of glasses were made to the general formula shown above with x = 0,8,17,24,36. Because of the high P_2O_5 content the glasses were mildly hydroscopic. To minimise the effect of atmospheric moisture the glasses were stored in a desiccator once annealing had been completed. In order to assess the relative durability of the glasses they were subjected to a prolonged dissolution rate study. Measured lengths of 4mm diameter glass rods were placed in sample bottles, each containing 100ml of distilled water. The bottles were fixed to a shaking table in a water bath held at 38°C. The distilled water was refreshed every 24 hours to minimise build up of glass ions in solution which might effect the dissolution rates (§1.3.2). Periodically the glass rods were carefully removed from the bottles, dried with acetone and weighed.

A typical set of results is presented in Figure 5.1. They show no evidence of $t^{1/2}$ dissolution behaviour, which would be indicative of a diffusion mechanism. Instead there is a linear dissolution rate indicating that the rate controlling step is the disentanglement of the hydrated phosphate chains (§1.3.2).

The glasses were weighed daily, with the exception of the last data point which corresponds to a three day interval from the previous reading. The slope of the graph remains constant across this larger interval, indicating that the build up of ions in solution has not effected the dissolution rate. In the absence of any evidence of incongruent dissolution it was not considered necessary to carry out compositional analysis (I.C.P. spectroscopy) of the solutes.

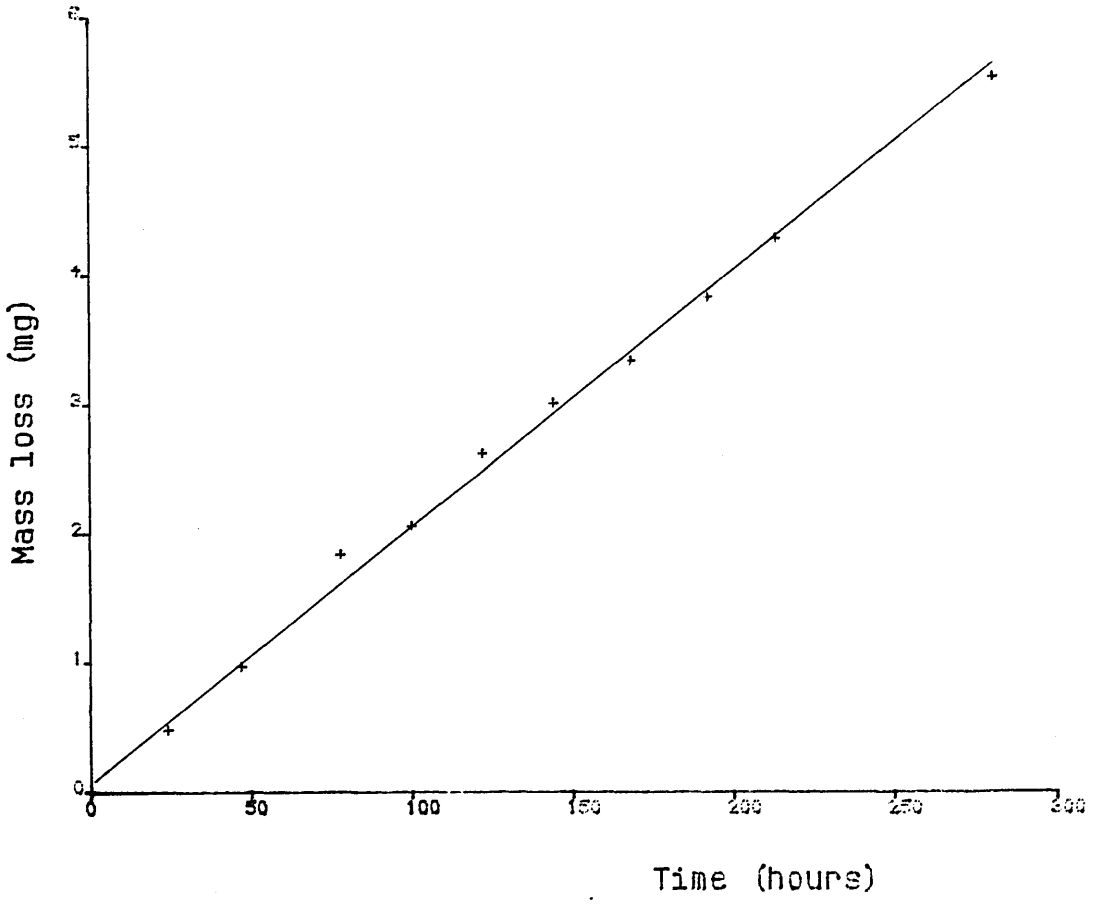

Figure 5.1 Mass loss of $8Na_2O$-$28K_2O$-$56P_2O_5$-$8Fe_2O_3$ glass immersed in water

Most of the glass compositions yielded a dissolution rate R $\simeq$ 0.5mg/mm²h whilst the sodium free glass (x=0) had a much higher dissolution rate of R=13.2 mg/mm²h (Fig. 5.2). This is consistent with work on non-iron containing alkali-phosphate glasses which noted that the hydroscopic nature increases in the order Li; Na; K [1]. The same trend is generally true for silicate glass [2]; increasing the radius of the alkali cation leads to a decrease in durability.

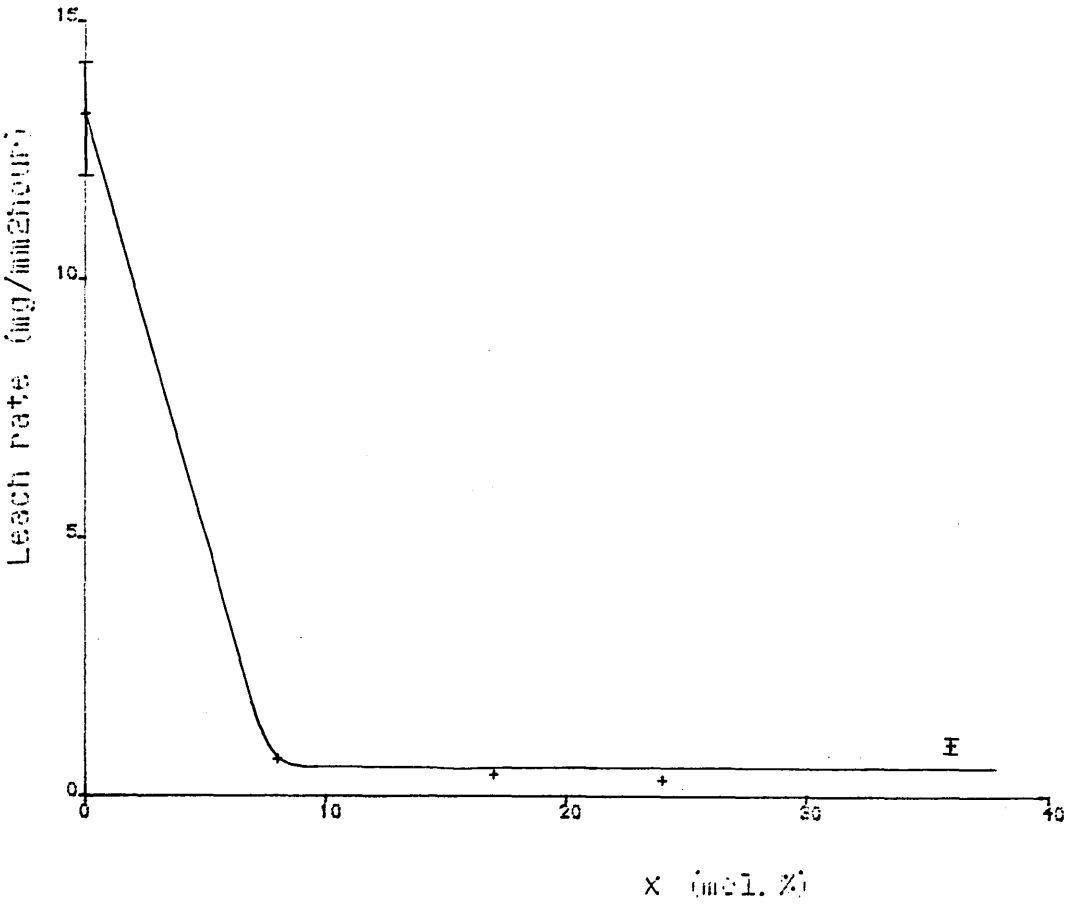

Figure 5.2 Dissolution rates for the xNa_2O-(36-x)K_2O-56P_2O_3-8Fe_2O_3 glass system

The Mössbauer spectra of these glasses did not reveal any compositional trends, with the isomer shifts, quadrupole splittings and Fe^{3+}/Fe^{2+} ratios remaining essentially constant. Thus the iron sites are insensitive to the replacement of sodium by potassium. The vast difference in dissolution rates of these glasses is therefore attributable to the influence of the sodium and/or potassium ions, with the iron environment remaining essentially constant as network modifying Fe^{3+} and Fe^{2+} sites.

The variation in durability is presumably due to the fact that the potassium ion has a larger ionic radius (r = 133pm) than the sodium ion (r = 97pm) and hence has a lower charge/radius ratio. It will therefore be less strongly bound within it oxygen polyhedron than sodium. Paper chromatography studies of alkali phosphate glasses have shown that [3] the chain length distributions for sodium and potassium glasses are, within experimental error, identical. Hence their different durabilities is solely due to the greater ease with which the K^+ ionic cross links between the phosphate chains are hydrolysed.

5.2 The xNa_2O-(92-x)-P_2O_5-$8Fe_2O_3$ glass system

The objective of this work was to make a comparative study of the xNa_2O-(92-x)-P_2O_5-$8Fe_2O_3$ glass system and to compare and contrast the results with those obtained by Nishida et al [4,5] from the equivalent xK_2O-(93-x)P_2O_5-$7Fe_2O_3$ glass system. The starting materials used by this group were K_2CO_3, $NH_4H_2PO_4$ and Fe_2O_3 melted under air in platinum crucibles and then quenched in water. A full compositional range was reported from x=0 to x=70 mol.% by this method, although there is no mention of any analysis to confirm the composition of the glasses produced.

A number of modifications were made to Nishida's glass production method. Firstly the muffle furnace used did not have a vent to the exterior of the building, hence the use of $NH_4H_2PO_4$ as the source of phosphate ions was dismissed as it leads to the liberation of ammonia gas. Instead potassium phosphates and phosphorous pentoxide were used. This did not solve the atmospheric pollution problem as it was found that upto 60 weight% of the

high P_2O_5 content glasses was liberated as P_2O_5 vapour. To determine the realistic composition limits it was decided to work out from a comparatively non-volatile composition (x=36 mol.%). The lower limit occurred at x=25 mol.% whilst an upper limit of x=52 mol.% was achieved. The upper limit could possibly have been increased with a higher furnace temperature. The lower limit could perhaps have been decreased by using smaller batch weights and a shorter melting time.

A further modification of Nishida's glass preparation method was the use of silica as opposed to platinum crucibles. At temperatures of the order of 1000°C iron will alloy with platinum. This is undesirable from a glass composition viewpoint and also from an economic viewpoint as the repurification procedure is both difficult and costly.

These production difficulties have limited the degree of comparison which can be made with Nishida's work because of the greatly reduced compositional range which has been achieved.

Dissolution rate studies have been performed following the method described previously (§5.1). Since it was not possible to cast the x=52 glass as a rod an accurate dissolution rate analysis could not be performed. Instead a comparative trial was conducted using known masses of powdered glasses. The powders were sieved to give equal particle size distributions and then added to equal volumes of distilled water. After 60 hours the glass powders were extracted from the water using filter papers and reweighed. The results indicate that the x=52 glass has a similar dissolution rate to the x=25 glass (Fig. 5.3). By comparison to the full dissolution rate analysis (Fig. 5.4) this

corresponds to a rate of the order $R = 2 \times 10^{-5}$ mg/mm^{2}h. Contrary to expectations based upon Van Wazers theory of glass durability (§1.3.2) the series shows a minimum durability at $x \simeq 42$ mol.%. This must be attributed to the effect of the Fe_2O_3 on the glass structure though the mechanism is unclear.

No discernible trends were visible in the Mössbauer results (Fig. 5.5, 5.6). The ferric iron parameters, with one unexplained exception, remained essentially constant over the available composition range. The isomer shifts and quadrupole splittings again identify distorted octahedral coordination. The ferrous iron doublets accounts for approximately ten percent of the total absorption area. The spread of isomer shifts and quadrupole splittings all lie within the range expected for octahedral coordination. Quadrupole distribution fits all yield similar parameters with a single, symmetric shape for the Fe^{3+} distributions. The Fe^{2+} sites yield extremely diffuse distributions with no discernible shape to the distributions.

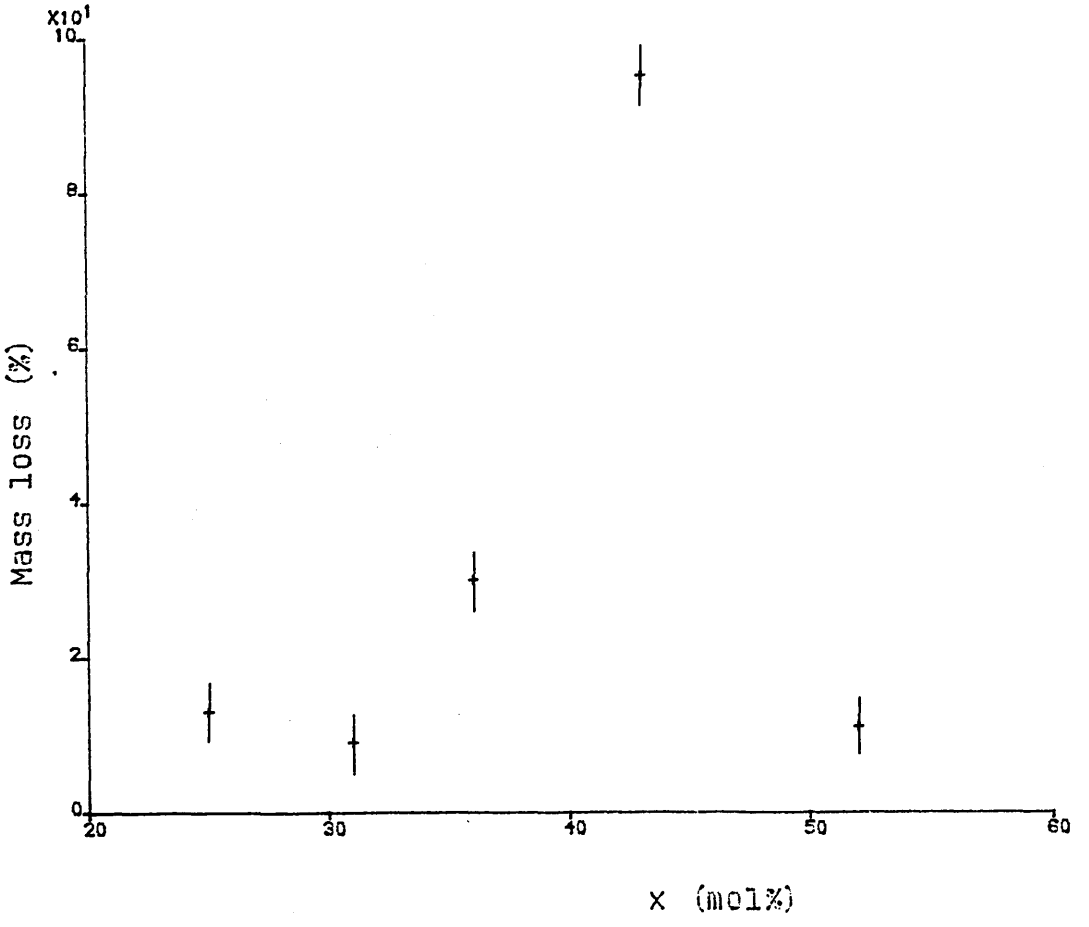

Figure 5.3 Percentage weight loss of xNa_2O-$(92-x)P_2O_5$-$8Fe_2O_3$ glass powders after immersion in water

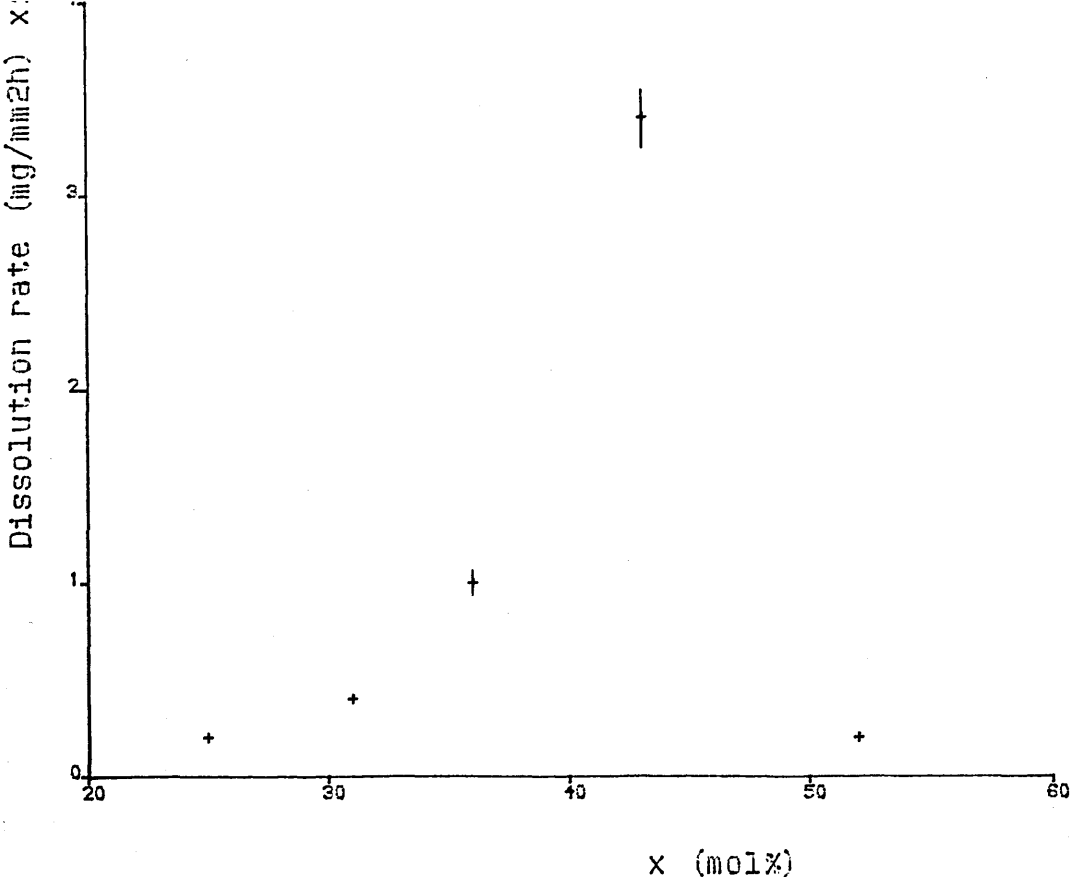

Figure 5.4 Dissolution rates for glasses from the xNa_2O-$(92-x)P_2O_5$-$8Fe_2O_3$ system

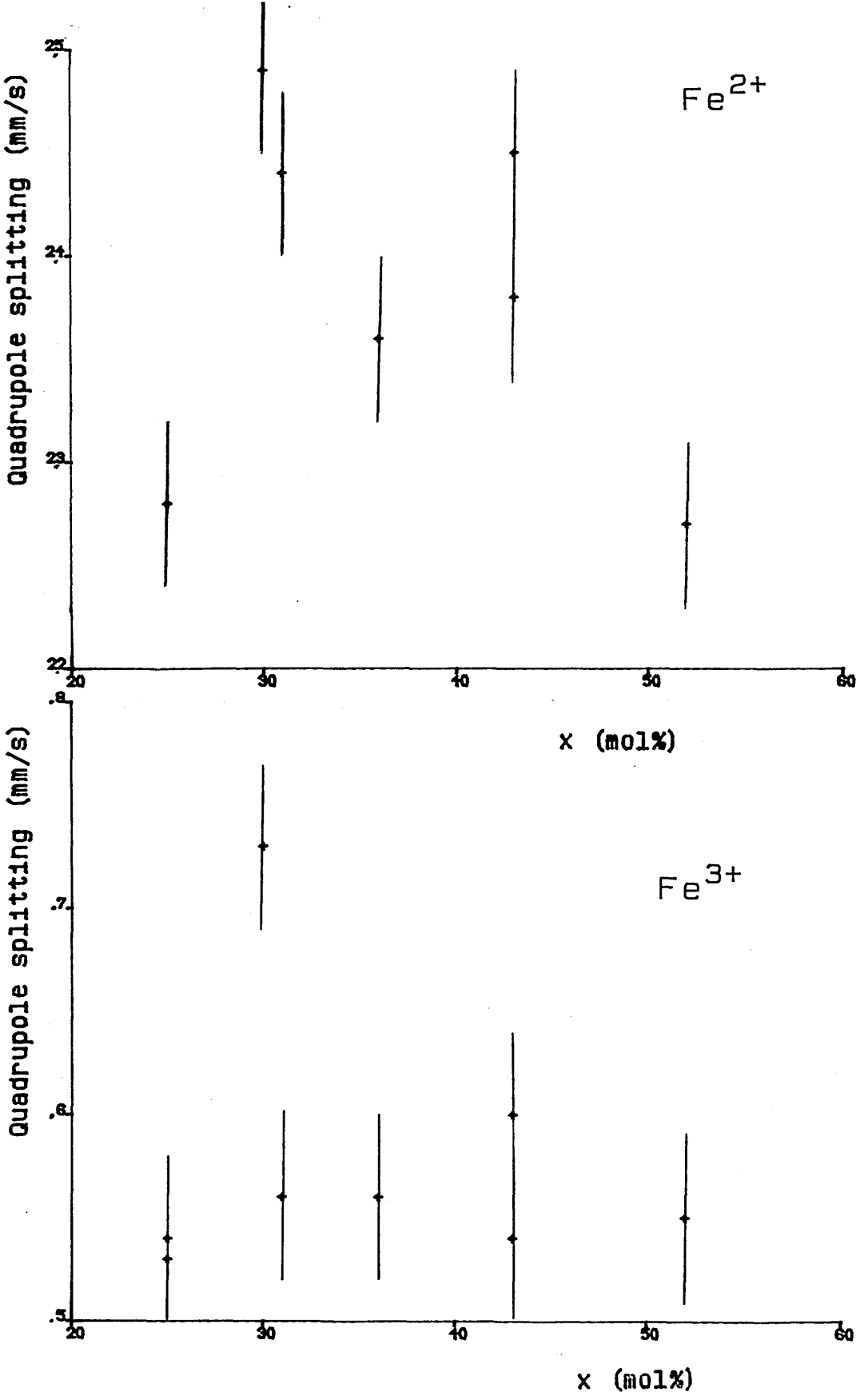

Figure 5.5 Quadrupole splittings for glasses from the xNa_2O-$(92-x)P_2O_5$-$8Fe_2O_3$ series

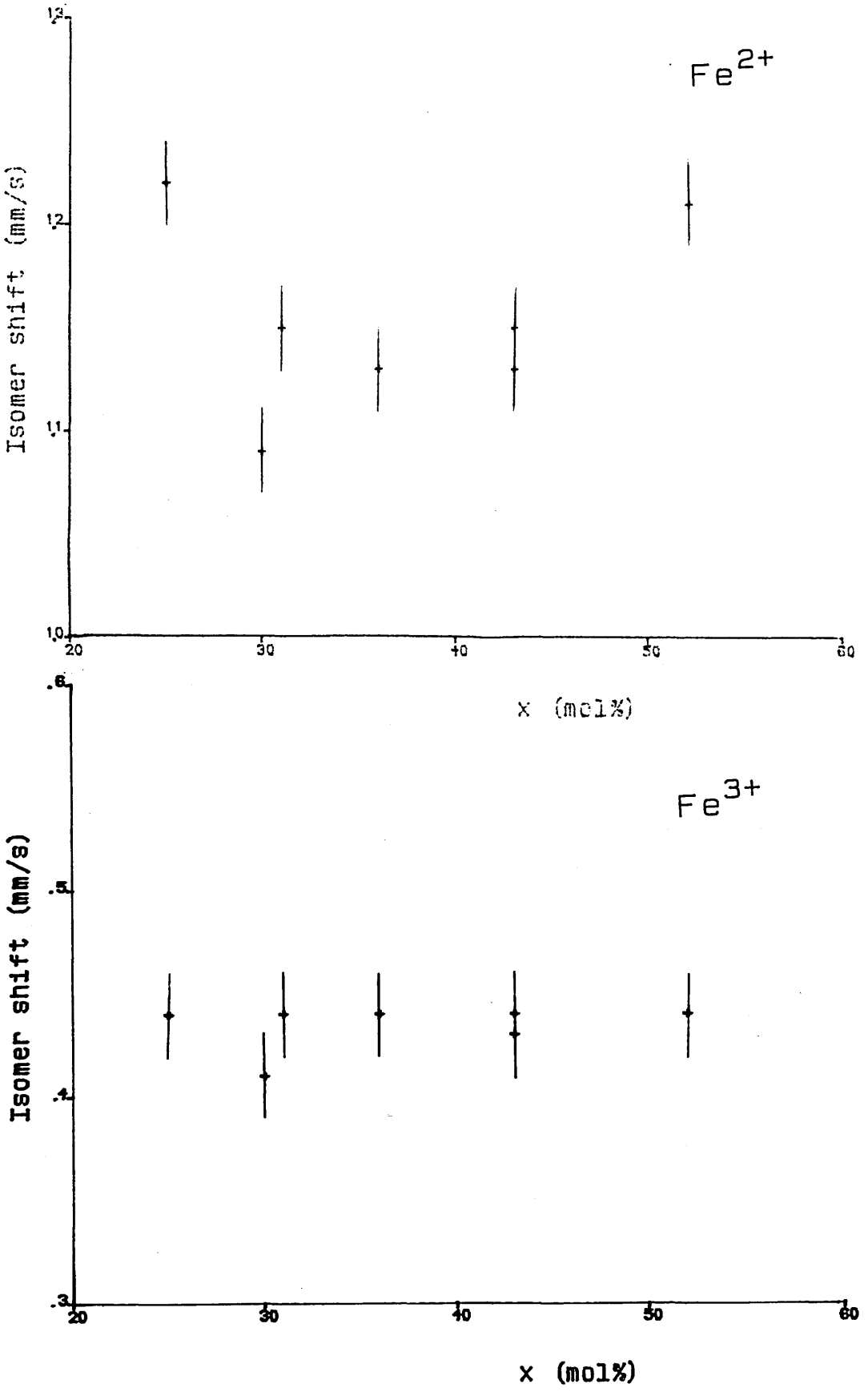

Figure 5.6 Isomer shifts for glasses from the xNa_2O-$(92-x)P_2O_5$-$8Fe_2O_3$ system

5.3 Variable Temperature Study of a sodium-iron-phosphate glass

A variable temperature study has been performed on a sodium-iron-phosphate glass with the molar composition $16Na_2O$-$73P_2O_5$-$11Fe_2O_3$ (GW21.13). This glass was produced subsequently to the series discussed in the previous section. A higher final P_2O_5 mol.% content for the glass was achieved by increasing the initial Fe_2O_3 content, using NaH_2PO_4 and Na_2HPO_4 as starting materials and decreasing the melt time to ten minutes. There was still a substantial amount of volatilisation of P_2O_5 and the final composition, as determined using I.C.P. spectroscopy, was significantly different to the desired composition containing 8 mol.% Fe_2O_3.

In order to ensure accurate absorption area data the powdered glass sample was dispersed in graphite to give a Mössbauer thickness t = 0.01, this ensured that there were no saturation effects. The main features of the results are illustrated in Figure 5.7. With increasing temperature the absorption areas show a steady decrease, the splittings of the doublets decrease and both doublets move to more negative velocities.

Analysis of the isomer shift data leads to a Debye temperature θ_D = 490K for the ferric iron (Fig. 5.8), however, the ferrous iron data could not be fitted to the Debye model. There is an unexpected abrupt change in the isomer shift data at the boundary between the two data subsets (Fig. 5.9). The phenomenon is reproduced by plotting the temperature dependence of the mean isomer shift $\bar{\delta}$ derived from the distribution fits to the data. This change is also evident in the Fe^{2+} data for the J3 sample (§4.2.3).

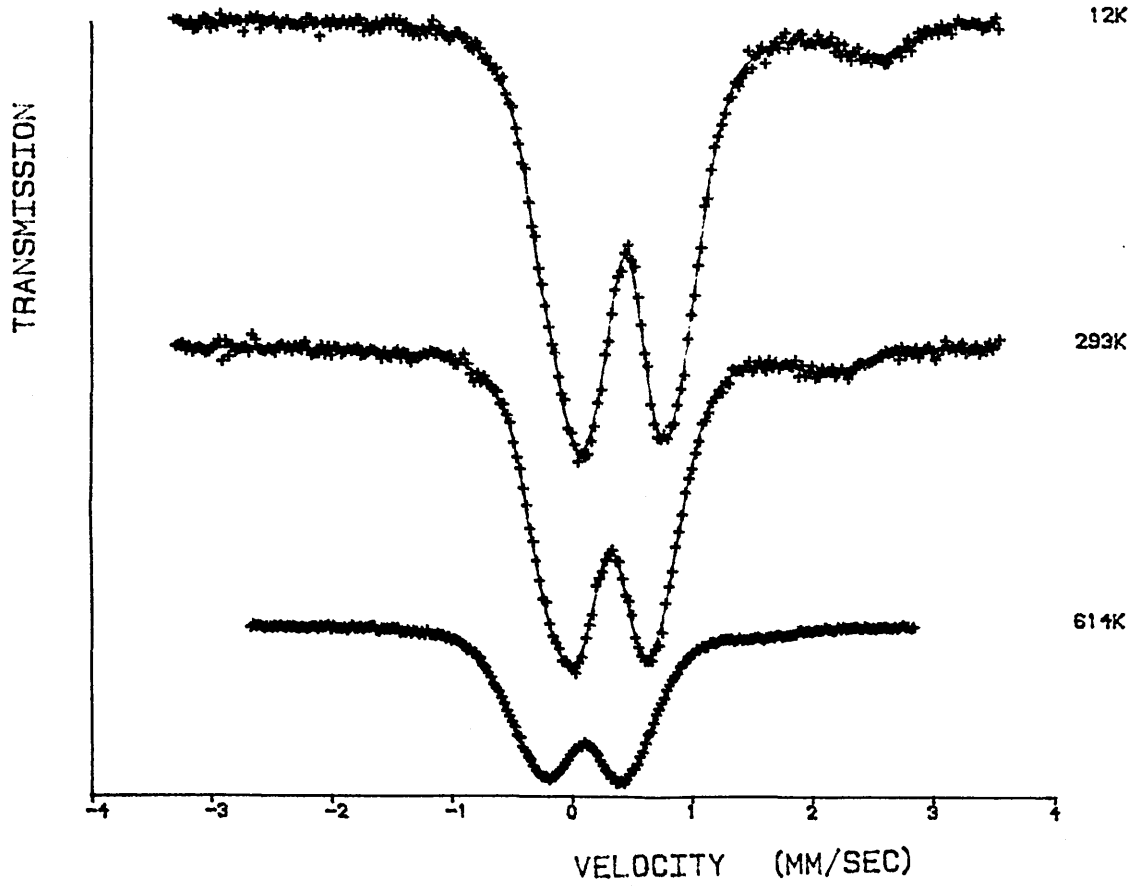

Figure 5.7 Temperature dependent variation of the spectrum of GW21.13

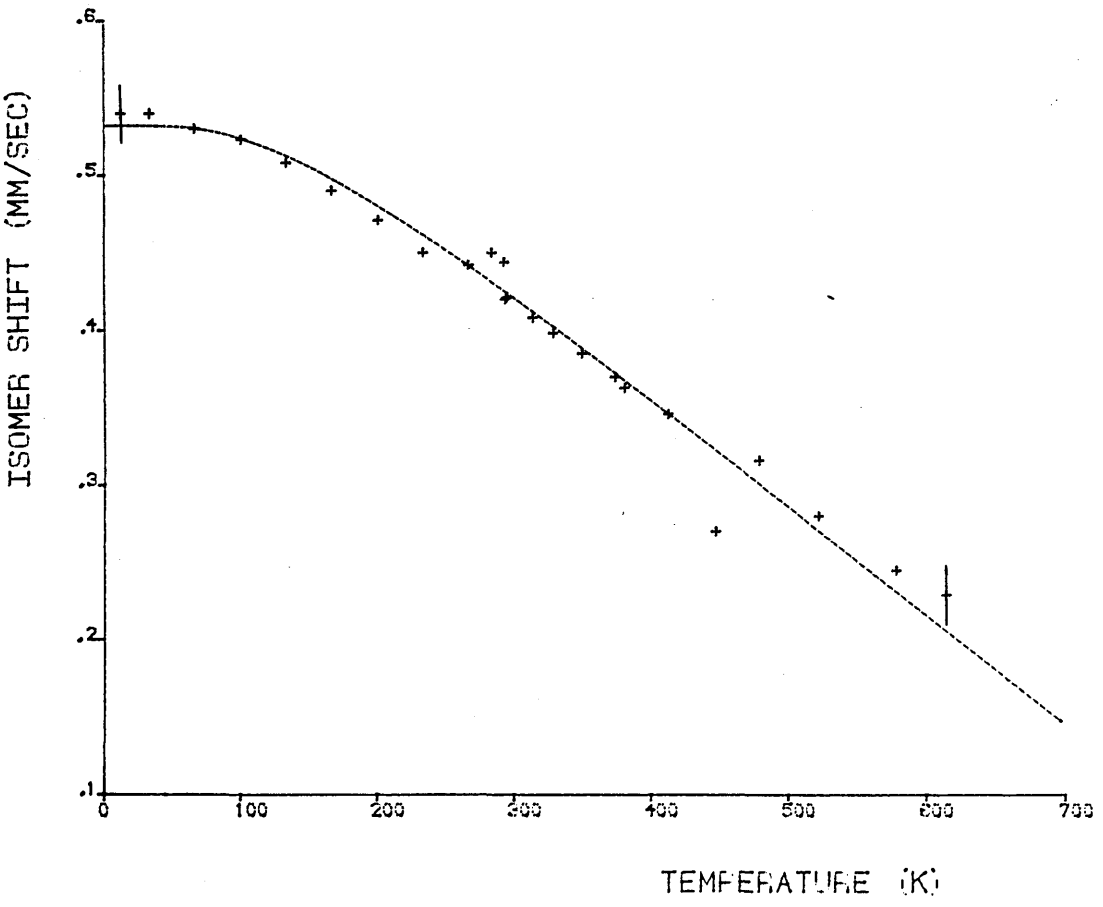

Figure 5.8 Temperature dependence of the Fe^{3+} isomer shift for GW21.13

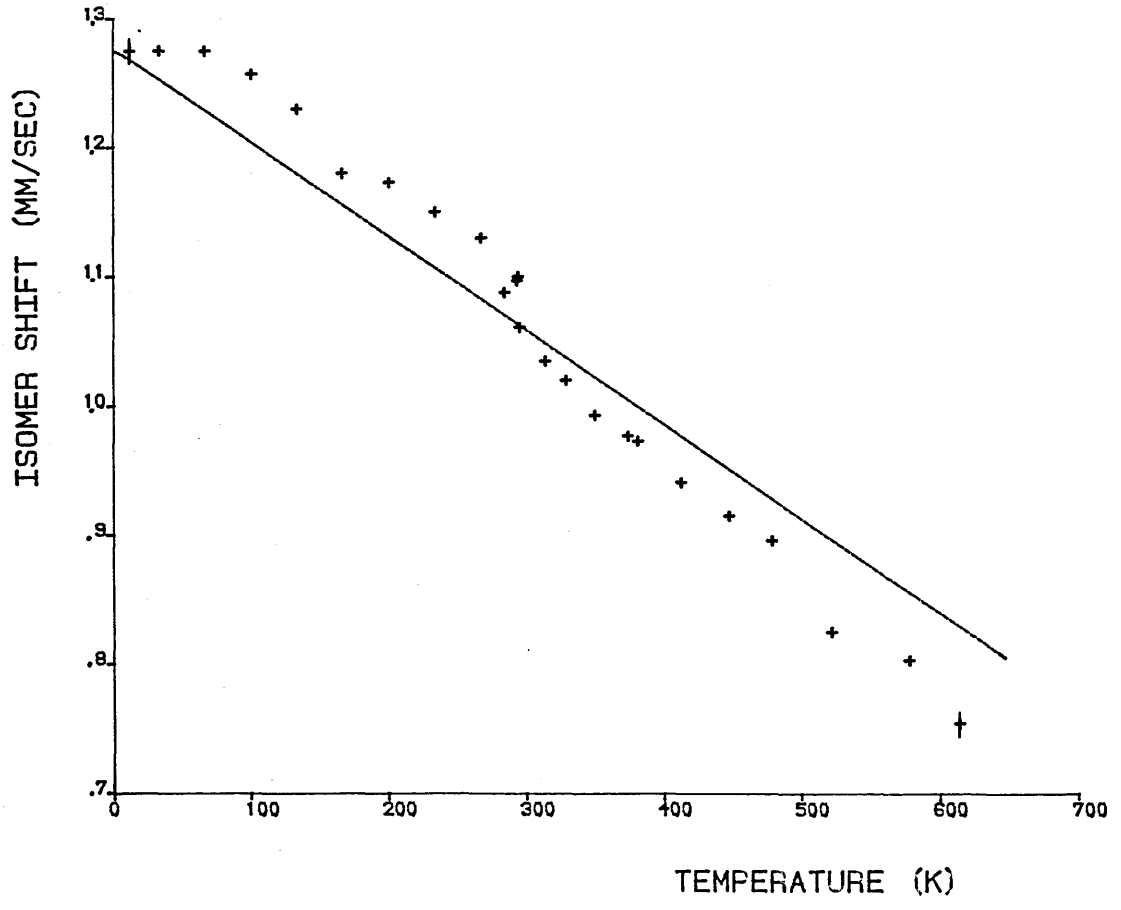

Figure 5.9 Temperature dependence of the Fe^{2+} isomer shift for GW21.13

Efforts were made to ascertain whether the change in isomer shift was related to the change in experimental geometry when moving from the Displex cryostat to the electric furnace. The vacuum pump port of the electric furnace (§2.2.7.3) was connected via tubing to a nitrogen gas cylinder. A needle value controlled the flow of gas into the sample area which could leak out around the edge of the furnace lid. Unfortunately the temperature controller was unable to stabilise the sample temperature below 10°C, despite attempts to insulate the furnace. It was also found that operating the heater of the Displex system to produce sample temperatures above room temperature was inadvisable, hence no appreciable overlap could be obtained between the two data subsets.

The reason for the discontinuity remains unknown. The same radioactive source was employed in the collection of both data subsets, hence the isomer shifts are all relative to the same source matrix, namely $^{57}Co(Rh)$. It seems unlikely that the low and high temperature data correspond to different compositions since the absorbers were made from the same piece of powdered glass. The only difference might be in the Mössbauer thickness t of the absorbers, but why this would lead to the observed result is unclear. Another possibility is that the time period between the collection of the low and high temperature data (~ 6 months) has seen some degradation of the glass through attack by water vapour. This is despite the glasses being stored in a desiccator. The spectra have been refitted in an attempt to eliminate the discontinuity but without success.

By considering solely the low temperature Fe^{2+} isomer shift data a Debye temperature θ_D = 150K could be obtained. The high temperature data could not be realistically fitted to the Debye model.

Absorption area data (Fig. 5.10) yielded a Debye temperature θ_D = 290K for the lattice. For ferric iron θ_D = 300K, while ferrous iron gave θ_D = 220K. As expected (§4.4) the absorption area data led to a higher θ_D (Fe^{3+}) than the S.O.D.S. data. For ferrous iron the S.O.D.S and absorption area data both gave poor fits to the Debye model with high χ^2 values. This accounts for the anomalous result that the S.O.D.S. data yielded an apparently higher Debye temperature than the absorption area data.

The temperature dependence of the ferric and ferrous iron quadrupole splittings (Figs. 5.11, 5.12) have been fitted in the same manner as J3 (§4.2.4). The splitting of the ferric iron doublet showed a steady decrease with

increasing temperature (Table 5.1), whilst the ferrous iron doublet could be fitted to the crystal field model (Eqn. 4.2). As with J3 the best fit to the Fe^{3+} data gave a very large ΔE_Q(lat) component to the total quadrupole splitting. Fitting the data using the Fe^{3+} temperature dependence gave crystal field splittings Δ_1 = 1100 cm^{-1}; Δ_2 = 2200 cm^{-1}.

Table 5.1 QUADFIT results for GW21.13.

Iron Site	Fitting Method	Parameters	Chi-squared
Fe^{3+}	Straight line	Gradient=-0.00054 mm/sK Intercept = 0.46mm/s	0.0028
Fe^{2+}	Eqn. 4.2 with variable ΔE_Q(lat)	Δ_1 = 335cm^{-1} Δ_2 = 670cm^{-1} ΔE_Q(lat) = 1.88mm/s ΔE_Q(0) = 2.79mm/s	0.0073
Fe^{2+}	Eqn. 4.2 withΔE_Q(lat) defined by Fe^{3+} temperature dependance	Δ_1 = 1100cm^{-1} Δ_2 = 2200cm^{-1} ΔE_Q (0) = 2.30mm/s	0.0565
Fe^{2+}	Eqn. 4.2 withΔE_Q(lat) = 0	Δ_1 = 810 cm^{-1} Δ_2 = 1620 cm^{-1} ΔE_Q(0) = 2.69 mm/s	0.1274

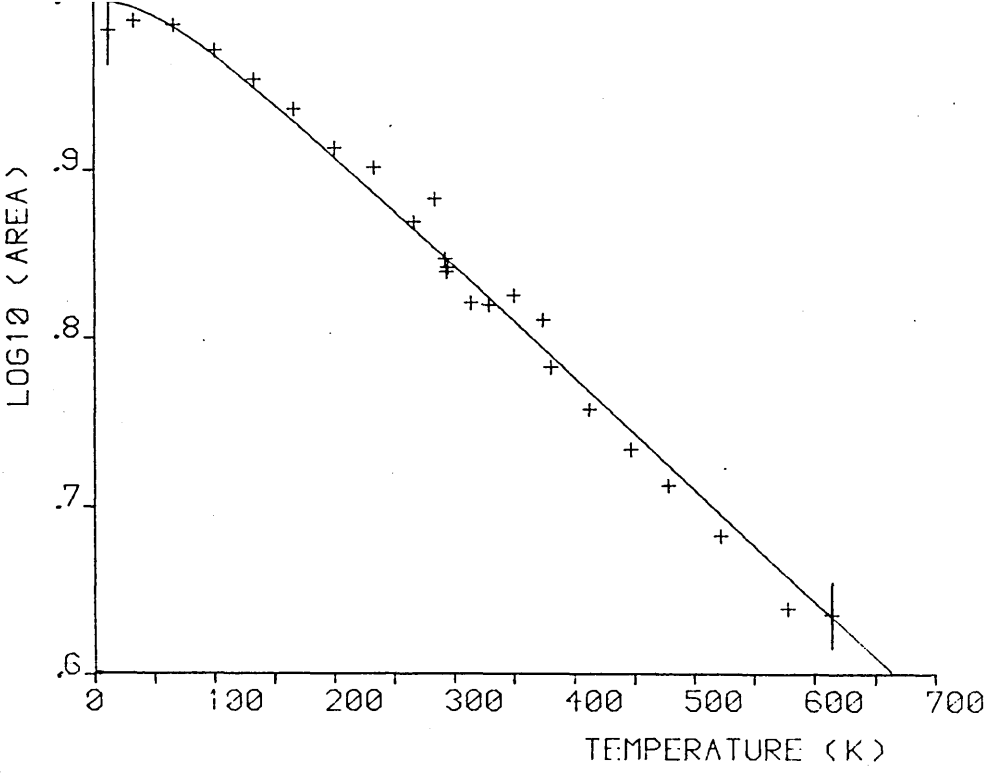

Figure 5.10 Total absorption area data for GW21.13

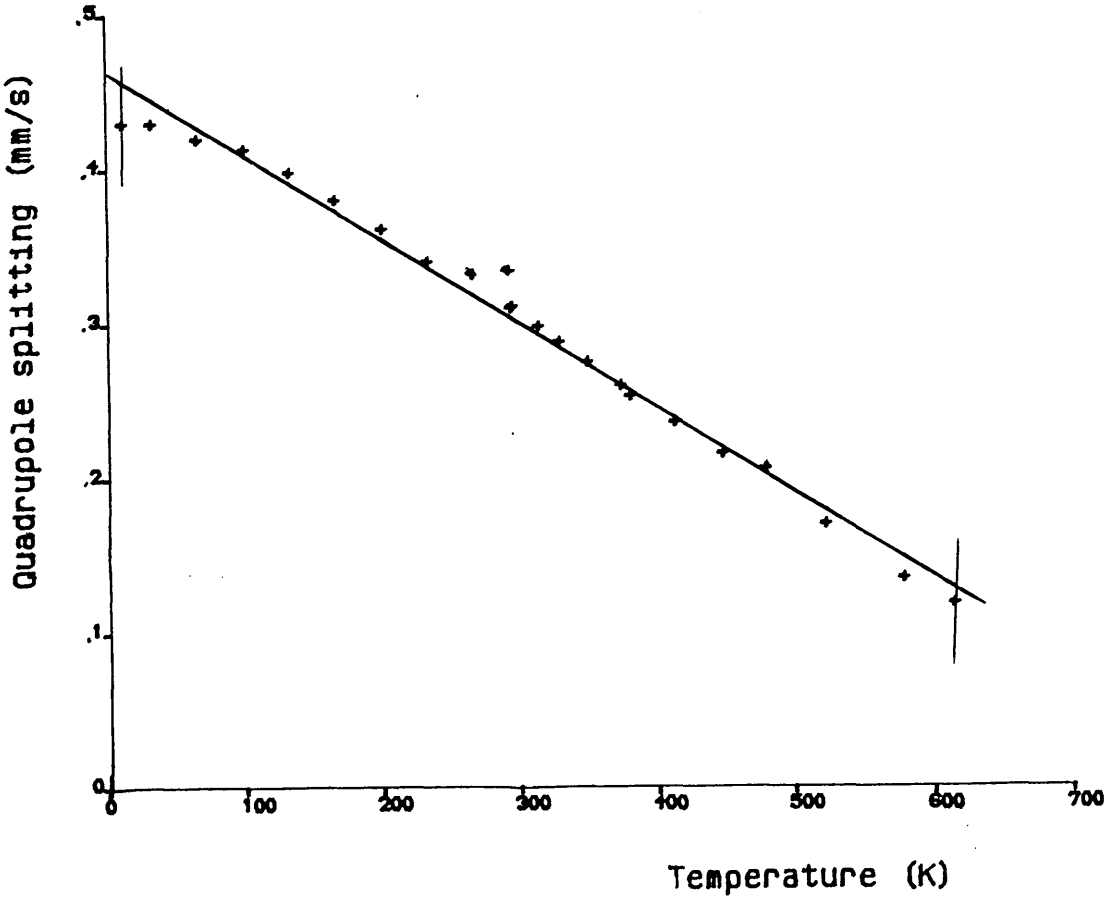

Figure 5.11 Temperature dependence of the ferric iron quadrupole splitting for GW21.13

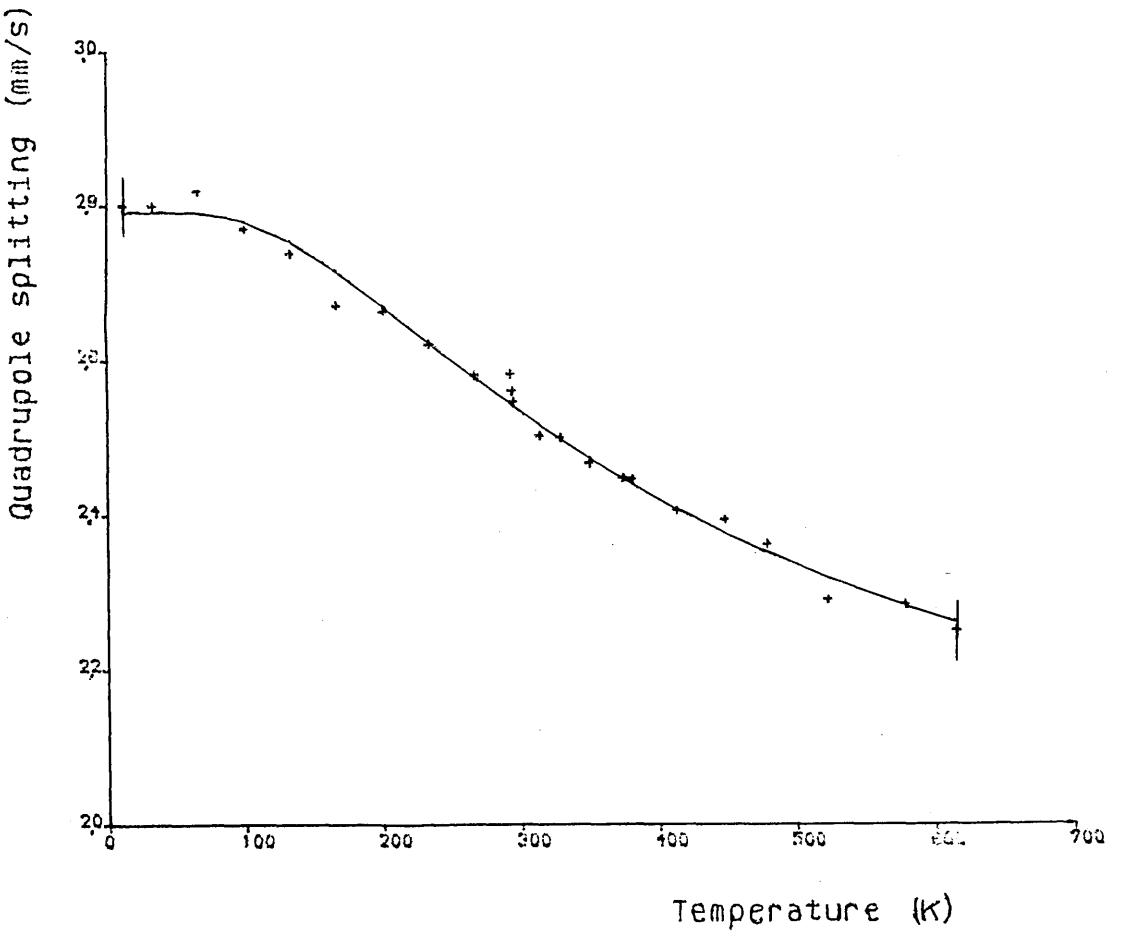

Figure 5.12 Temperature dependence of the ferrous iron quadrupole splitting for GW21.13

5.4 The Na_2O-CaO-P_2O_5-Fe_2O_3 glass system

Calcium oxide is often used to control the dissolution rate of phosphate glass, the durability being very sensitive to the CaO content [6]. An interesting phenomenon has been noted in the dissolution rate behaviour of sodium-calcium-phosphate glass. With a fixed CaO content an increase in Na_2O content leads to an increase in dissolution rate, even for glasses with greater than 50 mol.% P_2O_5. This is contrary to Van Wazers hypothesis [7] which states that the most durable glass should occur at 50 mol.% P_2O_5 (§1.3.2) as this corresponds to the maximum linear phosphate chain length.

In order to investigate this phenomenon a series of sodium-calcium-phosphate glasses were made with 2 mol.% Fe_2O_3. This is the minimum iron concentration which would enable Mössbauer spectra to be recorded, within an acceptable accumulation time, given the strength of the ^{57}Co source. It took 3-4 days to accumulate adequate room temperature spectra. It was not considered justifiable to use Fe_2O_3 enriched in ^{57}Fe. The molar compositions of the glasses produced were:

$$xNa_2O\text{-}20CaO\text{-}(78\text{-}x)P_2O_5\text{-}2Fe_2O_3$$

where x = 6, 11, 15, 19, 21, 24, 27, 28, 31, 32, 38, 41.

The small iron content ensured that the glasses were translucent; the low alkali glasses appearing a light pink colour, whilst the high alkali glasses had a green/brown tinge. It did not prove possible to quantify this trend using U.V./visible spectroscopy; the spectra remaining essentially constant. A frit with 45 mol.% Na_2O would not form a glass and instead devitrified to give an off-white ceramic.

The glass durabilities were determined using the normal method (\$5.1). The dissolution rates are a factor of 10^5 lower than for iron-free glasses indicating the dramatic effect which iron has on the durability of the glass. The results (Fig. 5.13) show a large decrease in durability as Na_2O is progressively added. The glass with x=15 is approximately 50 times more durable than the x=38 composition. Note that the dissolution rates are plotted to a logarithmic scale.

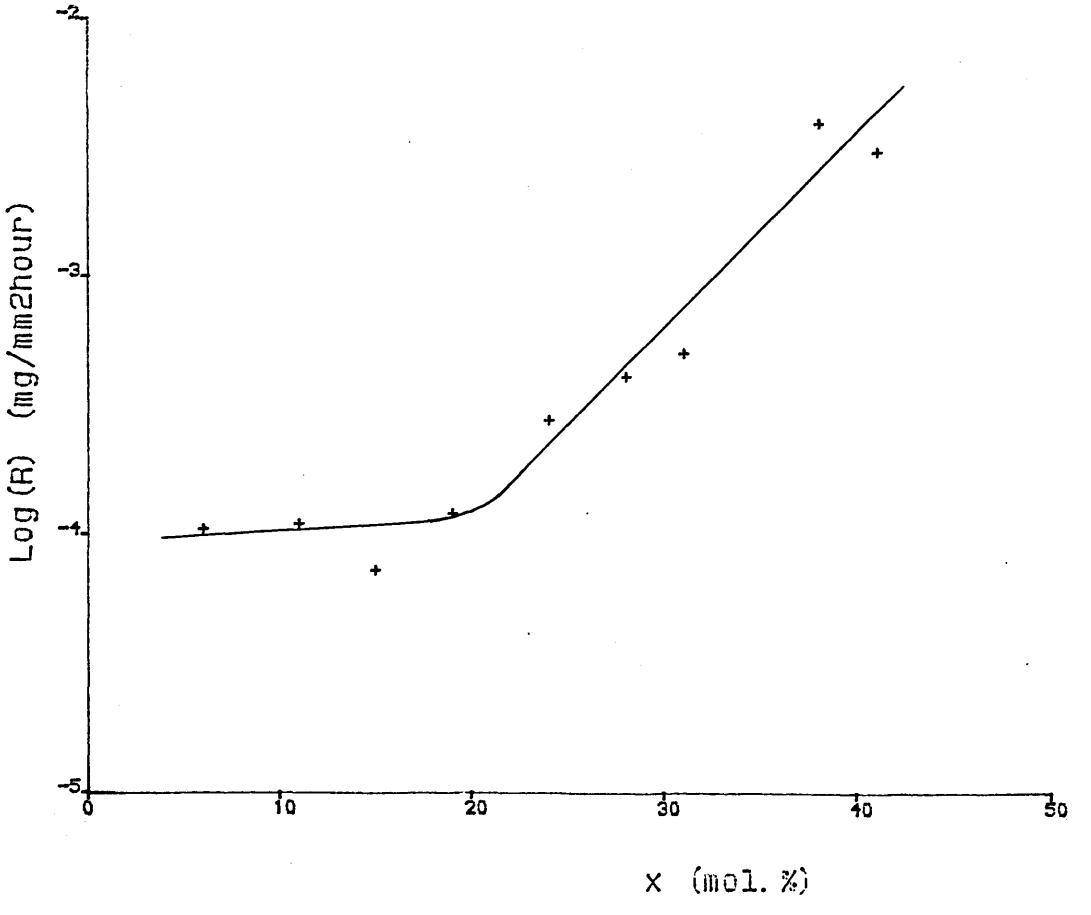

Figure 5.13 Compositional dependence of dissolution rate R for the xNa_2O-20CaO-(78-x)P_2O_5-Fe_2O_3 glass system

The Mössbauer spectra show some compositional variation in the ferric and ferrous iron doublets. The isomer shift and quadrupole splitting of the ferric iron doublet (Fig. 5.14) remain essentially constant with the exception of the devitrified sample (x=45). This composition shows a markedly lower quadrupole splitting of 0.44 mm/s compared to an average of 0.62 mm/s for the glasses indicating that the ferric iron in the ceramic occupies much more ordered sites than in the glass. The ferric isomer shift for the ceramic is the same as for the glasses. This indicates that the mean iron-oxygen inter atomic distance remains constant on devitrification because the isomer shift is a measure of the s-electron density at the ^{57}Fe nucleus and would be effected by any change in bond length.

The ferrous iron doublet accounts for approximately 25% of the total absorption area (Fig. 5.15). The isomer shift shows a steady decrease as the alkali content increases, indicating an increase in s-electron density at the Fe^{2+} nucleus (\$2.1.5.2). Since the coordination of the iron does not alter, the increase in s-electron density must be due to a decrease in the average Fe-O bond length. The quadrupole splitting increases significantly for Na_2O contents above 20 mol.%. This increase is interpreted as representing an increase in the order of the Fe^{2+} sites since the $q_{lattice}$ component of the EFG increases in the opposite sense to $q_{valence}$ [8,9] thus lowering the overall quadrupole splitting as distortion from perfect octahedral symmetry increases (\$4.2.4). This trend is in accord with the quadrupole splitting of the devitrified sample (x=45), which will have more ordered Fe^{2+} sites than the glass and also has a high quadrupole splitting.

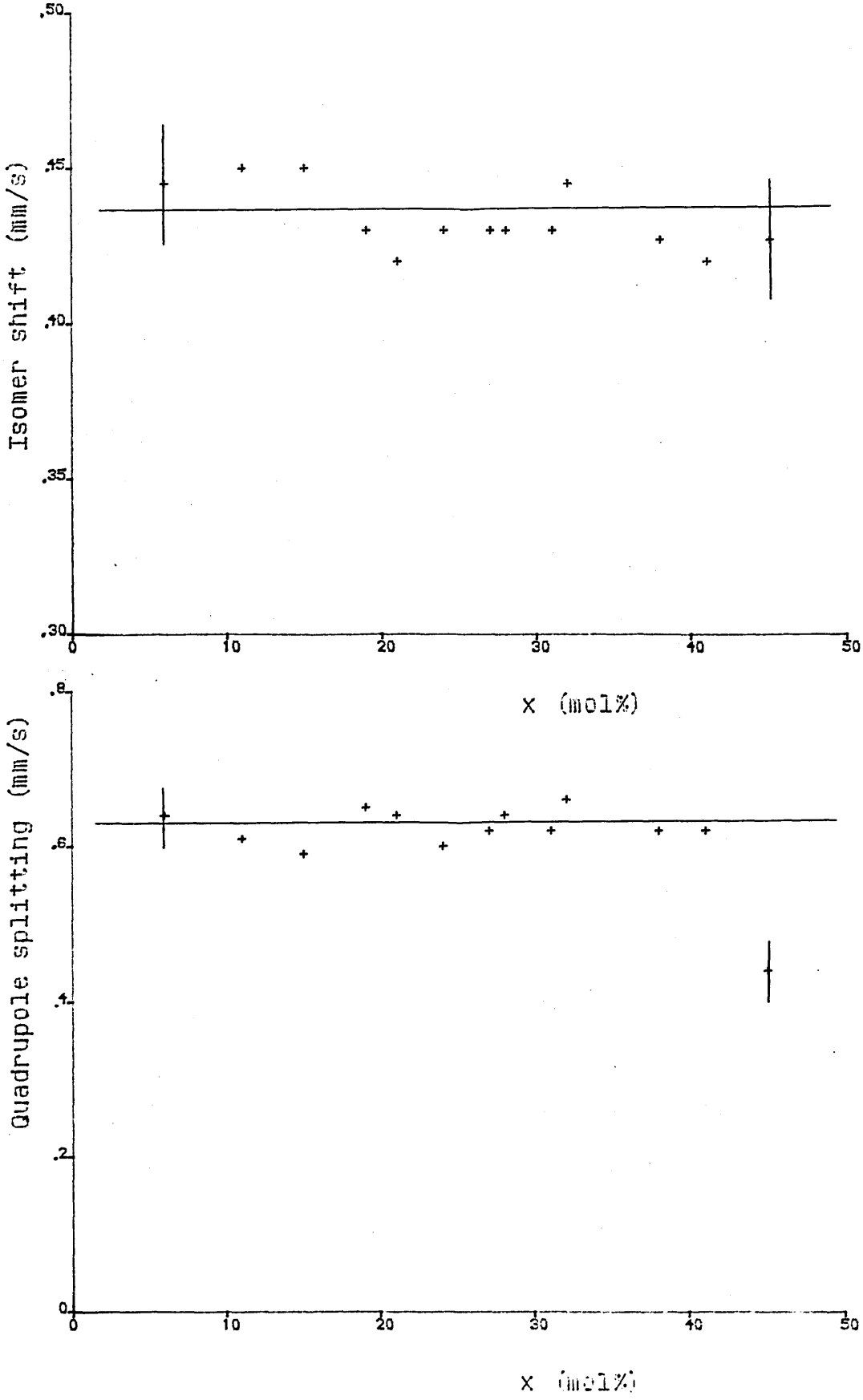

Figure 5.14 Compositional dependence of Fe^{3+} Mössbauer parameters for xNa_2O-20CaO-(78-x)P_2O_5-2Fe_2O_3 glass system

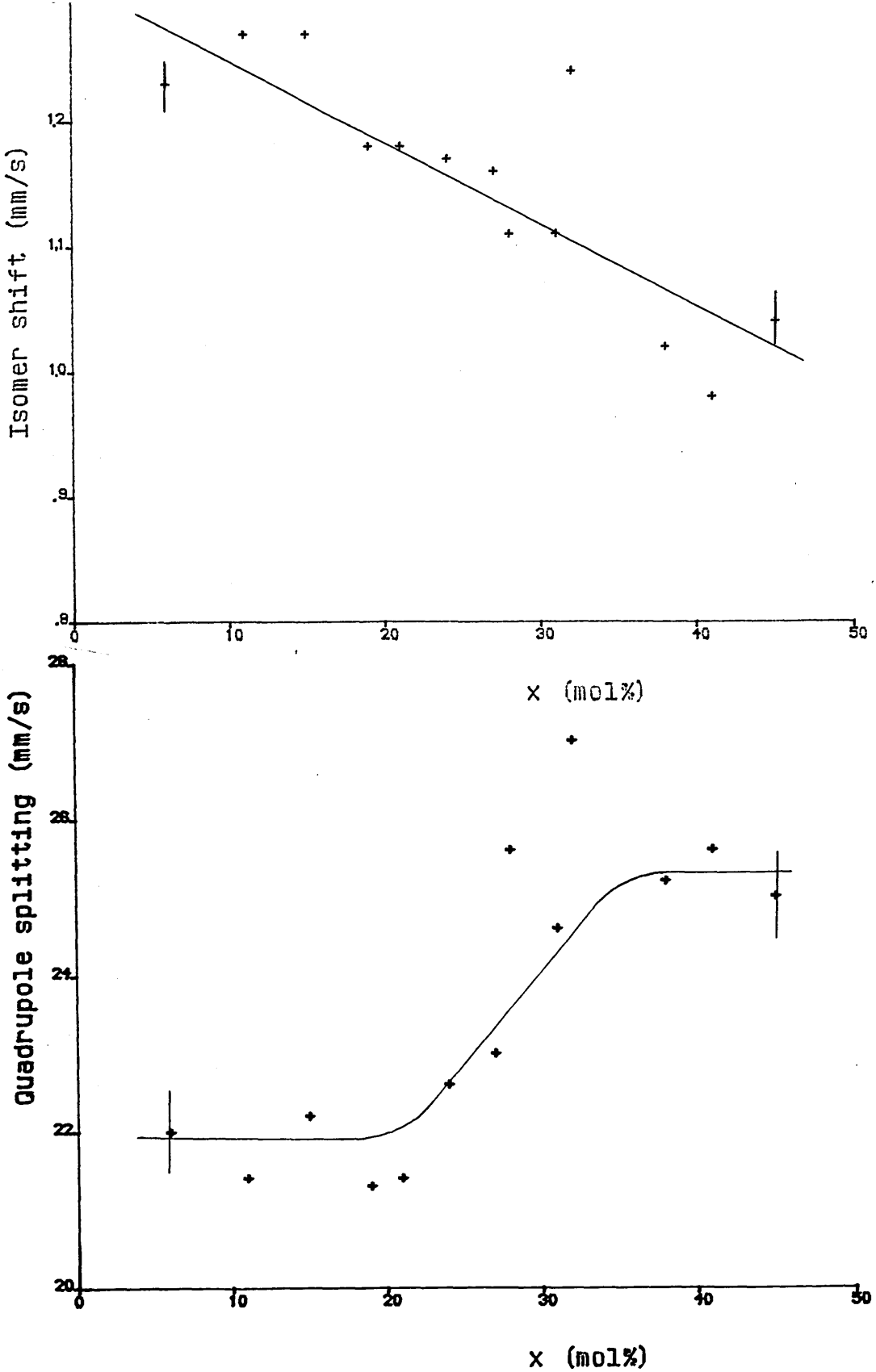

Figure 5.15 Compositional dependence of Fe^{2+} Mössbauer parameters for xNa_2O-20CaO-(78-x)P_2O_5-2Fe_2O_3 glass system

Addition of a modifying oxide, such as Na_2O, to a phosphate glass is known to lead to the formation of non-bridging oxygens (N.B.O.'s) (§1.3.1). These N.B.O.'s are able to coordinate with iron ions [4] and should lead to a decrease in both isomer shift and the lattice contribution to the quadrupole splitting $q_{lattice}$ [10,11]. The fact that the parameters for the ferric iron remained essentially constant indicate that N.B.O. does not effect the Fe^{3+} sites. However, the ferrous iron sites become more ordered as the number of N.B.O.'s is increased.

The Van Wazer theory [7] states that for network glasses (P_2O_5 > 50 mol.%) the addition of Na_2O should increase the glass durability because the ionic O-Na^+-O cross-links are less susceptible to hydrolysis than branched phosphate units. For linear polymer glasses ($P_2O_5 \leq 50$ mol.%) further Na_2O will lead to a shorter average phosphate chain length and thus a lower durability. These trends are contrary to the dissolution rate results (Fig. 5.13) which show that increasing the Na_2O content leads to less durable glass across both the network and linear polymer regions of the glass composition.

The difference between Van Wazers simple Na_2O-P_2O_5 glasses and these glasses is the additional presence of CaO and Fe_2O_3, both of which act as modifiers in phosphate glass. They will form strong cross links between phosphate groups (§1.3.2). The addition of Na_2O is seen from the Mössbauer results to lead to more steric ordering of the Fe^{2+} sites and also, by inference, more ordering of the Ca^{2+} sites since the Ca^{2+} has a similar ionic radius to Fe^{2+} and occupies the same type of network modifying sites. These more ordered Ca^{2+} and Fe^{2+} sites imply less flexibility in the geometry of the ionic

cross-linking between the phosphate chains. Hence the overall strength of the cross-linking may be reduced, leading to a less durable glass.

The Mössbauer spectrum of the ceramic (x=45) vividly shows the spectral differences between a micro-crystalline material and a glass (Fig. 5.16). The linewidths for the ceramic ($\Gamma \simeq$ 0.5 mm/s) are much narrower than for the glass (Γ = 1.1 mm/s) indicating the more regular atomic arrangement in the ceramic. The quadrupole splitting distribution profiles reinforce this view, with the ceramic giving much narrower profiles than the glass. The fact that the ceramic linewidth is not equal to the minimum experimental linewidth (Γ 0.23 mm/s) indicates that there are still a number of different iron sites, corresponding to a limited range of crystalline phases within the ceramic.

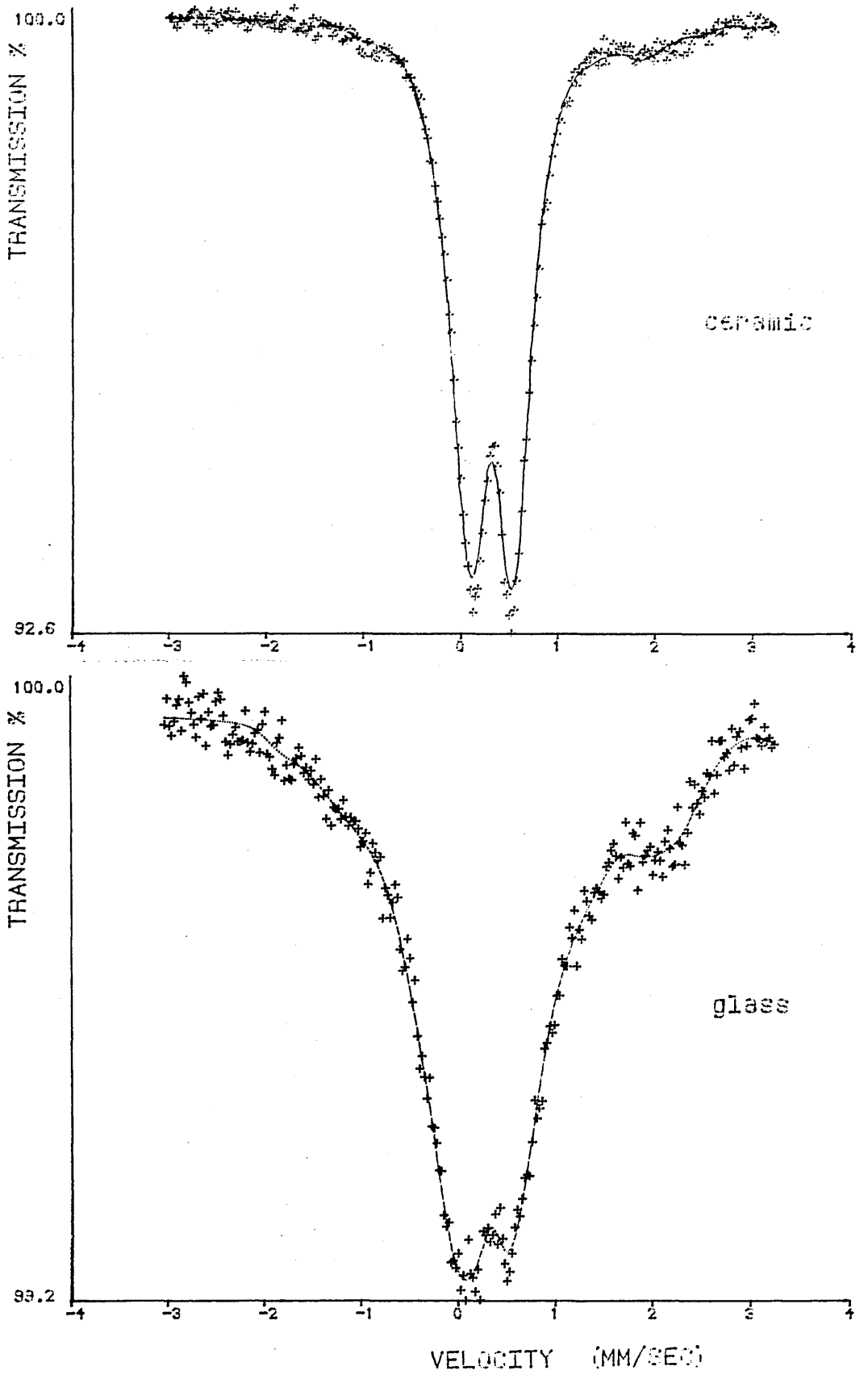

Figure 5.16a Room temperature Mössbauer spectra for ceramic (x=45) and glass (x=41) from the xNa_2O-20CaO-(78-x)P_2O_5-2Fe_2O_3 system Solid lines represent PQH fits to the data.

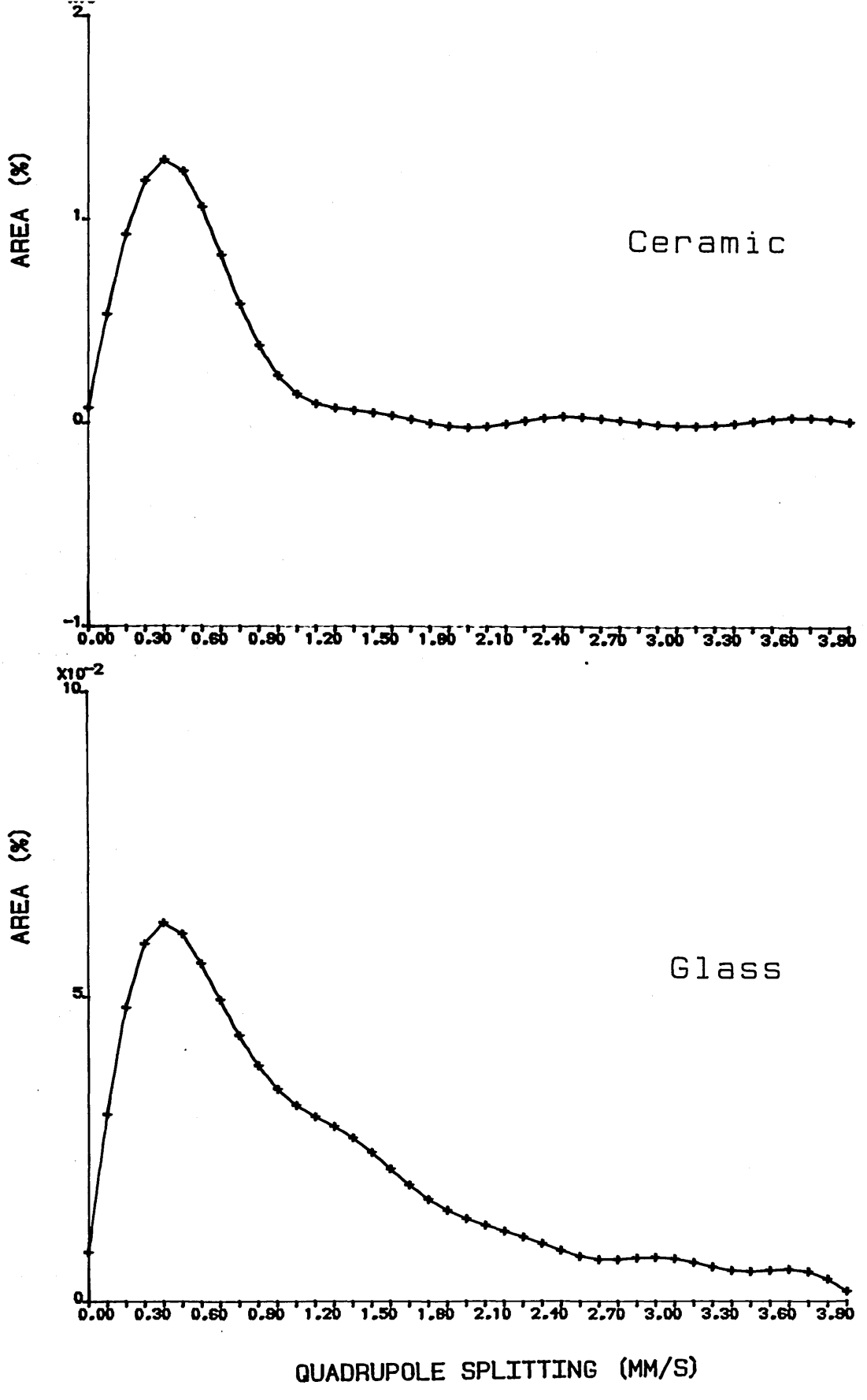

Figure 5.16b Ferric quadrupole doublet distributions for ceramic (x=45) and glass (x=41) from the xNa_2O-20CaO-$(78-x)P_2O_5$-$2Fe_2O_3$ system

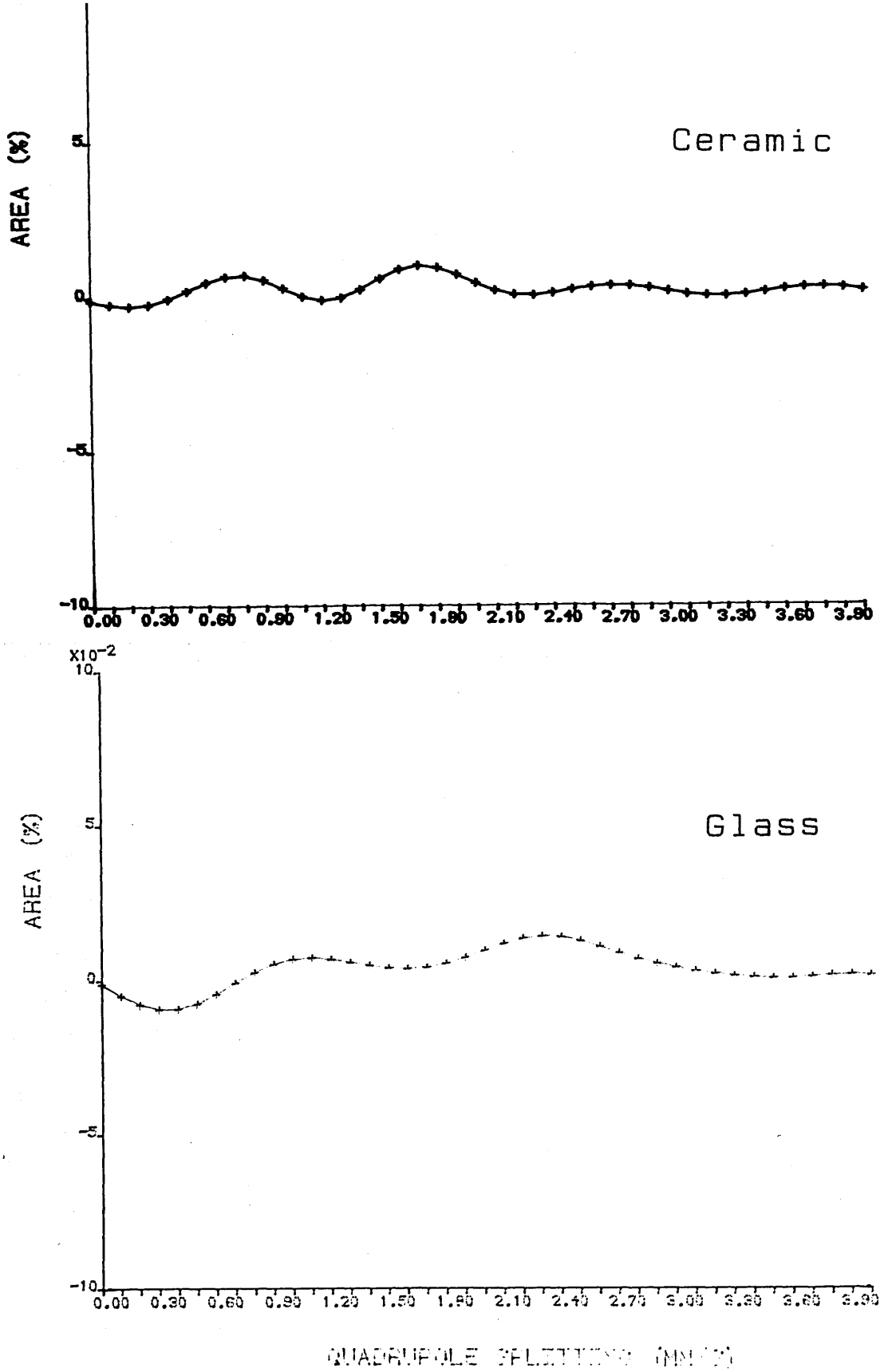

Figure 5.16c Ferrous quadrupole doublet distributions for ceramic (x=45) and glass (x=41) from the xNa_2O-20CaO-(78-x)P_2O_5-2Fe_2O_3 system

5.5 Variable temperature study of a calcium-sodium-iron-phosphate glass

A variable temperature study of the $32Na_2O$-$20CaO$-$46P_2O_5$-$2Fe_2O_3$ glass (GW14.2) has been carried out to complement the other investigations. The absorber contained an areal density of 2.5 x 10^{18} $^{57}Fe/cm^2$ which corresponds to a Mössbauer thickness $t \simeq 0.1$. The collection time for the spectra ranged from 4 days for the high temperature data points down to 2 days for the low temperature data points. This ensured that all the spectra had a similar signal/noise ratio. Despite the long run times the data was not of as high quality as for higher iron content glasses, thus the errors on the fitting parameters are substantially larger. With the exception of the Fe^{3+} isomer shift all the resultant temperature dependent data give a poor argument with theoretical curves, hence the calculated Debye temperatures and crystal field splittings are only qualitative.

ISODS (\$3.2.3.2) gives a Debye temperature θ_D = 565K for the ferric iron sites, whilst θ_D = 135K for ferrous iron (Fig. 5.17). LNAT (\$3.2.2.2) leads to a much lower Debye temperature θ_D = 285K from the total absorption area data (Fig. 5.18) and similar values for the ferrous and ferric iron sites. The quadrupole splitting of the ferric iron doublet showed a steady decrease with increasing temperature, the gradient being -3.6 x 10^{-4} mm/sK. The ferrous doublet splitting also decreased with temperature (Fig. 5.19) and was fitted to the crystal field model (\$4.2.4) yielding splittings of Δ_1 = 385 cm^{-1}, Δ_2 = 770 cm^{-1} and a lattice contribution $\Delta E_Q(lat)$ = 1.29 mm/s.

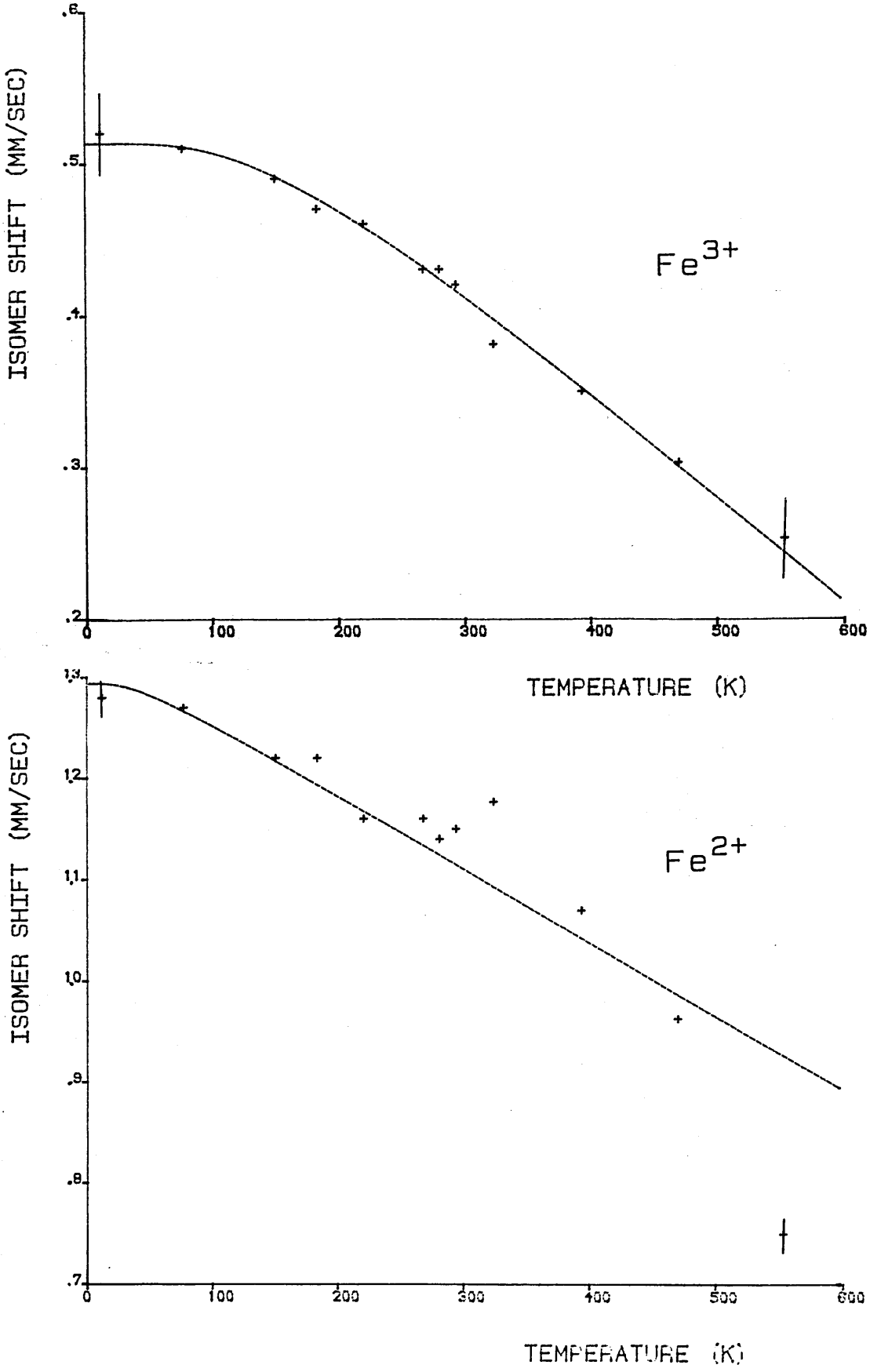

Figure 5.17 Temperature dependence of Fe^{3+} and Fe^{2+} isomer shift for GW14.2

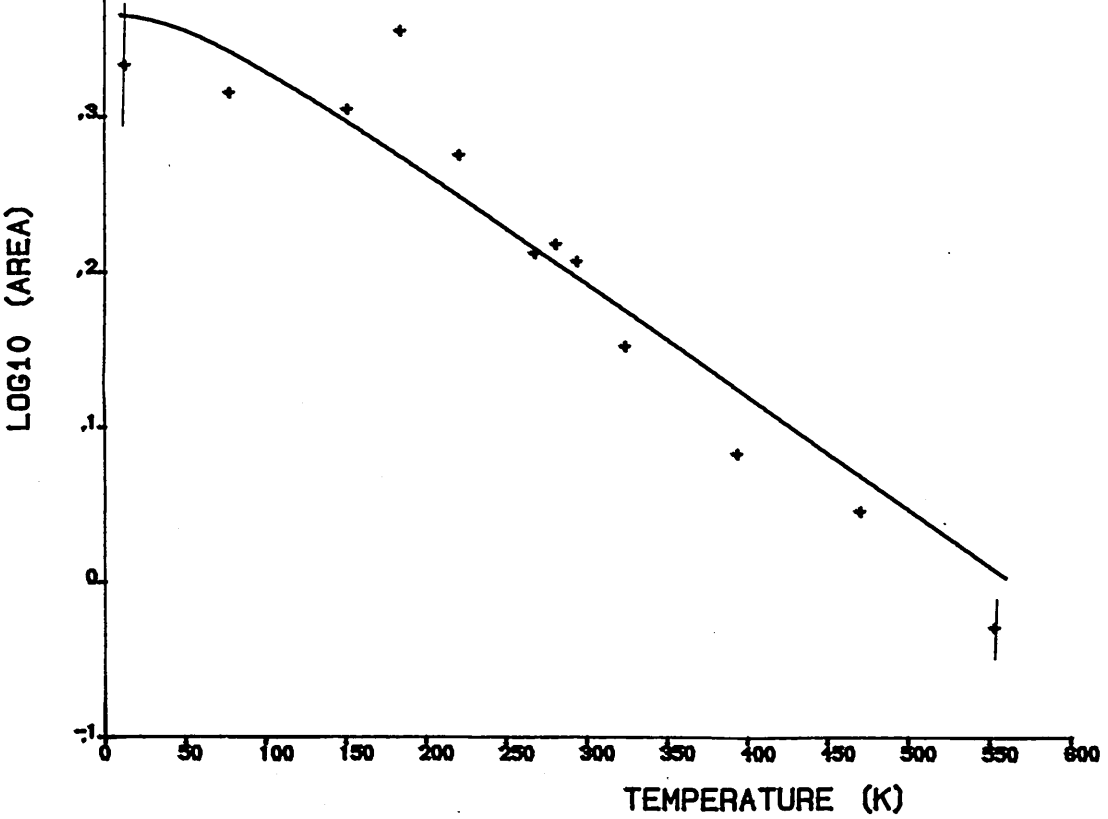

Figure 5.18 Temperature dependence of the total absorption area data for GW14.2

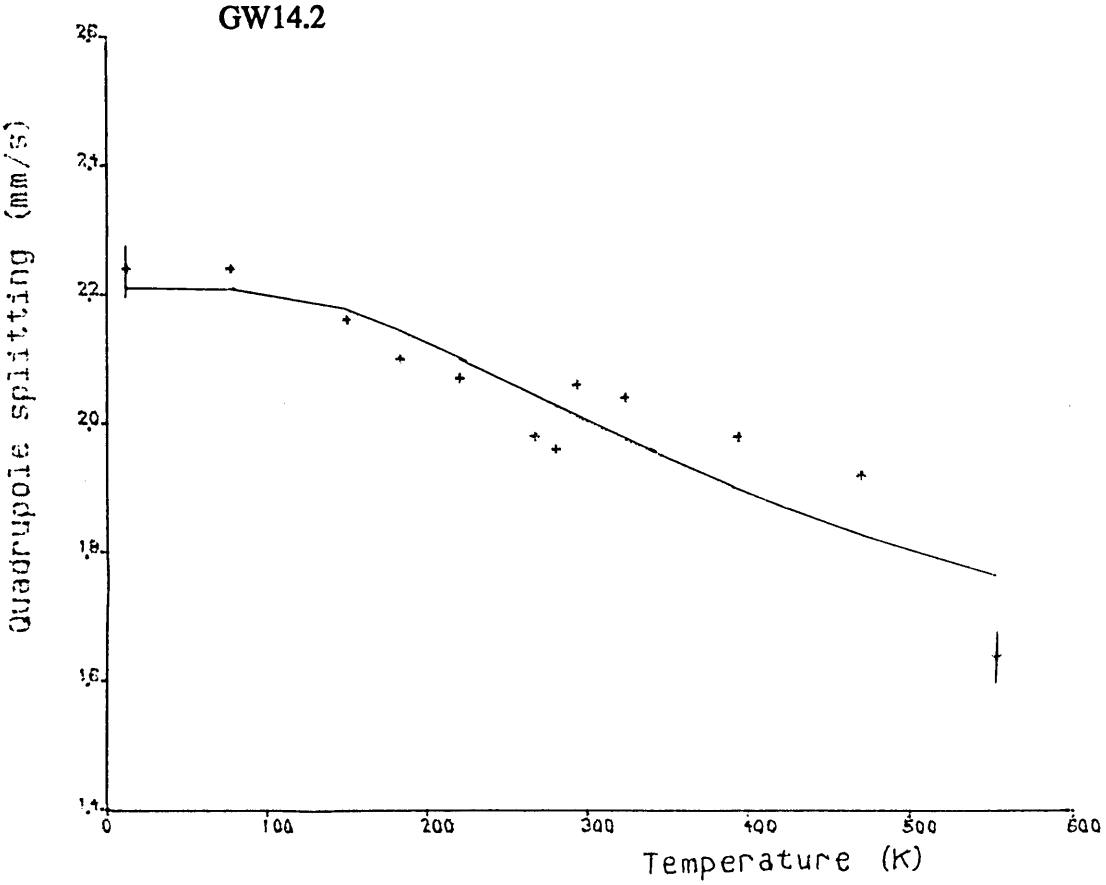

Figure 5.19 Temperature dependence of the Fe^{2+} quadrupole splitting for GW.14.2

The variable temperature studies of the three glass compositions have yielded remarkably consistent parameters for the iron sites. The isomer shift data leads to a Debye temperature $\theta_D \simeq$ 530K for the Fe^{3+} sites and $\theta_D \simeq$ 140K for the Fe^{2+} sites. This compares to values of $\theta_D \simeq$ 290K for the Fe^{3+} sites and $\theta_D \simeq$ 260K for the Fe^{2+} sites derived from the absorption area data. The crystal field splittings of the Fe^{2+} orbital energy levels are $\Delta_1 \simeq 360$ cm^{-1} and $\Delta_2 \simeq 720$ cm^{-1}; with a lattice contribution to the total quadrupole splitting $\Delta E_Q(lat) \simeq 1.4$ mm/s. The Fe^{3+} sites also show a temperature dependent quadrupole splitting with a gradient $g \simeq -4 \times 10^{-4}$ mm/sK.

The consistency of the results indicates that there is no significant difference in the bonding of the iron sites in the three glass compositions. The ferric iron sites exhibit higher Debye temperatures than the ferrous iron sites indicating that they are more rigidly bound within their distorted octahedral oxygen cages. The Fe^{3+} sites also show a lower $\Delta E_Q(lat)$ contribution indicating that they are more ordered than the Fe^{2+} sites.

5.6 References

1. Westman A.E.R.; Gartaganis P.A.

   Journal of the American Ceramic Society, 40(9), 293, 1957

2. Paul A.

   'Chemistry of Glasses', Chapman and Hall, 1982, p.117

3. Murthy M.K.; Smith M.J.; Westman A.E.R.

   Journal of the American Ceramic Society, 44(3), 97, 1961

4. Nishida T.; Shiotsuki T.; Takashima Y.

   Journal of Non-Crystalline Solids, 43, 115, 1981

5. Nishida T.; Shiotsuki T.; Takashima Y.

   ibid. 43, 123, 1981

6. Drake C.F.

   Vitreous controlled release fertiliser composition.

   British Patent 1 512 637, 1978

7. Van Wazer J.R.

   'Phosphorous and its compounds. Volume 1 : Chemistry', Interscience, 1958, p.270

8. Ingalls R.

   Physical Review, 133A(3), 787, 1964

9. Menil F.; Fournes L.; Dance J.M.; Videau J.J.

   Journal of Non-Crystalline Solids, 34, 209, 1979

10. Nishida T.; Takashima Y.

Journal of Non-Crystalline Solids, 37, 37, 1980

11. Tanaka K.; Hirao K.; Soga N.

Journal of Non-Crystalline Solids, 85, 228, 1980

CHAPTER SIX - SURFACE STUDIES

6.1 Introduction

In order to complement the dissolution rate studies two analytical techniques were used to examine the near surface regions of the iron-phosphate glasses. The first was backscatter ^{57}Fe Mössbauer spectroscopy (§6.2) and the second was secondary ion mass spectrometry (§6.3). These studies were made on glasses both before and after degradation in water, the aim being to monitor any changes which may occur in the glass surface as part of the dissolution process.

6.2 Backscatter Mössbauer Spectroscopy

6.2.1 Theory and Experimental Details

Chapter Two contains a discussion of the detection and energy spectra of γ-rays emitted from an excited state Mössbauer nucleus. However, the I = 3/2 → I=1/2 transition in ^{57}Fe possesses a large internal conversion coefficient α = 8.21 [1],hence 90% of the excited state nuclei decay via mechanisms which do not result in the emission of a 14.4 keV γ-ray (Table 6.1). The primary decay mechanism involves the reabsorption of the γ-rays by an inner (K) electron shell and the subsequent emission of 7.3 keV conversion electrons, together with associated 6.3 keV X-rays and Auger electrons.

Table 6.1 The principle decay products of an excited state ^{57}Fe nucleus.

Emitted particle/quanta	Energy keV	Probability (per absorption event)
γ - ray	14.4	0.09
K-shell conversion electron	7.3	0.81
L-shell conversion electron	13.6	0.09
M-shell conversion electron	14.3	0.01
K X-ray	6.3	0.27
KLL Auger electron	5.4	0.63
LMM Auger electron	0.53	0.01

The electron flux is rapidly attenuated by non-resonant scattering processes within the absorber. This results in a maximum range of ~300nm for the 7.3 keV conversion electrons [2] and a slightly smaller range for the 5.4 keV Auger electrons. Detection of these two electrons hence gives information about the near surface region of the sample. For each decaying nucleus 1.55 electrons are emitted compared to 0.09 γ-rays (Table 6.1) thus there is a potential seventeen fold increase in the percentage effect by detecting the conversion and Auger electrons. The electrons escaping from the absorber surface are further statistically weighted such that approximately two thirds result from resonance fluorescence within the top 50nm of the sample [3]. The 6.3 keV conversion X-rays are much more penetrating with a maximum range ~ 10 μm [2], thus they give information from a quasi-surface layer.

A simple conversion electron Mössbauer spectroscopy (C.E.M.S.) detector can be made by mounting the absorber material under study inside the chamber of a helium/methane gas proportional counter, as in Figure 6.1. Altering the gas to a more easily ionised argon/methane mixture enables conversion X-rays to be detected. With this system it is not easy to vary the sample temperature because of thermal insulation problems, hence other detectors such as channel electron multipliers are often used. The channeltron must operate in a vacuum, hence it becomes practicable to vary the sample temperature. A channeltron detector system has been developed at Sheffield City Polytechnic which includes a hemispherical copper mesh above the mouth of the channeltron (Fig. 6.2). Application of a 100V potential to this grid focuses electrons towards the channeltron and results in a four fold increase in counting efficiency [4]. The vacuum system attached to the detector is at present inadequate to permit low temperature spectra to be recorded as there is a rapid build up of an ice layer on the absorber surface which blocks the emission of conversion electrons. This is graphically illustrated by the spectra of an α-Fe foil (Fig. 6.3). Contrary to the known temperature dependence of the recoil-free fraction the 80K spectrum is of a much poorer quality than the room temperature spectrum. An improved vacuum system permitting a residual pressure of $\sim 10^{-7}$ Torr [5] would solve this icing problem.

The surface sensitivity of the C.E.M.S. technique can be improved by the use of high energy resolution electron detectors [6] since the emitted electron energy is a function of the depth at which it was formed. The surface can also be probed by the detection of totally externally reflected γ-rays [7]. These advanced methods have allowed surface layers as thin as 3nm to be studied.

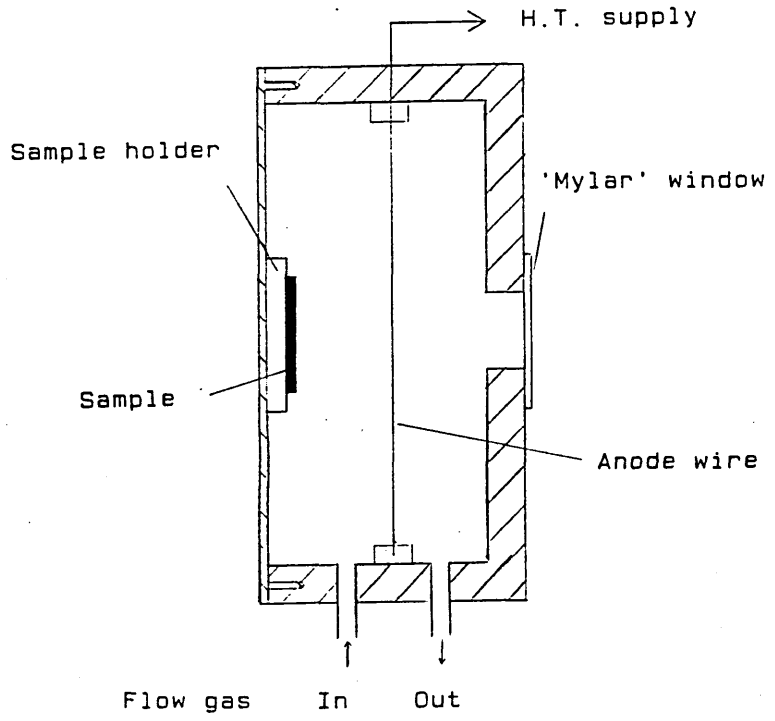

Figure 6.1 Cross-section of a C.E.M.S. proportional counter detector.

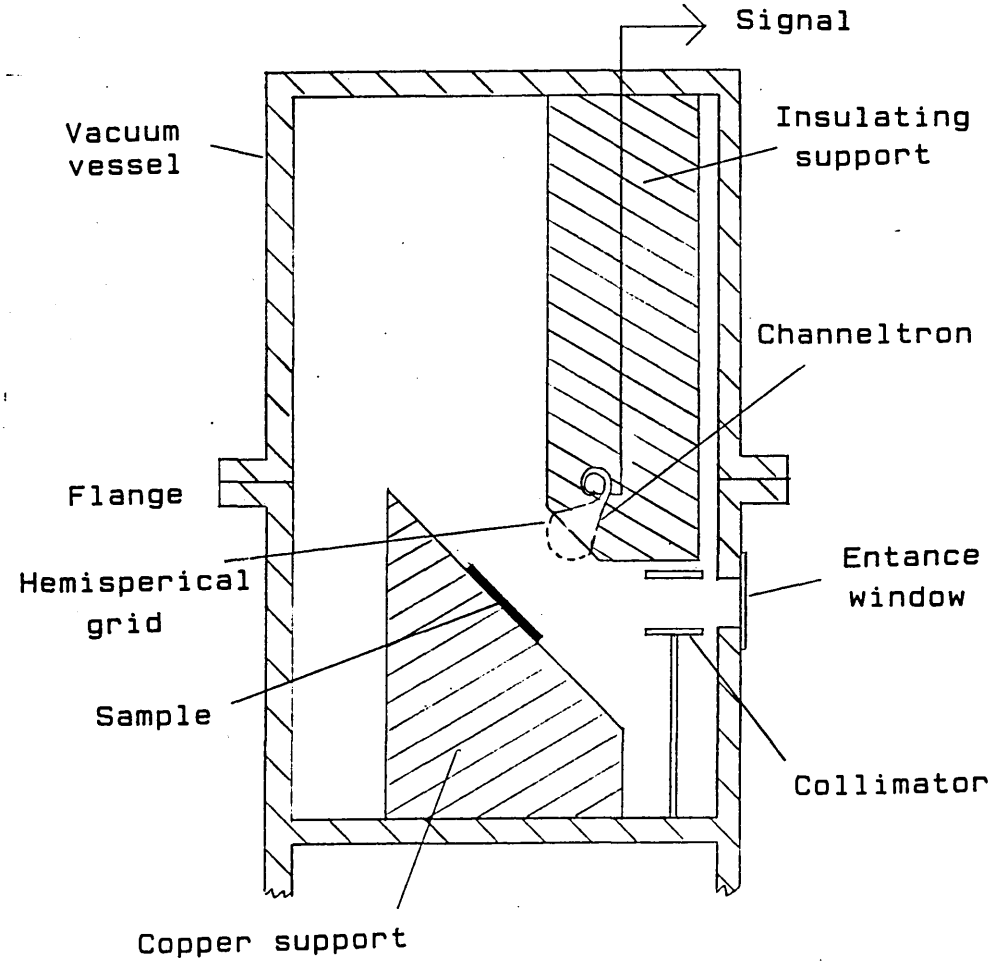

Figure 6.2 Cross-section of a C.E.M.S. channeltron detector

Room temperature spectra of iron-phosphate glasses have been recorded primarily using the He/CH_4 detection system. Most absorbers consisted of thin glass sheets, although some spectra have been recorded of powdered glass held in place using double sided adhesive tape.

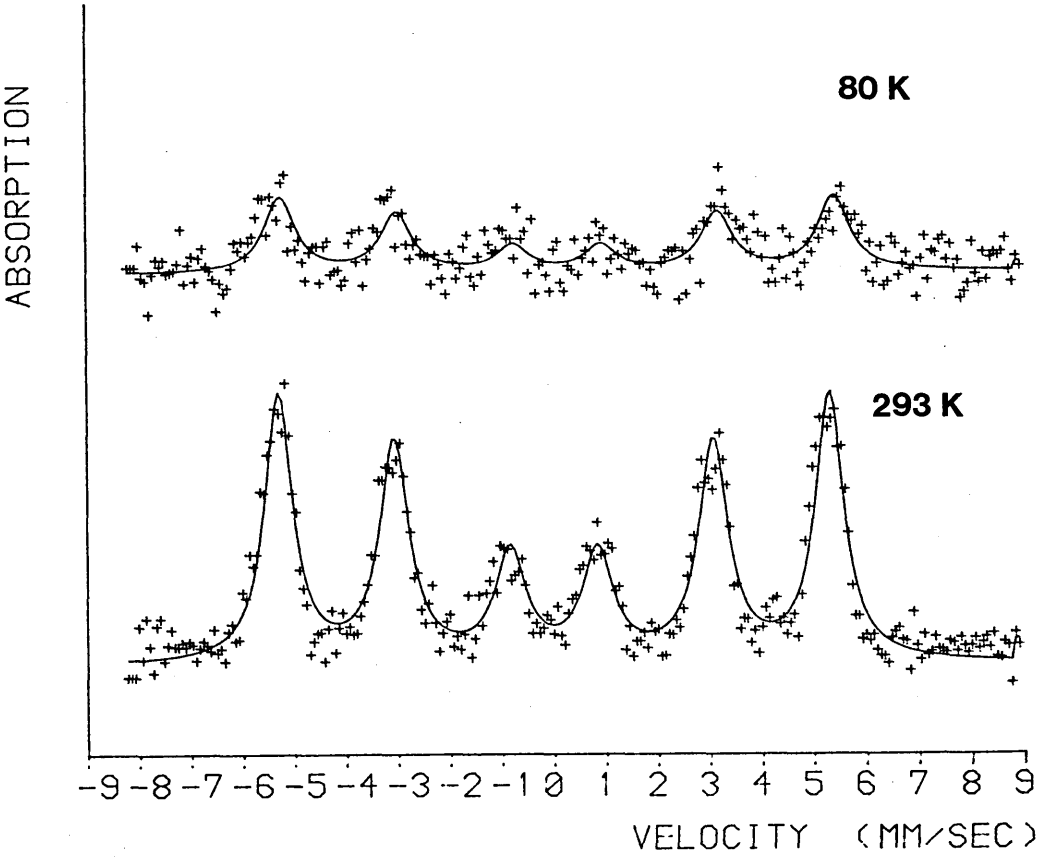

Figure 6.3 C.E.M.S. spectra of an α-Fe foil recorded using a Channeltron detector at a residual pressure of 10^{-5} Torr.

6.2.2 C.E.M.S. Studies of Iron-Phosphate Glasses

Initial backscatter studies were performed on a glass with a relatively high iron content: $25Na_2O$-$13K_2O$-$43P_2O_5$-$19Fe_2O_3$ (J3). The smooth surface of the 5mm thick glass plate was swabbed with acetone immediately prior to placing in the detector chamber in order to remove any grease layer. A collection time of four days resulted in the C.E.M.S. spectrum shown in Figure 6.4. The backscatter spectrum has, within error, identical Mössbauer parameters

(Table 4.2) to the transmission mode spectrum of a 'thin' absorber prepared by powdering the original glass and dispersing in graphite. Due to differences in geometry, velocity range and source strength it is not possible to compare the statistics of the two fits to the data.

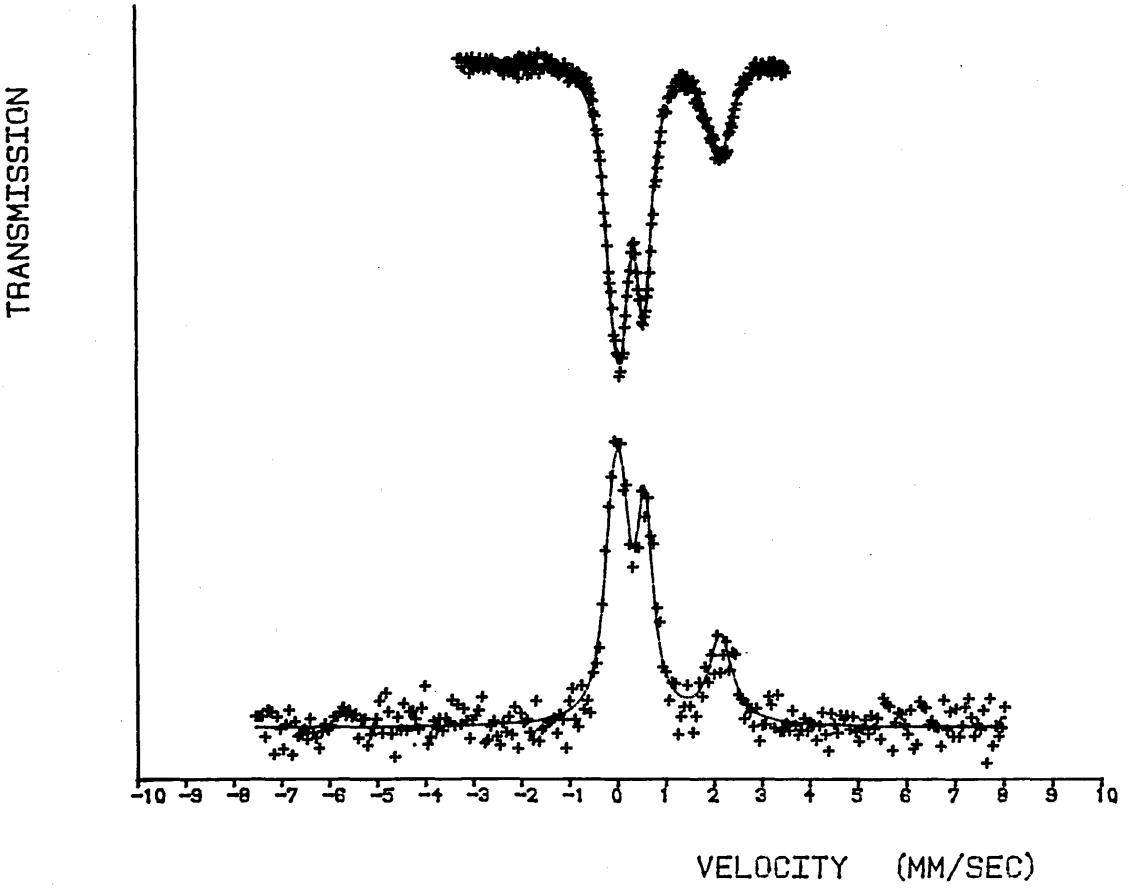

Figure 6.4 Transmission and C.E.M.S. spectra of an iron-phosphate glass (J3)

The Fe^{3+}/Fe^{2+} ratios are identical (3 : 2) in these two spectra (Fig. 6.4) suggesting that the glass has not suffered any surface oxidation. This result is contrary to the findings of Biñczycka and Sawicki [8] for a $10MgO\text{-}50P_2O_5\text{-}40FeO$ glass. Using C.E.M.S. they detected an enhancement of the Fe^{3+}/Fe^{2+} ratio in the surface region of the glass which they attributed to atmospheric oxidation of Fe^{2+} to Fe^{3+}. They found that the Fe^{3+}/Fe^{2+} ratio pertaining to

the bulk glass could be restored to the surface region by heating the glass in vacuo or by polishing the glass to produce a fresh surface.

Detecting the conversion X-rays (C.X.M.S.) from J3 resulted in a spectrum identical in shape to the C.E.M.S. transmission mode spectra. The percentage effect obtained with the C.X.M.S. spectrum was significantly larger than for the C.E.M.S. spectrum, despite the much lower probability of a given ^{57}Fe nucleus decaying to yield a conversion X-ray (Table 6.1). This result was due to a higher X-ray detection efficiency and the much greater range ($\sim 10\,\mu m$) resulting in a large X-ray flux.

In order to compare the quality of C.E.M.S. spectra it is essential that they are recorded under identical operating conditions. To this end the source-absorber geometry was kept constant and the anode H.T. was fixed at +1300V. A low level discriminator was used to reduce low energy amplifier noise in the pulse height spectrum whilst no upper limit was placed on the pulse height admitted to the M.C.A.

C.E.M.S. spectra of glass powders consistently gave better counting statistics than C.E.M.S. spectra of glass plates (Fig. 6.5). This was presumably due to the larger surface area of the powdered sample which would result in more backscattered electrons. An alternative explanation may involve the electrostatic charging of the glass which detrimentally effects the collection of electrons from the glass plate to a greater extent than from the powdered glass.

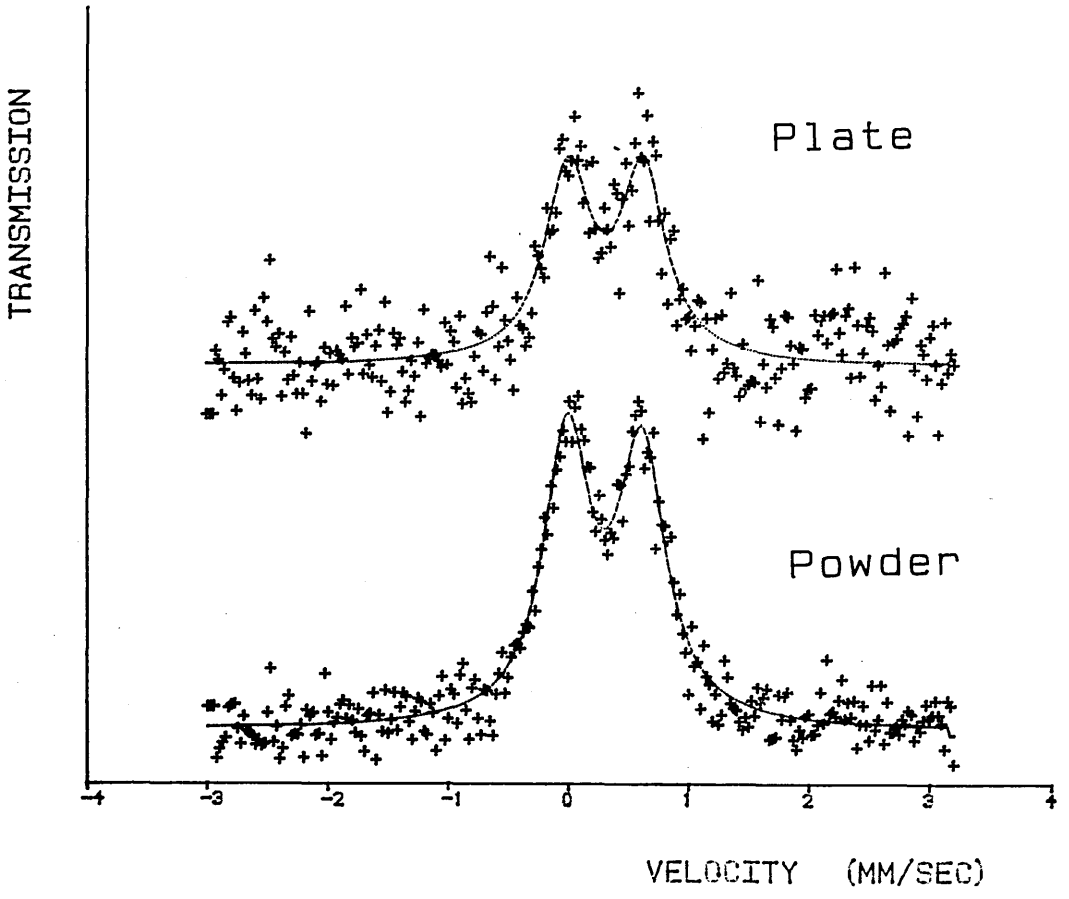

Figure 6.5 C.E.M.S. spectra of an iron-phosphate glass (GW22.4) in the form of a glass plate and a powder

The poor quality of much of the C.E.M.S. data meant that the Fe^{2+} component of the spectra was often lost in the background noise. This was especially true for the lower iron content glasses such as GW22.4 ($31Na_2O$-$61P_2O_5$-$8Fe_2O_3$) and in glasses with high Fe^{3+}/Fe^{2+} ratios. This severely limited the use of the C.E.M.S. technique to examine any changes occurring in the glass surface when degraded in water. The Mössbauer parameters describing C.E.M.S. spectra of glasses after immersion in water for a number of days where, without exception, indistinguishable from original spectra parameters. This was true of both leached powders and glass plates.

Despite the monotony of the Mössbauer parameters there was a consistent decrease in the percentage effect obtained from the leached glass spectra when compared to the unleached glass spectra (Fig. 6.6). This implies the C.E.M.S. analysis detects less iron in the leached glass than in the unleached glass. A number of explanations seem plausible:

Firstly, the observation may indeed indicate less iron in the surface of the leached glass. This is not unreasonable as the network modifying iron must pass into solution before the phosphate chains can free themselves from the glass network.

Secondly, there may be some modification of the iron sites by penetrating water molecules which weakens the binding of the iron ions to the phosphate chains, hence lowering the recoil-free fraction and resulting in a lower percentage effect.

Thirdly, the leached glasses may not have been satisfactorily dried before analysis, hence residual water would be present in the absorber which could effect the electron detection efficiency. This seems unlikely as the glass powders were thoroughly rinsed in acetone and then allowed to dry prior to analysis.

An attempt was made to detect surface changes by use of transmission mode Mössbauer spectroscopy. The spectra of a size graded glass powder (diameter ≤ 53 μm) were recorded before and after degradation in water. No differences could be discerned between the spectra, presumably because of the high (bulk volume)/(modified surface volume) ratio of the leached glass grains

which would result in the signal from the surface region being masked by the larger signal from the bulk.

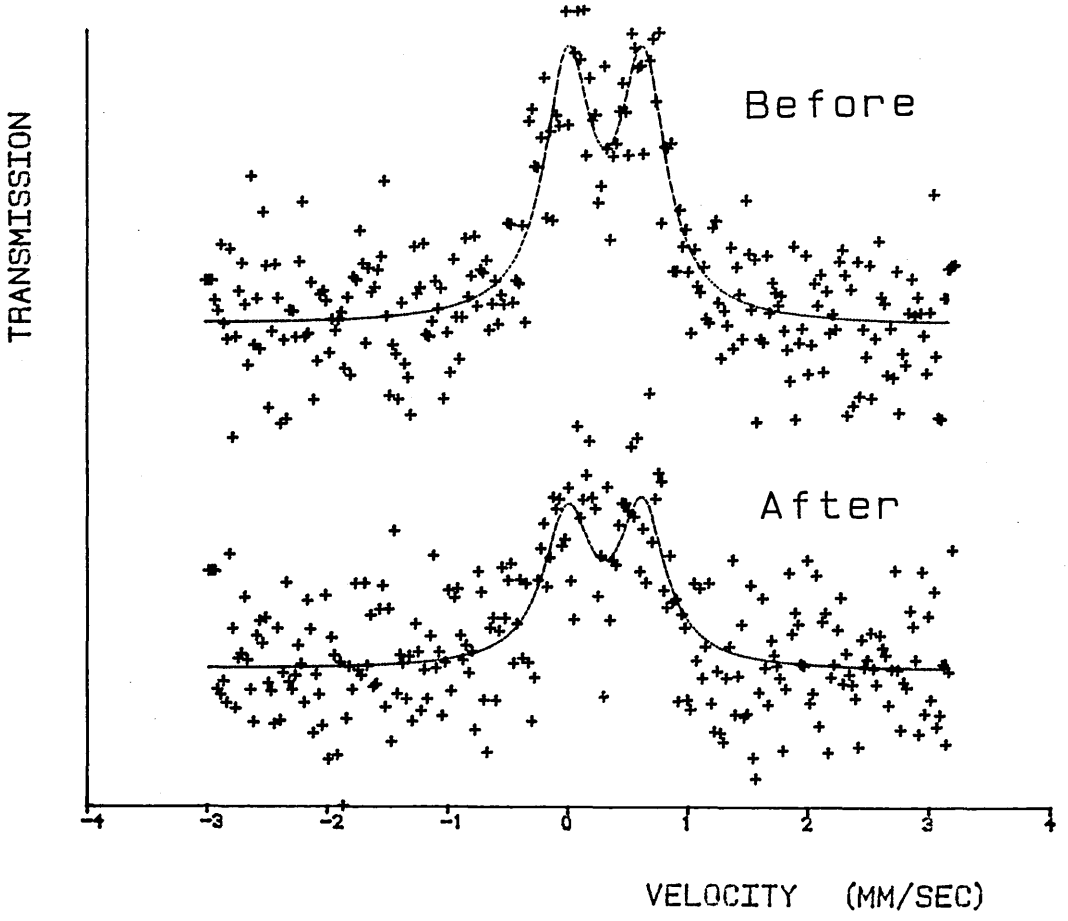

Figure 6.6 C.E.M.S. spectra of an iron-phosphate glass (GW22.4) before and after immersion in water for four days.

6.3 Secondary Ion Mass Spectrometry

6.3.1 Introduction and Experimental Details

Secondary ion mass spectrometry (S.I.M.S.) is a powerful technique for investigating the chemical nature of solid surfaces [9]. The method consists of the mass analysis of the particles which are ejected from a solid surface when it is bombarded with an energetic ion beam. The primary beam commonly consists of noble gas ions in order to minimise the chemical modification of the sample under analysis. The secondary particles which are knocked out of

the sample will be both atomic and molecular species. They will exist as positive and negative ions as well as electrically neutral particles. They can be analysed as function of mass/charge to produce a mass/charge spectrum of the sputtered ions in a similar way to conventional mass spectrometry.

If low primary ion current densities are used (I ~ 1nA/cm^2) the sample surface suffers little disturbance and the resultant SIMS spectrum gives information about the top few monolayers of the material. This is known as 'static SIMS'. Using liquid metal ion guns, which have a beam resolution of ~100nm, it is possible to build up a secondary ion map of the sample surface by raster scanning the primary beam. This technique of 'imaging SIMS' finds many uses in the field of microelectronics. In 'dynamic SIMS' a higher flux of primary ions is used. The sample surface is rapidly eroded, enabling composition/depth profiles to be derived.

The availability of a V.G. Microlab surface analysis instrument at Sheffield Polytechnic has allowed the static and dynamic SIMS analysis of some iron-phosphate glasses.

The primary ion beam was provided by an argon ion gun which had a minimum spot diameter of 2μm. For all the analyses a primary beam of 5 keV Ar^+ions was chosen, with beam currents ranging from 1nA for static SIMS upto 100nA during the ablation phase of the dynamic SIMS analysis. For dynamic SIMS the beam was rastered over an area of ~1mm^2. The mass analyser, a quadrupole mass spectrometer, was gated so that it only took information from the central region of the crater. This avoided spectral interference from the crater side walls. The schedule for the dynamic SIMS

analysis consisted of 10 seconds counting on each of the number of specified mass/charge numbers followed by 60 seconds etch with a high beam current. Upto 50 cycles of this procedure were performed, which was sufficient to encompass the surface region of the glass.

Due to the low conductivity of oxide glasses efforts must be made to prevent surface charging during SIMS analysis. This can be achieved by the evaporation of a thin conducting gold layer onto the sample, as with scanning electron microscopy, or by flooding the surface with low energy electrons. For these studies an electron flood gun operating with an emission current of 10nA has been used. The secondary ion yield is very sensitive to the oxygen partial pressure at the surface [10]. Even for the inherently high oxygen content phosphate glasses the use of an oxygen flood gun was found to further enhance the secondary ion yield.

A major problem with dynamic SIMS is the conversion of etch time (s) into crater depth (mm). A lot of data exists on the pure element sputtering yields (= secondary ions per primary ion) under various experimental conditions [11], however, for complex materials such as a glass no sputter yield data is available and it is necessary to adopt an empirical method. This usually consists of the mechanical measurement, using a stylus instrument, of the crater depth produced under known operating conditions [12,13]. This depth calibration technique has been employed in the examination of corroded nuclear waste glasses [14].

Etching of an optically flat silicate glass slide under the dynamic SIMS operating conditions stated above yielded a crater corresponding to an etch of

~ 0.5μm/h [15]. This is in close quantitative agreement with an etch rate of ~ 3 μm/h obtained with a 500nA primary beam current on a complex lead-silicate glass [14]. In the absence of etch rate data for a phosphate glass the figure of 0.5μm/h has been used in these studies.

6.3.2 SIMS analysis of iron-phosphate glasses

SIMS has been used to study a number of iron-phosphate glasses before and after their degradation by water. Each glass sample, in the form of a flat plate, was mounted on a copper stud and swabbed with acetone prior to insertion into the instrument. A period for outgassing was enforced before the sample was transferred to the analysis chamber which operates under an ultra high vacuum (pressure ~ 10^{-10} Torr).

Typical static SIMS spectra are shown in Figures 6.7, 6.8. The majority of the peaks are easily identified, corresponding to the various positive and negative ions expected from the glass. In addition there are a number of extra peaks. In the positive ion spectrum (Fig. 6.8) the peak at 41 amu/e corresponds to the primary bombardment ion Ar^+, whilst in the negative ion spectrum (Fig. 6.7) the two large peaks at 35 and 37 amu/e correspond to the two stable isotopes of chlorine. The chlorine is present as a volatile contaminant of the sample surface and the analysis chamber.

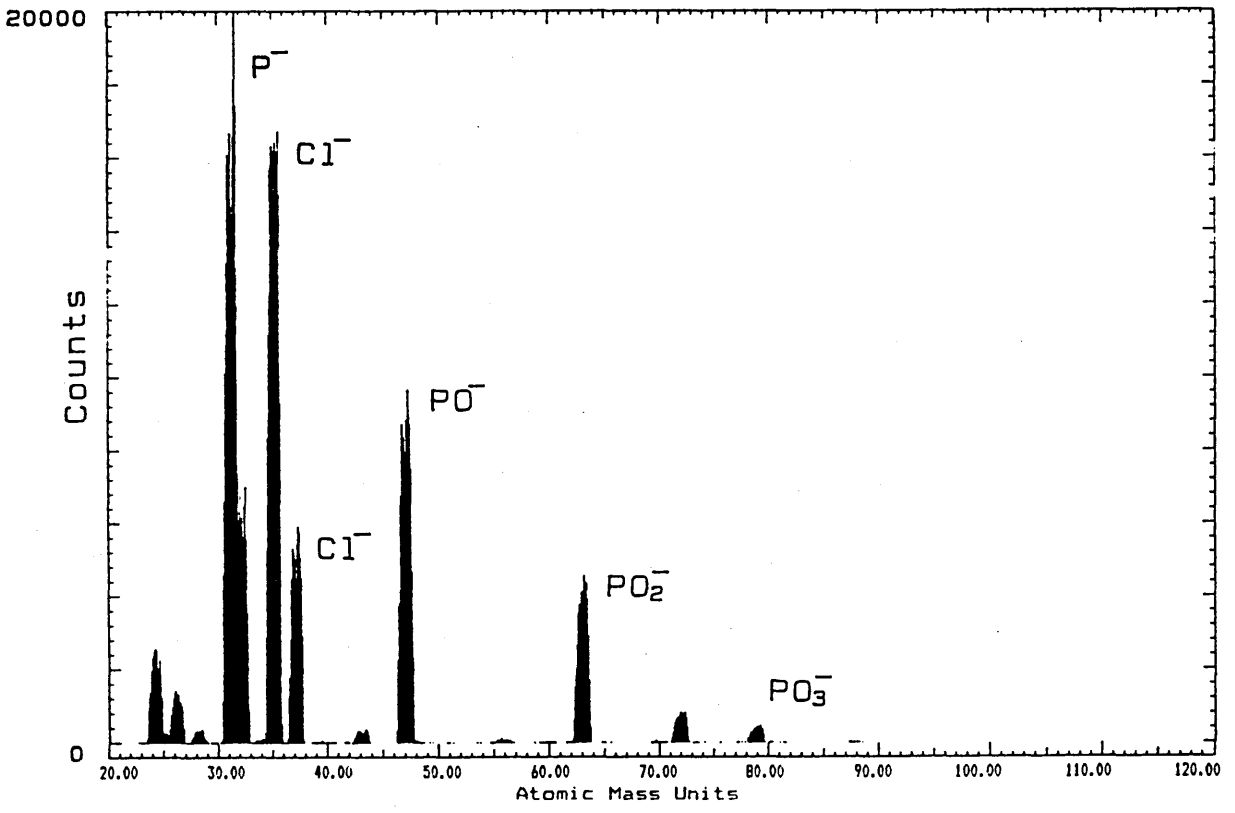

Figure 6.7 Negative ion static SIMS spectrum of $17K_2O$-$16Na_2O$-$59P_2O_5$-$8Fe_2O_3$ glass plate.

The mass spectrometer, operating with a mass/charge interval of 0.2 amu/e, is able to resolve the main isotopes of iron and gives a semi-quantitative analysis of their abundance: ^{54}Fe(6%); ^{56}Fe(92%); ^{57}Fe(2%). However, this quantitative nature is not easily extended to comparisons between the various elements because of different sputter yields [16]. Little or no sign of the ions expected from combined water (H^+, OH^-, H_3O^+) could be detected in the static SIMS spectra of leached glass samples. The spectra were essentially the same as for the unleached glasses. This suggests that water does not penetrate far below the glass surface during the dissolution process and is instead confined to the top few monolayers.

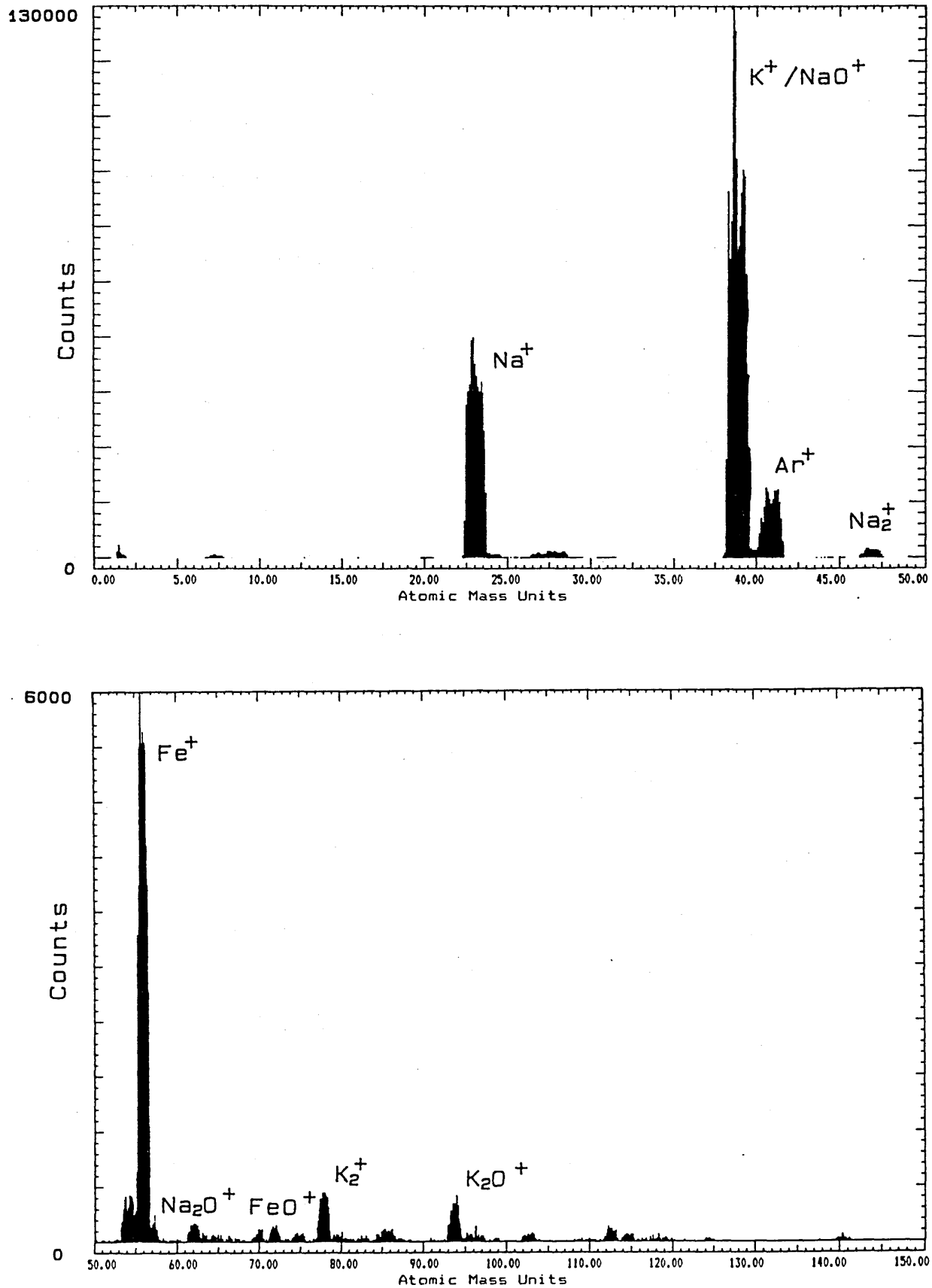

Figure 6.8 Positive ion static SIMS spectra of $17K_2O$-$16Na_2O$-$59P_2O_5$-$8Fe_2O_3$ glass plate.

The recording of accurate dynamic SIMS composition/depth profiles of iron-phosphate glasses proved difficult. The value of the emission current from the electron flood gun was crucial in avoiding charge build up on the sample, which dramatically altered the count rate. Charging of the surface also effected the etch rate and thus caused the profiles to depart from a linear scale. These factors, coupled with the lack of an etch rate calibration for glasses of this type (§6.3.1), means that the composition/depth profiles can only serve of a rough approximation to the actual surface characteristic of the glass. Considerably more time on the instrument would have been necessary to fully solve these problems.

The composition/depth profiles of selected mass numbers from a leached iron-phosphate glass are given in Figures 6.9, 6.10. The negative ion spectrum (Fig. 6.10) clearly shows the chlorine contamination down to a depth of ~ 40nm. The presence of chlorine below this level is due to contamination of the analysis chamber and possibly a low level impurity of the glass. The count rates for the various phosphorus-oxygen ions remain essentially constant indicating, as would be expected, a constant phosphorus concentration within the glass. The low count rates over the first couple of cycles were a common feature of all the depth profiles and are not thought to have any physical significance. The sharp troughs in the count rates at ~ 250nm and ~ 320nm are assumed to be instrumental fluctuations.

The positive ion depth profile of the same glass shows severe depletion of sodium and iron from the top ~ 60nm of the glass. Below this depth the two profiles quickly level off. This depletion of modifying cations from the glass surface is exactly as expected from the simple glass dissolution mechanism (§1.3.2) and has also been observed using SIMS in complex nuclear waste glasses [14].

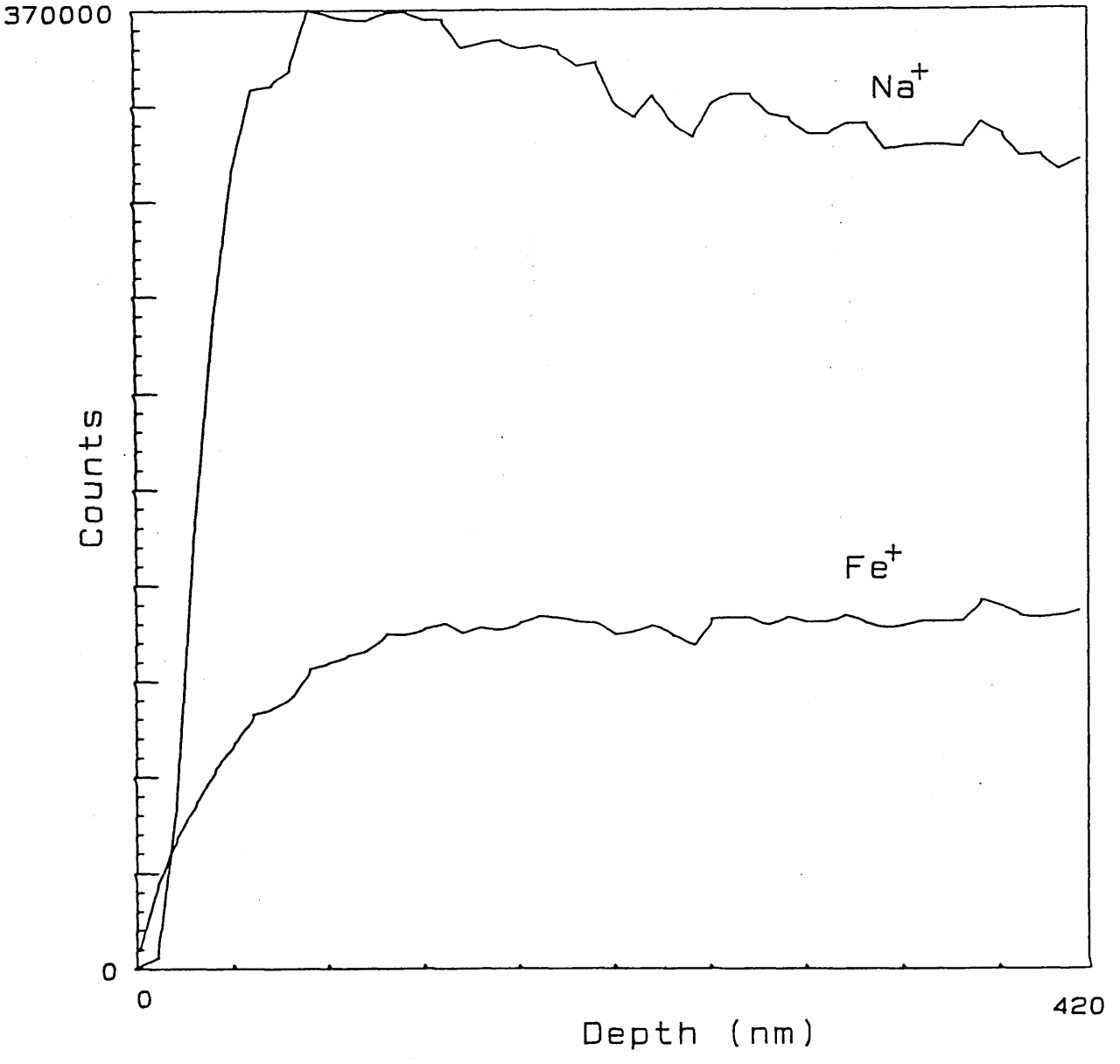

Figure 6.9 Positive ion dynamic SIMS depth profile of $43Na_2O$-$49P_2O_5$-$8Fe_2O_3$ glass after 4 days immersion in water

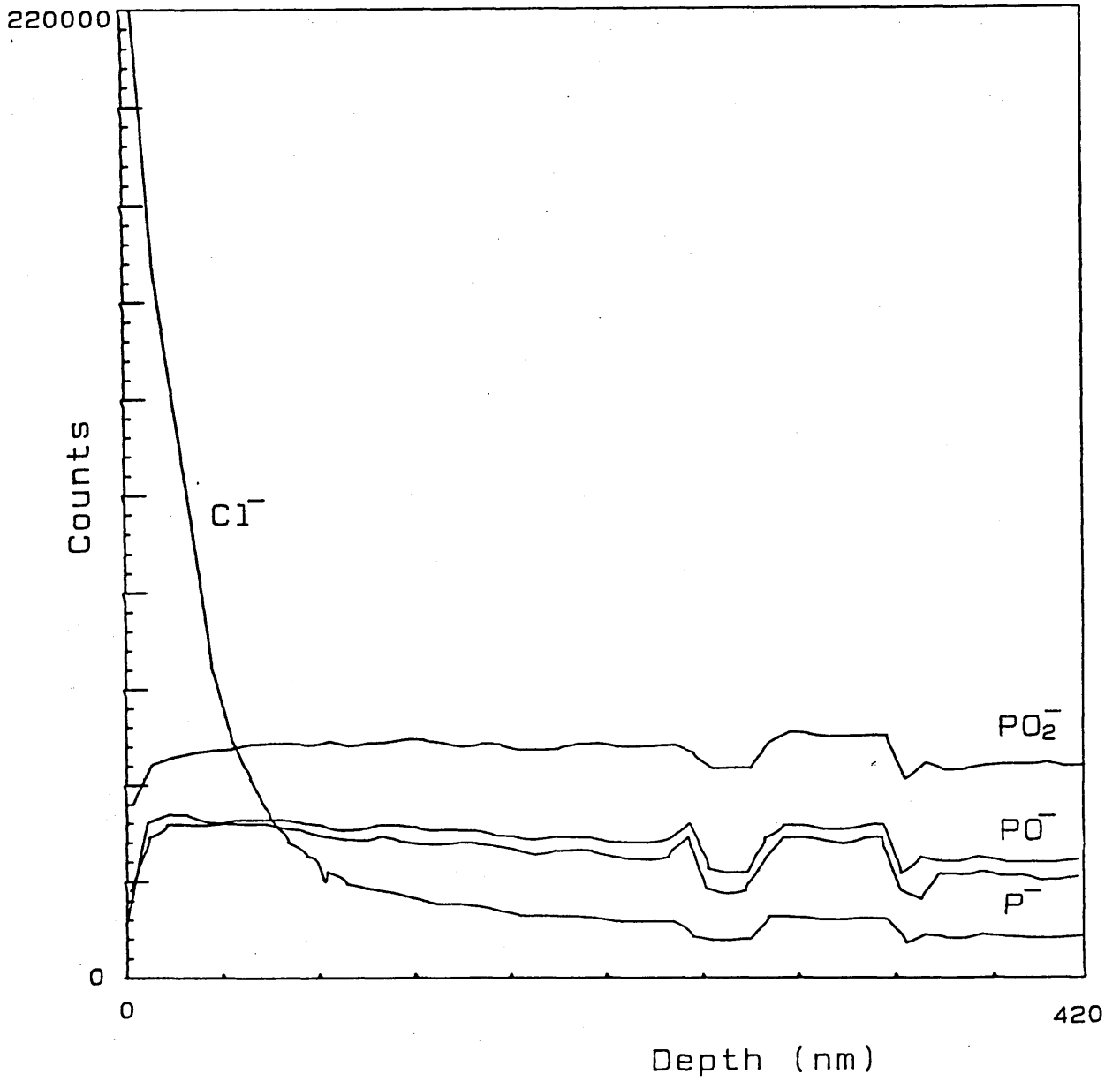

Figure 6.10 Negative ion dynamic SIMS depth profile of $43Na_2O$-$49P_2O_5$-$8Fe_2O_3$ glass after 4 days immersion in water

6.4 Discussion

The CEMS and SIMS studies have both indicated that there is a loss of iron from the surface region of these glasses as part of the dissolution process. The percentage effect observed for leached glass samples was at least two thirds that of the same unleached glass recorded under identical CEMS experimental conditions. This is supported by the SIMS data which showed a marked depletion of iron upto ~ 60nm into the glass, the surface region which would account for the majority of backscattered electrons. The SIMS analyses also revealed the depletion of sodium ions from the glass surface in accordance with the Van Wazer theory of phosphate glass durability (§1.3.2). However, the static SIMS spectra did not locate any structural water which should in part replace the network cross-linking sodium ions. The water is presumed to be sufficiently weakly bound to the phosphate network to be removed by the surface cleaning and drying procedure prior to analysis. The leached glasses did not cause any decrease in the quality of the Microlab vacuum, supporting the conclusion that little or no volatile molecules were present on the glass surface.

Taking as an example an average chain length of ten PO_4 tetrahedral units the depletion depth of sodium and iron (~ 60 nm) corresponds to at least 30 linear phosphate chains. The modifier free surface will be much less durable than the unleached glass and hence the phosphate chains will rapidly pass into solution. This accounts for the high, linear dissolution rates obtained for these iron-phosphate glasses.

6.5 References

1. Stevens J.G.; Stevens V.E.
   Mössbauer Effect Data Index, 1974, p.56

2. Swanson K.R.; Spijkerman J.J.
   Journal of Applied Physics, 41, 3155, 1970

3. Thomas J.M.; Tricker M.J.; Winterbottom A.P.
   Journal of the Chemical Society, Faraday Transactions 2, 71, 1708, 1975

4. Eaton T.W.; Smith R.
   unpublished

5. Atkinson R.; Cranshaw T.E.
   Nuclear Instruments and Methods in Physics Research, 204, 577, 1983

6. Kiselev A.A.; Kuz'min R.N.; Novakova A.A.
   Soviet Technical Physics Letters, 12(1), 14, 1986

7. Frost J.C.; Cowie B.C.C.; Chapman S.N.; Marshall J.F.
   Applied Physics Letters, 47(96), 581, 1985

8. Biñczycka H.; Sawicki J.A.
   Journal of Physics D : Applied Physics, 16, 197, 1983

9. Vickerman J.C.
   Chemistry in Britain, 23, 969, 1987

10. Benninghoven A.; Rüdeneuer F.G.; Werner H.W.
'Secondary Ion Mass Spectrometry', Wiley and Sons, 1987, p.219

11. Seah M.P.
Thin Solid Films, 81, 279, 1981

12. Odelius H.; Lodding A.R.E.; Werme L.O.; Clark D.E.
Scanning Electron Microscopy, 3, 927, 1985

13. Schreiner M.; Stingeder G.; Grasserbauer M.
Fresenius' Zerischrift fuer Analytische Chemie, 319, 600, 1984

14. Clark D.E.; Lodding A.R.E.; Odelius H.; Werme L.O.
Materials Science and Engineering, 91, 241, 1987

15. Gregory G.E.; Worth A.
unpublished

16. Benninghoven A.; Rüdeneuer F.G.; Werme H.W.
'Secondary Ion Mass Spectrometry', Wiley and Sons, 1987, p.209

CHAPTER SEVEN - CONCLUSIONS

The initial stages of this research program involved the production of a range of iron-phosphate glasses. It proved difficult to achieve all of the desired compositions because of the volatile nature of the required phosphate salts and the complex set of parameters controlling the glass formation. The mastering of these factors led to a significant reappraisal of the realistic glass composition limits, given the required time scale and available apparatus. Glasses from two distinct families were made. The first were Na_2O/K_2O - phosphate glasses with additions of up to 25 mol.% Fe_2O_3, whilst the second series contained, in addition, 20 mol.% CaO. All the glasses were produced under the same set of operating conditions, with the exception of a small number of sodium-iron-phosphate glasses produced under an argon atmosphere. The inaccuracies inherent in the glass production technique necessitated the use of ICP spectroscopy to ascertain their actual molar composition.

The composition of the glasses had a marked influence on their water durability, with dissolution rates ranging from $10^{-5}mg/mm^2h$ up to $10^{-2}mg/mm^2h$. The replacement of Na_2O by K_2O led to a ten fold decrease in durability due to the greater ease with which ionic K^+ cross-links could be hydrolysed. The replacement of Na_2O by P_2O_5 in a simple sodium-iron-phosphate glass system led to a minimum durability for a Na/P ratio of unity. This result is not in agreement with the Van Wazer theory of phosphate glass durability and must be attributed to the influence of Fe_2O_3 on the glass structure. In the $xNa_2O\_20CaO\_(78-x)P_2O_5\_2Fe_2O_3$ glass system the durability was seen to decrease by a factor of sixty as the Na_2O content increased from x=6 to x=41.

All the glasses dissolved at a linear rate indicating that the rate controlling step was the disentanglement of the phosphate chains subsequent to the leaching of modifier cations from the surface region. This was confirmed by SIMS studies which showed a depletion of Na^+ and Fe^+ in the top ~ 60nm of the degraded glasses and also by CEMS studies which yielded poorer quality spectra from degraded glasses indicating a lower iron content.

Transmission mode Mössbauer spectra consisted of two broadened quadrupole doublets characteristic of octahedrally coordinated ferrous and ferric iron. For the sodium/potassium-iron-phosphate glasses no correlations were found between Mössbauer parameters describing the two doublets and the durability of the glass. However, some substantial variation in the parameters was observed in the $Na_2O\_CaO\_P_2O_5\_Fe_2O_3$ glass system. An increase in Na_2O content coincided with an increase in the ordering of the ferrous iron sites and, by analogy, the Ca^{2+} sites. This ordering correlated with a decrease in glass durability.

The simple two doublet approximation to the iron-phosphate glass spectra was dramatically improved by implementation of a parameter distribution program PQH based on the method developed by Wivel and MØrup. After careful choice of the parameters constraining the distribution profiles this fitting procedure was able to confirm the presence of one type of ferric iron site and a second distinct ferrous iron type site within the majority of the glasses. The exceptions were glasses produced under argon which showed at least two types of ferrous site and some of the CaO containing glasses which revealed more than one type of ferric site. It appears that the two types of iron site are preferentially occupied by ferric and ferrous iron, but when all of the iron is

forced into either the ferric or ferrous oxidation state then it must occupy both types of site, resulting in asymmetric distribution profiles. The Mössbauer parameters indicate that both of the types of site are octahedrally coordinated, the physical difference between the two sites remaining unclear.

The spectra of three glasses were recorded over a temperature range of 12K to 600K using a closed cycle helium gas cryostat and an electric furnace. The absorption area data were fitted to the theoretical function incorporating the relevant Debye integral. The three data sets all yielded effective Debye temperatures of ~ 300K for the lattice. The effective Debye temperature for the ferric sites was always greater than the ferrous sites, indicating a difference in the recoil-free fractions of the two oxidation states. The average ratio at room temperature $f(Fe^{3+}) / f(Fe^{2+}) \simeq 1.2$. This factor has often been ignored in discussions of redox ratios in iron bearing glasses. Analysis of the second order Doppler shift (SODS) of the absorption lines was used to yield independent estimates of the Debye temperature. The Fe^{3+} Debye temperatures were considerably larger than those obtained from analysis of the absorption area data. This could be explained by reference to the statistical weighting applied to the vibrational modes in the two Debye expressions. For the three sets of Fe^{2+} data it proved impossible to obtain realistic fits to the SODS Debye integral. There was always an unexplained discontinuity in the data at ~ 300K.

The temperature dependence of the ferrous quadrupole splitting enabled estimates to be made of the perturbations to the energy levels of the $^5D_4$ orbital. The variation in quadrupole splitting is a result of the temperature dependence of $\Delta E_Q(val)$ and for the three glasses yielded $\Delta_1 \simeq 350\,cm^{-1}$. The

fits yielded a ΔE_Q(lat) component to the total ferrous iron quadrupole splitting of ~ 1.0 mm/s compared to ~ 0.5 mm/s for the ferric iron sites. This can be taken as an indication that the ferric iron sites are more ordered that the ferrous iron sites.

In summary these studies have demonstrated the presence of octahedrally coordinated ferrous and ferric iron in a range of soluble phosphate glasses. There appear to be two distinct types of site, one of which is preferentially occupied by Fe^{2+} and the other by Fe^{3+} ions. The more ordered type of site may be due to oxygen ligands attached to terminal phosphate groups, whilst the second, less ordered, type of site may correspond to iron ions coordinated to oxygens from the linear portions of phosphate chains. The oxygens attached to terminal groups will be subject to less steric hindrance and will thus be able to form more regular octahedra about the iron ions. Fe^{2+} preferentially occupies the less ordered type of site, but can be forced to occupy both if the Fe^{2+}/Fe^{3+} ratio is substantially increased. The presence of Fe_2O_3 in phosphate glass leads to a marked increase in durability, but for concentrations upto 25 mol.% Fe_2O_3, it does not hinder the congruent dissolution of the glass.

An important prerequisite for any further studies of iron-phosphate glasses would be an efficient and precise glass production technique. This requires a degree of experience on the part of the experimenter in view of the many operating parameters which must be controlled. By careful use of oxidising and reducing atmospheres and adjustment of melt time and temperature it would be possible to control the iron redox ratio in the final glass. This would enable the durability of the glass to be investigated as a function of

iron oxidation state. Iron in the ferrous state can be considered to occupy network modifying sites similar to other divalent cations including the alkaline-earth and many transition metals. Mössbauer studies would then yield structural information concerning the ionic cross-linking of the phosphate chains. The implementation of a Gaussian line fitting program would enable the quadrupole doublet distribution profiles generated by PQH to be deconvoluted in order to determine the number of types of iron site within a glass.

A more robust Mössbauer absorber furnace would allow the examination of the onset of softening of the phosphate glass via measurement of the temperature dependence of the absorption line area. With a stronger radioactive source spectra could be recorded quicker and it would be possible to systematically study any compositionally dependent trends in Debye temperature and crystal field splitting of iron-phosphate glasses. A low temperature facility seems essential for reasonable quality CEMS spectra to be recorded. However, the results presented in this thesis do not indicate the presence of any surface states in the degraded glasses, hence the resultant spectra would be expected to be identical to those of the bulk glass.

A natural extension to this work would be the study of actual CRG compositions rather than the considerably simpler model glass systems discussed in this thesis. Iron free CRG's could be doped with a small amount of Fe_2O_3 in order to enable Mössbauer analysis to be performed. This would yield considerable structural information and together with SIMS would enable the dissolution mechanisms of these highly versatile materials to be further investigated.

ACKNOWLEDGEMENTS

There is a collection of people whose efforts on my behalf have made the writing of this thesis a possibility and to whom sincere thanks and gratitude are due. Foremost on the list are Professor John Brooks, who admirably fulfilled the rôle of supervisor, providing much useful advice and encouragement and Dr. David Allen who must carry the credit for clarifying the chemical aspects of this work. I am indebted to Dr. Cyril Drake and Mary Tripp at Pilkington C.R.S. for useful discussions on glass production and for letting me loose with one of their furnaces. Sorry about the atmospheric pollution! Over my period at the polytechnic I have called on the services of many technicians and support staff, not only in the Applied Physics Department, but ranging into Chemistry, Metallurgy and Computer Services. Those warranting a special mention are Ann Wilson for much secretarial assistance; Roger Smith for considerable practical help in the Mössbauer laboratory; Terry Hudson for showing me how to turn the computer on; Gerry Gregory for operation of the Microlab and Alan Cox for help with I.C.P. analysis. To this long list must be added Sue Wainwright, of Type 2 Word Processing Services, who swiftly completed the onerous task of translating my scribble into English; the Department of Chemistry Research Staff Tea Club (Put the kettle on!) and finally the many friends and family who have sustained me over the past few years.

COURSES AND CONFERENCES ATTENDED

Courses:

Autumn 1986 'Introduction to Mössbauer Spectroscopy'

10 x 1 hour, S.C.P.

Conferences:

R.S.C. Mössbauer Discussion Group Meetings:-

July 1986 Nottingham University

July 1987 Royal Holloway College, University of London ***1**

July 1988 Manchester University ***2**

July 1990 Sheffield University ***1**

Third Seeheim Workshop on Mössbauer Spectroscopy

May 1988 Seeheim, F.R.G. ***2**

***1** Oral paper presented.

***2** Poster presented.